IAEA-TECDOC-1185

Iodine induced stress corrosion cracking of Zircaloy fuel cladding materials

INTERNATIONAL ATOMIC ENERGY AGENCY IAEA

November 2000

The IAEA does not normally maintain stocks of reports in this series They are however collected by the International Nuclear Information System (INIS) as non-conventional literature Should a document be out of print, a copy on microfiche or in electronic format can be purchased from the INIS Document Delivery Services

INIS Clearinghouse
International Atomic Energy Agency
Wagramer Strasse 5
P O Box 100
A-1400 Vienna, Austria

Telephone (43) 1 2600 22880 or 22866
Fax (43) 1 2600 29882
E-mail chouse@iaea org

Orders should be accompanied by prepayment of 100 Austrian Schillings in the form of a cheque or credit card (VISA, Mastercard)

More information on the INIS Document Delivery Services and a list of national document delivery services where these reports can also be ordered can be found on the INIS Web site at http //www iaea org/inis/dd_srv htm

PLEASE BE AWARE THAT
ALL OF THE MISSING PAGES IN THIS DOCUMENT
WERE ORIGINALLY BLANK

The originating Section of this publication in the IAEA was:

Nuclear Fuel Cycle and Materials Section
International Atomic Energy Agency
Wagramer Strasse 5
P.O. Box 100
A-1400 Vienna, Austria

IODINE INDUCED STRESS CORROSION CRACKING OF
ZIRCALOY FUEL CLADDING MATERIALS
IAEA, VIENNA, 2000
IAEA-TECDOC-1185
ISSN 1011–4289

Printed by the IAEA in Austria
November 2000

FOREWORD

This report documents the work performed by the Co-ordinated Research Project (CRP) on Stress Corrosion Cracking of Zirconium Alloy Fuel Cladding. The project consisted of out-of-pile laboratory measurements of crack propagation rates in Zircaloy sheet specimens in an iodine containing atmosphere. The project was overseen by a supervisory group consisting of experts in the field, who also contributed a state of the art review.

The study was undertaken in the framework of a CRP, with work carried out by a host laboratory and four laboratories from different developing countries. Besides the basic goal of obtaining stress corrosion cracking data, a secondary goal was the transfer of know-how at the laboratory level from the host laboratory and supervisory group to the four target institutes from developing Member States. Stress corrosion cracking experiments in iodine are notoriously difficult to carry out successfully.

The basic scope of the programme was originally formulated by the IAEA and the host laboratory in late 1992. Equipment was set up and qualified and a test procedure was devised during 1993. In early 1994 the supervisory group was formed and invited to review and oversee the programme, to finalise the test procedure and to select the participating laboratories. The CRP began formally with the signing of contracts in mid-1994. The first research co-ordination meeting (RCM) was held at the end of 1994, where the participants were briefed, the test matrix defined and samples distributed. Further RCMs were hosted by two of the participating laboratories in 1995 and 1997. Supervisory group meetings were also held at regular intervals to review the results obtained. Following the third RCM a one year extension to the programme, involving a further round of experimental tests, was proposed. This was endorsed by the IAEA in April 1998. The programme was completed and documented at the end of 1999.

This report describes all of the work undertaken as part of the CRP, and includes: a review of the state of the art understanding of stress corrosion cracking behaviour of zirconium alloy cladding material; a description of the experimental equipment, test procedures, material characterizations and test matrix; discussion of the work undertaken by the host laboratory and the specific contributions by each of the four participant laboratories; a compilation of all experimental results obtained; and the supervisory group's analysis and discussion of the results, plus conclusions and recommendations.

The IAEA wishes to thank the participants in the CRP and the members of the supervisory group for their contributions to this publication. Special thanks are also due to the host laboratory AEA Technology at Risley, United Kingdom, funded for the work in the CRP by British Nuclear Fuel Limited, and the fuel cladding vendors, Teledyne Wah Chang, Albany (United States of America) and Cezus (France) who kindly provided materials for study in the CRP. The IAEA officer responsible for the compilation of this TECDOC was I.G. Ritchie of the Division of Nuclear Fuel Cycle and Waste Technology.

EDITORIAL NOTE

The use of particular designations of countries or territories does not imply any judgement by the publisher, the IAEA, as to the legal status of such countries or territories, of their authorities and institutions or of the delimitation of their boundaries.

The mention of names of specific companies or products (whether or not indicated as registered) does not imply any intention to infringe proprietary rights, nor should it be construed as an endorsement or recommendation on the part of the IAEA.

CONTENTS

SUMMARY

This report documents the work performed during the Co-ordinated Research Project (CRP) on Stress Corrosion Cracking of Zirconium Alloy Fuel Cladding. The aims of the programme were to investigate pellet-clad interaction (PCI) failure, which is a licensing concern for many water reactor fuel designs. Failure propensity is at present generally assessed using empirical methodologies. Replacing empiricism by mechanistic models of the underlying processes is a desirable long term goal, which would have the advantage of facilitating the analysis of multiple power ramp events and non-standard fuel designs, and would help to reduce unnecessarily conservative constraints on reactor operation. One requirement of this mechanistic approach is to obtain information on the rate of crack propagation in Zircaloy materials stressed in an iodine environment. The purpose of the present CRP is to provide basic data on this phenomenon for a selection of different materials, using a matrix of different temperature and iodine levels, with the work conducted at five different laboratories around the world.

The major variables influencing stress corrosion cracking in these alloys are metallurgical state (including composition, orientation, thermo-mechanical treatment, texture and cold work), environment (composition, concentration and temperature) and stress. It was not feasible to investigate the effects of all these variables within the scope and time-scale of the programme. The test programme was thus focused on determining the dependency of stress corrosion crack propagation rate on temperature, iodine concentration and stress within the range of available materials. It was recognised at the outset that the use of unirradiated material and iodine vapour at relatively high concentrations would give crack propagation values not directly applicable to in-reactor behaviour. In PCI failures in cladding, the crack propagates in the radial direction under a hoop stress from thermal expansion of the fuel pellets. In sheet material, the analogous direction is the short transverse, i.e. with the crack growing through the sheet thickness. Two critical decisions were made at the outset of the CRP which influenced the specimen design. These were both associated with the practical experimental difficulties of initiating and monitoring the growth of a crack in these orientations in cladding and sheet material, particularly where one of the major aims of the CRP was technology transfer to the participating laboratories. Accordingly, the supervisory group of the CRP decided to use sheet material for the specimens rather than cladding tubing. It was also decided not to try to generate data in the short transverse direction, but that the crack should propagate in the longitudinal (rolling) direction instead.

In retrospect, the choice of test method did not make it easy for the participants to reproducibly obtain good stress corrosion cracking data from the specimens supplied. This arose primarily for two reasons. Firstly, by selecting a uniaxial rather than a biaxial stressing method, even though the specimens were fatigue pre-cracked, there was a tendency to blunt the crack tip if the chemistry conditions were not ideal. This resulted in much plastic deformation of some specimens. Secondly, the use of a uniaxial system generally resulted in participants building rather large specimen chambers that made it more difficult to achieve the right chemistry conditions at the crack tip. This situation was sometimes rendered more difficult by the use of high I_2/He flow rates that inhibited the development of the right chemical environment. Thus, for some of the participants, the CRP developed into an exercise in learning how to reproducibly obtain iodine stress corrosion cracking, rather than in the gathering of data which could be compared with the other results. Most participants had solved these problems by the originally planned end of the CRP. In the process, however, many of the original batch of specimens were tested unproductively. In order to capitalise on the learning that had occurred, an extension of the CRP was approved to test a new set of

specimens. The following summarises the results from the participating laboratories in terms of the main experimental variables.

Effect of creep

During the course of the experimental work, it was found that, at the beginning of a new experiment, significant changes in direct current potential drop (DCPD) could be measured without any observable crack propagation. This led to the consideration of a possible contribution of creep to the electric resistance changes of the sample, as measured by the DCPD. Since creep deformation reduces the cross section of the sample, the electric resistance of the sample is indeed expected to increase during these experiments, giving outputs that could be considered as crack growth. In order to evaluate this phenomenon, several samples were tested, in an inert environment to avoid crack growth, and the DCPD recorded. It was found that the creep contribution could give an output in DCPD corresponding to crack growth rates in the range of 10^{-7} to $3 \cdot 10^{-6}$ mm.sec^{-1}, depending on the applied load and on the time since the last increase in load. Indeed, it behaved like creep, i.e. high initial strain followed by slow constant deformation rate (primary and secondary creep). In addition, the creep rates were strongly dependant upon the applied stresses and any increase in applied load induced a new transient creep. Due to the lack of samples and time, these measurements were performed for only a few test conditions, not allowing a complete description of the phenomenon. The corrections required by this contribution have therefore not been performed, but restrictions have to be considered for the early measurements in crack growth rate (CGR) below these values, especially at the beginning of an experiment. For further work in this area using the DCPD technique, careful corrections should be performed, with respect to this creep contribution.

Effect of temperature

The test matrix included tests at three temperatures: 300, 350 and 400°C. The results from the participants do not show a clear, consistent effect of temperature on the threshold stress intensity factor or the crack propagation rate in the Stage II region. The host laboratory and the Argentinean and Chinese participants found $K_{I\text{-}SCC}$ to decrease with increasing temperature. The Argentinean and Chinese results also showed the Stage II crack propagation rate to increase with temperature. Scatter in the Korean results masked any temperature effect in their tests. Temperature would be expected to influence SCC due to its effect on the mechanical properties of the material and on the diffusion rate of iodine. This would be expected to produce a reduction in $K_{I\text{-}SCC}$ and increase in Stage II crack propagation rate as found in most of these tests.

Effect of material condition

Five materials were tested from two manufacturers. These were recrystallised Zircaloy-2 (Zr-2) and Zircaloy-4 (Zr-4) and stress-relief annealed Zr-4. By determining X-ray pole figures, each was shown to have a similar texture, so any effect on I-SCC would be expected to arise due to the effect on the mechanical properties and grain shape of the different heat treatments. The results from the host laboratory and the Korean participant were consistent with this, with both finding a higher $K_{I\text{-}SCC}$ for recrystallised materials compared to the stress relief annealed Zircaloy. The Argentinean and Chinese results were inconclusive in this respect.

Effect of iodine partial pressure

Iodine pressure was studied in the range 100 to 10 000 Pa I_2. Both the host laboratory and the Argentinean participant found no effect of iodine pressure on $K_{I\text{-}SCC}$. The Argentinean

tests on stress relieved Zr-4 and the Chinese results on recrystallised Zr-2 indicated an increase in Stage II crack growth rate with increasing iodine concentration. These results are consistent with literature observations of a threshold iodine concentration and with crack propagation being diffusion controlled, so that a higher external iodine concentration will produce more rapid diffusion of iodine to the crack tip and hence higher crack propagation rates. This latter effect has also been shown to saturate once sufficient iodine is present. The supervisory group believe that the iodine replenishment rate in the test chambers varied markedly between laboratories, so that the true iodine concentrations in each test were unlikely to be consistent between laboratories.

Effect of texture

The CRP was extended in order to capitalise on the improvements in test facilities and experimental technique of the participants, both from the advice provided to them by the supervisory group, and from their increased experience in performing the tests. All previous tests in the CRP were performed on specimens in the TL orientation, so the additional series of tests were to generate crack growth data in the opposite, LT, orientation. From texture considerations, SCC was expected to be more difficult in the LT specimens, producing a higher $K_{I\text{-}SCC}$. This was found to be the case by the host laboratory and the Argentinean participant. For the Korean participant, there remained too much experimental scatter for any firm conclusions on $K_{I\text{-}SCC}$ to be drawn. The Chinese found no difference between TL and LT oriented specimens.

Fractography

One important aspect of any experimental programme on iodine SCC of zirconium alloys is the fractography of the crack surfaces produced. The features to be expected are by now well known, and the extent to which they are observed can be very helpful in understanding the test results. The features that would be expected are:

(a) Transgranular pseudo-cleavage on the basal planes of suitably oriented zirconium grains.

(b) Prismatic slip on the planes of the zirconium hexagonal prism surfaces, giving rise to the very characteristic feature termed "fluting" because of the similarity of its appearance to that of a fluted pillar.

(c) Intergranular separation along the grain boundaries to reveal the characteristic grain shape of the metal.

(d) Some ductile tearing of residual webs in the fracture surface.

By the end of the CRP most laboratories were obtaining good fractographs showing the above features. One interesting general observation was the infrequency of fluting in these tests. The fracture surfaces obtained were a mixture of transgranular cleavage facets and grain boundary surfaces, with few fluting features, or their complete absence. Since the textures of these sheets were such that there should have been many grains in the crack propagation plane oriented for prismatic slip, rather than basal cleavage, the absence of fluting suggests that intergranular separation proved to be easier than prismatic slip as a crack propagation mechanism for the material used in this programme.

One other feature of the fractography produced from some tests was the extent of oxidation of the crack surfaces that occurred after the crack had passed. This is symptomatic of inadequate purity of the helium used to transport the iodine in the apparatus, or to a poor design of equipment that made it difficult to properly purge the corrosion chamber. By the end

of the CRP the heavy oxidation of the fracture faces was becoming less frequent, but was never completely eliminated from some of the experiments.

General comments

At the end of this programme, it appears that some comments specific to a particular participant could be of interest to all of them, or to any one interested in performing similar experiments. They are listed as the following points:

- When using a DCPD technique for the measurement of crack growth rates, any experimental contributions to the DCPD output should be carefully checked: current stability, electronic equipment drift, variations in electric current bypass through the loading frame, stability in temperature of the "cold end" of the wires used for potential drop, to avoid thermoelectric contribution to the output. At the beginning of a series of tests, one should try to evaluate them and extract a range of validity of the results.
- For crack propagation tests on rather thin plates, 1 mm in the case of this CRP, the high values of K_I are not valid according to fracture mechanics, and the results should be cut off at some reasonable maximum stress intensity factor value.
- In such experiments, the loading is often applied using an amplifying lever. In order to avoid any misunderstanding, it is recommended that the load be expressed as the one applied on the sample (or the corresponding stress) instead of the weight on the lever. In addition, due to the creep contribution during the initial loading, it is required that the loading changes be applied using a specific device to avoid impact overloads.
- The control of the atmosphere in these experiments is difficult and the amount of oxygen in the testing chamber has to be reduced to a minimum. Flushing out of the chamber has to be done several times before testing, and the sweeping flow during the test has to correspond to a renewal of the chamber environment in a few minutes. The observation of any sign of oxidation on the fracture surface after failure is a good check of this point.

Recommendations

If further studies in this area are proposed it is suggested that the following changes in methodology should be considered:

(1) For major improvements in this area, future experiments should be performed on typical LWR fuel cladding.
(2) The limitations on measuring crack velocities in the radial direction would still be present, but crack propagation in the radial longitudinal plane would probably be acceptable.
(3) Notched and pre-fatigued specimens are to be preferred. A number of possible specimen geometries are available.
(4) A static rather than dynamic loading technique should be maintained since this is closest to the conditions during in-reactor PCI events.
(5) Rate of loading should be considered as a variable.
(6) Specimen chamber volumes should be minimized to improve control of the iodine atmosphere.
(7) Effect of time after iodine release (incubation time) on the cracking potential of the environment should be considered as a variable.
(8) After each test, a fractography using scanning electron microscopy (SEM) at sufficiently high magnification that individual grains could be visualised, should be performed to check the mechanism of fracture and the occurrence of any unwanted oxidation.

Chapter 1

A REVIEW OF THE CURRENT STATE OF THE ART FOR IODINE INDUCED STRESS CORROSION CRACKING OF ZIRCONIUM ALLOYS

1.1. INTRODUCTION

Pellet-cladding interaction failures of Zircaloy clad UO_2 fuel were first discovered during the testing of high powered fuel at General Electric (GE) Vallecitos in 1963 [1.1], and research showing that stress corrosion cracking by iodine was a probable explanation was published by Hermann Rosenbaum in 1965 [1.2,1.3]. For a number of years after that PCI failures were infrequent, and were observed in a few loop tests where significant upratings of fuel occurred. It became evident that an epidemic of failures was starting when on-load refuelling in the CANDU-prototype reactors NPD and Douglas Point started in 1969, and the situation became serious with the start-up of Pickering-1 (the first CANDU full-scale plant) in 1971. As a result of this a crash programme to develop a cure was instituted by AECL, and the CANLUB graphite coating was tested and adopted for all new fuel by the end of 1972 [1.4].

Similarly, the early occurrence of BWR fuel failures led to the development of another type of solution: a thin inner liner of low oxygen, soft pure zirconium was metallurgically bonded to the bulk of the cladding. The aim of this solution was to reduce the initiation rate of inner cracks by having a soft material and to reduce the stress level by improvement of the sliding of the UO_2 fragments on the inner surface of the cladding. This solution was indeed implemented and currently almost all the fuel assemblies delivered for BWR reloads are provided with "liner fuel" [1.5]. The improvement in reducing the failure rate is evident as it allowed the attainment of a failure rate below 10^{-5} [1.6]. However the processing of such duplex cladding is more expensive and cost reduction pressures led to research for the development of standard cladding with improved resistance to iodine induced stress corrosion (I-SCC). Nevertheless, a few PCI failures still occur in barrier cladding.

In addition, although PCI type failures are rarely if ever reported in PWR fuel during normal operation, new safety requirements now include consideration of this possibility. This led to extensive R&D work in this area. Its aim was to acquire a better understanding of the mechanisms involved in this failure mode and to develop new fuel cladding with improved resistance to I-SCC under some accident conditions [1.7,1.8]. The same requirements led to comparable R&D work performed on Zr-1-%Nb Russian cladding alloy [1.9-1.12].

In order to duplicate PCI failures, power transient tests were performed on various fuel rodlets in test reactors. Fuel rods obtained from different reactors at different burnups were inserted in irradiation devices, after a specific refabrication process in order to shorten them. Moving them closer to the reactor core, or removing neutron absorber ^3He from coils surrounding the device, induced power increases in the fuel rodlet. Depending on the test irradiation conditions, a cladding failure may be observed or not.

Among the conditions controlling the fuel cladding behaviour, several parameters have been observed to have major contributions.

- The maximum power is often considered as a criterion for failure. Typical results are given in Fig.1 1. The maximum power that a fuel rod can support is plotted versus the

burn up. Starting at a high power at beginning of life, in the presence of a large initial gap and fresh fission product free fuel, the maximum power sustainable reduces to reach a stable value above a burn up of about 20 $GWd \cdot t^{-1}$. The answer to the question of whether or not this failure limit may increase again at high BU is still pending [1.7].

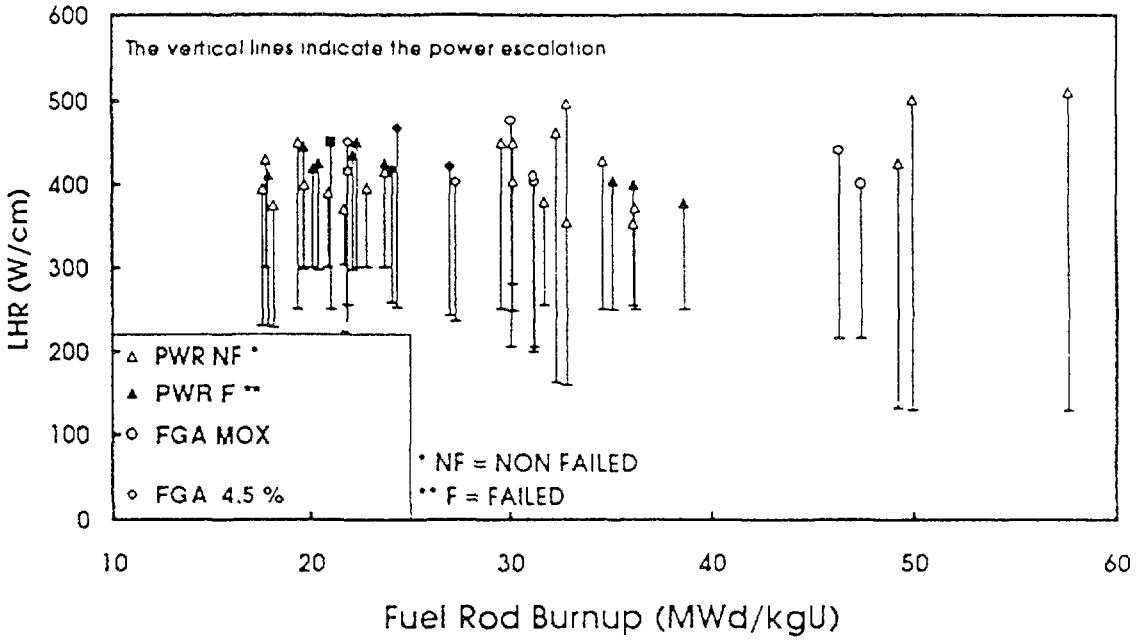

Fig.1.1. Maximum power allowed during a transient showing the failure/non failure limit as a function of burnup.

- A closer analysis of the conditions causing PCI failures allowed the introduction of other factors. Among these the power increase between the stable conditions before the power ramp and the maximum power reached. The process responsible for failure requires a consideration of the dynamic thermo-mechanical equilibrium between cladding and pellet. Indeed, the stress state in the cladding during the transient is controlled by the contact conditions between pellet and cladding. This is termed "conditioning" and focuses on the fact that the stress state of the cladding is relevant to the PCI failure mechanisms.

- The third factor is linked with the power change rate. Several experiments have been performed with very slow power changes. Maximum power levels well above the standard values were obtained without failure. Detailed thermo-mechanical analysis were able to show that during slow power ramping the cladding and the pellet will creep, reducing the stress state of the former [1.13].

All these observations are in agreement with a mechanism based on stress corrosion, where stresses are induced by thermo-mechanical interaction between pellet and cladding due to thermal expansion and the corrosive species being a fission product.

Various reviews have led to the conclusion that a compound of iodine should be the chemical species involved. Indeed, it has a relatively high fission yield, is known, as is any

halogen, to react with the IV B elements and experimental I-SCC has similar fracture surfaces to the those obtained during PCI test failures. However, it remains unclear whether iodine itself, or some compound resulting from reaction with zirconium, is the actual active species.

The aim of this review is to give a overview of the present understanding of I-SCC of Zr alloys.

1.2. PELLET–CLADDING INTERACTION AND IODINE INDUCED STRESS CORROSION CRACKING (I-SCC)

The first question requiring an answer relates to the exact chemical species involved in the I-SCC during PCI failure. Indeed, the chemical state of the different fission products has been a matter of extensive study for the high power rated fuel (as in fast neutron reactors), but in the water reactors, the thermal conditions are too low to obtain a thermodynamical equilibrium between all of them within the fuel [1.14]. However, it is well known that iodine has a significant fission yield (^{127}I and ^{129}I, considered as stable sum to 1.25 % in thermal reactors), but it is exceeded by Caesium (the 133, 135 and 137 isotopes have a total yield of more than 18.5%). Thus, it is expected that any iodine released will be trapped by a larger amount of caesium. Standard thermodynamics will lead to an insignificant iodine vapour pressure in the case of excess of Cs. More detailed computations with consideration of all the fission products having a significant yield (Mo, Zr, Ru, Ce...), gave similar conclusions. Nevertheless, the highly radiolytic environment in the gap, due to fission product recoils, continuously generates radical species like iodine atoms or ions, that will be able to react with any material instead of remaining trapped on other chemical compounds. Computations performed initially for breeder fuel and later extended to water reactor fuel have proven the possibility of a raise in the iodine partial pressure to $3 \cdot 10^{-10}$ atm, high enough to induce an I-SCC phenomenon [1.15]. Experiments using gamma irradiation in order to induce radiolysis lead to the same conclusions [1.16].Thus, the question of the availability of iodine is no longer valid and I-SCC is clearly a mechanism of high importance with respect to PCI failures.

The state of our understanding of PCI cracking in connection with I-SCC, can be summarised as follows:

- There was a degree of certainty that the culprit was iodine or an iodine compound and not a caesium/cadmium mixture, based on detailed fractography of the fuel failures [1.17].

- It had been established that, provided the fuel remained in a high power position for no more than half an hour, the probability of failures was small. Much higher failure frequencies occurred if the residence time at high power was between a half and two to three hours, and all the failures that were likely to occur had happened during this period [1.18].

- This apparent "incubation period" was also observed in laboratory testing (Fig. 1.2) and was thought to be a real phenomenon associated with the SCCC cracking process [1.19].

- The graphite coating was shown to both lubricate the UO_2/Zircaloy interface and to absorb the iodine in the form of a carbon stabilised zirconium iodide complex [1.20]. There remain some doubts about the precise chemical form in which the effect of the iodine is neutralised in the presence of a graphite coating.

- The observation of very rapid fuel failures (<1 minute) in some Swedish ramp tests cast doubt on the actual cause of the "incubation period" [1.21], although "pre-soaking" the fuel before ramping appeared to be necessary in order to obtain the very rapid failures.

- Tests in the laboratory using a cam-driven stressing system that could apply loads for very brief (<10 seconds) periods showed that it was necessary to allow the chemistry within the fuel cladding to come to equilibrium for about 30 minutes before it was possible to initiate a crack by a single <10 s stress pulse. It was clear from this work that getting the chemistry right was the essential feature of the "incubation period", and that I_2 vapour was not the key aggressive species [1.22].

- Unfortunately, funding to pursue these chemical studies to establish the form of the key species (ZrI_4, ZrI_3 or ?) was never forthcoming.

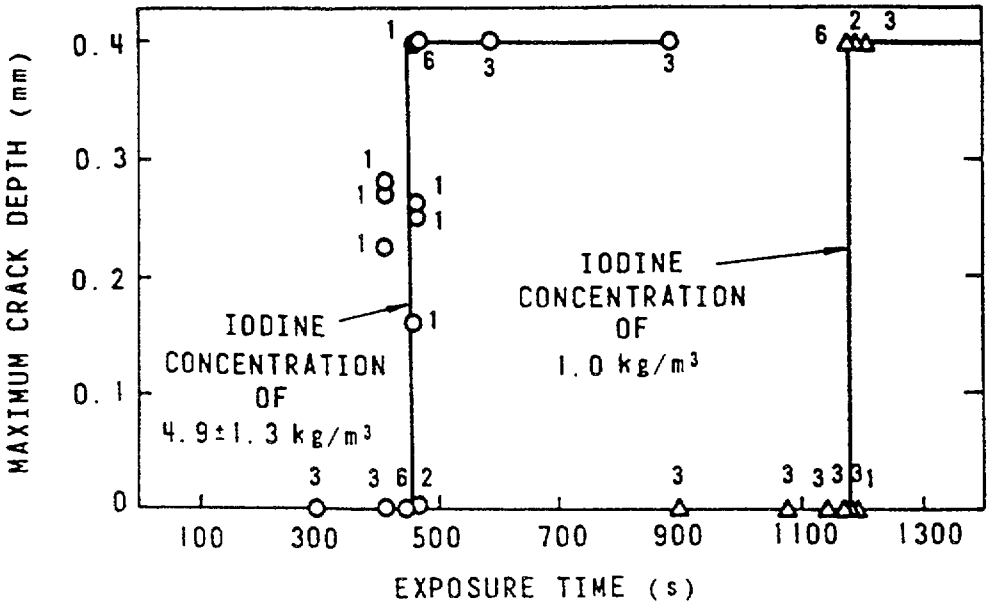

Fig. 1.2. Exposure time dependence of iodine-vapour-induced SCC.

It is possible to distinguish *four* distinct stages in the cracking process. The experimental conditions and the mechanisms operating during each of these stages will be discussed under the following headings:

- The incubation period
- Crack initiation
- Crack propagation through the tube wall
- Tubing degradation after wall penetration

1.2.1. The incubation period

Whatever the method used for studying iodine-induced SCC of Zircaloys, there appears to be an initial period when no crack-like features can be found in the highly stressed regions of smooth specimens. The length of the incubation period varies with the test method and the

testing conditions, but is always there, even for pre-cracked specimens, although it may be short in this instance. Incubation times appear to be longer for statically loaded specimens (20-30 minutes) than for dynamically loaded specimens (2-3 minutes), although this may be more apparent than real. Thus, static testing usually involves stressing the specimen before loading into the corrosive environment, and specimen and environment are usually brought up to temperature simultaneously with the specimen continuously under load. By contrast, dynamically loaded specimens are usually brought up to temperature in an unloaded condition, and may also have the corrosive environment added and equilibrated before loading the specimen.

The evidence obtained at Chalk River [1.22] suggested that I_2 vapour was not the most aggressive species and that chemical changes occurred in the environment (during the incubation period) without which a crack could not be initiated upon loading the specimen. The species being produced chemically during this period were never identified, so there is no advantage to speculation on what they might be. The more aggressive nature of ZrI_4 as the active species is still not enough to demonstrate that this is the key species. It appears that "incubation times" are still observed when adding ZrI_4 to the system, so further chemical modification of this species may be occurring during this period. The possibility that the process may be autocatalytic, with some minor alloying element or impurity as the catalyst cannot be eliminated on current evidence.

Such an interpretation of the incubation period can explain the need to pre-soak fuel if fast failures are to be obtained in ramp tests in-reactor, and to equilibrate laboratory specimens in the unstressed condition if rapid crack initiation is to be obtained. It emphasises the importance of the experimental start-up procedure on the results obtained, and raises the possibility in a flowing system that, if iodine flow rates are too high near the specimen, *no* cracking may be obtained.

A possible explanation of the incubation time may be linked with the time necessary for the chemical environment to react with the protective oxide layer always present on any Zr alloy sample and to weaken it. After this chemical reaction the SCC process will occur by interaction between the iodine bearing environment and the base metal. In this respect, the possibility of cracking fuel rod cladding during very short power transients [1.21] can be explained by the local absence of any oxide layer on the inner wall of the cladding, due to dissolution of the oxide layer in the base metal, during any pre-conditioning treatment. It should be noted that the fractography of the cracks initiated during very short power ramp transients has never been published.

1.2.2. Crack initiation

If the specimen has been equilibrated at temperature in a static iodine environment (without external stresses) for long enough (20-30 minutes) then a short (<10 s) stress pulse to beyond the yield stress can initiate cracks in an initially smooth specimen. These cracks were found to be completely transgranular in nature, and were often only one or two grains deep [1.22, 1.23]. It appeared that the number of these initiation sites could be related to the frequency of basal poles in the circumferential direction [1.23].

The number of such initiation sites, for any one batch of cladding, was greatly increased (by a factor >10), however, by the presence of trace impurities of organic iodides [1.24]. Thus, it is clear that not all suitably oriented basal planes crack in the absence of these agents. Since the density of basal poles increases rapidly for all batches as one moves from the

circumferential towards the radial direction, it may be that the effect of the organic iodides is merely to reduce the normal stress necessary to obtain pseudo-cleavage. Thus, for a given set of experimental conditions, a much larger number of basal planes would see a resolved stress high enough to cause pseudo-cleavage. Since we have only a speculative understanding of the mechanism of pseudo-cleavage, it is not possible to be more rigorous about the above effects.

In other types of test, intergranular initiation can be quite common. The extent of intergranular cracking is greater in statically loaded tests; with thick walled cladding rather than the 0.4mm wall thickness CANDU cladding; and particularly for iodine solutions in organic solvents some of which give almost completely intergranular features [1.25]. Both intergranular initiation and propagation are thought to result from removal of material from the grain boundaries - specimens lose weight during cracking. In iodine vapour the mechanism is thought to be a version of the van Arkel process [1.19], whereas in organic solutions grain boundary dissolution (not necessarily electrochemical since the solutions are usually non-electrolytes) is thought to be the mechanism [1.25, 1.26]. Crack initiation at fractured hydrides is relatively uncommon and was peculiar to one or two batches of early CANDU cladding [1.27], and to tests at elevated temperature with excessive moisture in the container (e.g. initial in-reactor tests in CsI) [1.28].

1.2.3. Initiation mechanisms

The initiation mechanisms for stress corrosion cracking in other alloy systems have been studied in detail for several systems of environment and metallic alloys. Reviews may be found in the proceedings of recent conferences in that field. The majority of them are related to the most common case of Fe based alloys in aqueous environments. In these cases the electrochemical aspects have to be taken into account and the role of hydrogen is clearly demonstrated in most cases. For Zr alloys, specific behaviours have to be considered. They include the fact that our case of interest is limited to the conditions found inside a fuel rod during in-reactor operation: The metal is in contact with an H-free gaseous phase and the hcp Zr matrix is highly anisotropic. In addition the initial SCC crack has usually been intergranular, even if only a few grain depth; but very few actual in-reactor failures have been studied.

Due to the limited number of slip systems activated in Zr alloys (prismatic and to a limited extent pyramidal), the strain compatibility from grain to grain during straining (the Taylor problem) is of high concern. Indeed, the five independent slip systems are not available in zirconium alloys. Therefore, some experimenters have tried to correlate the occurrence of crack initiation at a grain boundary with the crystallographic orientations of the two adjacent grains. Kubo [1.29] found that a crack may occur when dislocations pile-up at a grain boundary, while the grain on the other side has no easy slip system for relaxing the stresses induced by this family of dislocations. In addition, he found that large Fe-bearing precipitates enhanced the formation of an intergranular crack.

Detailed experiments performed in CEA Grenoble [1.30] aimed at finding a quantitative relation between grain to grain misorientation and intergranular crack nucleation. It was found that, in Zry-4, the density of intergranular cracks increased with local strain, as shown in Fig. 1.3. In addition, the orientations of all the grains of 3 Zr miniature tensile samples were determined, using the Electron Back Scattering Pattern (EBSP) technique. This technique is based on the analysis of the variation of the back scattered electron intensity as the incident beam rocks around the normal incident angle. The variations are linked with the channelling

of the electrons along preferential directions, and thus give access to the local crystallography. Examination of the locations of the incipient intergranular cracks after slow tensile tests in iodine vapour at 350°C led to the conclusion that the major parameter controlling the position of the crack was not the grain to grain misorientation, but the orientation of the grain boundary plane with respect to the maximum tensile stress orientation: the more normal to the tensile stresses, the higher the probability for a crack to nucleate at this grain boundary. This result reduces the effect of grain to grain internal stresses that would be expected from the anisotropic thermal expansion coefficient of the Zr matrix. Indeed, a_c is about twice a_a, leading to internal stresses close to the yield strength after cooling from any heat treatments on textured material. However, it should be noted that, unlike in the case of the power ramp tests, in actual PCI failures observed in power reactors there was little or no evidence of local strain at the crack initiation sites. Strain was visible ("rabbit ears") at the ends of the short through wall PCI crack, and this occurred after the PCI process by water ingress when the cladding wall was penetrated.

After crack initiation, at a size of about one grain diameter, the crack will grow in width and depth along the grain boundaries. Observations on the initiation sites found in smooth tensile specimens tested in iodine allow the observation of a sharp difference between the initial inter-granular crack and the growth by pseudo-cleavage and fluting to be described later.

In laboratory tests performed in iodine vapour on non-irradiated materials, and in methanol/I_2 solutions on irradiated materials, close to the free surface, the intergranular crack grows to a depth of not more than 100 μm. By analysis of the depth of these cracks, an average intergranular crack growth rate can be calculated. It increases from 5 nm·sec^{-1} at

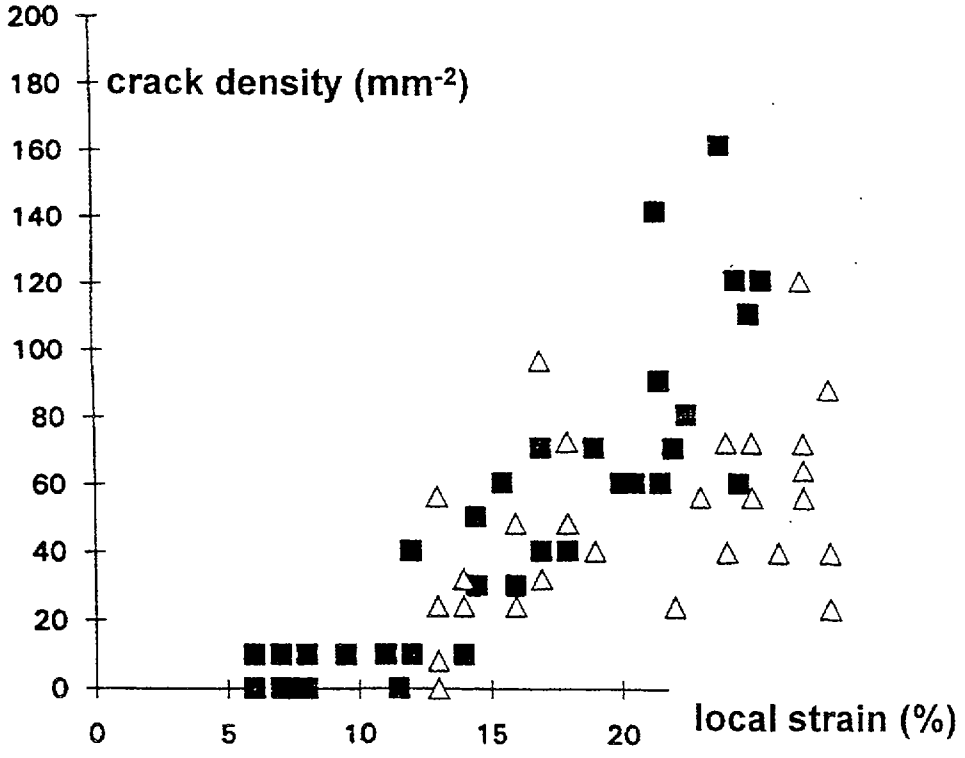

Fig. 1.3. Effect of local strain on initiation crack density during I-SCC cracking of a Zry-4 plate (350°C, iodine vapour) The square and triangles refer to two different samples.

300 MPa to 20 nm·sec^{-1} at 400 MPa [1.31]. The transition between the intergranular cracking mode and the pseudo-cleavage mode occurs when the stress intensity factor at the crack tip exceeds a critical value for transgranular SCC to proceed.

Similar work has been undertaken in the case of the Russian Zr-1%Nb alloy [1.11, 1.12]. Recrystallised WWER fuel cladding has been tested in the laboratory under internal pressure (120 to 220 MPa) at 320 and 380°C with an iodine content corresponding to a Zr surface concentration of 0.2 mg·cm^{-2}. Interruption of the tests before failure was used to analyse the effect of creep strain on intergranular crack density. Indeed, by varying the applied hoop stresses and the testing times, different hoop strains may be obtained as shown in Fig. 1.4. A careful examination of the inner surfaces of the cladding allowed the characterisation of the intergranular cracks: a minimum plastic strain was required for the formation of the intergranular cracks. Similarly to the Zircaloys, an increase in number of cracks with strain was found and their orientation density was higher when they were perpendicular to the tensile stresses. A semi-empirical relationship between crack density and hoop strain was obtained: $\mu(e) = A\,(e-e_{th})^m$, where A, e_{th} and m are experimental constants.

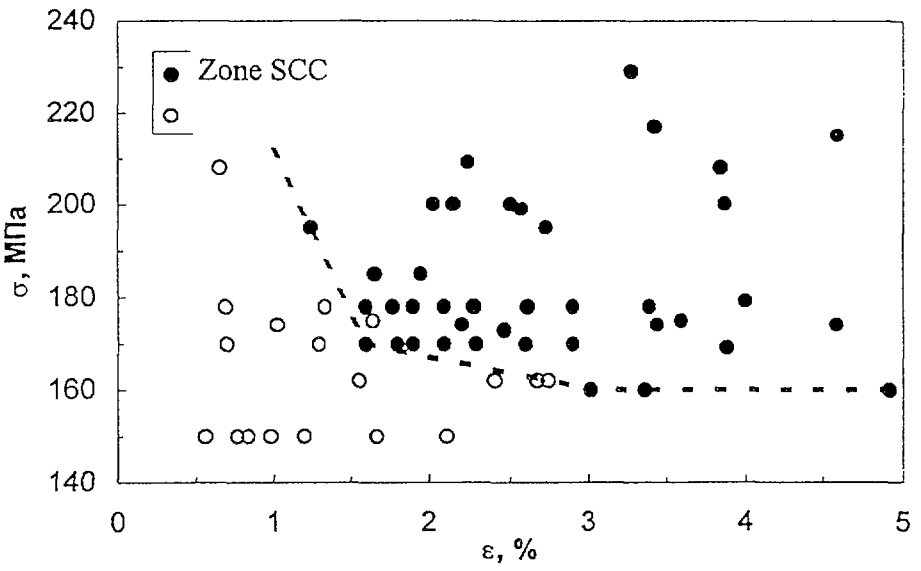

Fig. 1.4. Threshold conditions for the observation of I-SCC for Zr-1%Nb alloy in laboratory tests under internal pressure at 380°C.

Cross sections permitted the description of the shape in depth of the intergranular cracks: the crack opening displacement was found to increase slightly more than linearly with crack depth, according to the following relation:

$$\delta/c=0.173+0.0001c$$

where δ is the crack opening and c the crack length.

This allowed the growth of numerous cracks under SCC conditions to be followed. It was found that increasing the stress level above the critical value for initiation did not change the mean crack length. The surface density was increased mostly due to the nucleation of new

small size micro-cracks. Surface crack widening occurred faster than its increase in depth. This effect is clearly illustrated by the Fig. 1.5 where the aspect ratio of the cracks is plotted versus crack length: the more extended is a crack, the smaller its relative crack opening. This confirms the grain boundary nature of the crack propagation. Inner surface irradiation damage due to fission recoils.

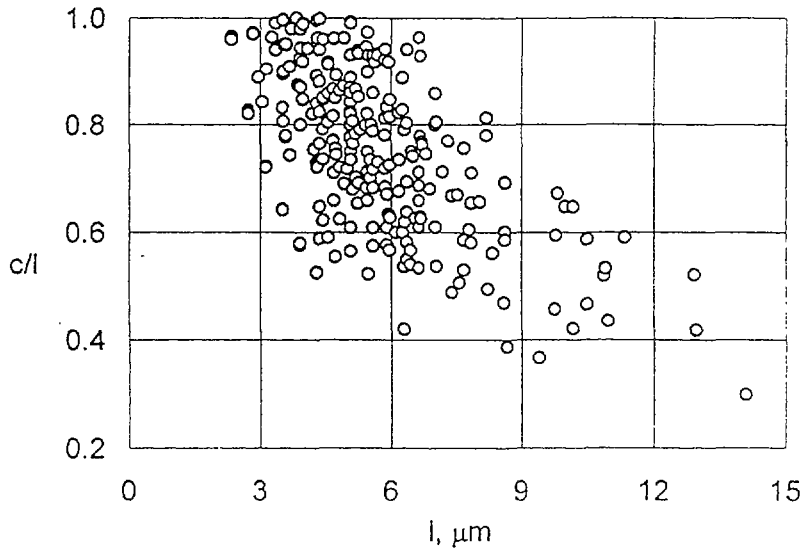

Fig. 1.5. Aspect ratio of the external mouth of I-SCC cracks versus crack length.

During irradiation, the fission fragments recoil from the original nucleus with energies in the range of 60-80 MeV. Due to their masses and to the density of the fuel and of the cladding, the typical ranges for these ions are between 6 and 8 μm. Thus, the inner cladding surface is slowly doped with the fission products throughout their ranges. In addition the rim region of a fuel pellet is a site of a higher fission rate due to the transmutation of ^{238}U to Pu by the epithermal neutrons. The computation of the amount of fission products within the cladding gives a value of about 5 % foreign atoms at the inner surface, declining to zero at a depth corresponding to the fission product range [1.32]. Most of these are deposited in the oxide formed on this surface which can be from 1-2 μm up to 10 μm as a function of the burn up.

The extensive damage induced by these recoils (well above 100 dpa), as well as the chemical doping corresponding to it, has been considered as a possible cause for the formation of a brittle surface layer that could ease the initiation step of the I-SCC process. Several experimenters have analysed in detail the consequences of such a surface irradiation on the susceptibility to I-SCC. Using different ions for the irradiation of the inner surface of Zr alloys plates or cladding, it was found that no significant cracking can be induced by this process [1.33]. The reason may be due either to the limited impact of the rather low level of the implanted iodine (about 120 ppm for two PWR cycles), or to the iodine having a very low diffusion coefficient in Zr [1.22, 1.34], so that it can not reach the grain boundaries [1.32].

1.2.4. Crack propagation through the tube wall

It is generally agreed that the cracks at the initiation sites grow, most often by intergranular corrosion, until the stress intensity at the crack tip exceeds a critical value named $K_{I\text{-}SCC}$. A faster, primarily transgranular crack propagation process then takes over. The transgranular pseudo-cleavage process occurs only on (or very close to) basal planes [1.35]. If

very few of these planes lie in the crack propagation plane then a large number of uncracked grains will be left behind the propagating crack front. These residual webs then fail either by ductile tearing on the prism planes (to give the characteristic fluting features), or by the slower intergranular corrosion process. Fluting is generally restricted to residual webs that are only one (or a few) grains thick [1.36]. If the transgranular cracking is widely dispersed and the residual webs represent a large fraction of the crack area then high stresses will be needed to fail the specimen and a mainly normal ductile fracture will occur by void nucleation and growth (Fig. 1.6).

The mechanism of the transgranular pseudo-cleavage process is not well understood. By elimination, it has been suggested that an adsorption-induced reduction in bond-strength at the crack tip is operating. A computation of the surface energy and its modification due to iodine adsorption shows a much higher reduction of basal plane surface energy, compared to other planes. Thus the pseudo-cleavage may be enhanced by the lowering of the surface energy of the <c> planes, making a favourable energy balance for crack propagation on these planes [1.37].

Other possible mechanisms can be eliminated since no electrochemical processes are possible in iodine vapour; cracking occurs in a hydrogen free system and when all internal hydrogen must be in solution (and hydride cracking is distinguishable fractographically) [1.38]; and, although heavy corrosion of the fracture surfaces may occur after the passage of the crack, no evidence for repetitive film growth and cracking processes has been found at

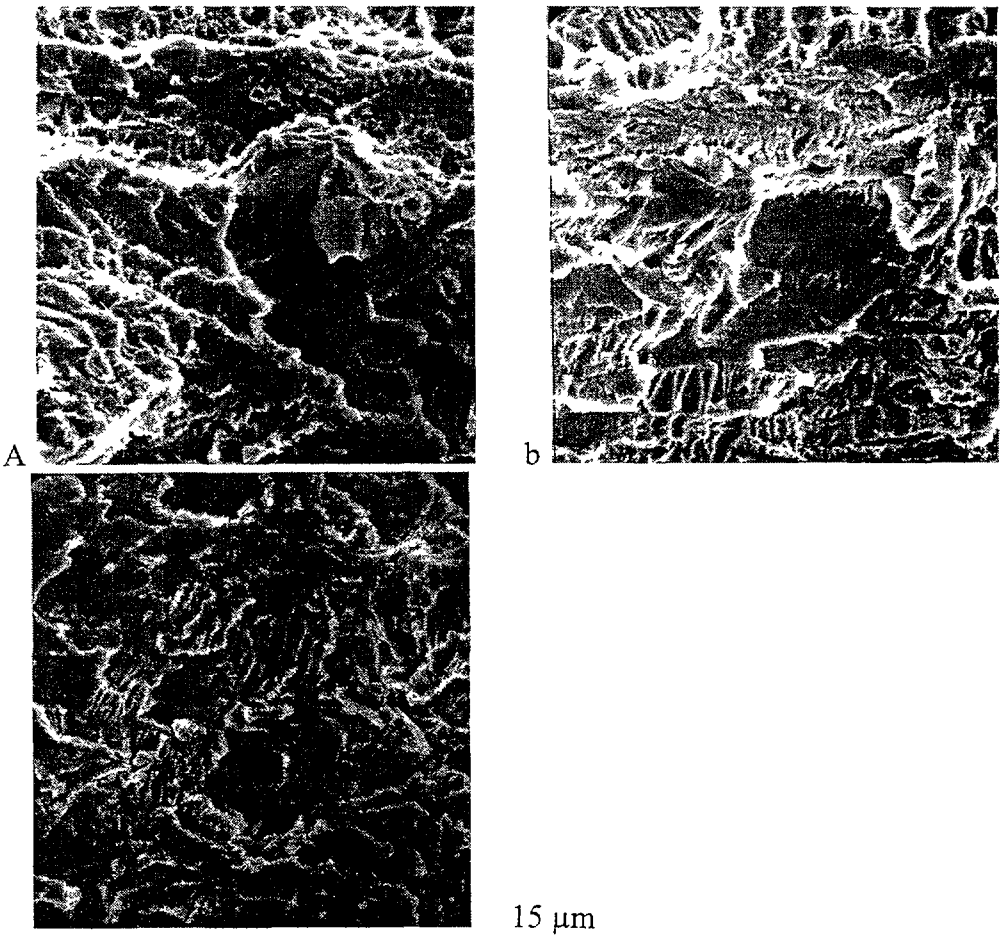

Fig. 1.6. Fractography of an I-SCC crack : the increase of K_I as the crack grows allows the observation of the different fracture modes.

crack tips. A modified void nucleation and growth process that gives very small micro-voids is difficult to eliminate, but no clear evidence for such features has been found on pseudo-cleavage surfaces.

The shapes of the velocity versus stress intensity curves that are obtained using different experimental techniques and conditions (Fig. 1.7) can be very different and, if the velocity does not fall rapidly at low K_I, this can cause difficulties in establishing $K_{I\text{-}SCC}$. Measured values for $K_{I\text{-}SCC}$ seem to differ significantly for results obtained on sheet and tubing, the latter usually giving significantly lower values (3-6 $MPa{\cdot}m^{-1/2}$) whereas the former often give values of 10-15 $MPa{\cdot}m^{-1/2}$. It has been shown that these differences can be explained by the specimen texture [1.39]. Using thick plates having strong textures, Knorr and Pelloux were able to machine fracture mechanics samples for which the effect of texture on crack growth could be highlighted. Their results show a strong decrease in $K_{I\text{-}SCC}$ as the density of <c> planes parallel to the crack surface increases. A comparison of their results with the case of cracks grown in fuel cladding tubes, permits the rationalisation of the results with the texture parameter [1.40]. This makes it essential to have values of $K_{I\text{-}SCC}$ and V vs. K_I from fuel cladding if modelling of in-reactor behaviour is intended.

Using fatigue pre-cracking of cladding tubes, it was possible to measure the I-SCC crack growth rate of cladding tubes under iodine vapour between 300 and 400 °C [1.41]. The standard fracture mechanics approach requires that the plastic zone size remains small compared to the wall thickness of the sample considered. In the case of a cladding tube, the thickness of which is generally less than a millimetre, this restricts the upper limit of the investigation range of K_I to about 10-20 $MPa{\cdot}m^{1/2}$, depending on the yield strength of the material. In the case of Zry-4, crack growth rates and $K_{I\text{-}SCC}$ values have been measured and gave a minimum stress intensity factor for crack growth of 3.5 $MPa{\cdot}m^{1/2}$, depending of material conditions, and an average crack growth rate of about 1 $\mu m{\cdot}sec^{-1}$ at K_I values corresponding to the plateau of the da/dt-K_I curves (Fig. 1.7) [1.42].

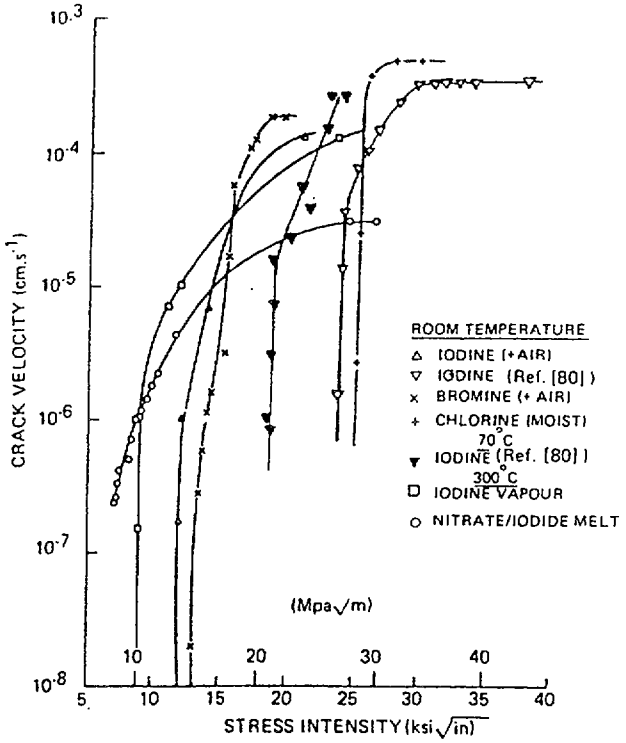

Fig. 1.7. Crack growth rates versus stress intensity factor for Zircaloy in halogen vapours (Cl_2, Br_2 and I_2) [1.38].

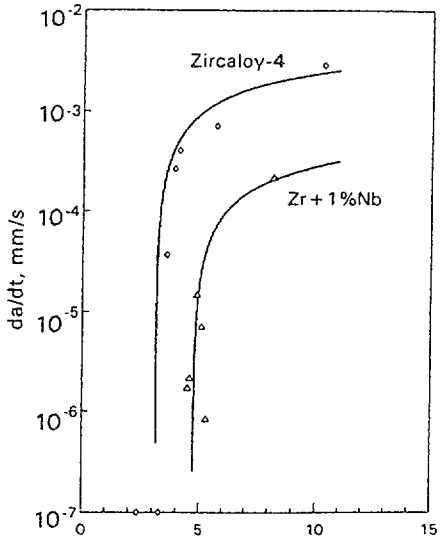

Fig. 1.8. Comparison of I-SCC crack growth rates of Zr-1%Nb and Zircaloy-4.

Similar experiments on Russian Zr 1% Nb cladding gave good I-SCC resistance, probably due to the weak recrystallized state of the Zr matrix at 350°C. It was possible to express the results of the crack rate measurements in the following form:

$da/dt = A \ln (K_I/K_{I\text{-}SCC})$

with $A = 3.9 \cdot 10^{-4}$ mm·sec^{-1}, and $K_{I\text{-}SCC} = 4.8$ MPa·m$^{1/2}$.

A comparison of the different crack growth rates is presented in Fig. 1.8.

1.3. TUBING DEGRADATION AFTER WALL PENETRATION

Once a PCI crack has penetrated the tubing wall then the subsequent degradation of the tubing depends upon the test conditions. Fuel failed in service in a water-cooled reactor will flood with water immediately after penetration of the wall occurs, stopping the PCI cracking process. Thus, the initial penetration of the outer wall may be very short (1-2 mm) and oxidation of the crack surfaces often effectively plugs the crack so that only a limited volume of water enters the fuel pin. Therefore, primary PCI failures usually show secondary hydriding degradation quickly at some point well removed from the initial PCI crack, provided the fuel-clad gap is closed. The secondary hydriding will then be the most obvious feature of the failed pin. The primary PCI failure may not grow any further, but will develop "rabbit ears" by ductile deformation at the ends of the arrested crack. It will appear as an "X-mark" on the outer cladding surface, and can usually be easily found by virtue of the local surface deformation in the "rabbit ears". Rotating the pin in the fuel-pool or hot-cell using a single light source will often show up the "X-mark" clearly. No clear evidence of deformation at the site of the through wall part of the crack is seen. When deliberate ramp tests are performed some longitudinal extension of the original crack may occur mechanically if the ramp was large and the ductility of the cladding was reduced by prior irradiation, or by hydriding.

When pressurised tube tests are performed in the laboratory without restricting the internal gas volume and with an inert external atmosphere, the stored energy can be very large and the crack may grow until it becomes unstable, leading to the bursting of the tube. Hydraulic pressurisation (with the aggressive atmosphere on the outside) or the use of an internal mandrel in a small volume closed pressurisation system for gas pressurisation tests

will not usually result in a tube burst. In general, conditions that give a high frequency of crack initiation sites are more likely to yield cracks long enough to become unstable than are conditions giving only a few initiation sites. Under these circumstances the presence of organic iodides from reactions of iodine with either rubber O-rings, or lubricating oil in the pressurisation system become important [1.24].

If tests are performed on open-ended lengths of tubing, the penetration of a crack through the tube wall will not cause any change in the chemical conditions at the crack tip, and growth of long cracks will be more common. These will only be limited by the stressed length of the tube. This is typically the effect in tests with internal mandrels (e.g. SIMFEX-type tests [1.4]) or externally compressed tubes using short anvils to apply the stress [1.23]. Hoop tensile testing of small sections of the cladding may be another good way to test the susceptibility of given tubes to I-SCC. These tests can be performed either with smooth sections of the tube or with machined and/or pre-fatigued notched ones, to induce a localised strain condition, similar to plane strain occurring during PCI.

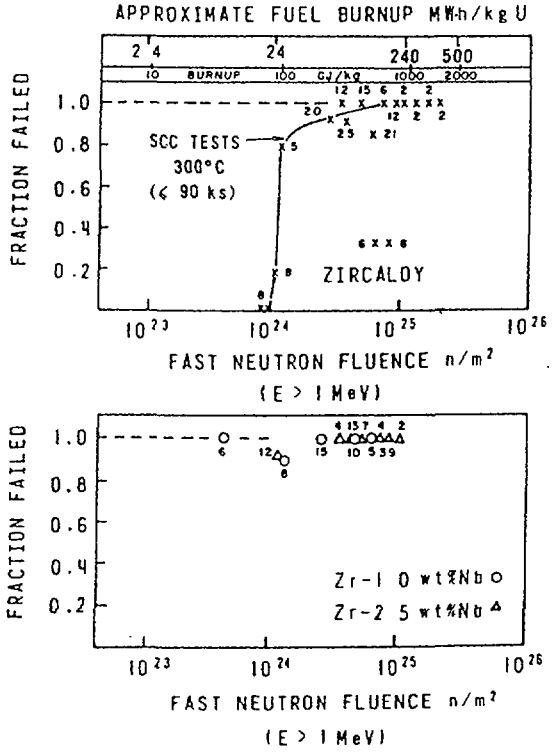

Fig. 1.9. Effect of neutron irradiation on the susceptibility to I-SCC of different Zr alloys.

1.4. EFFECTS OF IRRADIATION

Whether the susceptibility of tubing to iodine-induced SCC can be related to the tube texture appears to depend on the method of testing. When using split-ring tests with a fixed deflection no clear correlation of susceptibility and texture was evident [1.19], whereas for pressurised tube tests [1.43] and compressed tube tests [1.22], a relationship between texture and susceptibility does appear to be present. Once the tubing is irradiated, however, all batches of tubing appear to become susceptible to cracking (Fig. 1.9), and this susceptibility develops at irradiation doses lower than those necessary for a saturation of the irradiation induced changes in mechanical properties. No clearly established mechanism for this effect has been established, but it obviously cannot just be related to the increased ability to sustain a high stress intensity at the crack tip without blunting, since it occurs before major irradiation

hardening of the matrix is evident [1.44]. Dislocation channelling in irradiated cladding was suggested as a possible explanation, but no unequivocal evidence for this was found.

There is no evidence for any changes in crack velocity during irradiation, but specimens tested after irradiation by the pressurised tube technique show reduced times to failure. This does not necessarily imply an increased crack velocity, but may be explained by the irradiation induced hardening of the zirconium matrix.

Testing performed on pre-irradiated materials usually shows a higher resistance to I-SCC for the pre-irradiated case, when expressed in terms of time to failure in an iodine environment. This seems to be clearly an effect of the irradiation hardening induced by the <a> dislocation loops. Indeed, the lifetime at a given stress under iodine is much longer for pre-irradiated alloys, than for unirradiated ones; but the reductions in life, compared to the tests performed on un-irradiated materials, are similar for irradiated and unirradiated alloys. For Zircaloy-4 the reduction in $K_{I\text{-}SCC}$ was really significant, dropping from 3.2 to 1.5 MPa·m$^{1/2}$ [1.45].

For the Zr 1%Nb alloy, the results presented in Fig. 1.10 can be described in the following way:

The samples were irradiated in BOR-60 at a temperature of 325-345 °C, up to a fluence of 0.45 to 0.90·10^{22} n·cm^{-2}. The stress corrosion testing (in the time to failure mode) was

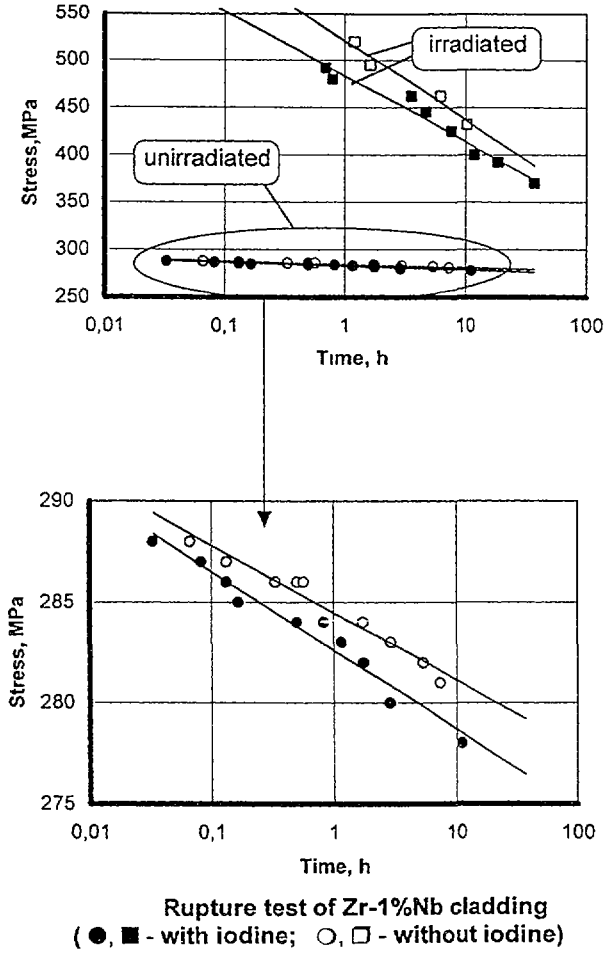

Fig. 1.10. Effect of irradiation on the stress dependence of I-SCC of Zr-1%Nb.

performed both with and without iodine for up to 40 hours over a stress range of 200 to 520 MPa. The analysis of the results indicated the following points:

- the rupture mode, as revealed by fractography, is the same for unirradiated and irradiated material;
- compared to unirradiated material, the reduction of time to failure due to iodine is higher for irradiated material;
- under iodine, the life time of irradiated materials is higher compared to unirradiated ones.

Zr 1%Nb cladding irradiated to a fluence of $0.9 \cdot 10^{22}$ n·cm^{-2} and tested in iodine for up to 40 hours develops I-SCC only for stress levels above 370 MPa. The results on internally pressurised recrystallised Zr-1%Nb demonstrate that the iodine only slightly reduces the rupture time below 20 hours. However, after irradiation to a fluence of about 10^{22} n·cm^{-2}, the Zr cladding is more sensitive to I-SCC than the unirradiated material.

1.5. CONCLUSIONS

Tentative models are based on the distinction between the different steps presented in this review (incubation time, crack initiation and growth and final instability). Since they are based on parametric adjustments of results obtained on a self consistent series of tests and are not based on physical grounds only, they are not suitable for forecasting the behaviour of any specific material in any conditions [1.31].

There are still many gaps in our knowledge of the mechanisms of PCI cracking that make it difficult to develop a model for the behaviour of fuel. In the past there has been a tendency to develop "accumulated damage" models as an approach to this, however, it is not obvious that such an approach is valid. This is particularly so because the chemical as well as the mechanical conditions for cracking must be satisfied [1.4, 1.22].

Once a crack has initiated, then, if it does not rapidly penetrate the cladding wall, and the crack arrests (e.g. because the stress has relaxed) perhaps an accumulated damage model is valid. However, during the "incubation period" it appears that no damage is done to the cladding and that changes are purely in the environment. If a failure does not then ensue, as was the situation for rapid (<30 min.) fuel movements in early CANDU's [1.18], then a number of such events could theoretically occur without any damage accumulating. In developing a model such factors would need to be accommodated.

REFERENCES TO CHAPTER 1

[1.1] LYONS, M.F., COPLIN, D.H., JONES, G.G., High performance UO_2 Fuel Program., US Report (1964) GEAP 3770-10.

[1.2] ROSENBAUM, H.S., DAVIES, J.S., PON, J.Q., US Report (1966) GEQP-5100-5.

[1.3] ROSENBAUM, H.S.,ELECTROCHEM. Tech. **4** (1966) 153.

[1.4] COX, B., Pellet-cladding interaction (PCI) failures of zirconium alloy fuel cladding - a review, J. Nucl. Mater. **172** (1990) 249-292.

[1.5] WILLIAMS, C.D., et al., "Zircaloy 2 lined zirconium barrier fuel cladding", Zirconium in Nuclear Industry (proc. 11th Int. Symp. Garmisch-Partenkirchen), ASTM STP 1295 (1996) 676-694.

[1.6] HARBOTTLE, J.E., et al., "The behaviour of defective BWR barrier cladding, non-barrier fuel" (proc. Int. Top. Mtg on LWR Fuel Performance, West Palm Beach, 1994) ANS (391-397).

[1.7] JOSEPH, J., ATABEK R., TROTABAS, M., "The CEA-Fragema ramp test programme for the study of the effect of power cycling on PCI at high burn-up", (Proc. Specialists Mtg on Power Ramping, Cycling Behaviour of Water Reactor Fuels, Petten) IAEA-IWGFPT-14, Vienna (1982) 36.

[1.8] CAILLOT, L., LINET, B., LEMAIGNAN, C., Pellet Clad Interaction in PWR Fuel: Analytical Irradiation Experiment, Finite Element Modelling, SMIRT-12 (1993) 69-74.

[1.9] NOVIKOV, V.V., et al., "Study of crack initiation, propagation mechanism on SCC of Zr-1%Nb VVER fuels" (proc. Int. conf. on radiation material science, Alushta, USSR) **8** (1990) 158-164.

[1.10] NOVIKOV, V.V., "Mechanism of fuel cladding failure in PCI", Fuel Failure in Normal Operation of Water Reactors, Experience, Mechanisms, Management (Proc. Tech. Committee Mtg Dimitrovgrad), IAEA-TECDOC 709, Vienna (1992) 255

[1.11] GORYACHEV, S.B., et al., Iodine induced SCC of Zr alloys at constant strain rate, J. Nucl. Mater. **199** (1992) 50-60.

[1.12] BIBILASHVILI, Y.K., et al., Propagation of stress corrosion cracks in Zr-1%Nb claddings, J. Nucl. Mater. **224** (1995) 307-310.

[1.13] PORROT, E., CHARLES, M., LEFEBVRE, F., LEMAIGNAN, C., "Mechanisms of cladding deformation, fission gas release during power transients at high burnup.", LWR Fuel Performance, Williamsburg, Va. (1988).

[1.14] MATZKE, H. , Oxygen potential in the RIM region of high BU UO_2 fuel., J. Nucl. Mater. **208** (1994) 18-26.

[1.15] KONASHI, K., et al., Radiation effect on the chemical state of fission product iodine, J. Nucl. Mater. **248** (1997) 220-225.

[1.16] BIBILASHVILI, Y.K., et el., "Studies of radiation-thermal decomposition of caesium iodide, stress corrosion cracking of VVER fuel clads in gamma-irradiation", Fuel Internal Chemistry, Fission Product Behaviour, IAEA-IWGFPT/25, Vienna (1985) 167.

[1.17] COX, B., SURETTE, B.A., WOOD, J.C., "Pellet-clad interaction failures: stress corrosion cracking by iodine or metal vapour embrittlement by cesium/cadmium vapours", Environmental Degradation of Materials in Agressive Environments (Proc. Conf. Blacksburg, VA) **2** (1981) 293-302.

[1.18] PENN, W.J., LO, R.K., WOOD, J.C., Nucl. Technol. **34** (1977) 249-268.

[1.19] WOOD, J.C., J. Nucl. Mater. **45** (1972) 105-122.

[1.20] WOOD, J.C., SURETTE, B.A., AITCHISON, I., J. Nucl. Mater. **88** (1980) 81-94.

[1.21] MOGARD, H., HOWE, D., GROUNES, M., "The international Trans-Ramp II Fuel Project - A study of the effects of rapid power ramping on the PCI resistance of PWR Fuel.", LWR-Fuel Performance, ANS, Williamsburg, VA (1988) 232-244.
[1.22] COX, B., HADDAD, R., "Recent studies of crack initiation during stress corrosion cracking of Zirconium alloys", Zr in Nuclear Industry (Proc. 7th Int. Symp. Strasbourg) ASTM STP 939 (1987) 717-733.
[1.23] COX, B., HADDAD, R., J. Nucl. Mater. **138** (1986) 81-88.
[1.24] COX, B., HADDAD, R., J. Nucl. Mater. 137 (1986) 115 - 123.
[1.25] COX, B., "Stress corrosion cracking in iodine containing environment", Zr in Nuclear Industry (Proc. 2nd Int. Symp. Portland), ASTM STP 551 (1974) 419-434.
[1.26] COX, B., Corrosion **33** (1977) 79-84.
[1.27] COX, B., "Hydride cracks as Initiators for stress corrosion cracking of Zircaloy.", Zr in Nuclear Industry (Proc. 4th Int. Conf. Stratford upon Avon), ASTM-STP 681, (1979) 306-321.
[1.28] COX, B., SURETTE, B.A., WOOD, J.C., J. Nucl. Mater. **138** (1986) 89-98.
[1.29] KUBO, T., WAKASHIMA, Y., AMANO, K., NAGAI, M., Effects of crystallographic orientation on plastic deformation, SCC initiation in zirconium alloys, J. Nucl. Mater. **132** (1985) 1-9.
[1.30] JACQUES, P., LEFEBVRE, F., LEMAIGNAN, C., J. Nucl. Mater. **264** (1999) 239-256
[1.31] SCHUSTER, I., LEMAIGNAN, C., JOSEPH, J., Testing, modelling the influence of irradiation on iodine-induced stress corrosion cracking of Zircaloy-4, Nucl. Eng., Design **156** (1995) 343-349.
[1.32] FREGONESE, M., LEFEBVRE, F, LEMAIGNAN, C., MAGNIN, T., Influence of recoil-implanted, thermally released iodine on I-SCC of Zircaloy-4 in PCI conditions: chemical aspects; J. Nucl. Mater. **265** (1999) 245-254.
[1.33] SCHUSTER, I., LEMAIGNAN, C., Embrittlement, induced by fission recoils, of the inner surface of PWR fuel cladding - a simulation using heavy ions, J. Nucl. Mater., **151** (1988) 108-111.
[1.34] GLADKOV, V.P., et al., Iodine diffusion in alpha-phase of Zr-1%Nb alloy, Atomnaya Energiya **75** (1993) 2 97-103.
[1.35] HADDAD, R., DORADO, A.O., "Grain-to grain study of the mechanisms of crack propagation during iodine stress corrosion cracking of Zircaloy-4.", Zirconium in Nuclear Industry (Proc. 10th Int. Symp. Baltimore), ASTM STP 1245 (1994) 559-575.
[1.36] AITCHISON, I., COX, B., Corrosion **28** (1972) 83-87.
[1.37] HWANG, S.K., HAN, H.T., "Anisotropic surface energy reduction of Zr by chemisorption", J. Nucl. Mater. **161** (1989) 175-181.
[1.38] COX, B., "Environmentally induced cracking of zirconium alloys - A review", J. Nucl. Mater. **170** (1990) 1-23.
[1.39] KNORR, D., PELLOUX, R.M., Effect of texture, microstructure on the propagation of iodine stress corrosion cracks in Zircaloy, Metal. Trans. **A 13** (1982) 73-83.
[1.40] SCHUSTER, I., LEMAIGNAN, C., "Influence of texture on iodine-induced stress corrosion cracking of Zircaloy-4 tubes", J. Nucl. Mater. **189** (1992) 157-166.
[1.41] BRUNISHOLZ, L., LEMAIGNAN, C., "Iodine induced stress corrosion cracking of Zircaloy fuel cladding: Initiation, growth", Zr in Nuclear Industry (Proc. 7th Int. Symp. Strasbourg), ASTM STP 939 (1987) 700-716.
[1.42] SCHUSTER, I., LEMAIGNAN, C., "Link between stress corrosion, corrosion-fatigue behaviour of Zircaloy in an iodine environment", Zirconium in the Nuclear Industry (Proc. 8th Int. Symp. 1989) 535-547.

[1.43] MATTAS, R.F., YAGGEE, F.L., NEILNARK, L.A., "Effect of zirconium oxide on the stress corrosion susceptibility of irradiated Zircaloy cladding", Zirconium in the Nuclear Industry (Proc. 5th Int. Symp. Boston) ASTM STP 754 (1982) 158-170.

[1.44] NELSON, H.G., WACHOB, H., Conf. on the environment sensitive fracture of engineering materials, Chicago, AIMMPE, Warrendale PA (1977) 314

[1.45] SCHUSTER, I., LEMAIGNAN, C., JOSEPH J., "Influence of irradiation on iodine induced stress corrosion cracking behaviour of Zircaloy4.", SMIRT-12 (KUSSMAUL, K, Ed.) (1993) 45-50.

Chapter 2

OVERVIEW OF CO-ORDINATED RESEARCH PROJECT

2.1. BACKGROUND TO THE CRP

Pellet-clad interaction (PCI) failure is a licensing concern for many water reactor fuel designs. Failure propensity is at present generally assessed using empirical methodologies. Replacing empiricism by mechanistic models of the underlying processes is a desirable long term goal, which would have the advantage of facilitating the analysis of multiple power ramp events and non-standard fuel designs, and would help to reduce unnecessarily conservative constraints on reactor operation. One requirement of this mechanistic approach is to obtain information on the rate of crack propagation in Zircaloy materials stressed in an iodine environment. The purpose of the present CRP is to provide basic data on this phenomenon for a selection of different materials, using a matrix of different temperature and iodine levels, with the work conducted at five different laboratories around the world.

The major variables influencing stress corrosion cracking in these alloys are metallurgical state (including composition, orientation, thermomechanical treatment, texture and cold work), environment (composition, concentration and temperature) and stress. It was not feasible to investigate the effects of all these variables within the scope and timescale of the programme. The test programme was thus focused on determining the dependency of stress corrosion crack propagation rate on temperature, iodine concentration and stress within the range of available materials. It was recognised at the outset that the use of unirradiated material and iodine vapour at relatively high concentrations would give crack propagation values not directly applicable to in-reactor behaviour.

AEA Technology at Risley, UK, acted as host laboratory for the experimental work. The role of the host laboratory was:

(a) to develop an experimental technique, capable of being carried out by the other participating laboratories, for initiating and propagating a stress corrosion crack in an iodine-containing environment and for monitoring the growth of the defect to allow crack propagation rates to be determined,

(b) to design a specimen suitable for manufacturing from the available material which was capable of being used to generate crack growth rates due to stress corrosion cracking,

(c) to manufacture and precrack specimens for testing by the other participating laboratories,

(d) to assist participating laboratories in setting up their equipment and with generating and analysing the results,

(e) to carry out part of the test matrix,

(f) to act as repository for results from the participating laboratories, to review their results and to ensure that these were analysed on a consistent basis.

2.2. TEST DESIGN AND PROCEDURE

2.2.1. Specimen design

In PCI failures in cladding, the crack propagates in the radial direction under a hoop stress from thermal expansion of the fuel pellets. In sheet material, the analogous direction is the short transverse, i.e. with the crack growing through the sheet thickness. Two critical decisions were made at the outset of the CRP which influenced the specimen design. These were both associated with the practical experimental difficulties of initiating and monitoring the growth of a crack in these orientations in cladding and sheet material, particularly where one of the major aims of the CRP was technology transfer to the participating laboratories. Accordingly, the Supervisory Group of the CRP decided to use sheet material for the specimens rather than cladding tubing. It was also decided not to try to generate data in the short transverse direction, but that the crack should propagate in the longitudinal (rolling) direction instead.

Having made these decisions, a simple uniaxial tensile specimen was designed as shown in Fig. 2.1. Since it was intended that crack growth rates should be monitored using an in-situ potential drop monitoring technique, the specimen needed to contain a means of localising

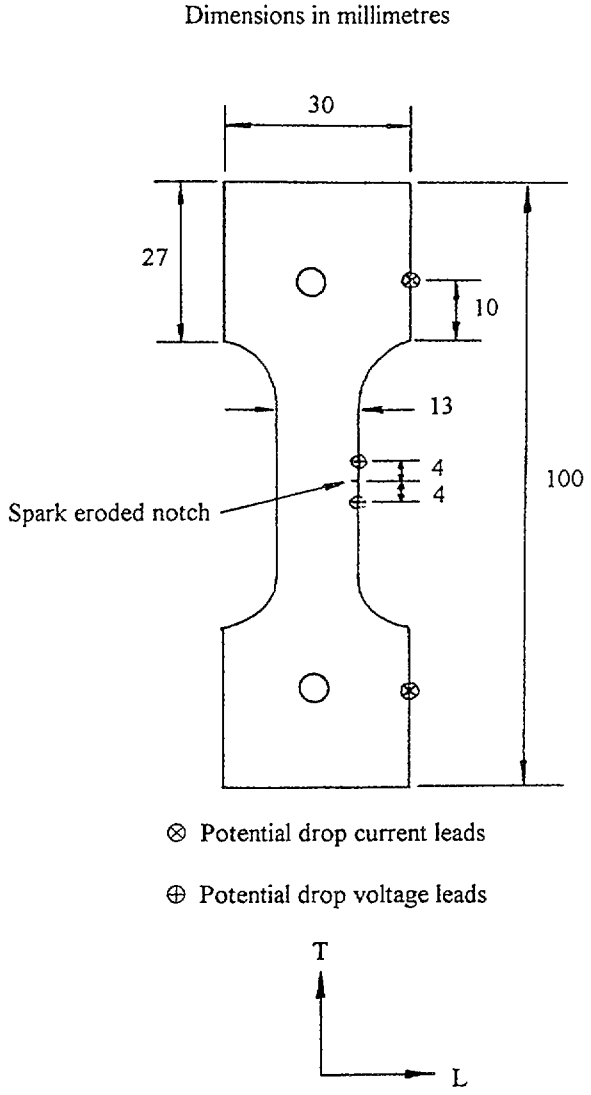

FIG. 2.1. Specimen design, showing locations of potential drop crack monitoring wires.

SCC initiation to a site between two monitoring wires. This was achieved using an electro-discharge machined notch and fatigue precrack. A load was applied to the specimen using pins through holes in the shoulders of the specimen. Fig. 2.1 also shows the positions of the potential drop monitoring wires. Specimens for the major part of the test programme were cut from the sheet material such that the crack would propagate in the longitudinal (rolling) direction under a tensile load applied in the transverse direction (i.e. specimens were in the TL orientation). Later in the CRP, each laboratory also carried out some tests on specimens in the LT orientation.

The stress intensity factor (K) solution for this specimen design was taken from [2.1] for an edge crack in a finite width sheet under uniaxial tensile stress.

$$\frac{K_I}{K_0} = 1.12 - 0.23(a/b) + 10.6(a/b)^2 - 21.7(a/b)^3 + 30.4(a/b)^4$$

where $K_0 = \sqrt{(\pi a)}$, a = crack length and b = specimen width.

This equation also allows for the bending moment that the specimen will be subjected to as the crack propagates in a specimen where the ends are free to rotate (as they are in this design with pin loading). Calibration of the direct current potential drop (DCPD) crack monitoring system showed the specimen to have a good voltage-crack length response capable of resolving small changes in crack length (Fig. 2.2).

2.2.2. Equipment and test technique

The basic system to be used by the participants for carrying out these tests is shown in Fig. 2.3. The specimen was to be mounted in a pair of grips, from which it was electrically insulated using oxidised Zircaloy bushes. One side of the grips was attached to a pull-rod which extended through the base of the test chamber via a sliding seal and was attached to a servo-electric mechanical test machine to apply the load to the specimen. The test chamber was to be made from a borosilicate glass tube, sealed at both ends with stainless steel flanges. The central part of the test section was to be heated using a furnace, whilst the ends remained cooler to minimise reaction between the iodine and the stainless steel closure flanges. The temperature over the height of the specimen was to be monitored using a number of thermocouples at various locations around the hot zone. Conax fittings in the flange were to be used to seal the potential drop monitoring wires into the test section, whilst also ensuring that they were electrically insulated from each other and the test section. These wires, made from zirconium, were attached to the specimen in the positions shown in Fig. 2.1 by spot welding.

Iodine vapour was to be supplied to the test section by passing ultra high purity helium through a flask containing iodine crystals (Fig. 2.4). The temperature of this flask governed the iodine partial pressure and hence concentration fed to the test section. A by-pass allowed the test section to be flushed with helium during start-up and shut-down so that iodine was only introduced when steady conditions had been achieved. The outlet gas was to be fed through molecular sieve and propanol scrubbers to remove iodine before passing to the vent. Glass vessels and pipework were to be used in the iodine supply system, again with the intention of minimising reaction of the iodine with components other than the specimen. This pipework was to be heated (using electrical tape heaters) to a temperature above that of the iodine flask to ensure that deposition of iodine did not occur in the pipework.

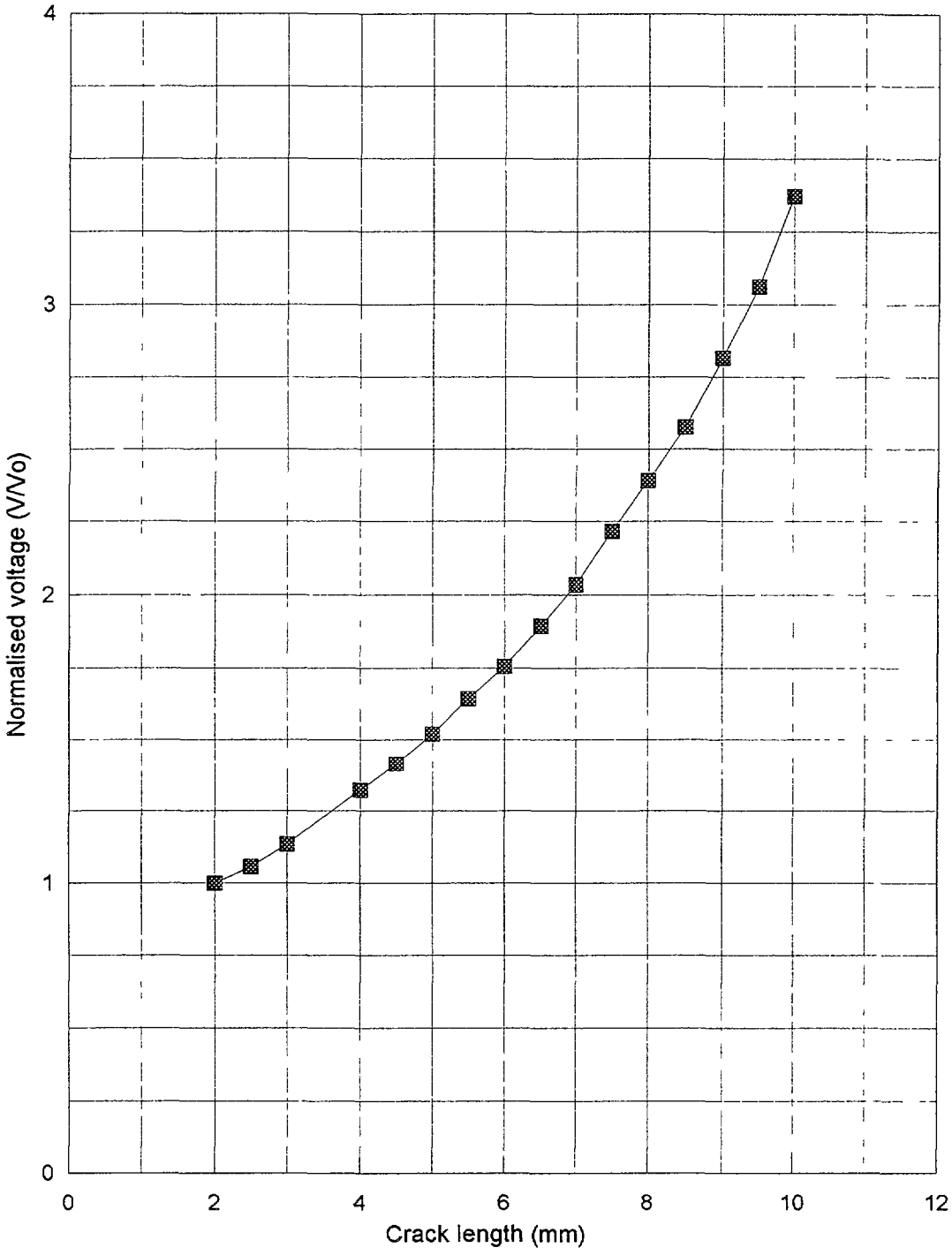

FIG. 2.2. Voltage versus crack length relationship for direct current potential drop crack monitoring system with wires in locations shown in Fig. 2.1.

The test procedure was to be as follows. On mounting the specimen in the grips and sealing the test chamber, the pipework and chamber were to be flushed with helium to remove as much air as possible before the furnace and iodine heater were switched on. On reaching the test temperature, the helium flow was to be switched through the iodine container. After allowing an hour for steady state conditions to be achieved, the specimen was to be loaded to the required stress intensity factor and any crack extension monitored on the potential drop system. One of two loading schemes were to be used :

- the specimen was to be loaded to ~5 MPa$\sqrt{m}$. If crack extension was not detected after 24 hours, K was to be increased by 10%. This was to be repeated until crack growth occurred. This scheme was used for the earlier tests in the CRP.

- the specimen was to be loaded to 10 MPa$\sqrt{m}$ and the crack allowed to grow by 0.25 to 0.5 mm, at which time the load was to be reduced by 10% and the crack allowed to grow a further distance (through the plastic zone from the previous load). This was to be repeated until the crack arrested or the crack growth rate became very low, at which point the specimen

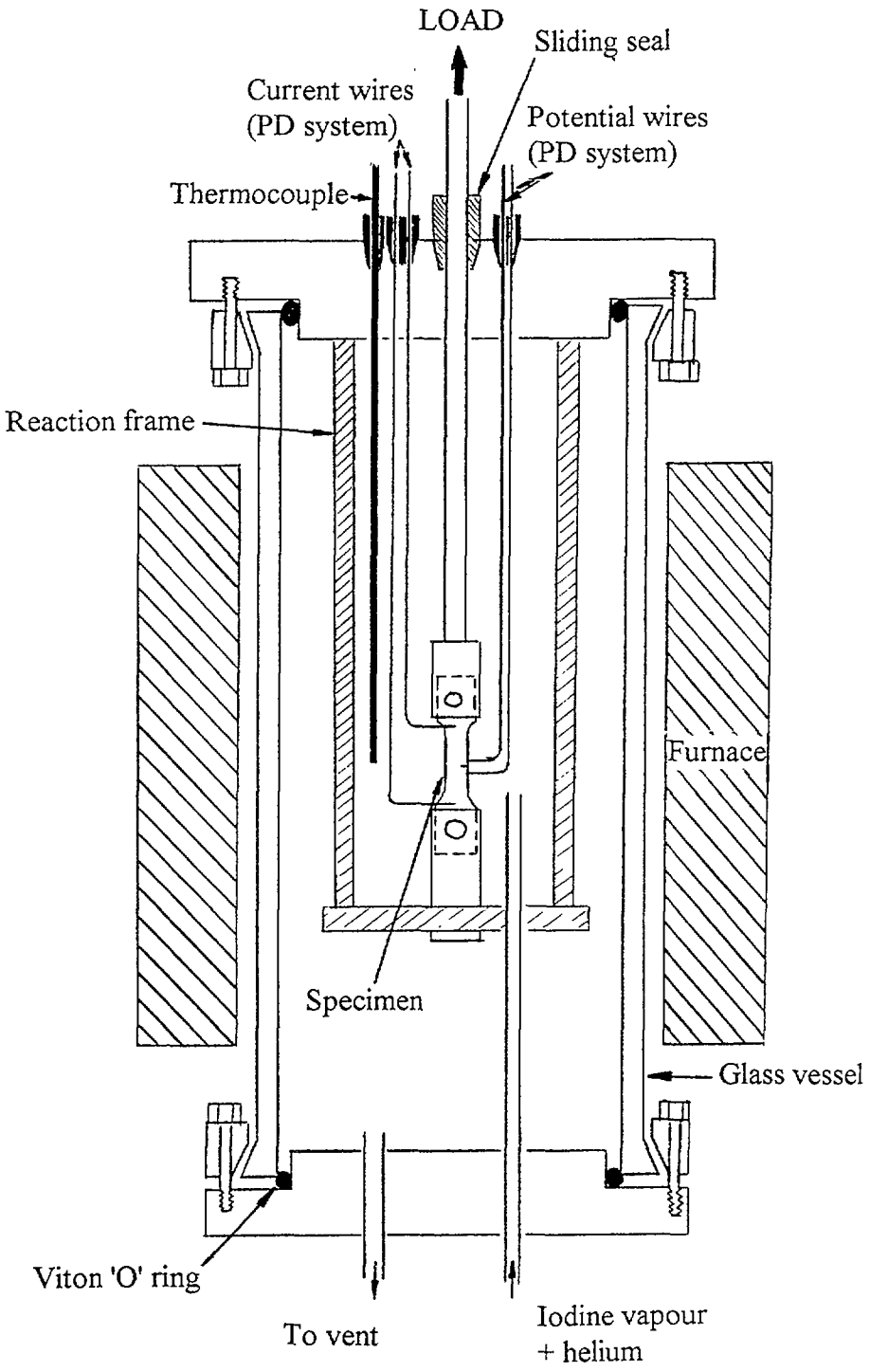

FIG. 2.3. Arrangement and design of AEA Technology test chamber.

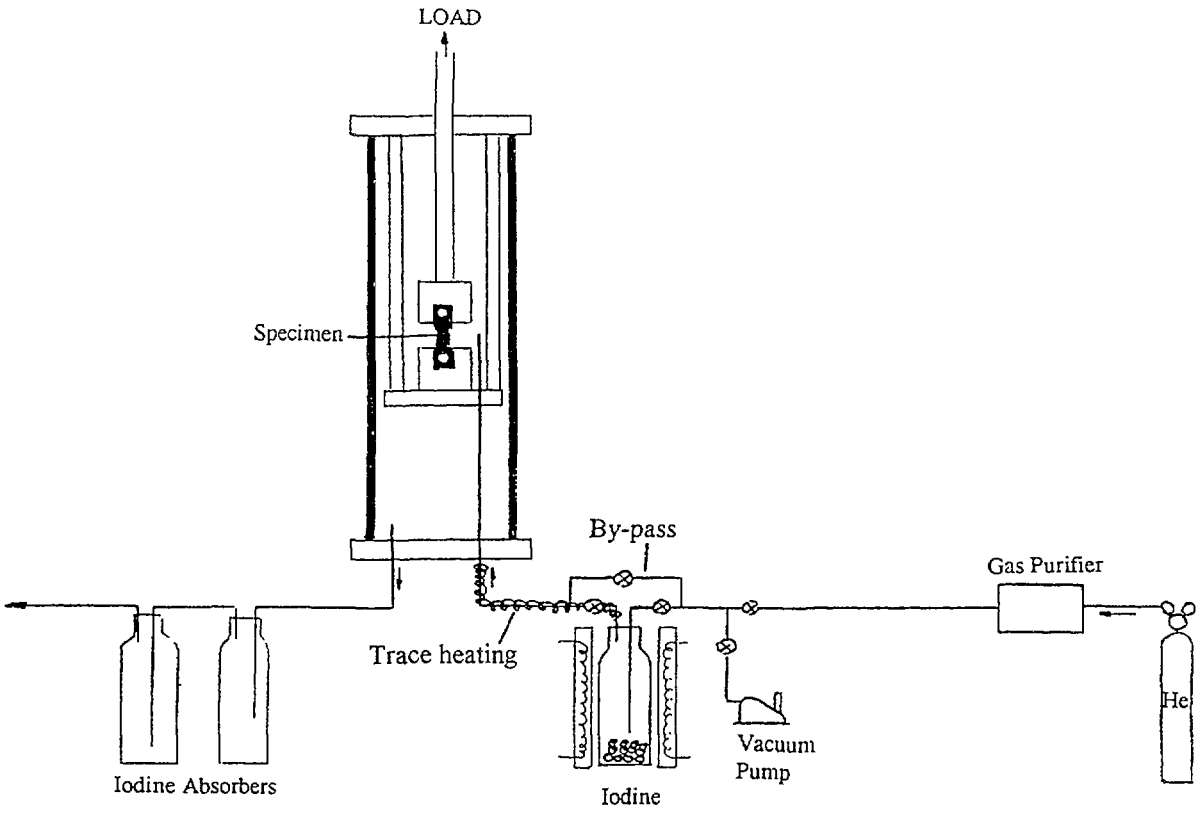

FIG. 2.4. Flow diagram for AEA Technology experimental system.

was to be reloaded to ~12 MPa$\sqrt{m}$ and the remainder of the crack growth curve at higher values of K was to be generated. This scheme was to be used for later tests.

On completion of the test, the specimen was to be broken open and the fracture surface measured to back-calibrate the crack monitoring system. The data was then to be split into increments with constant experimental conditions, the stress intensity factor calculated for the mid-point of the increment, and the crack growth rate determined by linear regression.

2.3. MATERIALS

Teledyne Wah Chang Albany (USA) and Cezus (France) agreed to provide some Zircaloy plate material for use in the experimental programme. The materials were each given an identification number of the form "OMxx" and these identities were used by each laboratory to prevent confusion as to the material being used or referred to. The plate materials supplied were:

(a) Recrystallised Zircaloy-4, 1.0 mm thick, supplied by Wah Chang - identified as OM40.

(b) Stress-relief annealed Zircaloy-4, 1.0 mm thick, supplied by Wah Chang - identified as OM41.

(c) Recrystallised Zircaloy-2, 1.0 mm thick, supplied by Wah Chang - identified as OM42

(d) Recrystallised Zircaloy-2, 1.2 mm thick, supplied by Cezus - identified as OM44

(e) Recrystallised Zircaloy-4, 1.2 mm thick, supplied by Cezus - identified as OM45.

The characterisation information available from the manufacturers on these materials, together with further investigations performed by the host laboratory, is summarised in Appendix I. These data were supplied to the participants, but the Chinese and Korean participants also carried out some characterisation work on these materials which method is reported in Appendix II and Section 6.

2.4. RESULTS FROM THE HOST LABORATORY

2.4.1. Creep test

Unlike the other participants, the host laboratory did not carry out any tests specifically to generate creep data on the test materials. However, early in the test programme, apparent crack extension was recorded on the DCPD crack monitoring equipment at stress intensity factors below the threshold for SCC. An example of this is shown in Fig. 2.5. There was a rapid change in normalised voltage (and hence apparent crack length) following increases in applied load, but the rate of change reduced with time. This was due to the influence of primary and secondary creep processes on the zone of plastic deformation at the crack tip. Whilst recognising that this was not real crack extension, it was important to quantify the

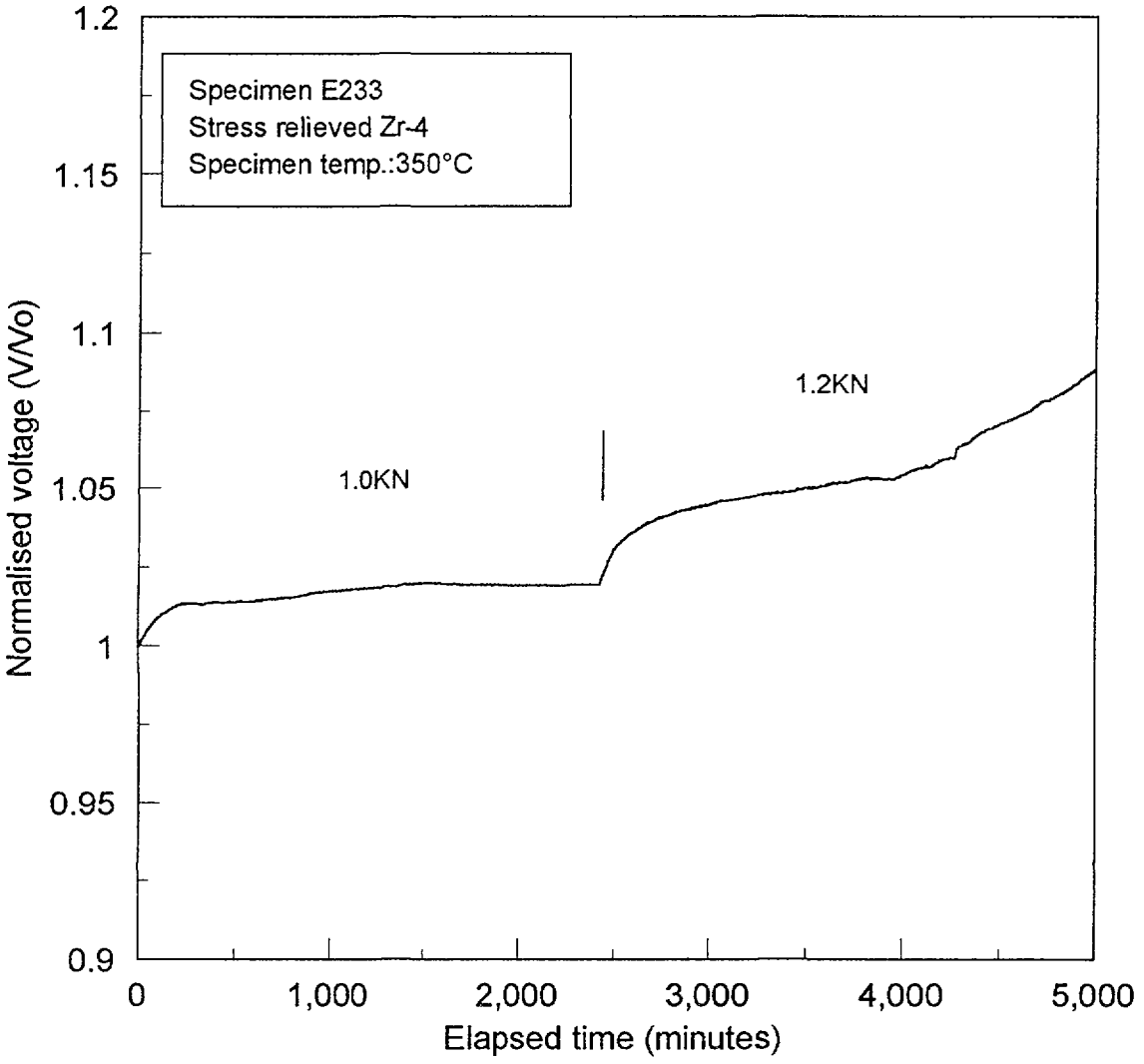

FIG. 2.5 Normalised voltage versus elapsed time at loads below K_{Iscc}, showing primary and secondary creep following step load increases.

apparent crack growth rate due to creep so that the influence of this on the crack propagation rate at stress intensities close to K_{Iscc} could be determined and separated from true crack propagation due to SCC.

Fig. 2.6 shows the apparent crack growth rate due to primary and secondary creep on a precracked specimen of stress-relief annealed Zr-4 (material OM41), made in the TL orientation and tested at 350°C. At a stress intensity factor of around 8 MPa$\sqrt{m}$, the initial apparent crack growth rate was around 10^{-5} mm/s due to primary creep, but rapidly reduced to around $3x10^{-7}$ mm/s due to secondary creep. As expected, the apparent crack growth rates (both the rapid transient rate due to primary creep and the lower, more persistent rate due to secondary creep) increased with increasing stress intensity factor. In the important range from 10 to 20 MPa$\sqrt{m}$, the apparent crack growth rate due to secondary creep was of the order of 10^{-6} mm/s. This defined a minimum crack growth rate that could be identified from the SCC tests and this value was subtracted from the crack growth rate measurements during the SCC tests.

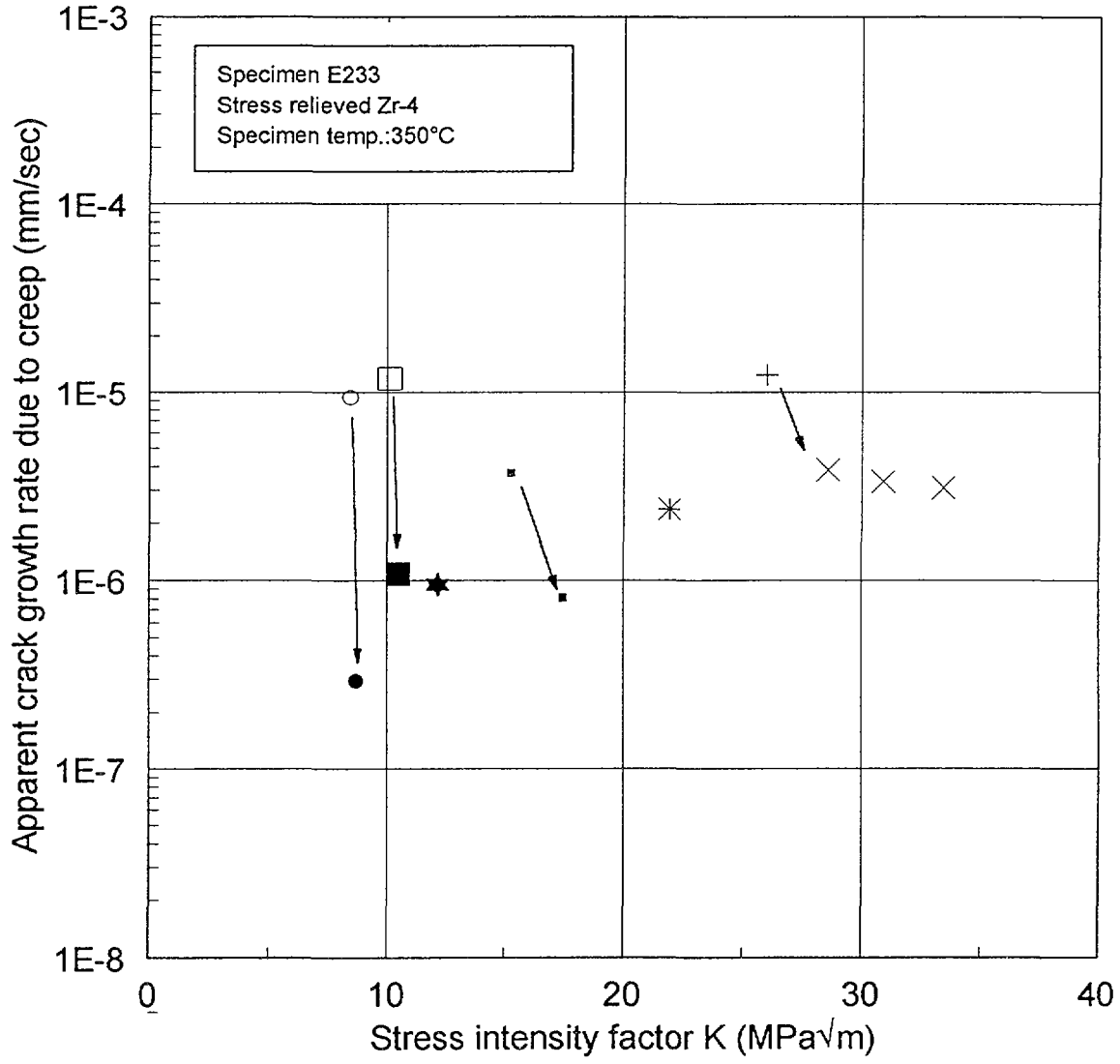

FIG. 2.6 Apparent crack growth rate recorded on DCPD crack monitoring system due to creep.

2.4.2. SCC tests

The test matrix carried out by the host laboratory was concentrated on the Wah Chang stress-relief annealed Zr-4 (material OM41) in the TL orientation, with one test condition replicated on a LT orientation specimen and on the recrystallised Wah Chang Zr-4 (material OM40).

2.4.2.1. Stress relief annealed Zr-4, TL orientation

Tests were carried out at 300°C with 1000 Pa I_2, at 350°C with 100 and 1000 Pa I_2, and at 400°C with 1000 Pa I_2. The general trend in each test was the same. On exceeding a threshold stress intensity factor (K_{Iscc}), crack propagation rates increased rapidly to approach a plateau crack growth rate (Stage II crack growth). Below the threshold, the crack did not propagate by SCC, but the potential drop crack monitoring system usually indicated a crack growth rate around 5×10^{-7} mm/sec due to changes in the plastic zone at the crack tip caused by creep under the applied load.

The results from duplicate tests at 300°C are shown in Fig. 2.7. Whilst the threshold stress intensity factor for both specimens was similar (in the range 10-12 MPa√m), there was

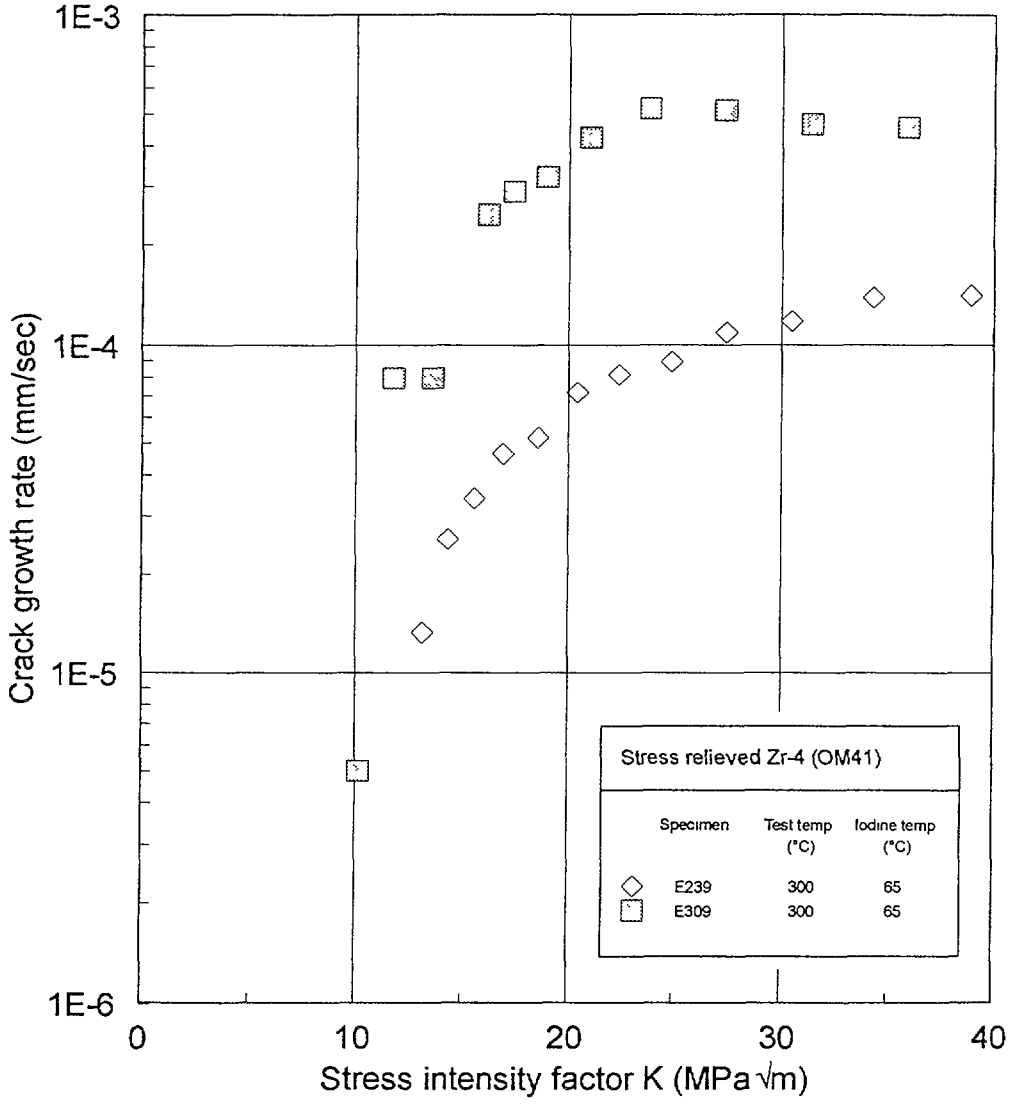

FIG. 2.7 Crack growth rate versus stress intensity factor for specimens of stress-relief annealed Zr-4 (material OM41) tested by AEA Technology at 300°C with 1000 Pa of iodine.

considerable variation in behaviour between the two specimens in the plateau region. Specimen E309 showed a plateau in the crack growth curve around $5x10^{-4}$ mm/s, compared to around 1×10^{-4} mm/s for specimen E239. There were no obvious differences in experimental procedure or test conditions which would account for these differences.

Data from a number of tests at 350°C are shown in Fig. 2.8 (for a test with 100 Pa I_2) and Fig. 2.9 (for three tests with 1000 Pa I_2). The results in the higher iodine concentration showed a high degree of consistency with very little experimental scatter between the tests. All tests at this temperature showed a threshold for SCC of 11-13 MPa$\sqrt{m}$, although there were small differences in the plateau crack growth rate between tests in the two iodine concentrations, the plateau rate in the lower iodine concentration being slightly higher than for the other tests. In the absence of replicate tests at 100 Pa I_2, it was not possible to determine whether this was a real effect or due to experimental scatter. In any event, any effect of iodine concentration was small and only affected the plateau region of crack growth.

The results of two tests at 400°C and 1000 Pa I_2 are shown in Fig. 2.10. The crack growth curve for specimen E237 was, unfortunately, not fully developed due to detachment of

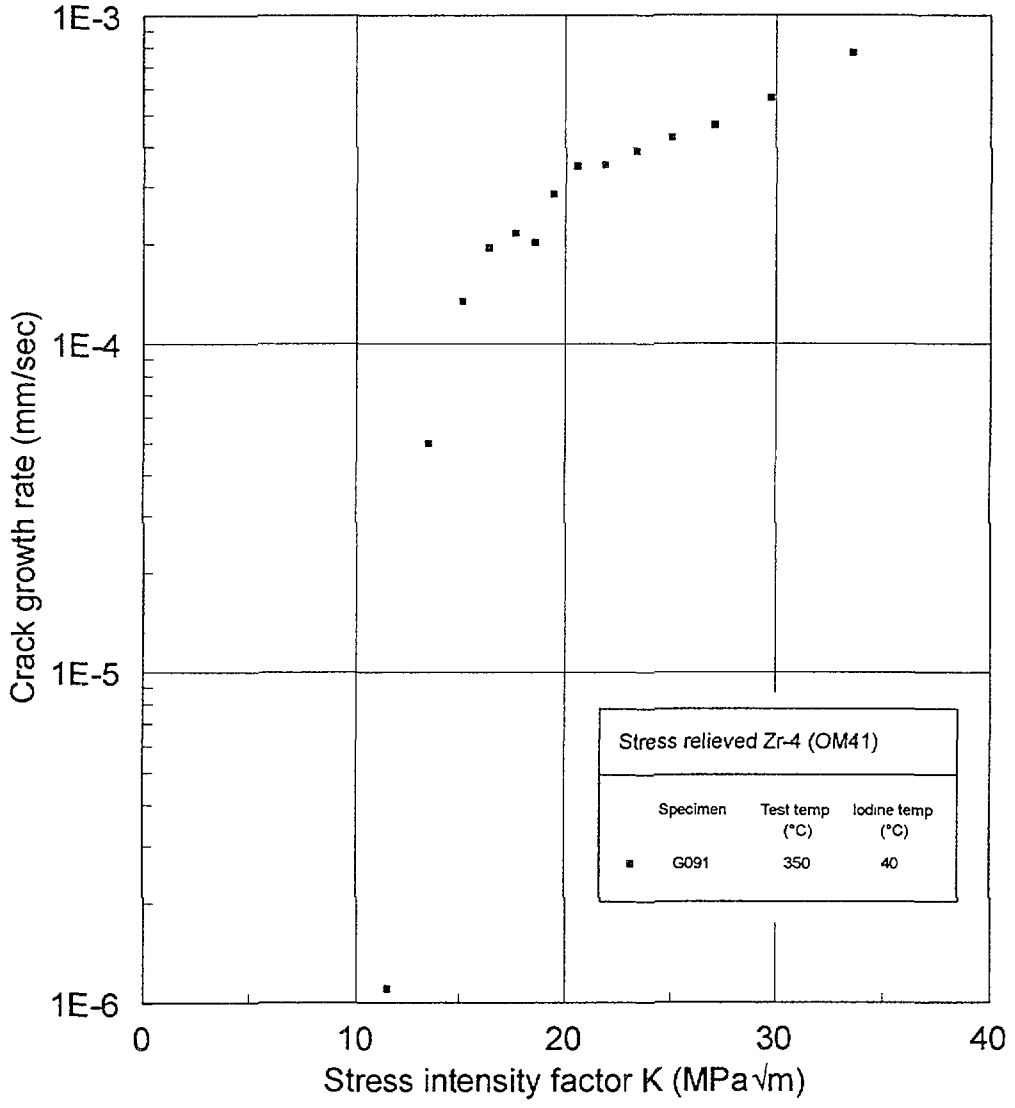

FIG. 2.8. Crack growth rate versus stress intensity factor for specimen of stress-relief annealed Zr-4 (material OM41) tested by AEA Technology at 350°C with 100 Pa of iodine.

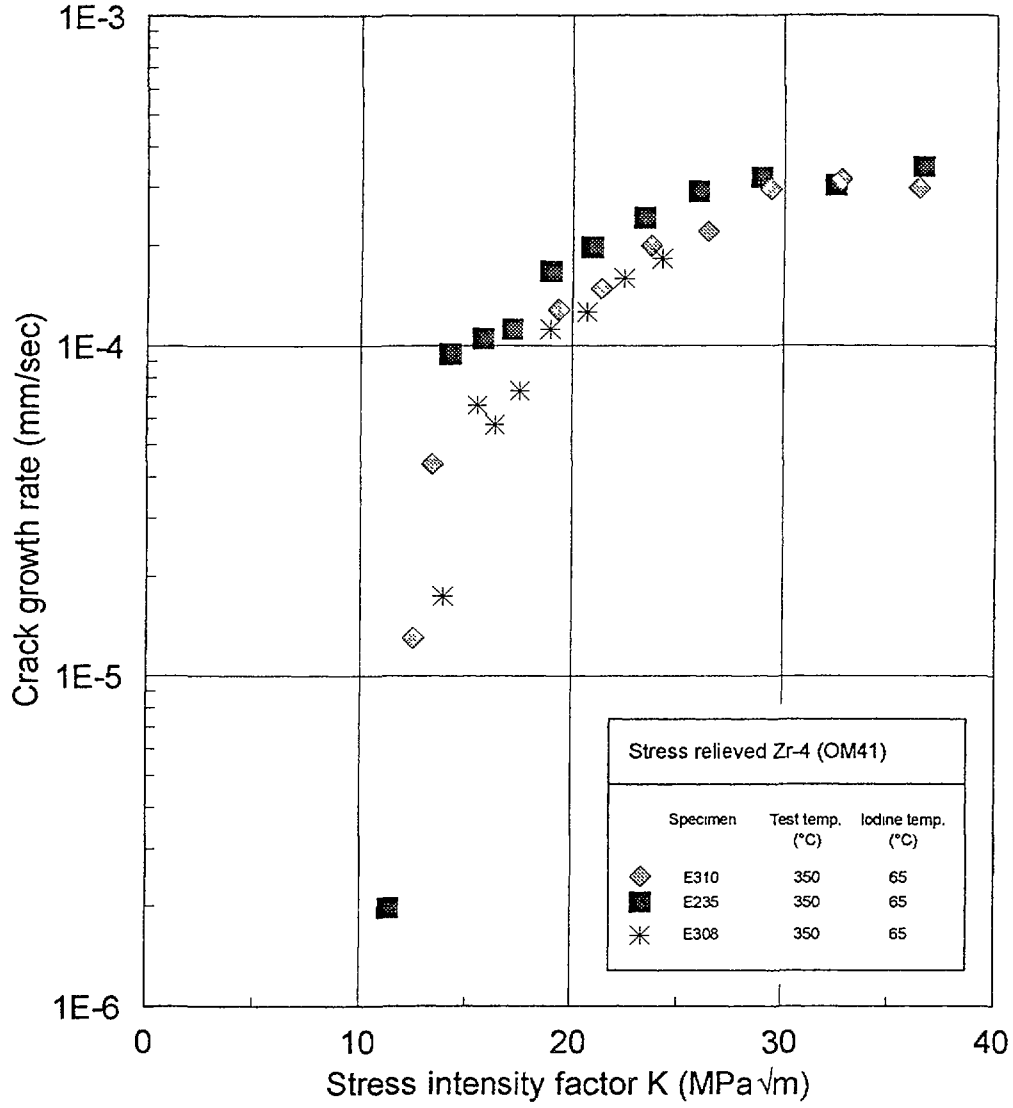

FIG. 2.9. Crack growth rate versus stress intensity factor for specimens of stress-relief annealed Zr-4 (material OM41) tested by AEA Technology at 350 °C with 1000 Pa of iodine.

one of the DCPD crack monitoring wires part-way through the test. Nevertheless, there was a reasonable degree of consistency between the tests. Both showed a threshold stress intensity factor around 8 MPa√m, which was lower than found in the tests at lower temperatures. The plateau in the crack growth curve also occurred at lower crack growth rate than found at 300 and 350°C. These observations are discussed further below.

2.4.2.2. Recrystallised Zr-4, TL orientation

A single test was performed on a specimen of Wah Chang recrystallised Zr-4 (material OM40), made in the same TL orientation as in the previous tests on stress relief annealed material. The test was carried out at 350°C with 1000 Pa of iodine and the results are shown in Fig. 2.11. The threshold stress intensity factor was higher than found in the stress relieved material at around 17 MPa√m. Stage II (plateau) crack growth was reached around 2×10^{-4} mm/s, which was slightly lower than in the comparable tests on stress relieved material.

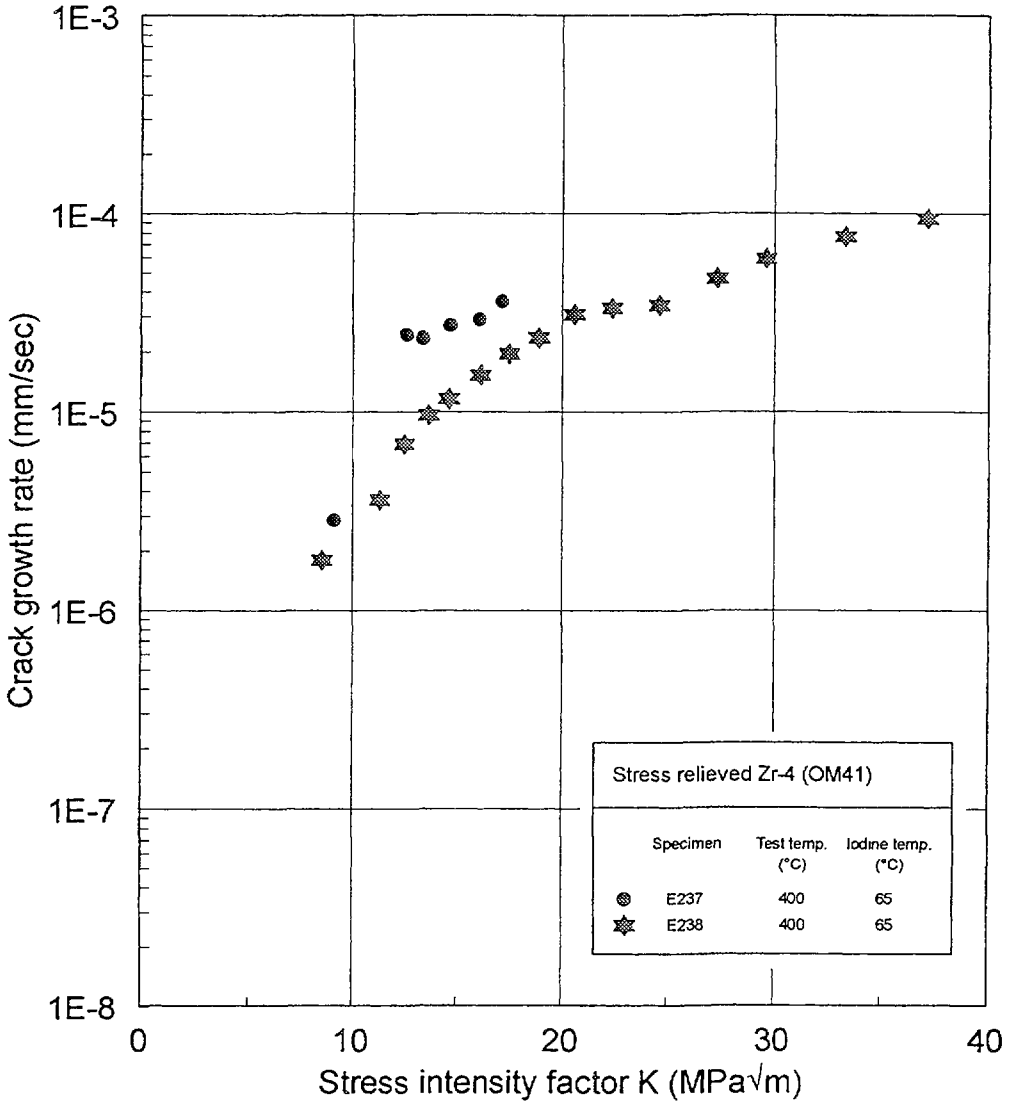

FIG. 2.10. Crack growth rate versus stress intensity factor for specimens of stress-relief annealed Zr-4 (material OM41) tested by AEA Technology at 400 °C with 1000 Pa of iodine.

2.4.2.3. Stress relief annealed Zr-4, LT orientation

A single specimen of the same stress relief annealed Zr-4 as used for the majority of tests by the host laboratory (material OM41) was manufactured in the LT orientation. As SCC of Zircaloy is well known to be strongly texture-dependent, the aim of the test was to investigate the magnitude of this effect for this type of test specimen. The same test condition was used as for the recrystallised Zr-4 and three of the stress relief annealed Zr-4 specimens, i.e. 350°C and 1000 Pa I_2. The results are shown in Fig. 2.12. The threshold stress intensity factor was higher than found in previous tests at around 20 MPa√m compared to 8-12 MPa√m for TL specimens. The stage II plateau crack growth rate was, however, very similar.

2.4.3. Fractography

The fracture surfaces of each specimen were examined using a Jeol S-520 Scanning Electron Microscope.

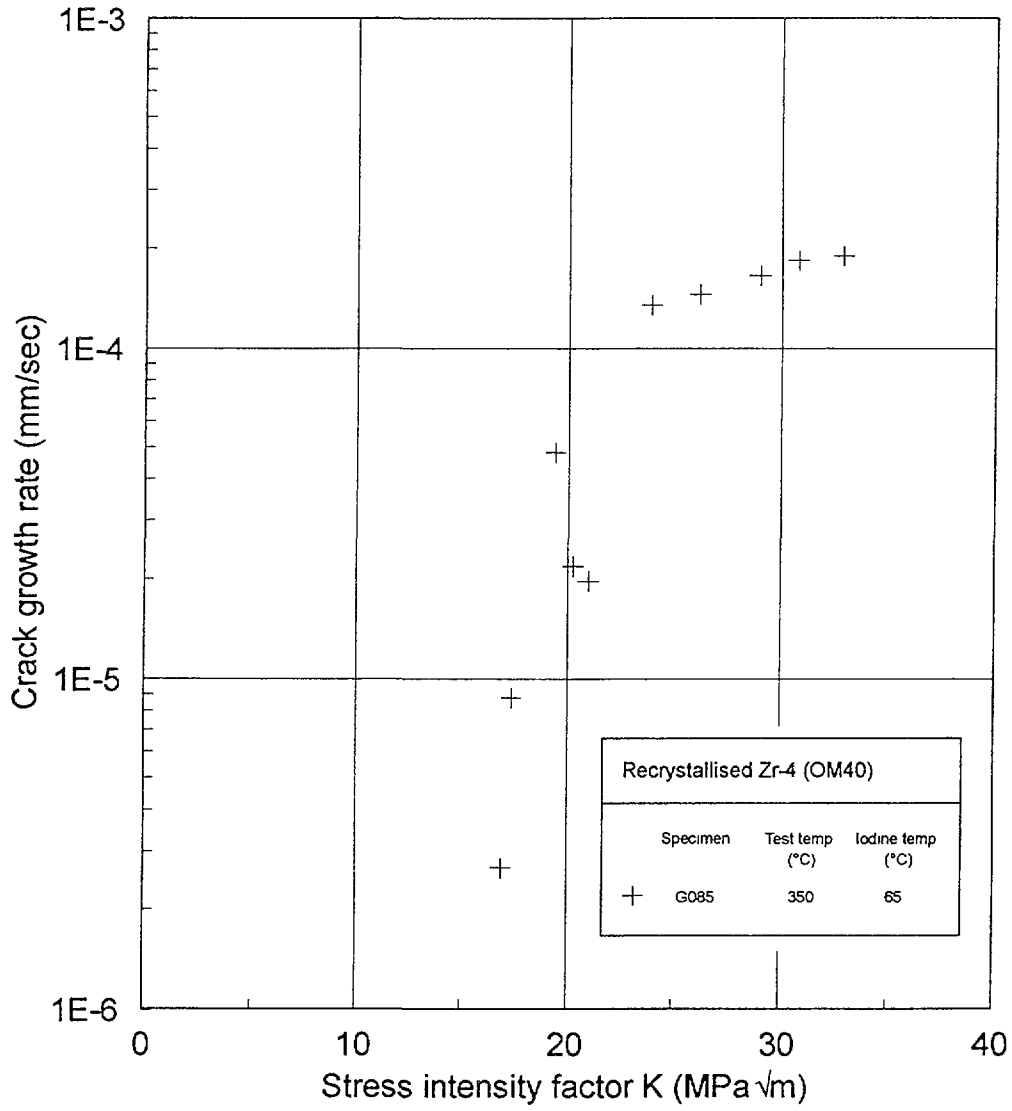

FIG. 2.11. Crack growth rate versus stress intensity factor for specimen of recrystallised Zr-4 (material OM40) tested by AEA Technology at 350 ℃ with 1000 Pa of iodine.

The fracture surfaces of the Wah Chang stress-relief annealed Zr-4 (OM41) tended to have a very "wooden" appearance (for example Fig. 2.13), caused by extensive out of plane cracking which led to a very rough fracture surface and the presence of deep "trenches" perpendicular to the crack front. There was evidence of cracking proceeding on a number of different planes with ductile tearing of the material between them, Fig. 2.14. These features could be evidence of a "layered" microstructure, with bands of material with a different texture throughout the sheet thickness. The fracture surfaces also showed evidence of both river patterns and fluting (Fig. 2.15) which are characteristic of iodine SCC in zirconium alloys. There were no differences in the appearance of specimens exposed at different temperatures or with different iodine concentrations.

Only one test was completed on the recrystallised Zr-4 (material OM40) and the fracture surface of the specimen was almost completely covered with a thick layer of zirconium oxyhydroxide when taken off test. This has prevented detailed fractography of this material at the host laboratory.

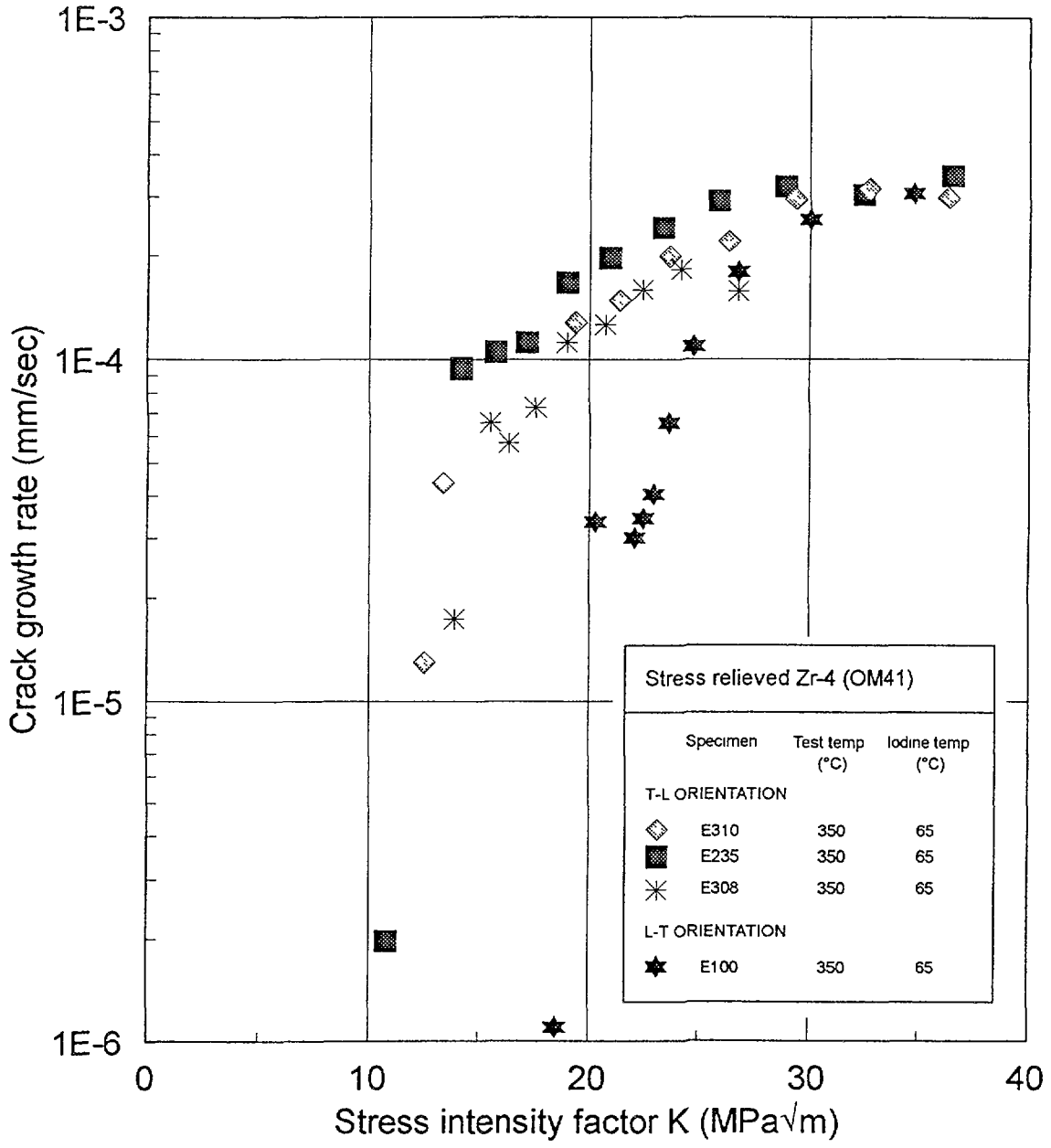

FIG. 2.12. Effect of specimen orientation on crack propagation for stress relief annealed Zr-4 (material OM41) tested by AEA Technology at 350 ℃ with 1000 Pa of iodine.

2.4.4. Discussion

The overall test matrix for the CRP included three temperatures, three iodine concentrations and five materials, together with tests on one material in the opposite orientation to the other tests in the programme. The host laboratory performed tests under a relatively narrow range of these test conditions. Only two iodine concentrations were used and only two materials were tested, recrystallised and stress relief annealed Zr-4 supplied by Wah Chang. The full range of temperatures were covered, however, together with a test on the effect of texture. The lack of duplicate test results, and a certain amount of experimental scatter, has hampered the firm identification of trends in the data.

FIG. 2.13. Fracture surface of specimens E308 and E310 (stress-relief annealed Zr-4, material OM41) tested at 350 °C and 1000 Pa of iodine, showing the uneven crack path and "trenches" running perpendicular to the direction of crack propagation.

FIG. 2.14. Specimen E308 showing ductile tearing of material between cracks proceeding on different planes.

2.4.4.1. Effect of temperature

Fig. 2.16 shows the results of all the tests performed by the host laboratory on stress relief annealed Zr-4 at 1000 Pa I_2 at 300, 350 and 400°C. The three tests at 350°C fell in a narrow scatter band with a high degree of consistency between them. By comparison, the tests at 400°C had a lower K_{Iscc} and lower crack growth rate in Stage II than found at 350°C. Whilst both tests carried out at 300°C had similar threshold stress intensities, both to each other and to the tests at 350°C, there was a wide degree of scatter in the subsequent propagation behaviour. One test produced the highest Stage II crack growth rates, whereas the other was intermediate between the 350 and 400°C tests. Whilst this scatter made the identification of clear trends in crack propagation rate difficult, a reduction in K_{Iscc} with increasing temperature is consistent with the results from other participating laboratories and with literature data. Temperature would be expected to influence SCC due to its effect on the mechanical properties of the material and on the diffusion rate of iodine. This would be consistent with a reduction in K_{Iscc} with increasing temperature, but the Stage II crack propagation rate might be expected also to increase. No firm conclusion on the effect of temperature on crack propagation rate may be drawn from these tests.

2.4.4.2. Effect of material condition

Fig. 2.17 compares tests under the same experimental conditions on recrystallised and stress relief annealed Zr-4. The threshold stress intensity factor was found to be 11-13 MPa$\sqrt{m}$

FIG. 2.15. "River patterns" left and "fluting" right on the fracture surface of specimen G091, a stress-relief annealed Zr-4 specimen (material OM41) tested at 350 ℃ with 100 Pa of iodine.

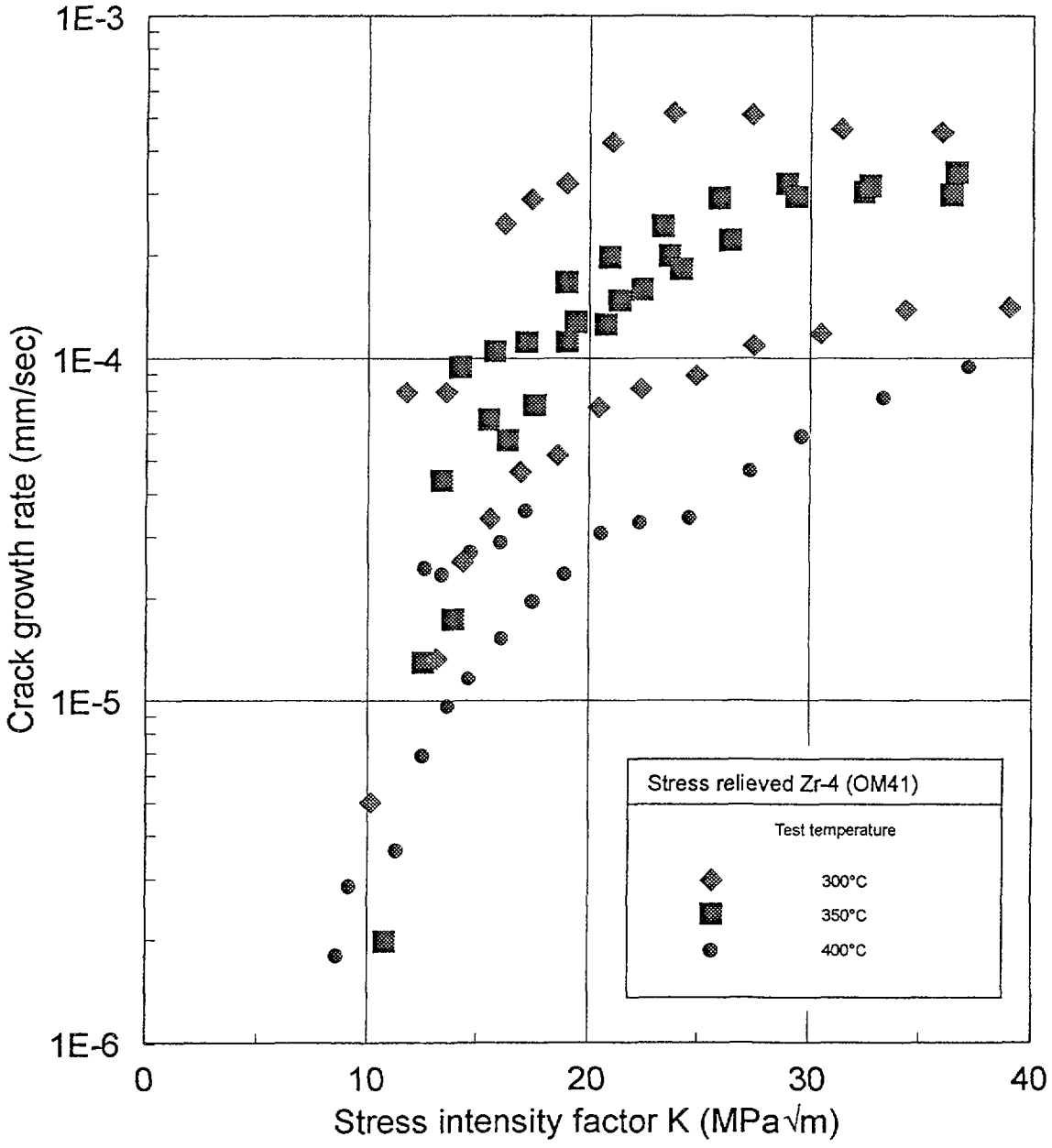

FIG. 2.16. Effect of test temperature on crack propagation in AEA Technology tests with 1000 Pa of iodine.

in the stress relieved material and around 17 MPa√m in the recrystallised material. The Stage II crack propagation rate was slightly lower in the recrystallised material, although with the scatter seen in this region in other tests, this observation may not be significant. However, the higher K_{Iscc} value for recrystallised material is consistent with the results of Knorr and Pelloux [2.2] in double cantilever beam (DCB) and wedge opening load (WOL) specimens made from Zircaloy plate and exposed in iodine at 300°C. Both the recrystallised and stress relieved materials had similar textures (see Appendix I, Fig. AI-2 and AI-3), so the difference in K_{Iscc} was probably related to the lower strength and higher ductility of the recrystallised microstructure. As noted in Section 2.5.3 above, it did not prove possible to compare the fracture surfaces of these specimens because of the thick layer of oxyhydroxide found on the specimen of recrystallised material at the end of the test which obscured any characteristic features.

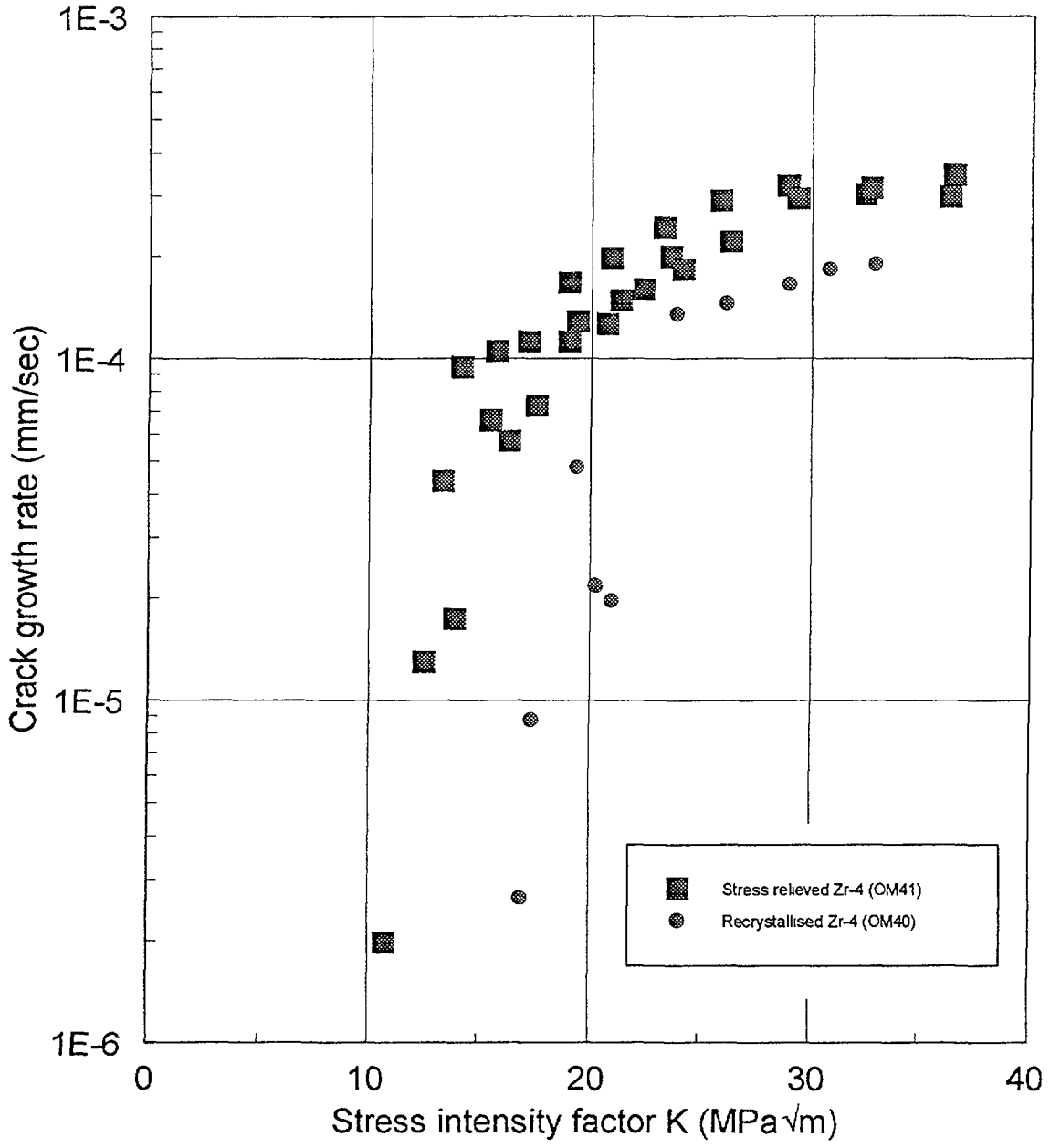

FIG. 2.17. Effect of material condition on crack propagation in AEA Technology tests at 350 °C and 1000 Pa of iodine.

2.4.4.3. Effect of iodine partial pressure

Fig. 2.18 shows the results of tests on stress relief annealed Zr-4 at 350°C and two different iodine partial pressure. There was no apparent effect of iodine pressure on the threshold stress intensity factor, which is consistent with results from other participants in the CRP, and is consistent with the observations of Peehs [2.3] and Tucker [2.4] of a threshold iodine concentration for SCC. This was attributed to the concentration of iodine required to form condensed layers of zirconium iodides on the specimen surface. In the current tests, the Stage II crack propagation rate was slightly higher for the test with 100 Pa I_2 than for the tests with 1000 Pa I_2. It should be noted, however, that the difference in crack growth rate in this region between iodine pressures was smaller than the variability recorded in other tests between nominally identical tests, so that this observation may be due to experimental scatter.

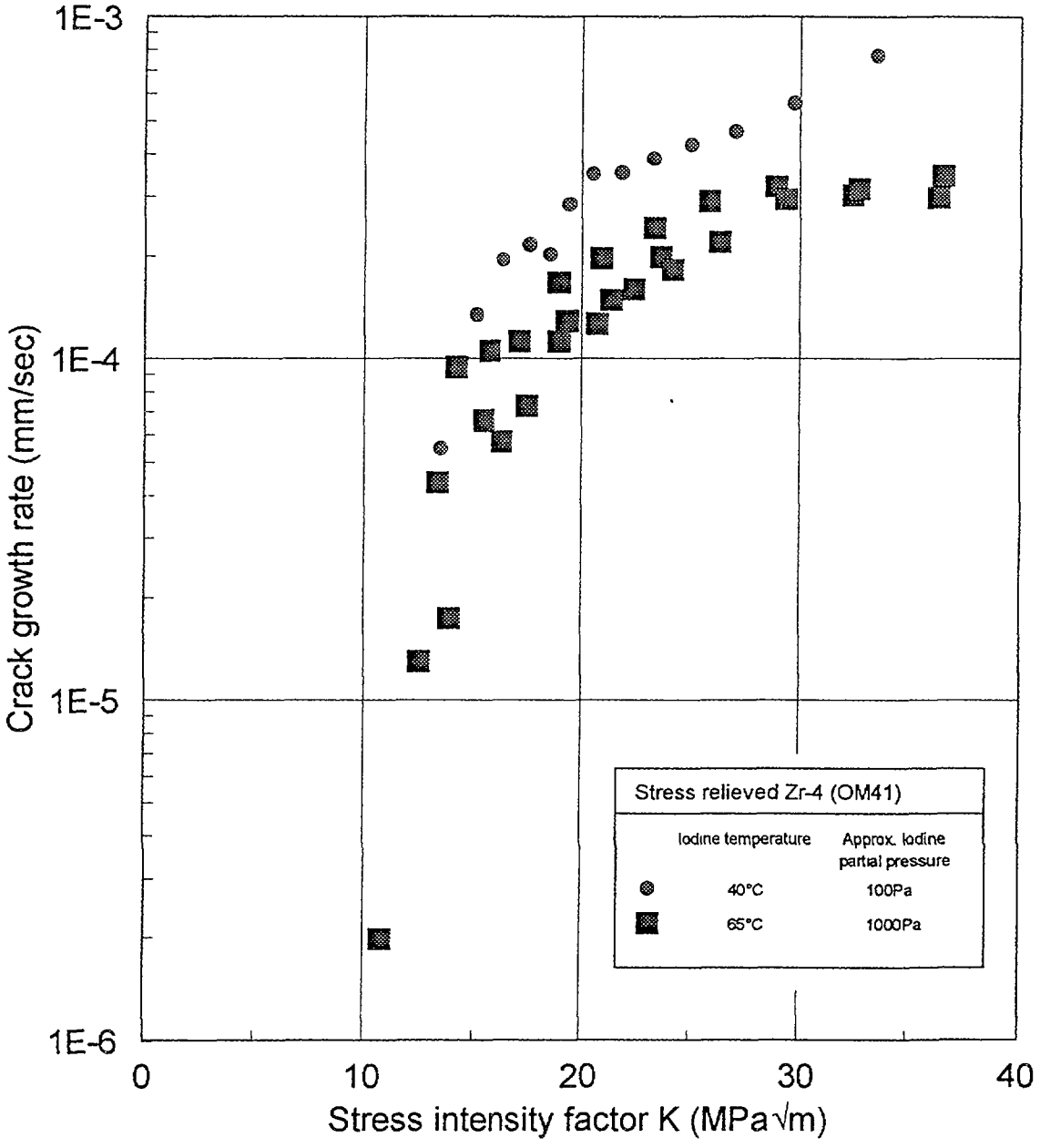

FIG. 2.18. Effect of iodine partial pressure on crack propagation in AEA Technology tests at low temperatures.

A decrease in crack propagation rate with increasing iodine partial pressure would also be inconsistent with the results of Peehs and Tucker, where crack propagation rate increased with increasing iodine concentration, at least up to a point where there was sufficient iodine present for the effect to "saturate". This is consistent with crack propagation being diffusion controlled. As diffusion is driven by the magnitude of the iodine concentration gradient, a higher external iodine concentration will produce more rapid diffusion and hence higher crack propagation rates, at least up to a saturation level.

2.4.4.4. Effect of texture

Stress corrosion cracking of Zircaloys has been shown to be strongly texture dependent. Cleavage (or pseudo-cleavage), the principal mode of crack propagation, is known to occur

along basal planes in the hexagonal close-packed (hcp) Zircaloy structure. Crack propagation will therefore occur more readily in materials with a texture in which a high number of basal planes are oriented perpendicular to the applied stress (and so parallel to the plane of crack propagation). In such materials, the threshold stress intensity factor will be lower and the crack propagation rate higher for values of K above the threshold. For the stress relief annealed material in the TL orientation, the basal planes are oriented approximately 30° from the crack propagation axis with the tilt axis parallel to the rolling (longitudinal) direction. The resolved fraction of basal planes in the crack opening direction (f-factor) is 0.321. For the LT specimens, the basal planes are also oriented around 30°C to the crack propagation axis, but the tilt axis remains parallel to the rolling direction and so the resolved fraction in the crack opening direction is only 0.124. From these texture considerations, crack propagation would be expected to be easier in the TL specimens than the LT specimens, as was found to be the case (Fig. 2.12). The threshold stress intensity factor was higher in LT specimens than for TL specimens, although the expected differences in crack propagation rate in the Stage II region were not evident in these tests.

REFERENCES TO CHAPTER 2

[2.1] ROOKE, D.P., CARTWRIGHT, D.J., Compendium of Stress Intensity Factors, HMSO, London (1976) 84-85.

[2.2] KNORR, D.B., PELLOUX, R.M., Effects of texture and microstructure on the propagation of iodine stress corrosion cracks in Zircaloy, Metal. Transact. **13A** (1982) 73-83.

[2.3] PEEHS, M., STEHLE, H., STEINBERG, E., Out-of-Pile Testing of Iodine Stress Corrosion Cracking in Zircaloy Tubing in Relation to the Pellet-Cladding Interaction Phenomenon, Zirconium in the Nuclear Industry (Fourth Conference), ASTM STP 681, American Society for Testing and Materials (1979) 244-260.

[2.4] TUCKER, R.P., KREYNS, P.H., KEARNS, J.J., The Effects of Internal Surface Flaws, Iodine Concentration and Temperature on the Stress Corrosion Cracking Behaviour of Zircaloy-4 Tubing, WAPD-TM-1248, Westinghouse Bettis Atomic Power Laboratory (1976).

Chapter 3

IODINE STRESS CORROSION CRACKING OF ZIRCONIUM ALLOYS IN ARGENTINA

3.1. INTRODUCTION

The computer codes used to simulate Zircaloy-clad fuel behaviour are fed with different parameters, including those belonging to the material, such as its strength, radiation hardening, temperature dependence of properties, etc. Among them, the susceptibility of the alloy to fission product induced SCC is normally introduced through the threshold tangential stress needed to promote this type of cracking; however, it is not really known if propagation could occur at lower stresses, since normally there is no data from tests conducted for more than 240 hours. Furthermore, the lowest measured value is a bit less than 200 MPa for irradiated material [3.1]; however, it is known that both intergranular (IG) crack initiation [3.2] and transgranular (TG) propagation [3.3] can occur in laboratory tests at stresses as low as 50 MPa.

One of the ways of measuring the I_2 SCC susceptibility of the Zircaloy cladding is to determine the crack growth rate (CGR). Under tension, this parameter is controlled by the stress intensity factors K_I, that represents the stress state at the tip of a propagating crack; K_I is a function of the applied stress, the length and the geometry of the crack:

$$K_I = \sigma \cdot a \cdot (\pi \cdot a)^{1/2}$$

where	σ	is the applied stress
	α	is a geometry dependent coefficient
and	a	is the length of the crack.

A characteristic threshold value of K_I exists, named $K_{I\text{-}SCC}$, below which cracks will not start. Above it, there is a strong dependence of the CGR on K_I. The determination of this relationship in different experimental conditions and in materials with different fabrication histories would help to understand the mechanisms of fuel cladding failure and would give a way of comparison of relative susceptibility for tubes of different origin, giving a more reliable base for failure prediction.

3.2. EXPERIMENTAL SET-UP

In order to conduct I_2 SCC tests on Zircaloy, a test machine was constructed, consisting of a stressing device, a furnace, a load cell, an atmosphere controller and direct current potential drop (DCPD) detecting equipment.

3.2.1. Materials

Coupons of different origins were tested. Some of them were supplied by the host laboratory and others were manufactured in CNEA from Zircaloy-4 sheet from a local supplier. Table 3.1 shows de chemical composition of this material; part of it was used in the Cold Worked (70%) condition and some portion was recrystallized 10 hours at 650°C.

TABLE 3.1: CHEMICAL COMPOSITION OF ARGENTINIAN ZIRCALOY

ALLOY CONCENTRATION (wt. %)									
Sn		Fe		Cr					
1.55		0.21		0.105					
Element	Al	B	C	Cl	Co	Cu	Hf	Mn	Mo
ppm	21	<0.5	194	<10	<10	68	93	22	<10
Nb	Ni	N	Pb	Si	Ta	Ti	W	U	V
26	29	45	<20	< 0	<100	23	33	<3	<10

Some of the specimens contained an initial fissure built up from an electro-eroded notch and a fatigue precrack, as detailed in Table 3.2. In addition, several samples with only the electro erosion notch have been used for part of the work, mainly for tests in methanol-iodine solutions or for calibration purposes. The annealing of recrystallized samples was conducted in vacuum. The dimensions of the samples can be seen in Fig.3.1; all numbers are given in millimetres. In Fig. 3.2 two samples already containing a fatigue precrack can be seen; one is shown intact and other broken in two pieces after overloading it in air at room temperature (RT). Five types of samples were supplied by the host laboratory for the IAEA program: designated OM40, OM41, OM42, OM44 and OM45, they were respectively: TWCA RX Zircaloy-4, TWCA SRA Zircaloy-4, TWCA RX Zircaloy-2, Cezus RX Zircaloy-2 and Cezus RX Zircaloy-4. In addition, coupons of identical geometry of batch OM41 have been used; they were cut along the rolling and the long transverse direction, to account for the effect of texture; these were designated J-LT and J-TL.

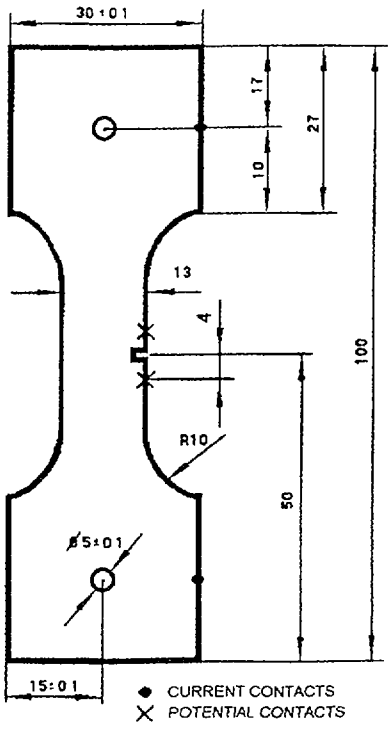

Fig. 3.1. Sample dimensions.

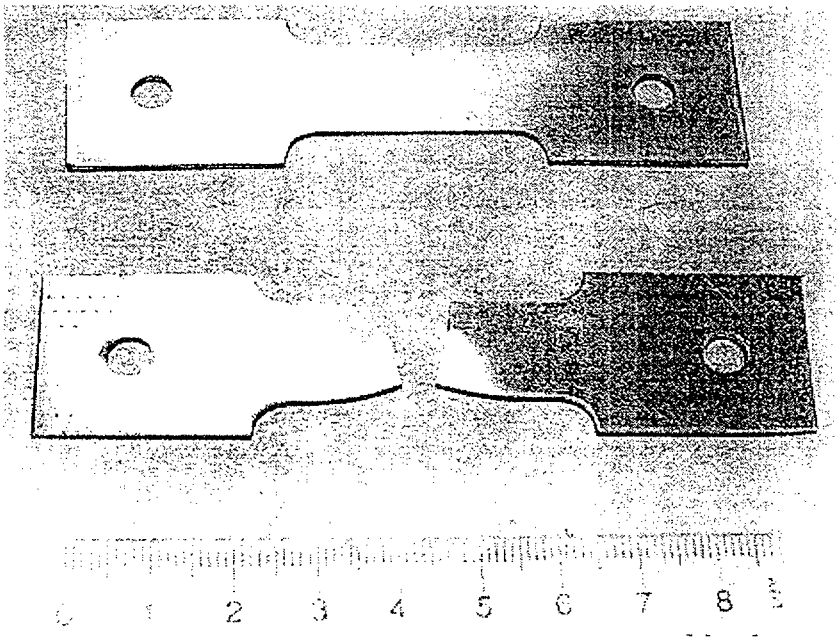

Fig. 3.2. Samples with fatigue precrack. Intact and broken.

3.2.2. Loading device

The stress system consists of a lever mounted on a rack, with a graduated water tank, as a dead weight, hanging from one end. The lever system was designed with a mechanical advantage of ten, thus making the load applied to the samples ten times greater than the weight used, as seen in Fig. 3.3. A careful calibration procedure was conducted to insure that applied load could be applied with a precision better than 5 %, normally about 2 %.

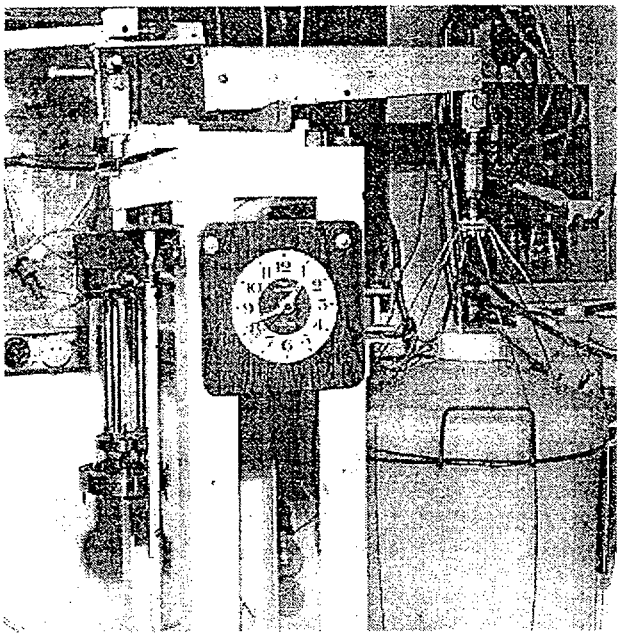

Fig. 3.3. Tensile machine.

The samples were mounted as depicted in Fig. 3.4, on grips with oxidised Zircaloy pins, to avoid electrical contact between the samples and the rig; the oxidising procedure consisted of an 8 hour anneal in air at 650 °C. The sample was enclosed in a glass cell, shown Fig. 3.5, with stainless steel caps, designed to contain the controlled I_2 atmosphere, allowing the stress line to actuate through them, all the sealing was made of Viton, a material with good resistance to both temperature and iodine attack. The furnace was built in two complementary pieces that embrace the cell as a book, as seen in Fig.3.6.

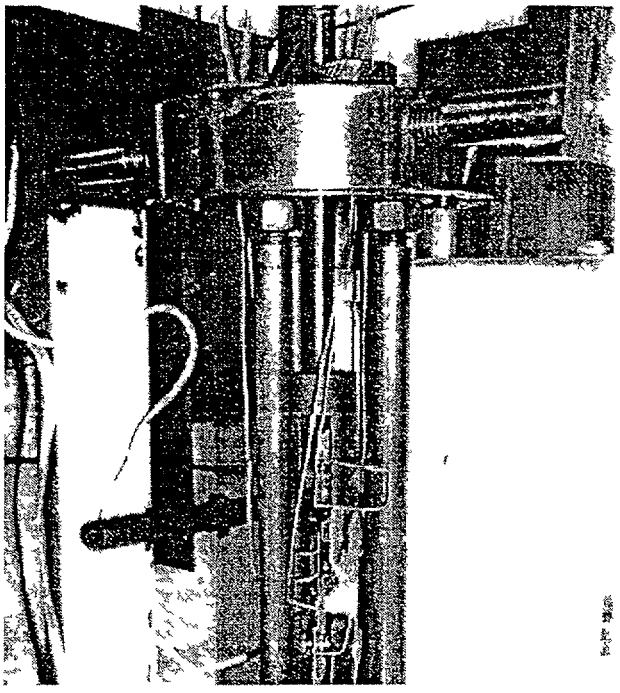

Fig 3 4 Sample mounted on stressing device

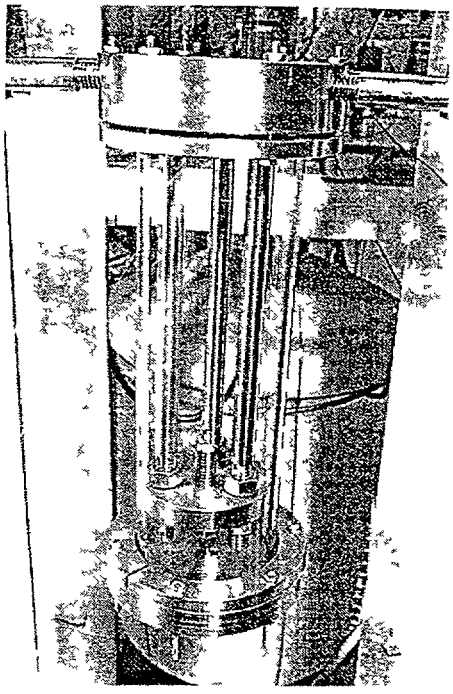

Fig 3 5 Glass cell

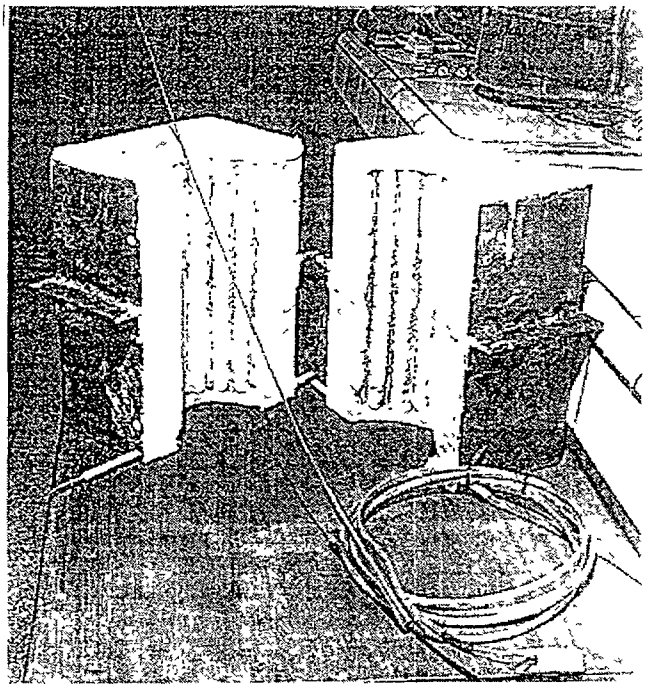

Fig. 3.6. Furnace and thermocouple.

TABLE 3.2: PRECRACKING CONDITIONS OF ARGENTINIAN SAMPLES

SAMPLE ID.	ΔK ($MPa.m^{1/2}$)	N° OF CYCLES	CRACK (mm)
A2	29.3	26 500	4.00
A3	26.3	4 200	3.64
A4	12.5	71 000	4.38
A5	10.7	78 000	3.83
A6	11.0	45 000	3.94
B1	4.75	70 000	1.65
B2	6.53	80 000	1.82
B3	6.08	130 000	1.03
B4	6.25	110 000	1.25
B6	6.29	87 700	1.47
B7	4.22	74 000	1.23
B8	3.10	116 000	1.44

3.2.3. Measuring technique

To measure real-time crack velocities, a detection device was developed, based on the direct current potential drop (DCPD) technique. This essentially consists in the determination of the instantaneous electrical resistance of a sample undergoing cracking, that increases as the section of the sheet is reduced by the crack propagation process. Fig. 3.7 is a drawing of the sample, showing the way a direct current is applied and the corresponding potential drop detected. The electric contacts are taken through 1 mm thick Zircaloy-4 wires precisely spot

welded in position as shown. A custom made DC power supply was used, capable of driving up to 5 A. with a measured stability of 3 parts per thousand during a ten day period with temperatures varying in the range of 30 ± 20 °C.

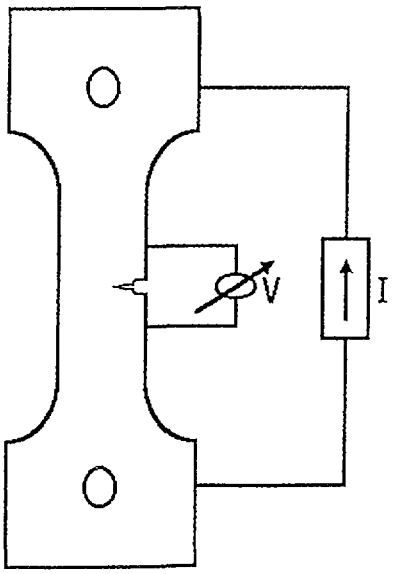

Fig. 3.7. Sample and connections.

Each value of measured PD corresponds to a precise crack length as defined through a calibration curve. Instead of recording the PD values, the $V_n = V/V_0$ ratio is considered, between the measured PD value and an initial one corresponding to a null length. This normalized non-dimensional quotient has the advantage of being independent of current and temperature, provided both parameters remain constant during the test. Fig. 3.8 shows the calibration curve V_n vs. $a_n = a/w$, where a is the crack length l normalized with respect to the width w of the sample: $a = l/w$, produced by means of measuring the PD voltage for different calibrated crack lengths. For this purpose, a standard sample was successively cut using an electro-erosion machine. The precision of crack measurement was 0.01 mm.

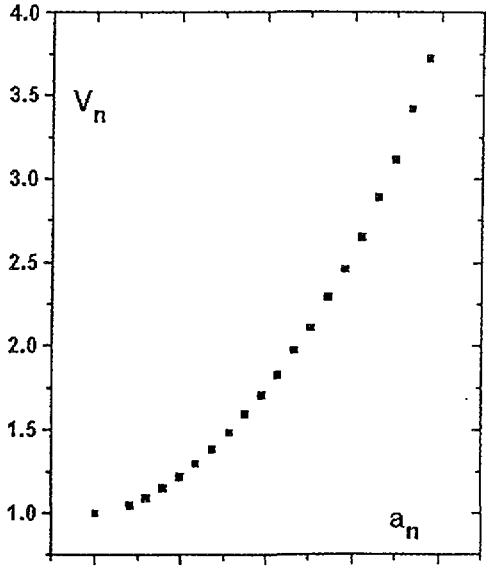

Fig. 3.8. DCPD calibration curve.

3.2.4. Environment

In order to generate the controlled iodine partial pressure a generation and circulation system was built, as described in Fig. 3.9. High purity argon was blown into the system from a cylinder, at a constant flow rate; the gas is made to pass through a glass bottle containing iodine crystals obtained by trisublimation; the bottle is kept at a controlled constant temperature by a thermostatic bath, thus creating an atmosphere with a known iodine partial pressure inside the bottle, which is pushed by the argon into the cell.

For the tests with methanol-iodine, the glass cell was not used. The corrodant solution was injected onto the sample by means of a special device shown in Fig. 3.10; the methanol that was used complies with the ACS (American Chemical Society) specifications, containing less than 0.2% of water. It was saturated with iodine.

TABLE 3.3: DETAILED COMPOSITION OF GAS.

ELEMENT	CONCENTRATION
Ar	99.999 %
CH_4	<1 ppm
CO	<1 ppm
H_2	<1 ppm
H_2O	<3 ppm
N_2	<4 ppm
O_2	<1 ppm

TABLE 3.4: IODINE IMPURITIES LIST.

ELEMENT OR COMPOUND	CONCENTRATION (wt: %)
iodine	>99.8
Non volatile compounds	<0.01
Br, Cl	<0.005
$SO_4^=$	<0.01

3.3. RESULTS

Twenty six Zircaloy SCC tests in I_2 vapours were conducted at three different temperatures: T1 = 300, T2 = 350 and T3 = 400 °C and at three I_2 partial pressures: I1 = 100, I2 = 1000 and I3 = 10 000 Pa on materials OM40, OM41, OM42, OM44, OM45, J-TL and J-LT. Two others were run without iodine in order to establish the system behaviour with respect to other processes than SCC. Several tests have been carried out also in iodine vapours and methanol-iodine solutions using Argentinian samples designated ARG. In several cases, the work was interrupted by experimental problems and later reinitiated. Sometimes only partial but valuable information was obtained; three samples have been lost. The tests from which significant data was obtained from CRP samples (at least one point in the Crack Growth Rate vs. K_I curve) are resumed in Table. Those conducted on locally manufactured samples are described in Table 3.6. In brackets: number of tests.

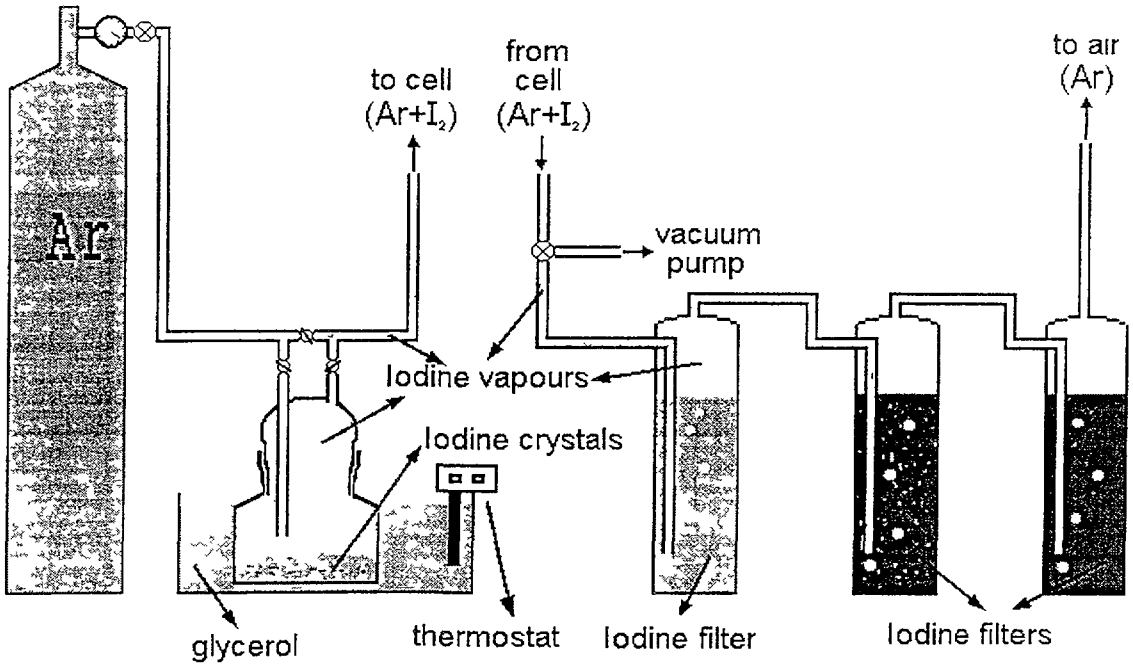

Fig 3.9. Iodine generation and circulation system

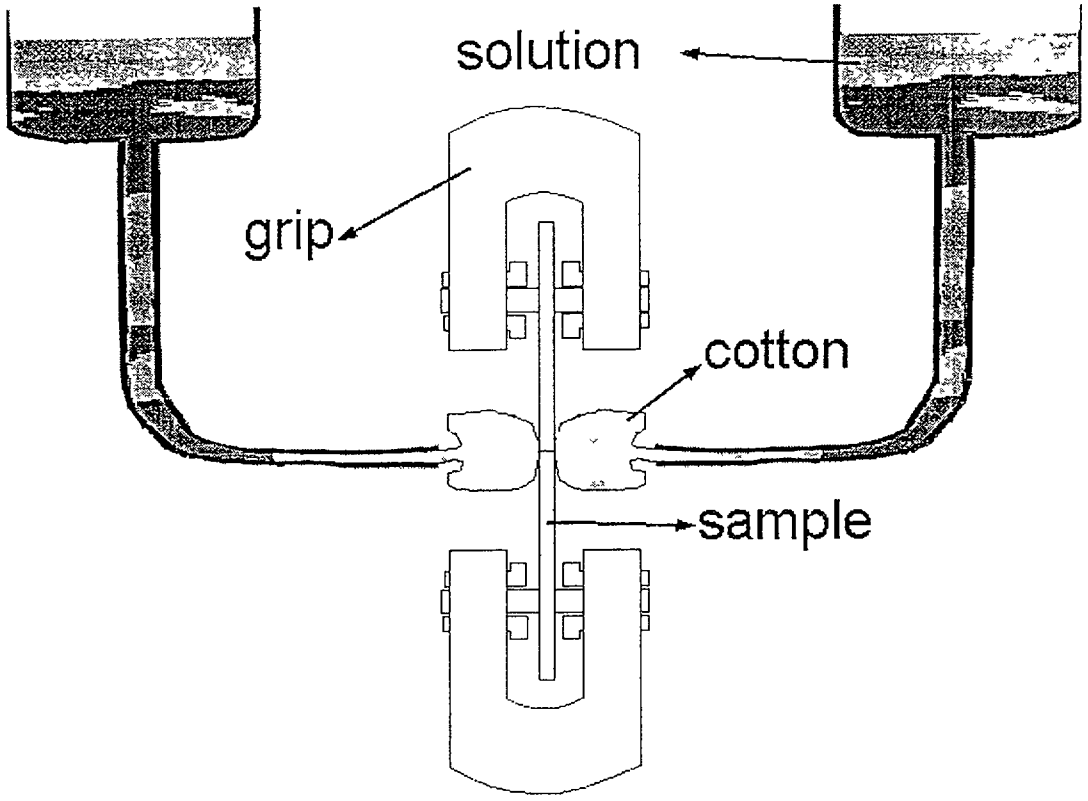

Fig 3 10 Special device to feed methanol-iodine solution onto the sample.

TABLE 3.5: TESTS CONDUCTED WITH CRP SAMPLES

	I0=0 Pa	I1	I2	I3
T1			OM45 (1)	
T2	J-TL (1) J-LT (2)	OM41 (1)	OM40 (3) OM41 (1) OM44 (3) OM45 (1) J-LT (2) J-TL (2)	OM40 (1) OM41 (1) OM42 (1) OM44 (1)
T3			OM41 (2)	

TABLE 3.6: TESTS CONDUCTED WITH ARGENTINEAN SAMPLES

T2 I2	CW (3) RX (3)
T3 I2	CW (1)
T3 I3	RX (1)
RT – METHANOL-IODINE	CW (7)

3.3.1. Resolution of the detection system

Fig. 3.11 shows how the values resulting from a typical SCC test fall into the DCPD calibration curve. In the region of lowest CGR values, corresponding to the initiation of the cracks, when the length of the fissure is close to the initial value, the variation ratio of normalised voltage with respect to normalised crack length is about 1.66. The DCPD response at that stage can be seen in Fig. 3.12. Even though the error band width is about 5 μV, the PD variation can be integrated over a statistically significant number of points giving an error of about 0.03 μV/h; if the voltage level is about 3000 μV, this is equivalent to a normalised voltage increase of 10^{-5}, which gives -taking into account the slope in the calibration curve- a normalised crack length increase of $6 \cdot 10^{-6}$, or a fissure increment of $7.83 \cdot 10^{-5}$ mm/h, (that is $2.18 \cdot 10^{-8}$ mm/sec). This would be the resolution limit of the detecting system; to achieve this level, a collection of points over a 10 hours period is required. Any PD variation at a higher level should be due to some physical process occurring in the sample, either crack growth, plastic deformation, etc.

3.3.2. Argentinean samples

3.3.2.1.Tests in iodine vapours

All the locally manufactured samples tested behaved in the same manner. Fig. 3.13 and Fig. 3.14 shows the DCPD response, characterised by an initial heating ramp and subsequent increments upon successive applied loads. However, the voltage remained constant after completion of each step of loading, without indications of any significant crack growth.

Those samples that were submitted to the highest values of stress showed the largest amount of plastic deformation, which in a few cases led to their complete plastic rupture. The

fracture surfaces showed the common features expected for this kind of process: ductile dimples and shear, as seen in Fig. 3.15; in one case, corresponding to sample A6, RX Zircaloy-4 tested at T2 and I2, only one spot of brittle fracture, 50 to 70 µm long, has been found, showing the typical transgranular pseudo cleavage facets, as shown in Fig. 3.16.

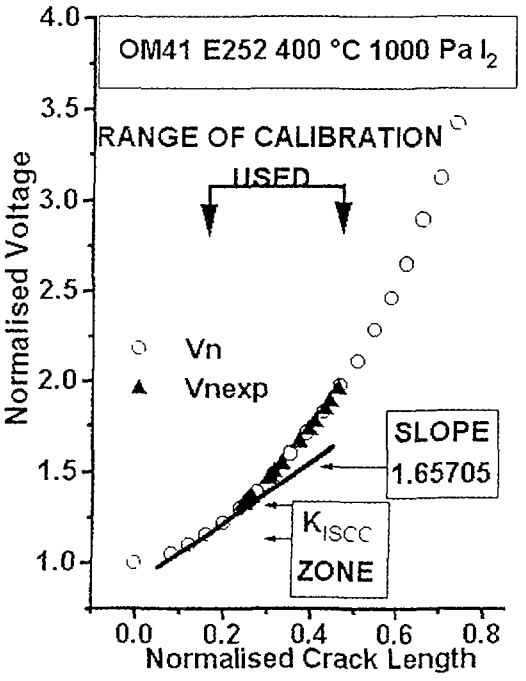

Fig. 3.11. Sensitivity of DCPD in the $K_{I\text{-}SCC}$ region.

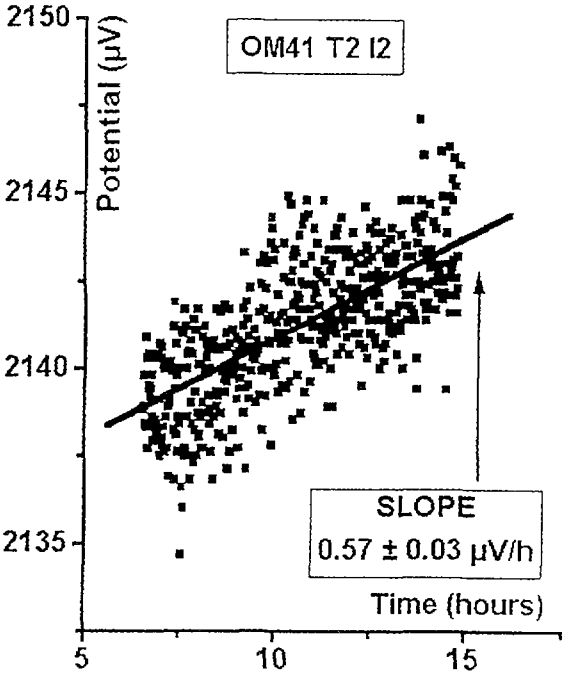

Fig. 3.12. Typical DCPD response obtained in the SCC tests.

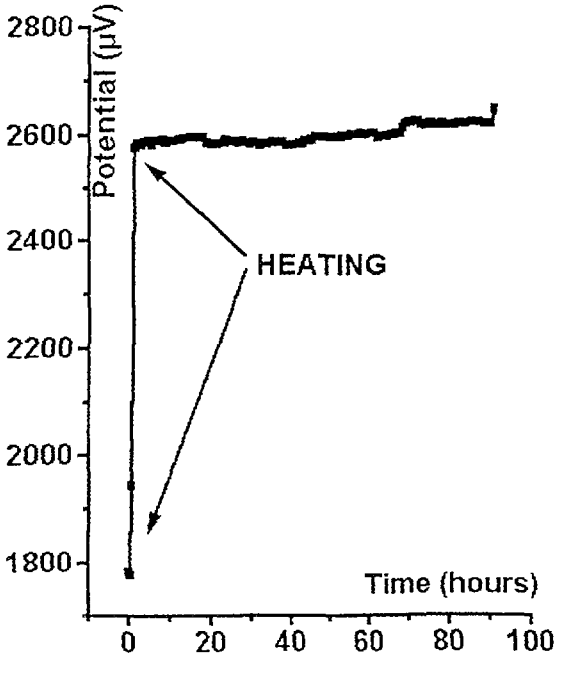

Fig. 3.13. Typical response of ARG. samples.

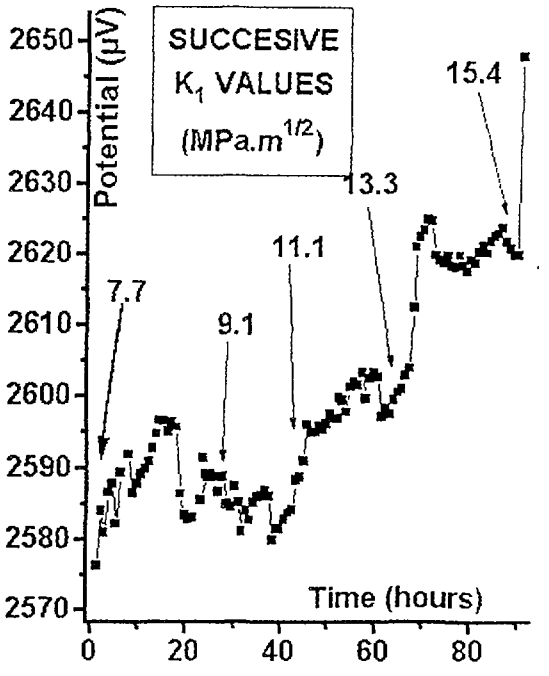

Fig. 3.14. Zoom of preceding graph.

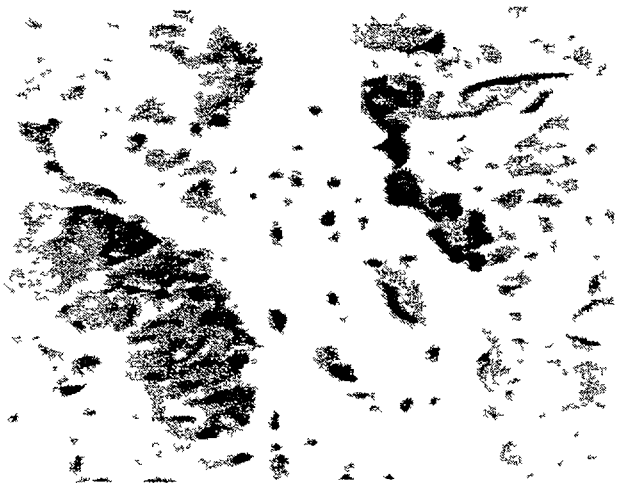

Fig 3.15 Ductile fracture in ARG samples

Fig. 3.16 Small brittle fracture area in A6

3 3 2 2 Tests in methanol-iodine solutions

In view of the apparent immunity of the locally produced samples to I_2 SCC, several of them were loaded in methanol-iodine solutions at room temperature, a more aggressive environment. These tests also served to try out the experimental set-up, establish the sensitivity, noise level, calibration, etc.

Fig. 3.17 shows the type of DCPD variation obtained in these tests. Cracks advanced very rapidly, leading to sample failure in less than an hour in some cases. Fig. 3.18 is a SEM picture of one of the fracture surfaces obtained. The fatigue and initiation zones can be seen. One of the characteristic features that appeared in these tests is that the fissures tend to propagate perpendicularly to the surface, through planes quite parallel to the applied stress.

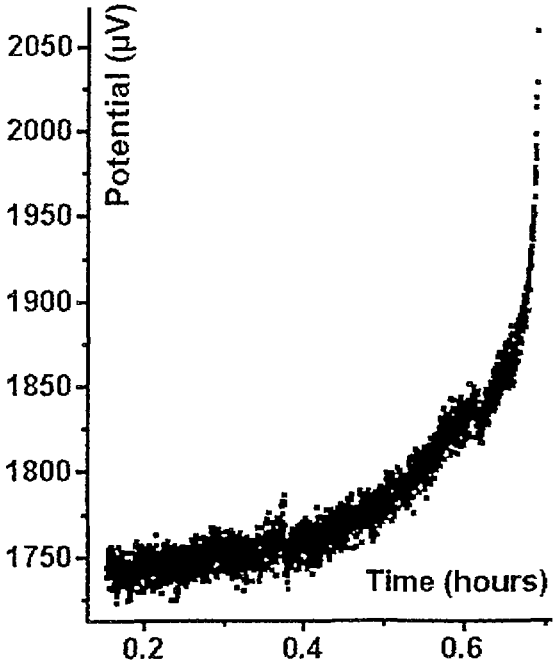

Fig. 3.17. Result of a test in methanol-I_2.

Fig 3 18. Fracture surface of a sample tested in methanol-iodine solution The fatigue and SCC initiation zone can be seen The crack tends to propagate perpendicular to the surface. (23 X)

3.3.3. CRP samples

3 3 3 1 Creep tests

During the development of the work it has become evident that there is some DCPD increase that is not due to crack advance, but to some other effect Having discarded temperature variations (controlled within a ± 0.5 °C range), current instability (better than 3%) or growing joint potentials (equal to or lower than 1 μV), this is undoubtedly due to the change of sample geometry due to plastic deformation by creep. This increment may result in errors in CGR and K_I estimations, because it would simulate a crack growth when this does not happen. Fig.3.19 and Fig.3.20 show the results of the tests conducted on samples J-002-LT and J-017-TL at 350°C in an argon atmosphere, without iodine. A potential increase after each step of loading is observed, followed by a stabilisation with slope decreasing in time. Resting times typical of those used during SCC tests have been considered.

3 3 3 2 Tests in iodine vapours

From Fig. 3.23 to Fig. 3.35 the CGR vs. K_I curves for all the tests in iodine vapours can be seen. When more than one sample have been tested in the same conditions (same iodine partial pressure and temperature), all the results are shown superposed, with the indication of sample identity. The raw data obtained for each test was converted to CGR and K_I values in an analytical way. However, due to the calculation noise generated, the final derivative needed to get the CGR values was sometimes performed using average of ten points, or manually from the crack length vs. time curve. Fig. 3.21 shows a typical aspect of the CGR vs. K_I curve obtained with each treatment.

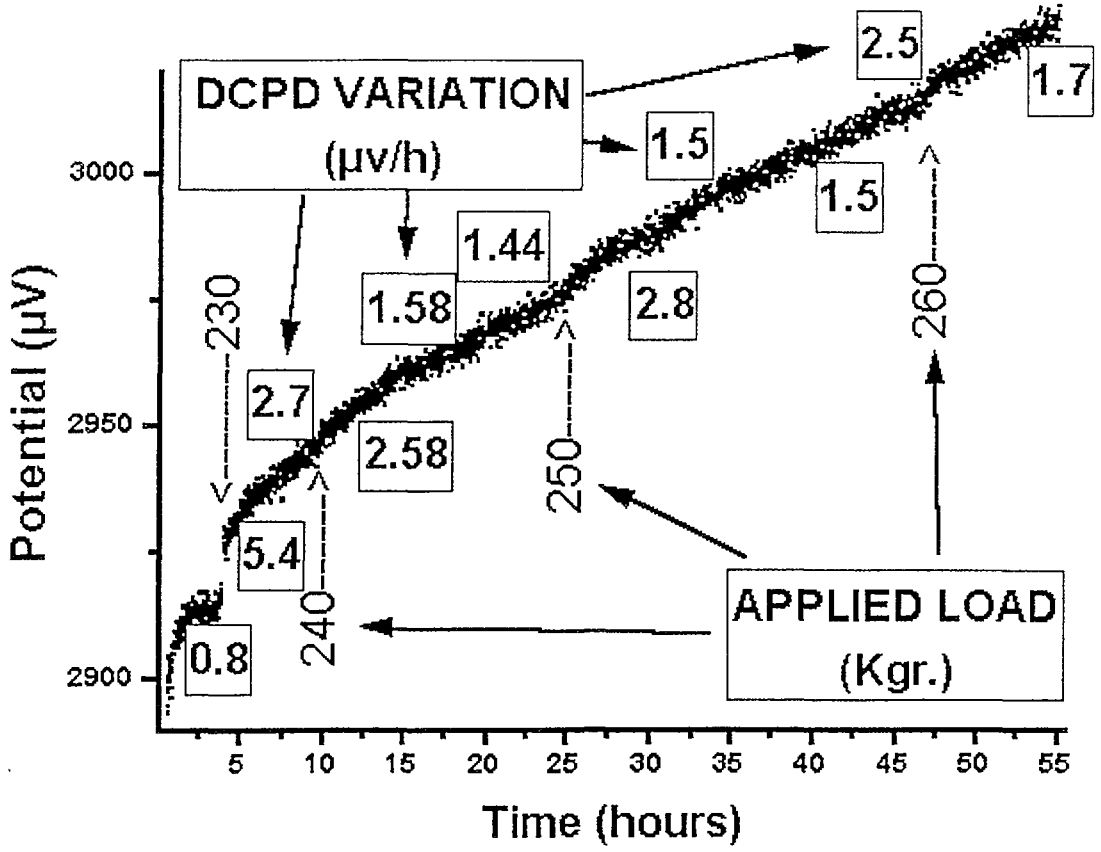

Fig. 3.19. Creep test conducted on sample J-002-LT at T2.

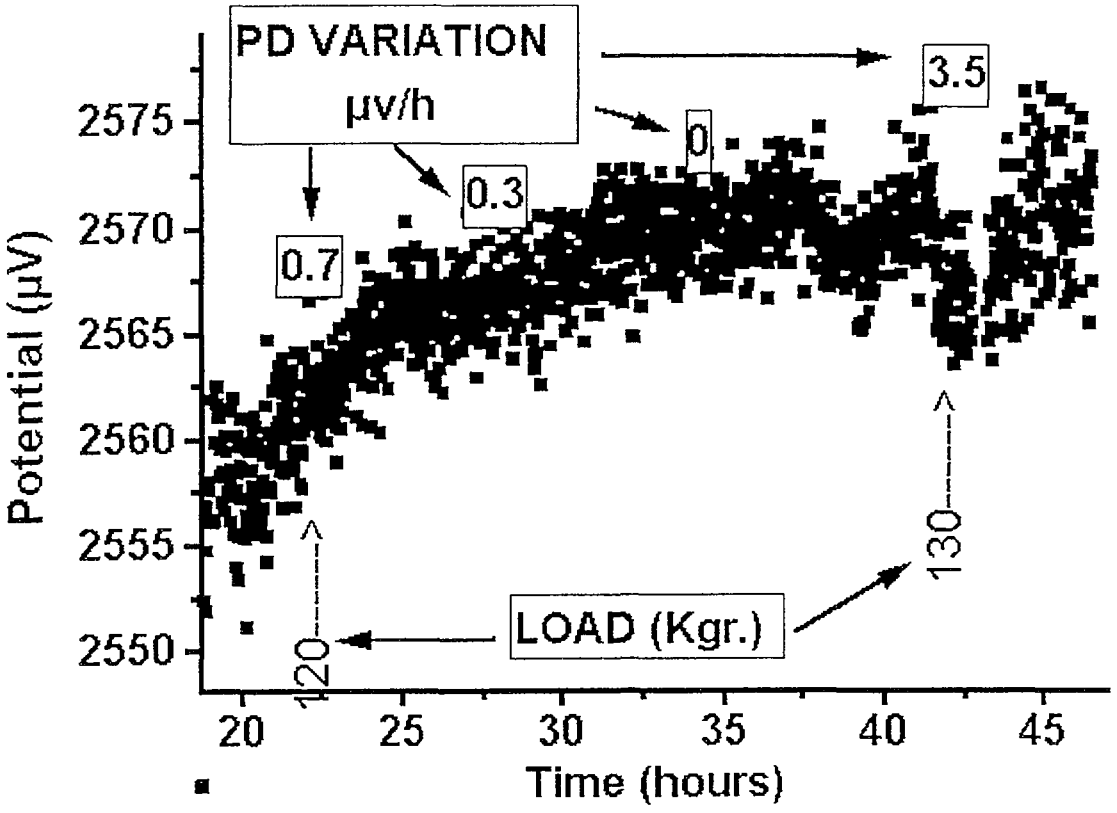

Fig. 3.20. Creep test on sample J-017-TL at T2.

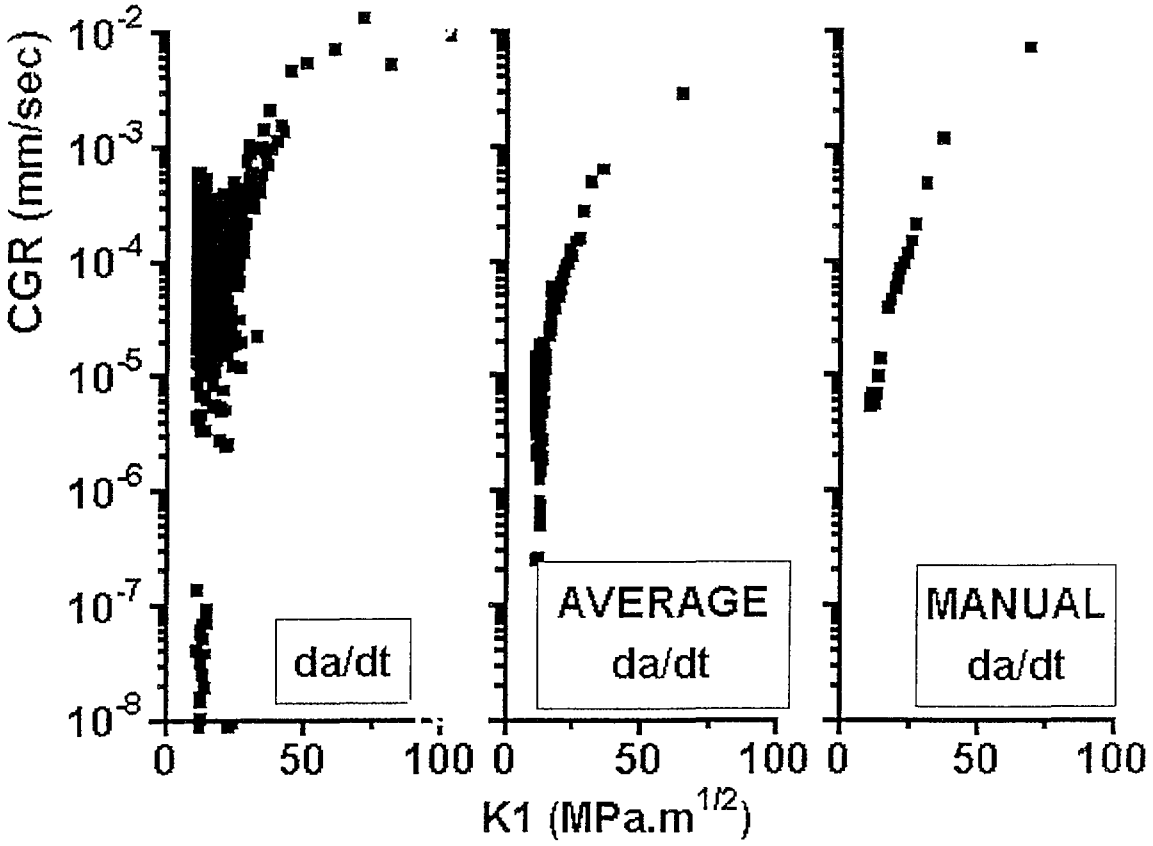

Fig. 3.21. Comparison of different methods of making the derivative.

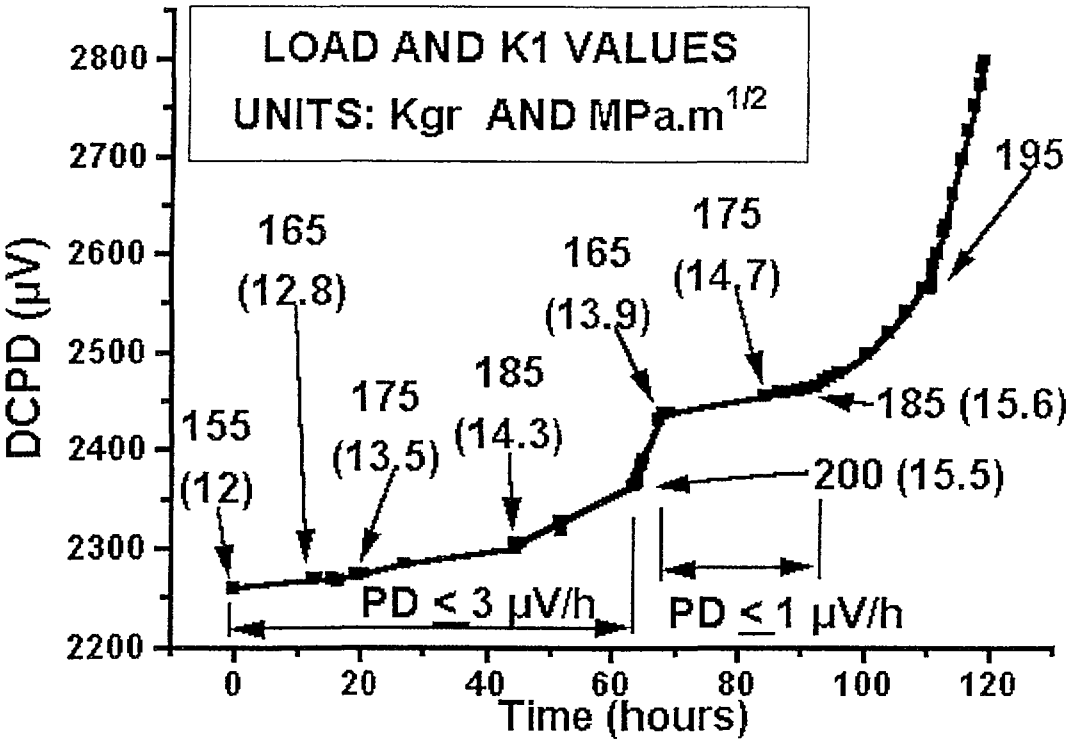

Fig. 3.22. Effect of successive K_I values applied on sample OM44 E-284 at T2 I2.

3.3.3.3. Reproducibility

The results obtained in iodine vapours in CRP samples showed an acceptable degree of reproducibility, from the CGR vs. K_I curve point of view, as seen in Fig. 3.23, Fig. 3.30 and Fig. 3.34, with a few exceptions, such as the behaviour of sample E-285 in Fig. 3.30. This particular test was affected by several experimental problems: leaking through the seals that permitted the ingress of air, bending of the pins that resulted in deformation of the sample that ended up with a slight curvature around the vertical direction, etc.; the total duration of this experiment marked a record: 221 hours. At the other end, sample J-019-LT also performed unusually, as shown in Fig. 3.21; it broke in about 2 hours when tested at T2 I2.

A point of special concern is the one referred to the $K_{I\text{-}SCC}$ values obtained. These are generally higher than those found in similar work done for the CRP [3.4]. Nevertheless, some of the numbers arising from the present experiments have been validated not only by duplication of tests but by the unloading-reloading procedure in the same run. In Fig. 3.22, the case of sample E-284 of material OM44 tested at T2 I2 can be seen.

The first load applied was 155 kg., corresponding to a K_I value of 12 MPa.m$^{1/2}$ (initial crack length was 2.07 mm). The DCPD did not show any significant increment in the following 10 hours; therefore, the load was increased to 165 kg. (K_I = 12.8 MPa.m$^{1/2}$); another load increase followed 10 hours later and a third one after 42 hours of testing; at this point the potential had been growing at a rate of about 1 μV/h or less. As more than 20 hours had passed since the last increment, with a PD rate increase of less than 3 μV/hour, a new load was applied, 200 kg. (K_I = 15.5 MPa.m$^{1/2}$). This action resulted in an acceleration of the voltage increase, associated with a growing crack. This process was allowed to continue until the calculations indicated the plastic zone had been passed through; then the load was lowered to 165 kg. (K_I = 13.9 MPa.m$^{1/2}$) and the crack arrested. Only 25 hours later and after successive load increases ending with a load of 185 kg. (K_I = 15.6 MPa.m$^{1/2}$), the fissure

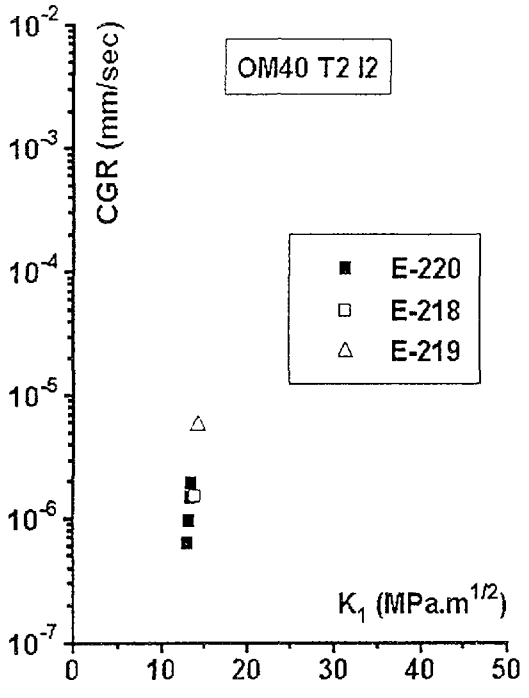

Fig. 3.23. Three tests on OM40 T2 I2.

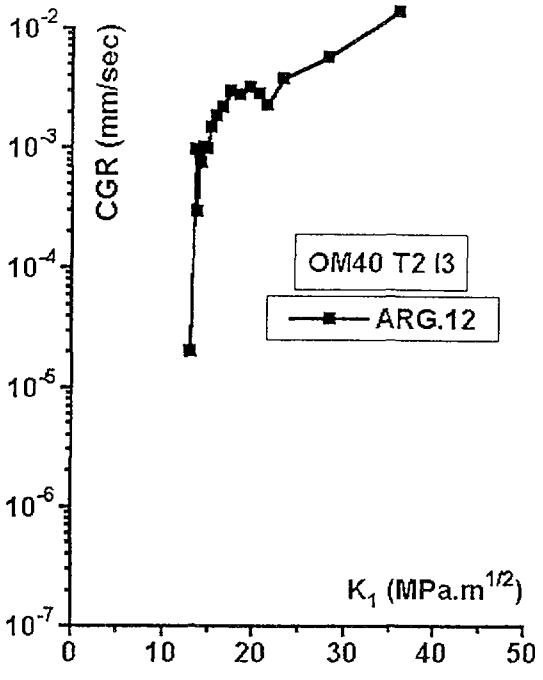

Fig. 3.24. One test on OM40 T2 I3.

advance restarted. This indicates a consistent K_I threshold of 15.5 ± 0.1 MPa.m$^{1/2}$, unless there was some length increment between time 44 and time 64 hours, with a PD increment rate of 3 μV/h, with a K_I value of 14.3 MPa.m$^{1/2}$, still higher of those reported elsewhere.

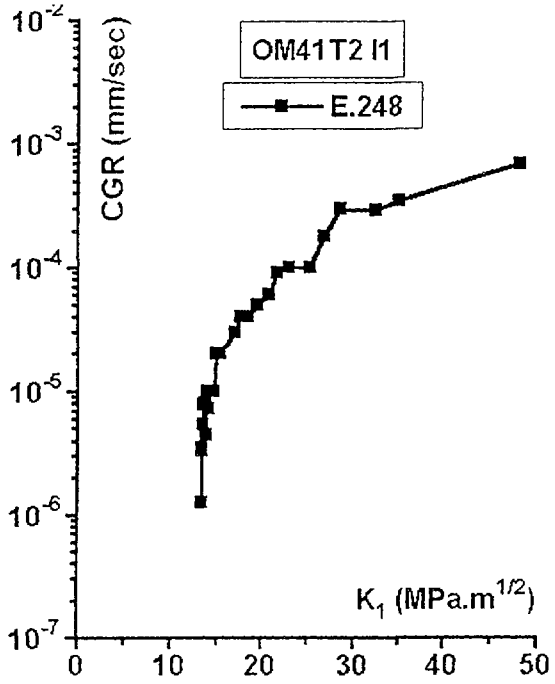

Fig. 3.25. One test on OM41 T2 I1.

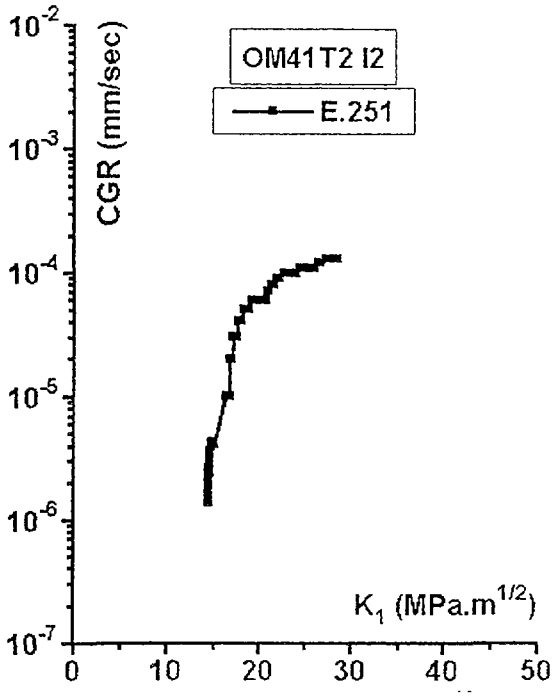

Fig. 3.26. One test on OM41 T2 I2.

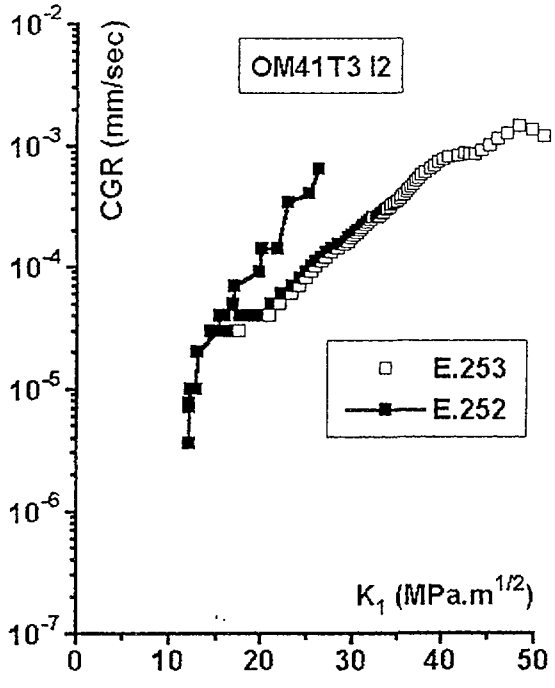

Fig. 3.27. Two tests on OM41 T3 I2.

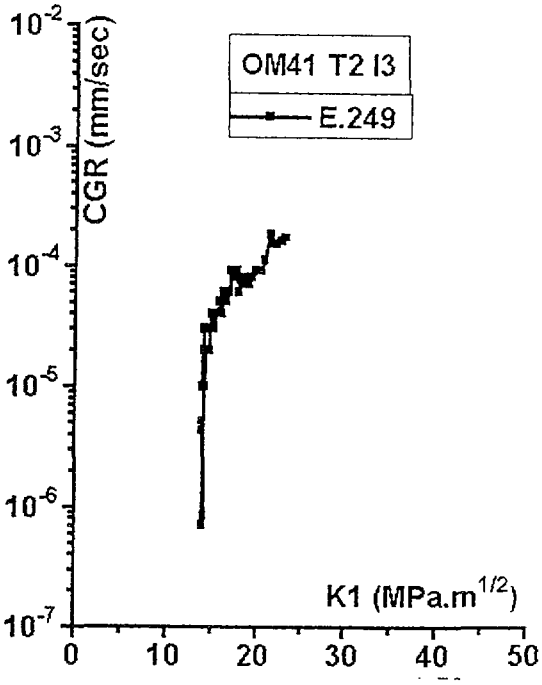

Fig. 3.28. One test on OM41 T2 I3.

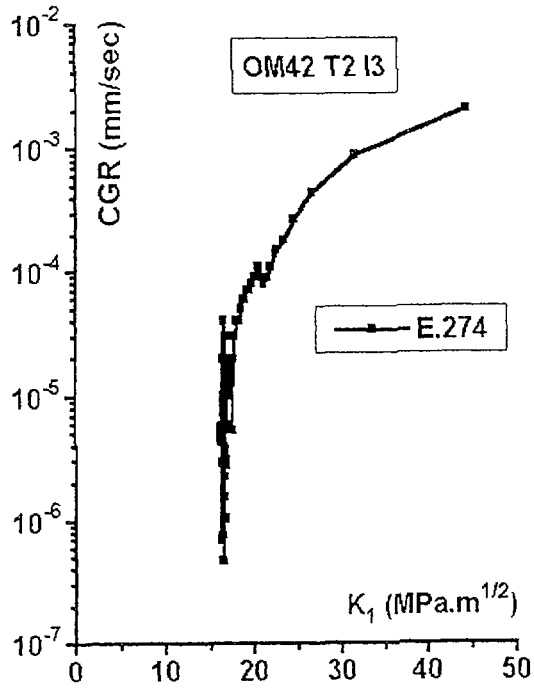

Fig. 3.29. One test on OM42 T2 I3.

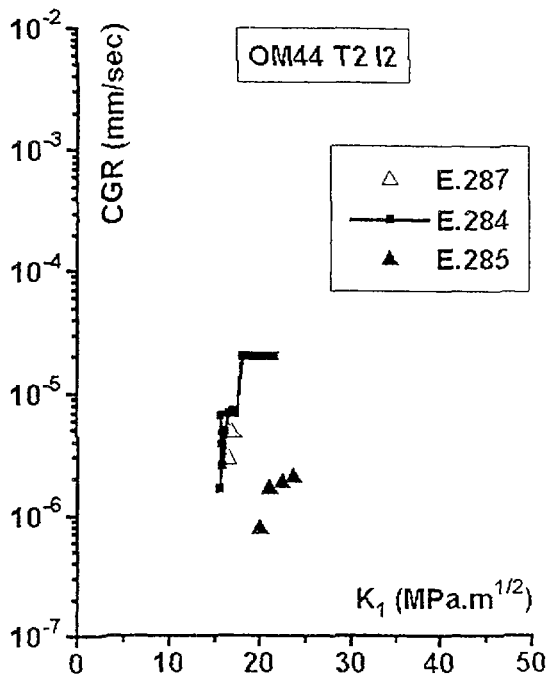

Fig. 3.30. Three tests on OM44 T2 I2.

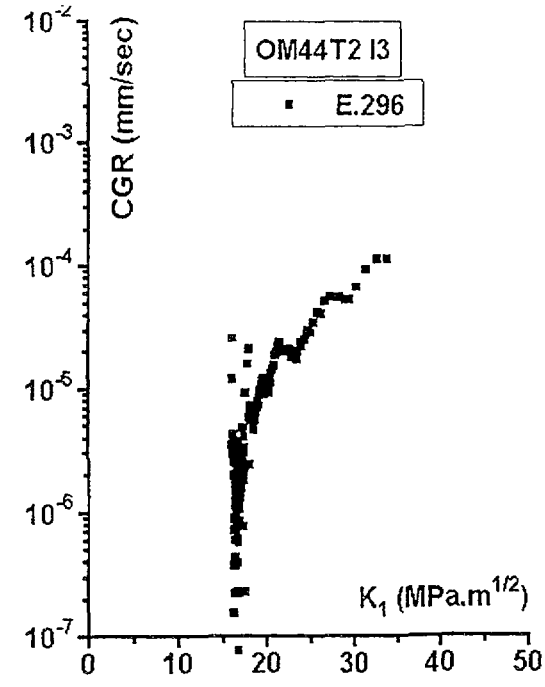

Fig. 3.31. One test on OM44 T2 I3.

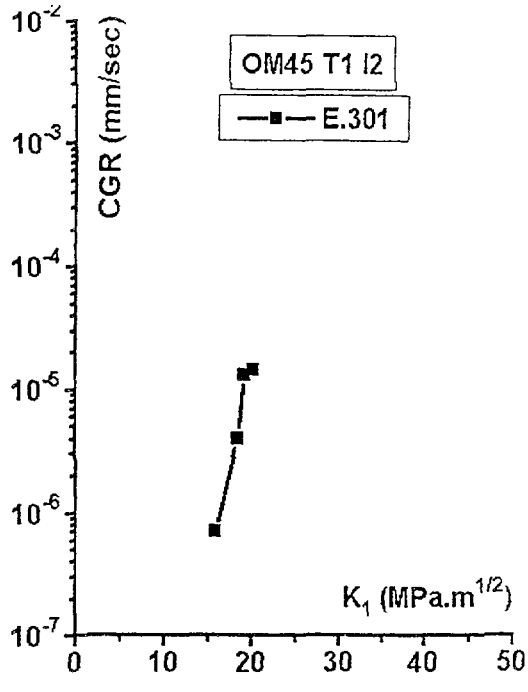

Fig. 3.32. One test on OM45 T1 I2.

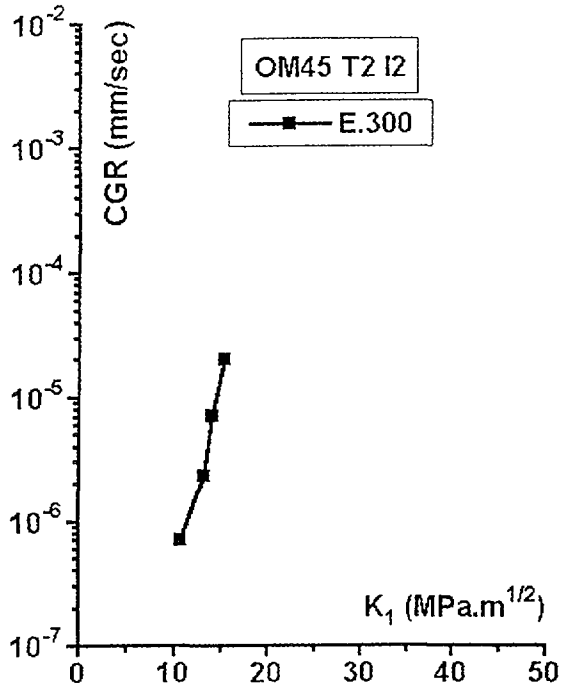

Fig. 3.33. One test on OM45 T2 I2.

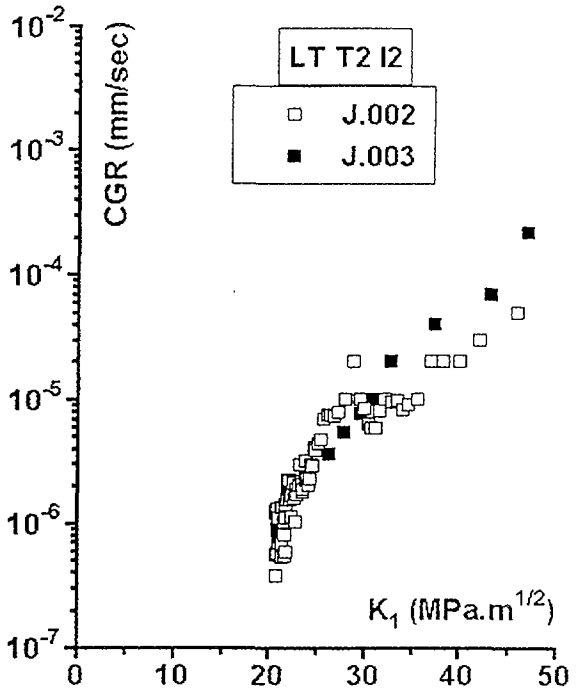

Fig. 3.34. Two tests on LT at T2 I2.

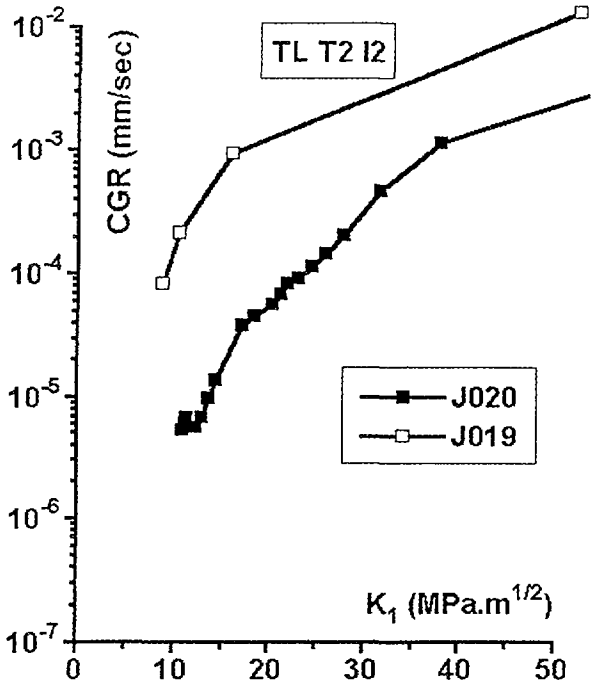

Fig. 3.35. Two tests on TL T2 I2.

Nevertheless, this would not be consistent with the fact that when the sample was reloaded there was not any sign of crack progress with K_I of 14.7 during 8 hours (potential increase of about 1 μV/h between times 84.4 and 92.6 hours).

3.3.4. Crack length

The following table shows the values of final crack lengths of several samples, calculated from the DCPD numbers obtained, compared with those actually measured Of those tested samples that were preserved from breaking in two pieces, some have been allowed to grow cracks of several millimetres, whereas some of the experiments were interrupted sooner; hence, two different ranges of final crack lengths have been produced. one around 3 mm and another around 6 mm The differences between the actual numbers and those computed from the experimental PD data tend to be higher for the longer cracks.

TABLE 3 7: COMPARISON OF MEASURED AND CALCULATED CRACK LENGTHS.

SAMPLE AND CONDITIONS	a_0 (mm)	$a_{CALCULATED}$ (mm)	$a_{MEASURED}$ (mm)	Δa (mm)
OM41 E251 T2 I2	2.06	5.00	5.32	0.32
OM40 E220 T2 I2	2.12	2.50	2.48	0.02
OM44 E287 T2 I2	2.07	2.45	2.38	0.07
OM44 E285 T2 I2	2.00	2.67	2.66	0.01
OM41 E252 T3 I2	2.21	6.00	7.15	1.15
OM41 E248 T2 I1	2.08	6.71	6.29-6.7	$\leq$ 0.42
OM44 E284 T2 I2	2.070	3 34	3.29	0 05
OM45 E300 T2 I2	1.99	3.03	3.15	0 12
OM41 E249 T2 I3	2.085	4.08	4.11	0.03
OM44 E296 T2 I3	2.18	5.41	5.47	0.06

In Fig. 3.36, Fig. 3.37 , Fig. 3.38 and Fig. 3.39 the fracture surfaces and side view of one sample of each case can be seen. In the longer cracks, their tips tend to be branched with higher deformation and the fracture surface tends to end with an arrow shape; in the shorter ones, instead, the tip is much more defined and the fracture ending is more even.

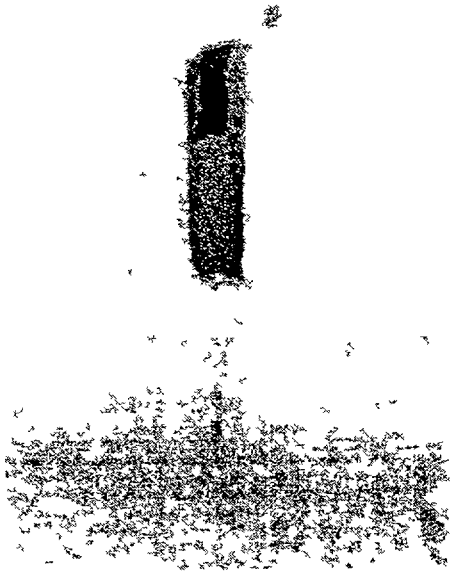

Fig 3 36 Side view of short fissure

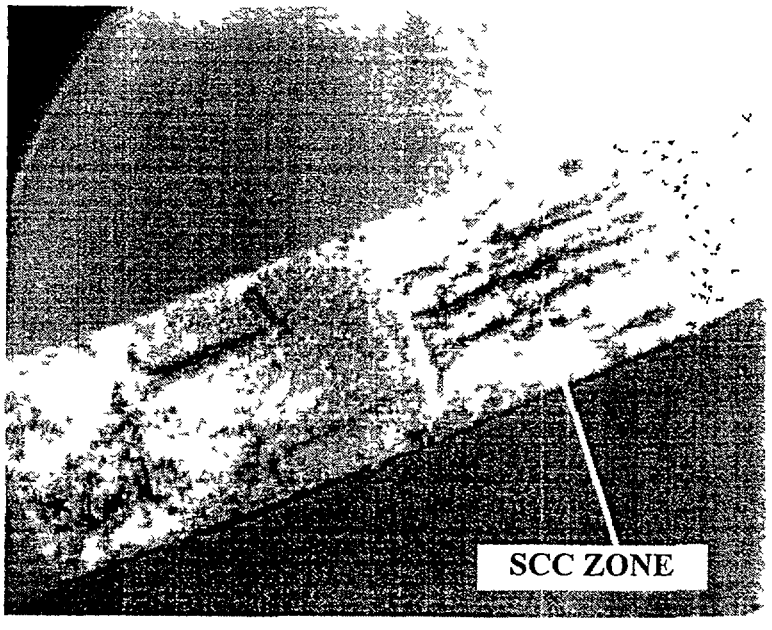

Fig 3 37 Fracture surface of fissure shown in Fig 3 36, produced in air at room temperature

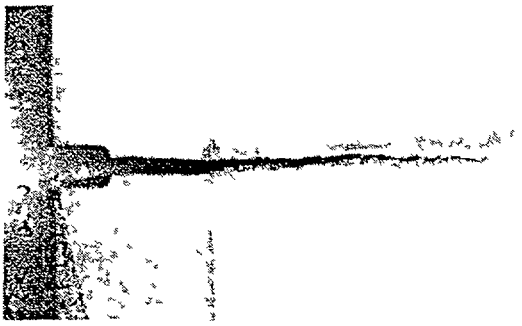

Fig 3 38 Side view of long fissure.

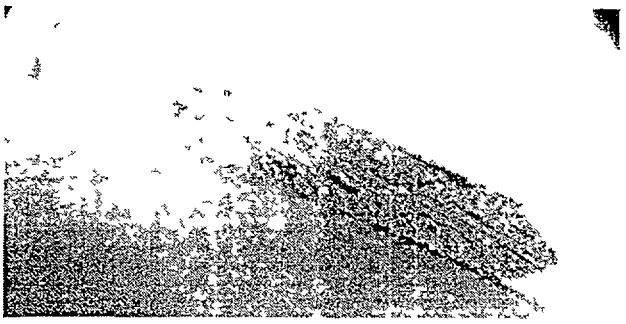

Fig 3 39 Fracture surface of crack of Fig 3 38

3.3.5. Fractographic aspects

In Fig. 3.40, the general view of a typical fracture surface is depicted; all the different parts can be seen, including the notch, fatigue precrack, SCC propagation and final ductile rupture. When viewed in detail, each one has its corresponding fractographic appearance.

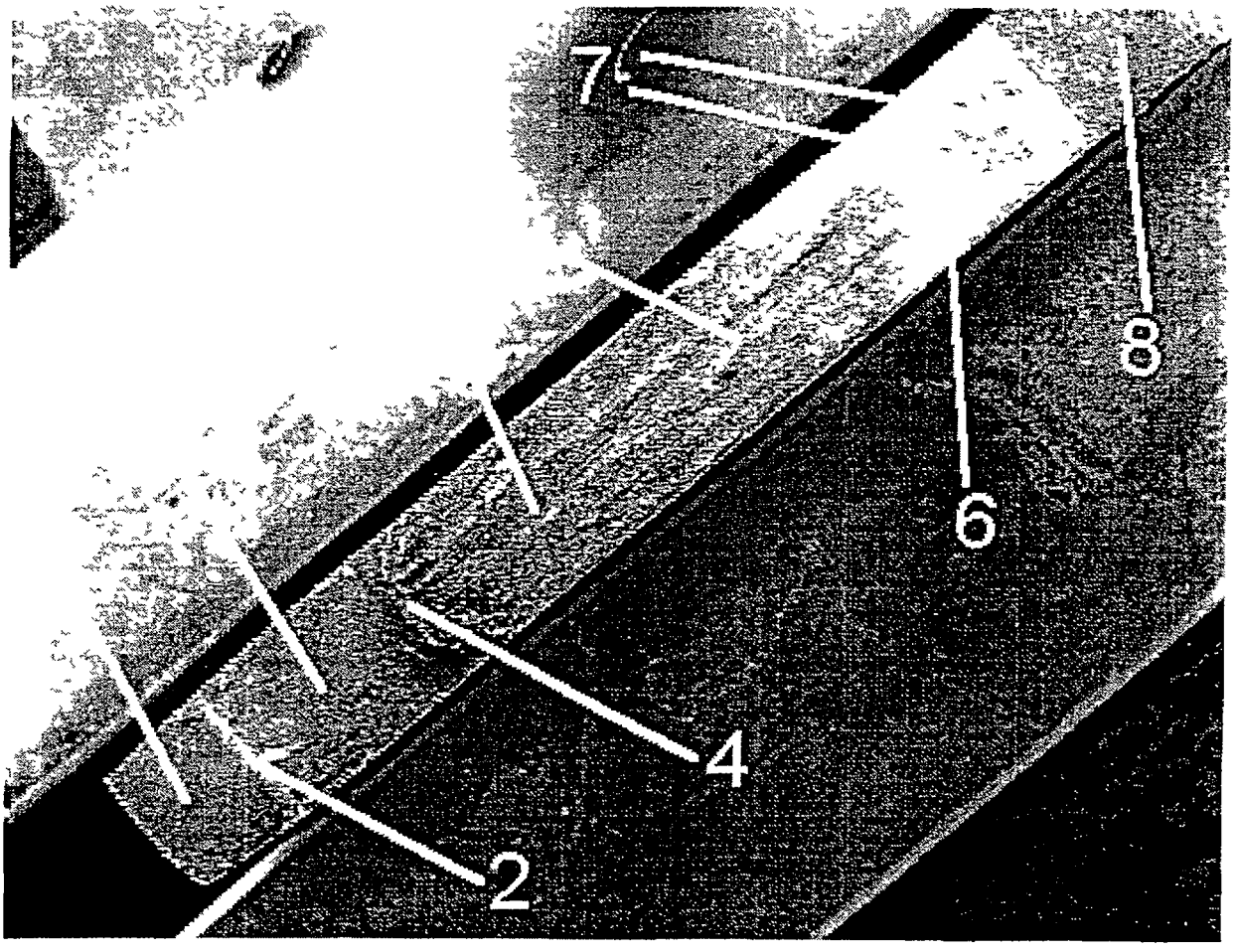

Fig 3 40 General SEM view (25 X) of a fracture surface. Sections that can be identified 1) Notch, 2) Notch-precrack limit, 3) Fatigue precrack, 4) Fatigue-SCC limit, 5) SCC zone, 6) Tip of SC crack, 7) Ductile rupture, 8) Cut made to facilitate post-test breaking

In a relatively long crack, as the one depicted in Fig. 3.40, it was common to find a fairly visible transition zone between the SCC region and the final ductile rupture. In this zone the SC crack is not completely opened, but the crack front is composed of many microcracks still not coalesced.

This can be seen in Fig. 3.41. When splitting the sample open at a low temperature, this band breaks in a brittle manner; in Fig. 3.42 the many microcracks heading into the material of the coupon can be clearly distinguished.

In the SCC zone in particular, the fracture looks mainly transgranular, the characteristic flat planes with river patterns can be seen everywhere, as illustrated in Fig 3.43 Intergranular attack (Fig. 3.44) has been also encountered in a few occasions.

Fig 3 41 Tip of the crack (outlined) (100 X)

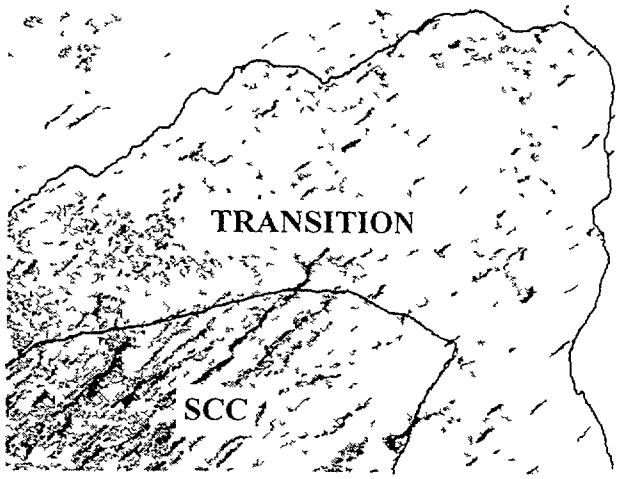

Fig 3 42 Brittle to ductile transition (400 X)

Fig 3 43 Transgranular features (6400 X)

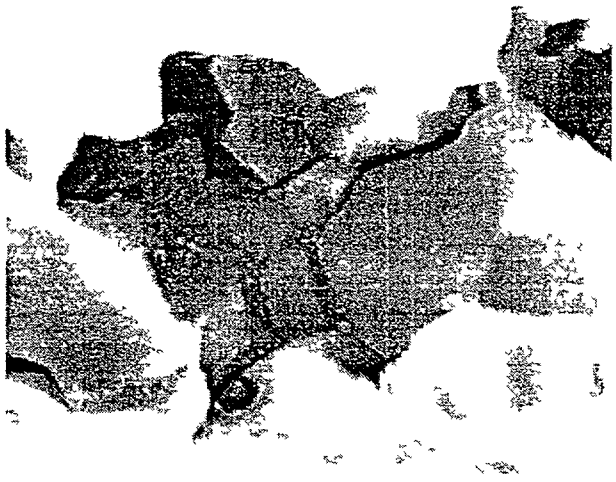

Fig 3 44 Intergranular attack (6400 X)

3.4. DISCUSSION

3.4.1. Argentinean material

No cracking was observed in samples fabricated using locally produced Zircaloy-4 sheet, as seen in Figs 3.13 and 3.14. This behaviour is quite probably due to the manufacturing procedure, that included successive rolling in perpendicular directions. This explains the immunity of this batch to the I_2 SCC; it is known [3.3] that the transgranular SCC proceeds only on basal planes; these are normally aligned within 30 degrees of the rolling plane; in this case, there is a significant proportion of grains favourable oriented for the transgranular propagation. However, an enhancement of this alignment can be produced by cross-rolling, leaving an insufficient amount of grains in such condition, reducing the material susceptibility to transgranular SCC. When tested in methanol iodine solutions at room temperature, the fracture surfaces show clear signs of branching along the sheet plane (Fig. 3.18), parallel to the applied stress. In such a textured material, the crack prefers to proceed in that direction, even though is the less favourable from the point of view of the resolved stresses.

3.4.2. CRP samples

Despite the acceptable degree of reproducibility obtained in several experiments, the fact that in most cases only one test has been conducted in each specific condition, makes it difficult to draw any definite conclusion on the effect of the different variables on the CGR. However, it is an interesting observation that there is an apparent trend to obtain consistent variations of CGR values as a function of several variables. This may only be the result of a fortunate casual distribution of otherwise randomly dispersed data or a real trend, to be confirmed only through additional work.

3.4.3. Creep tests

The PD variation due to creep decreases with time after a load is applied. As seen in Fig. 3.19 and Fig. 3.20, these numbers can drop from about 5 μV/h to less than 2 μV/h for higher loads and less than 1 μV/h for the lower ones. This is equivalent to an apparent range of CGR values of $3.6 \cdot 10^{-6}$ to $7 \cdot 10^{-7}$ mm/sec. This means that all data that lead to lower crack propagation velocities must be corrected or discarded; therefore, all the representations of CGR vs. K_I should be considered valid only above 10^{-6} mm/sec, as long as the PD has been recorded after a sufficient time has passed after loading.

3.4.4. Effect of temperature

In two cases it is possible to compare tests at different temperatures. In Fig. 3.45 and Fig. 3.46 an apparent increment in the critical stress intensity with temperature can be seen, indicated by more elevated CGR values for the same K_I at the higher temperature and higher $K_{I\text{-}SCC}$ for the lower one. This is consistent with data gathered from the literature [3.5, 3.6] for a temperature range below 400°C. It would indicate the existence of a temperature-dependent kinetics. At the same time, there is a slight difference in the $K_{I\text{-}SCC}$ values, more noticeable for the batch OM45 than OM41; again, these results are consistent with those mentioned in the literature [3.7].

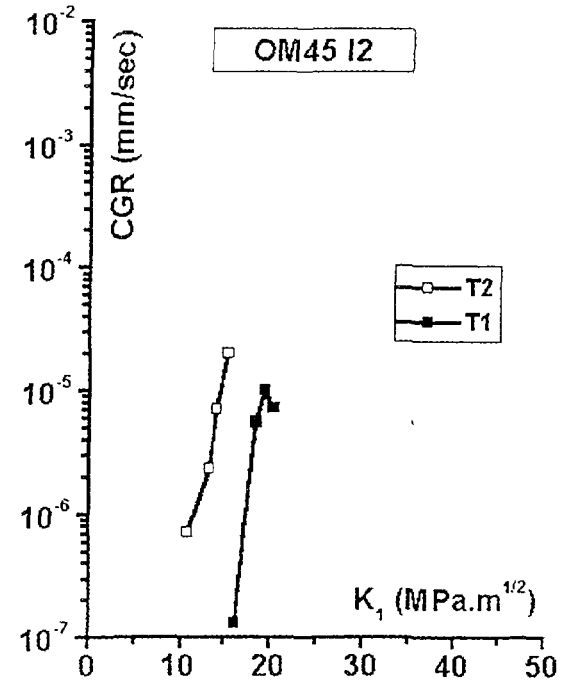

Fig. 3.45. Comparison of behaviour of OM45 at two different temperatures.

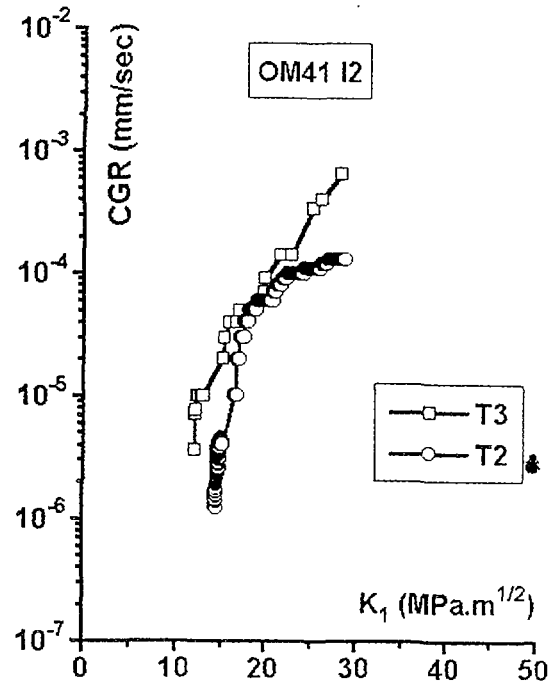

Fig. 3.46. Comparison of behaviour of OM41 at two different temperatures.

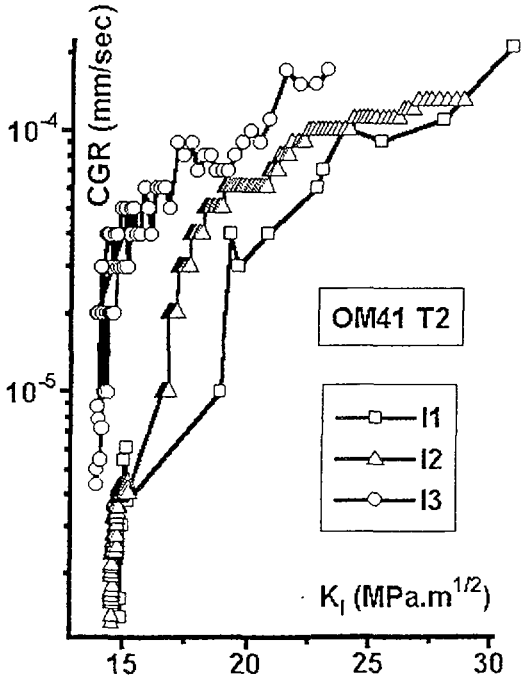

Fig. 3.47. Effect of iodine on OM41 at T2.

3.4.5. Effect of iodine concentration

In Fig. 3.47 and Fig. 3.48 CGR measured at different iodine concentrations are compared. Whereas there seems to be a consistent influence of the I_2 partial pressure in the tests conducted on OM41 samples, the curves obtained in the two tests using OM44 samples are very coincident. Unlike the case of temperature variations, $K_{I\text{-}SCC}$ threshold is not affected at all.

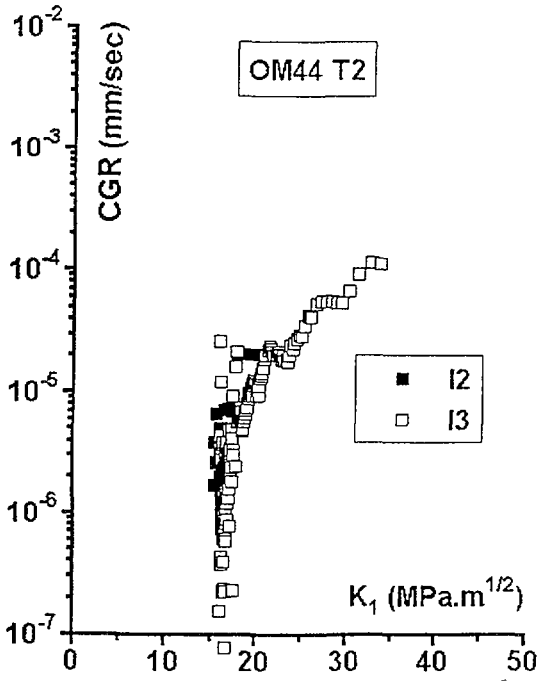

Fig. 3.48. Effect of iodine on OM44 at T2.

3.4.6. Behaviour of different materials

In Fig. 3.49 the CGR vs. K_I curves for 4 materials tested at T2 I3 are shown. In Fig. 3.50 those made at T2 I2 can be seen.

Although little effect of the alloy composition on $K_{I\text{-}SCC}$ has been found in the literature, substantial susceptibility differences have been reported [3.8] for different batches of material, what could justify that OM42 and OM44 Zircaloy-2 curves show higher $K_{I\text{-}SCC}$ than OM40 and OM41 Zircaloy-4 at T2 I3, as seen in Fig. 3.49. As for the higher susceptibility manifested by RX Zircaloy-4 OM40 with respect to SRA Zircaloy-4 OM41, Videm [3.7] claims to have measured much lower CGR for SRA material than for RX at the same K_I. The same behaviour is verified at T2 I2; in Fig. 3.50, a recrystallized sample of OM45 appears to be the most susceptible to SCC and the OM44 Zircaloy-2 coupon appear to be more resistant than those made of Zircaloy-4.

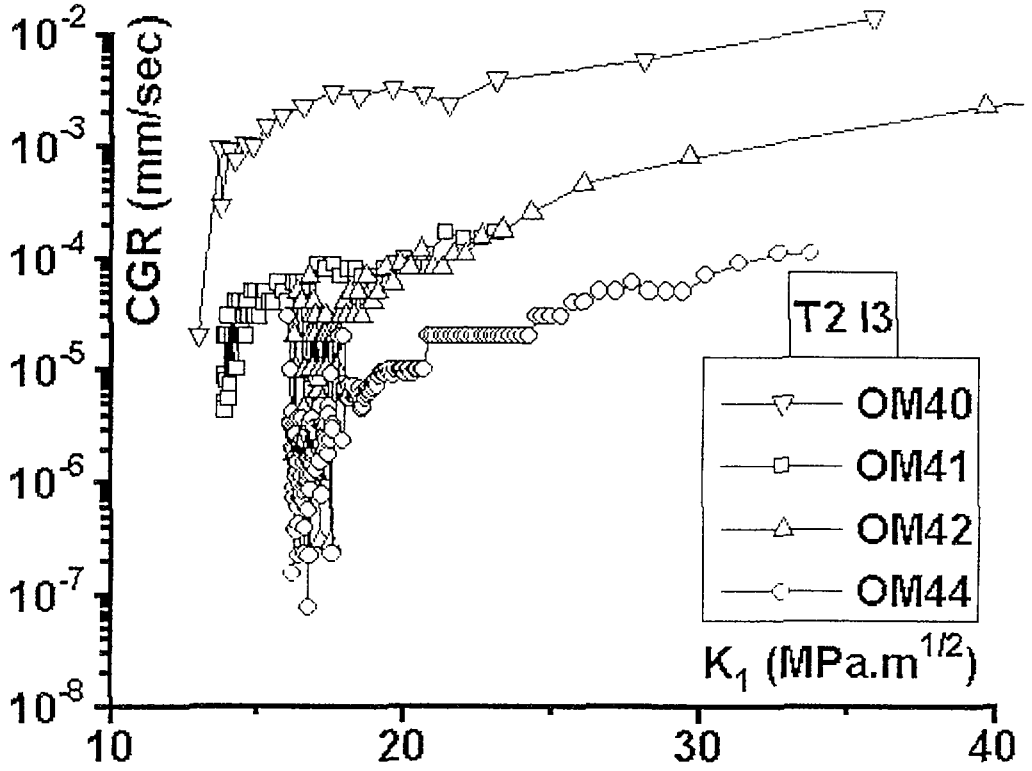

Fig. 3.49. Comparison of curves for different materials at T2 I3.

3.4.7. Effect of texture

A strong influence of the sample manufacturing orientation on the propagation velocity as well as on the $K_{I\text{-}SCC}$ is indicated by the results shown in Fig. 3.51. This was expected in view of the known fact that transgranular propagation proceeds only along the Zr basal plane [3.5], which makes it more difficult to raise the necessary resolved tensile stress on those planes for the less favourably textured sheet, when the propagation is mainly transgranular, as verified in this case (see Fig. 3.43). This is also the reason why the Argentinian Zircaloy proved to be immune to I_2 SCC in the present tests, as pointed out before.

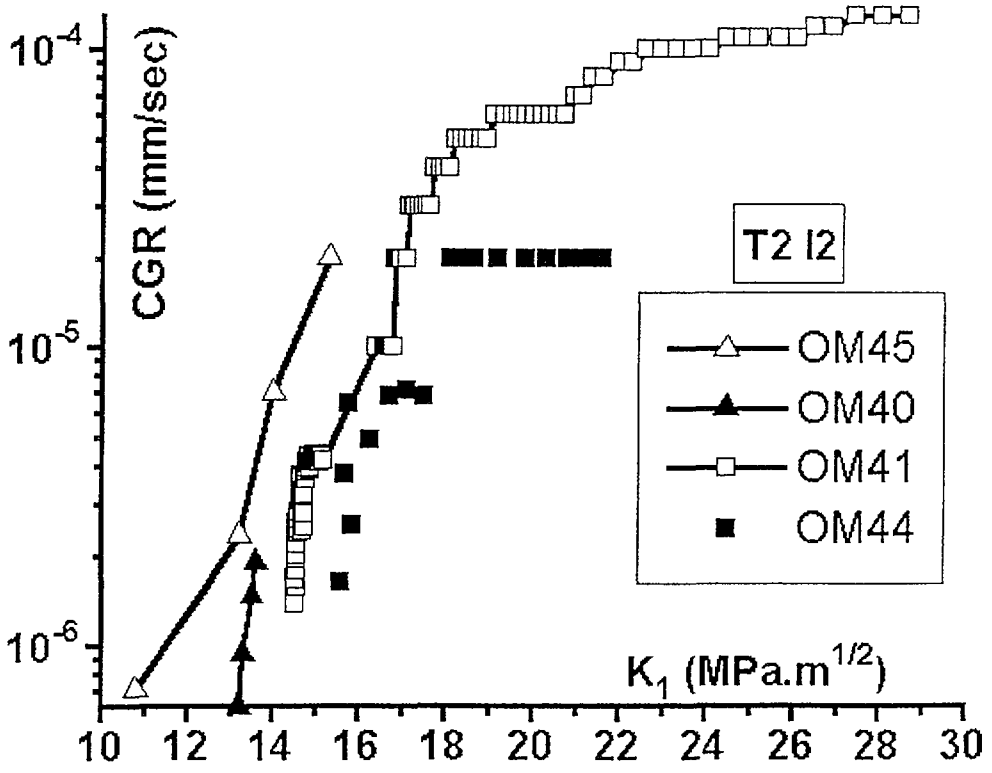

Fig. 3.50. Comparison of curves for different materials at T2 I2.

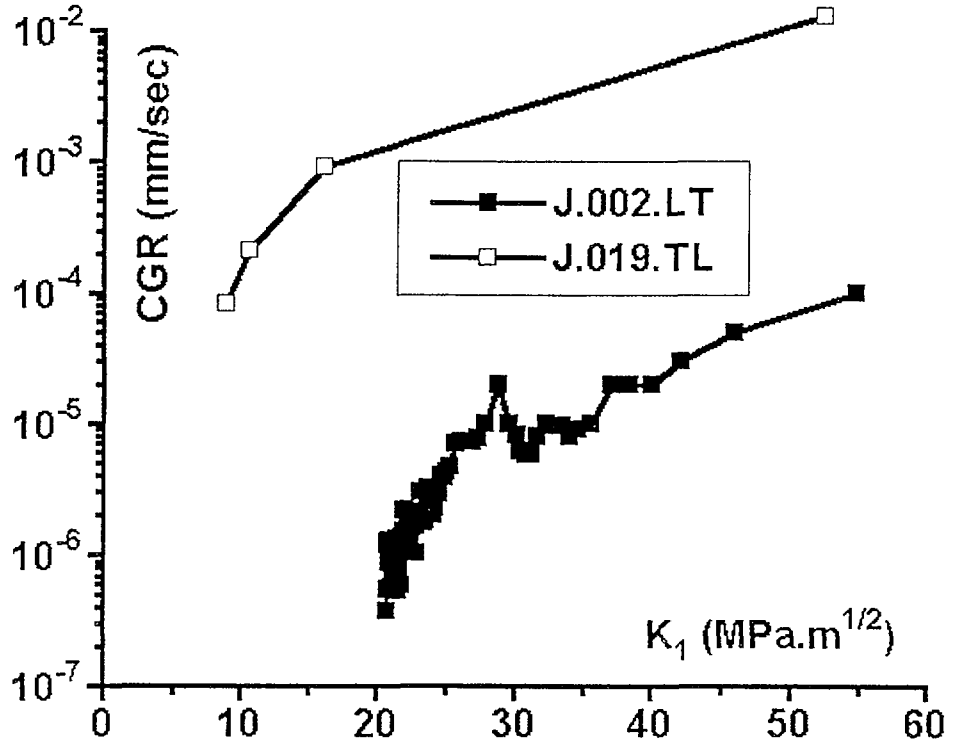

Fig. 3.51. Comparison of behaviour of materials LT and TL at T2 I2.

3.5. CONCLUSIONS

The DCPD technique is suitable for accurately measuring crack velocities as low as 10^{-7} mm/sec (error is about $2 \cdot 10^{-8}$) provided the resolution of the PD detection is better than 5 μV and good statistics are gathered. However, factors that are specific to the investigated system (creep of Zr alloys under load at 300 to 400°C), reduce the lower limit of detectable CGR to about 10^{-6} mm/sec.

A strong effect of texture on both $K_{I\text{-}SCC}$ and CGR values has been measured, which accounts for the immunity exhibited by the Argentinian material.

Other than for the texture influence, it is not possible to draw conclusions about the effect of the different studied variables from the results obtained, unless they are confirmed by those achieved by the other groups involved in the CRP. The apparent trend is to have CGR increase with temperature and iodine concentration. The susceptibilities of the different batches of Zr alloys are apparently as follows: Zircaloy-4 OM40, OM41 and OM45 cracks easier than Zircaloy-2 OM42 and OM44; RX material of one specific alloy cracks easier than SRA.

REFERENCES TO CHAPTER 3

[3.1] YAGGEE, F.L., et al., Trans. ANS. **30** (1978) 199.

[3.2] CUBICCIOTTI, D., JONES, R.L., Final Report on SCC Program, EPRI-NP-717 (1978).

[3.3] HADDAD, R., DORADO, A.O., "Grain-by-grain study of the mechanisms of crack propagation during iodine stress corrosion cracking of Zircaloy-4" (Proc. 10th Int. Symp. on Zr in Nuclear Industry), ASTM STP 1245, American Society for Testing and Materials, Philadelphia, PA (1994) 559.

[3.4] WOO-SEOG-RYU, Progress Report for the 3rd RCM of the present CRP.

[3.5] BUSBY, C.C., et al., J. Nucl. Mater. **55** (1975) 64.

[3.6] PEEHS, M., et al., Proc. Int. Symp. on Zr in Nuclear Industry, Stratford-Upon-Avon (1978).

[3.7] VIDEM, K., LUNDE, L., paper presented at the OECD Enlarged HPG-meeting, Sanderstølen (1977).

[3.8] COX, B. "Pellet-Clad Interactions (PCI) Failures of Zirconium Alloy Fuel Cladding - A Review.", J. Nucl. Mater. **172** 3 (1990).

Chapter 4

A STUDY OF IODINE INDUCED STRESS CORROSION CRACKING OF ZIRCONIUM ALLOYS IN CHINA

4.1. INTRODUCTION

PCI fuel cladding failures were observed in light water reactor fuel rods during power ramps after significant fuel burn-up (BU). The mechanism of failure was believed to be iodine-induced stress corrosion cracking (SCC). Obviously, PCI failure is a potential problem for water reactor fuel design. Until now, however, attempts to model the crack propagation mechanism from fracture mechanics considerations have not been universally accepted. At present, the evidence is very limited, and it should be treated with appropriate care. It is recommended that deliberate efforts to obtain further evidence on this topic would be worthwhile [4.1]. A perfectly, satisfactory mechanistic model would be very useful. It would assist the development of new PCI-resistant fuels and explain mechanism in SCC failure of Zircaloy fuel cladding.

A co-ordinated research project (CRP) was sponsored by the IAEA and supported by BNFL. This systematic study has been carried out in a number of laboratories around the world. Tensile tests have been carried out on specimens cut from unirradiated zirconium alloy plates, and the rate of crack propagation has been determined in each test. [4.2] At present, the main investigation is focused on the behaviour of iodine induced stress corrosion cracking on the zirconium alloys.

4.2. MATERIALS AND EXPERIMENTAL PROCEDURE

The test materials included Zr-2 and Zr-4 alloys after different heat-treatments (stress-relieved or recrystallized). The chemical compositions of the materials are given in Table 4.1. Some uniaxial tensile tests in the different iodine partial pressure atmospheres were conducted on zirconium alloys to get basic data on crack propagation. Each tensile specimen had a notch and a pre-crack (about 1mm). The iodine concentrations were selected as the saturation vapour pressures at 40°C, 65°C, 110°C (i.e. 100Pa, 1,000Pa and 10,000Pa). Test temperatures were 300°C, 350°C and 400°C, respectively. The direct current potential drop (DCPD) method was adopted to monitor the growth of the crack.

The samples of the two chosen texture orientations (L-T and T-L) have been tested at 350°C and 1,000Pa of iodine. J015 and J032 were cut from the sheet orientated in the L-T direction; and J036 was cut from the sheet orientated in the T-L direction. Creep tests of the samples of different orientations were performed at 350°C, the testing loads were selected as those typically used in SCC tests in a series of steps. For the L-T sample (J014), the $K_{I\text{-}SCC}$ values corresponding to the three loading levels were 8.23 $MPa{\cdot}m^{1/2}$, 10.59 $MPa{\cdot}m^{1/2}$ and 16.76 $MPa{\cdot}m^{1/2}$. For the T-L sample (J029), the K_I values corresponding to the three loading levels were 6.89 $MPa{\cdot}m^{1/2}$, 10.57 $MPa{\cdot}m^{1/2}$ and 12.17 $MPa{\cdot}m^{1/2}$.

TABLE 4.1. CHEMICAL COMPOSITION IN wt% OF Zr-2 AND Zr-4

Composition	Sn	Fe	Ni	Cr	O
Zr-2	1.33	0.19	0.07	0.11	0.12
Zr-4	1.31	0.22	---	0.12	0.11

In order to analyze the effects of microstructures on SCC behaviour, the grain size, the second phase particles, texture and fractographs were also investigated. An MeF-3A optical microscope; a JEM-200CX transmission electron microscope; a Dmax/1400 X-Ray diffractometer and an AMRAY 1845FE scanning electron microscope were used accordingly.

4.3. EXPERIMENTAL RESULTS

4.3.1. Mechanical test results

Strain versus time for the samples of different orientations at 350°C are shown in Fig. 4.1. The strain-time curves include both a transient creep and an apparent strain decrease with time at lower loads. When the load is high enough, the creep behaviour of the L-T sample is

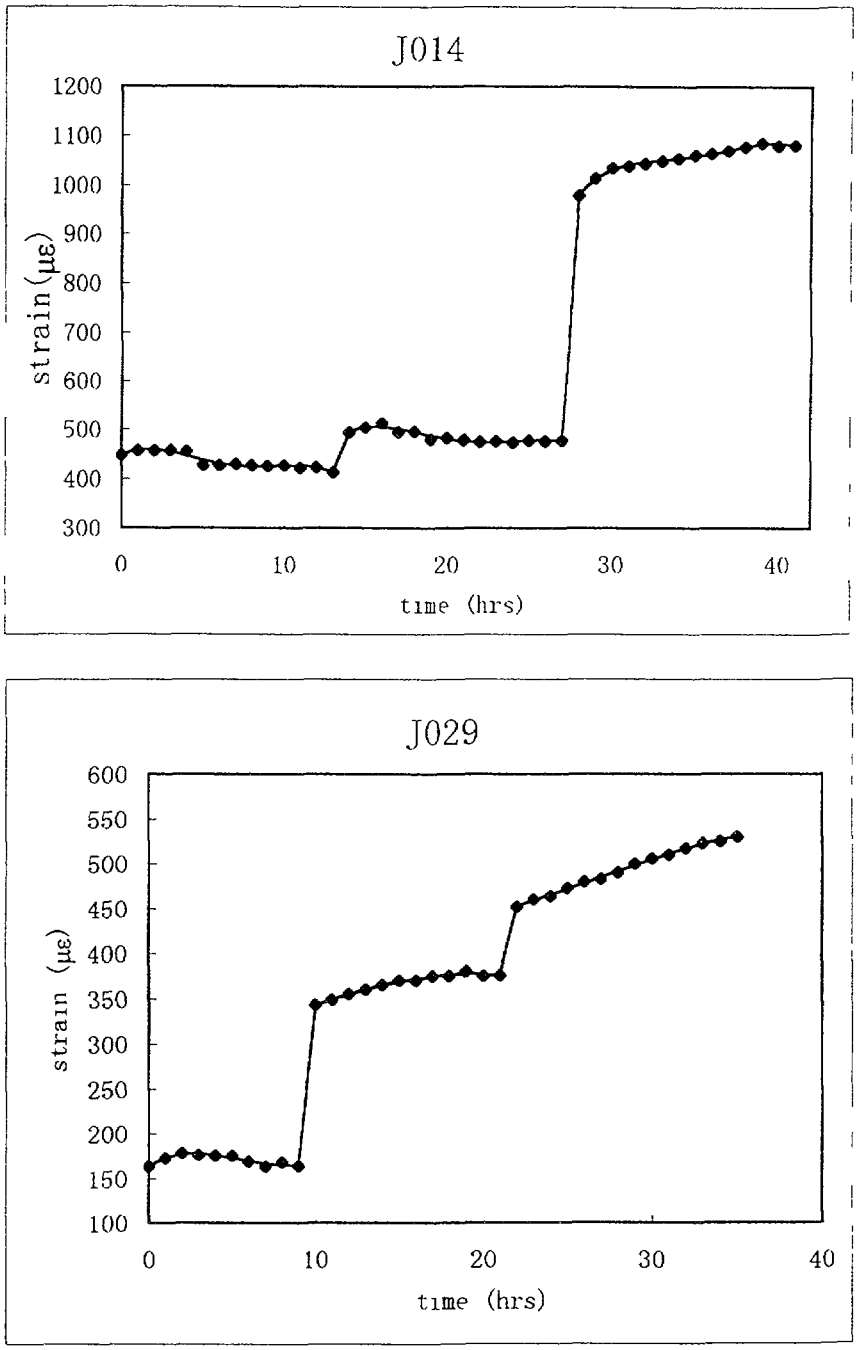

Fig. 4.1 Creep behaviours of L-T and T-L samples.

better than that of the T-L sample. With increasing iodine concentration, the time needed for cracking is obviously shortened and the rate of crack growth accelerates (Fig.4.2). Moreover, it can be observed in Fig. 4.6 that, at the crack initiation stage, the differences between the materials become very small when the iodine concentration is rather high. In our tests, for the same material and the same iodine concentration, the SCC performance is better when temperature is comparatively low (Fig.4.3). By comparing Fig. 4.4(a) and Fig. 4.4(b), it can be seen that, when the concentration of iodine is low, the curves can be divided into two parts. In the first stage, the samples of OM40 (Zr-4 RXA ,E226 and E227) are easier to crack; in the second stage, on the contrary, the cracks of OM41 (Zr-4 SRA, E262 and E263) samples are

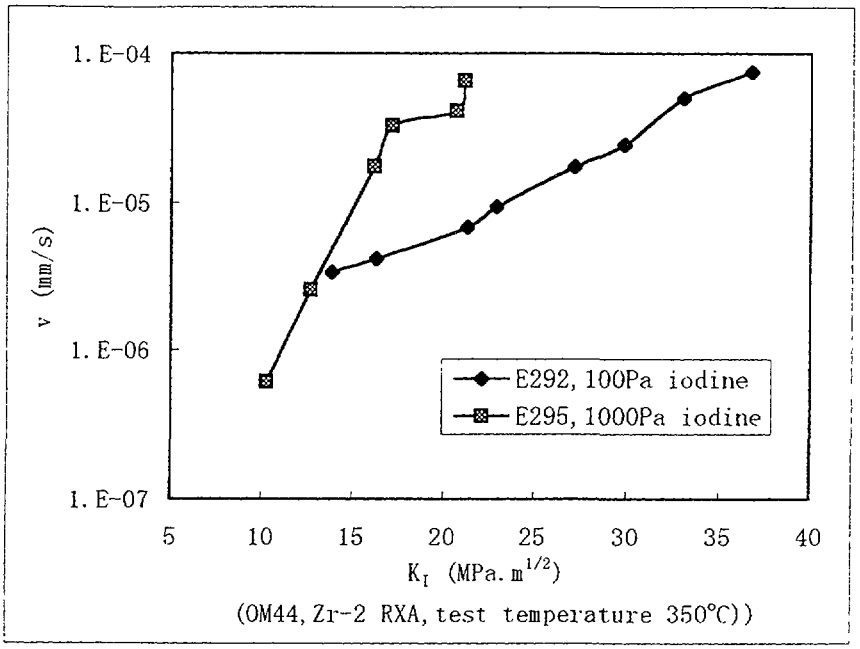

Fig. 4.2. The effect of various temperature on SCC behaviour.

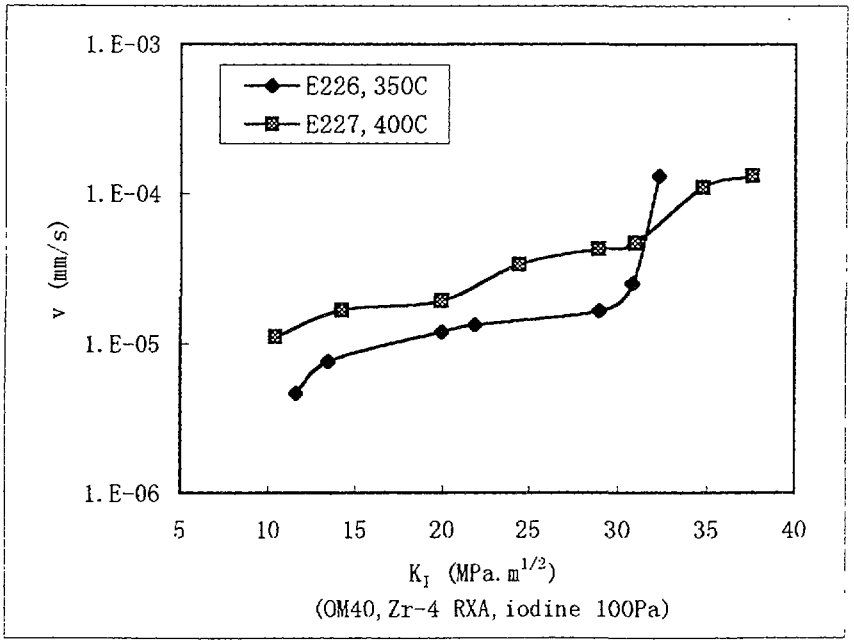

Fig. 4.3. The effect of various iodine concentration on SCC behaviour.

easier to propagate. It should probably be inferred that, at the crack initiation stage, the samples of OM40 are more susceptible to iodine-induced stress corrosion cracking than those of OM41.

From Fig. 4.5 we can find the effects of chemical composition on iodine-SCC behavior. The curves can be divided into three parts. In the first stage, the SCC cracks of OM40 (Zr-4 RXA, E226 and E227) are easier to initiate. In the second stage, the differences between the two curves become minimal. In the last stage, the behaviour of OM40 is worse than that of OM41. When the concentration of iodine is rather high, the performance of OM42 (Zr-2 RXA) is better than that of the other samples (Fig. 4.6). There are apparent differences

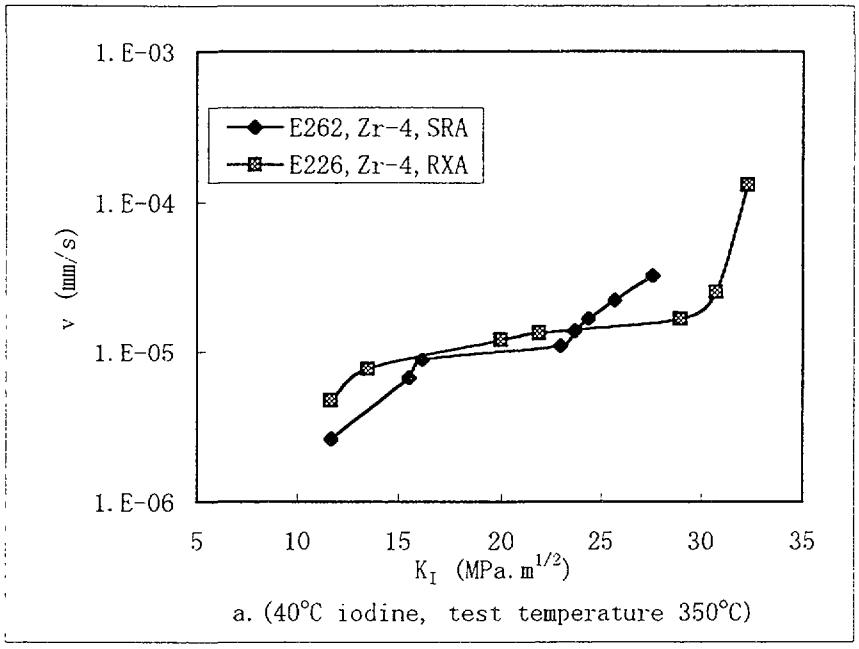

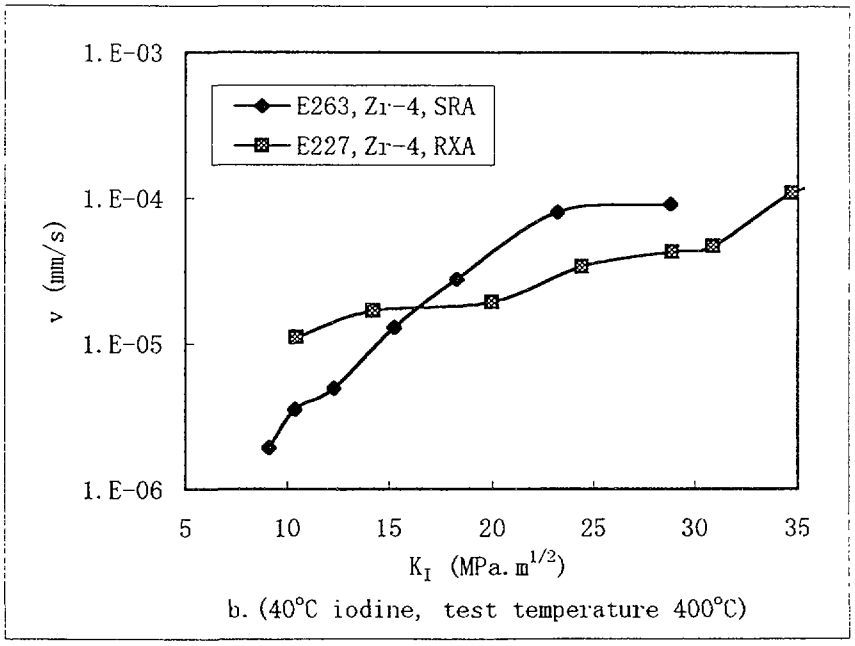

Fig. 4.4. The effect of different heat treatment on SCC behaviour.

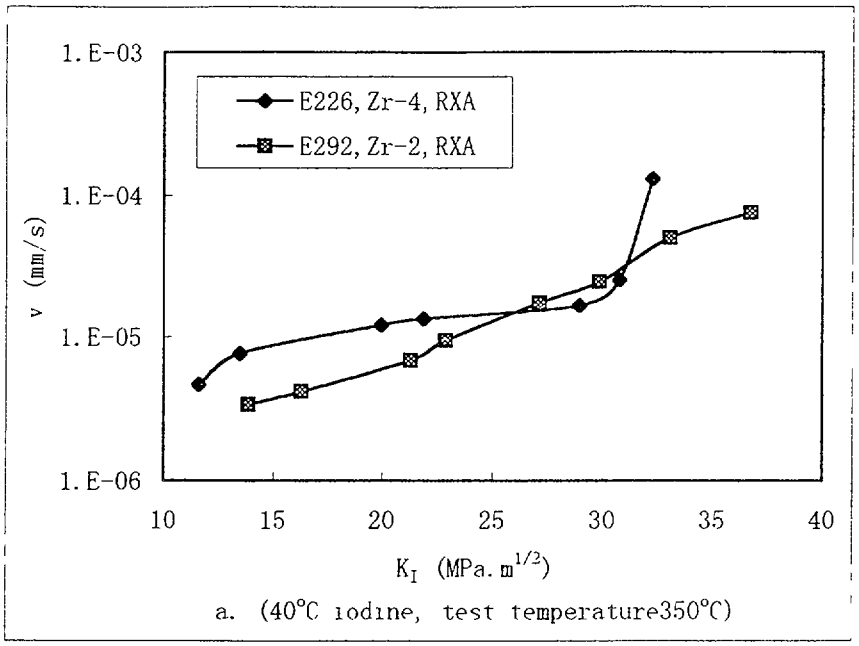

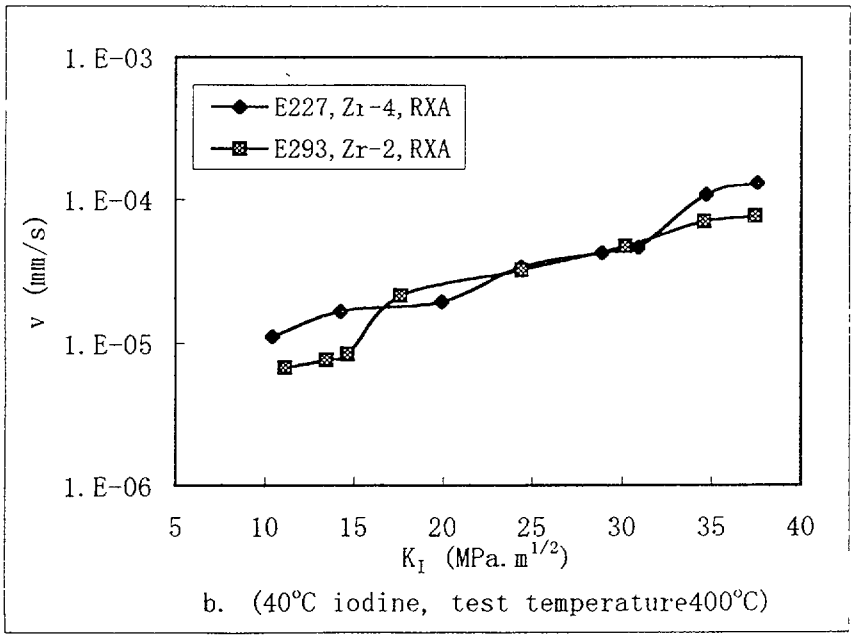

Fig. 4.5. The effect of different chemical composition on SCC behaviour.

between the SCC behaviours of the two chosen texture orientations (Fig. 4.7). The behaviour of the SCC resistance is better for the L-T specimen than for the T-L specimen due to texture differences.

4.3.2. Material analysis

The results of the material examinations are given in Table 4.2. It was found that, for Zircaloy in the recrystallized and the stress-relieved states, the grain size was obviously different. The grains in the recrystallization annealed material all tend to be equiaxed. The

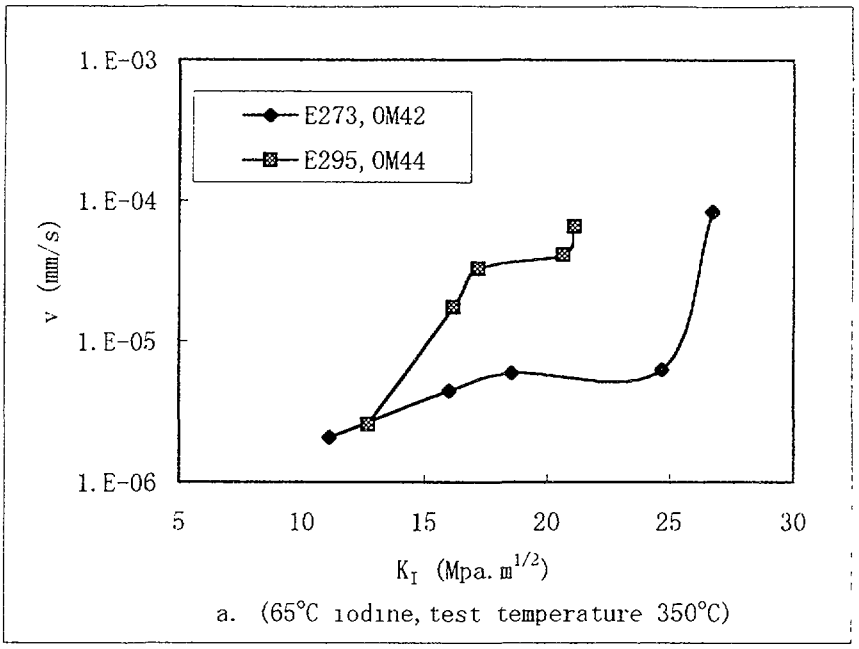

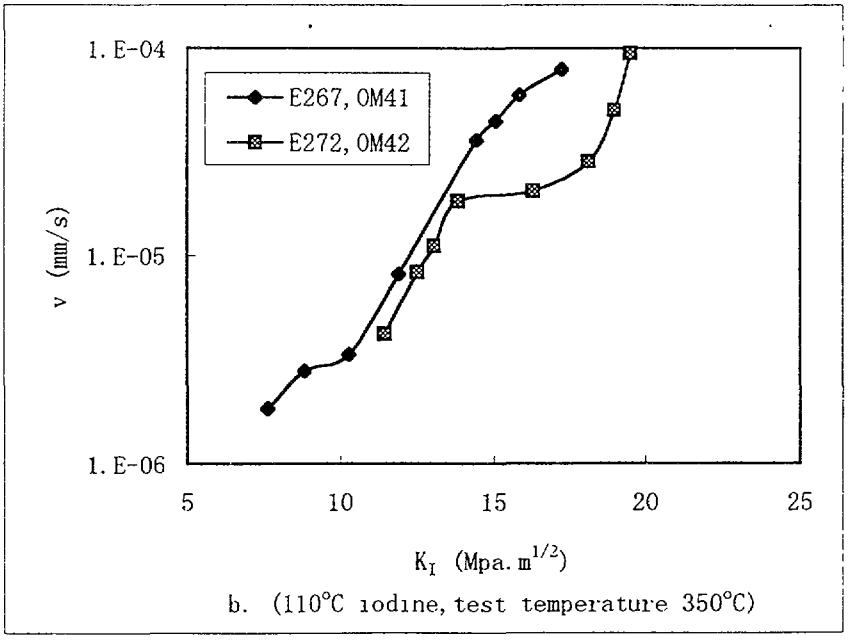

Fig. 4.6. The effect of different material state on SCC behaviour when iodine concentration is high.

grains in stress-relieved material were mostly elongated in the rolling direction. The extent of recrystallization in the OM40 and OM42 materials is fuller than for OM44.

The precipitates in OM40 (Zr-4, RXA) are very fine; they are dispersed randomly in the matrix, most of them are distributed within the grains. Precipitates can be observed both within the grains and on grain boundaries in OM41 (Zr-4, SRA). The size and distribution of the precipitate particles of OM42 (Zr-2, RXA) and OM44 (Zr-2, RXA) are very similar.

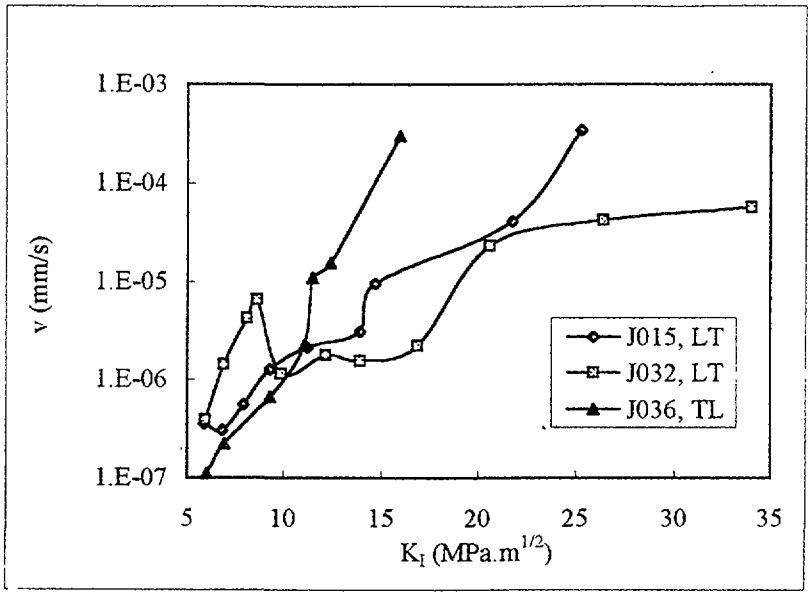

Fig. 4.7. K_I versus v for L-T and T-L samples' SCC.

TABLE 4.2. MATERIAL ANALYSIS RESULTS

No.	Material	Average grain size (μm)	Second phase size (μm)	Texture			
				ψ(deg)	f_r	f_n	f_t
OM40	Zr-4,RXA	5.6	0.095	40	0.330	0.549	0.123
OM41	Zr-4,SRA	3.3	0.108	35	0.300	0.607	0.098
OM42	Zr-2,RXA	6.3	0.094	35	0.308	0.580	0.114
OM44	Zr-2,RXA	4.8	0.096	30	0.261	0.620	0.124

The texture of the material is defined by the deviation angle ψ of c-axis orientation maximum, i.e. angle between the most grains' c-axes and normal direction of the plate. f_x is the basal pole [0002] texture orientation factor along the selected direction, that means the resolved fraction of basal poles in the direction x (normal, rolling and transverse). There are not big differences among these samples.

4.3.3. Fracture examination

The fractrographies are different depending upon the materials and experimental conditions (Fig. 4.8). The features of these fractographs are described in Table 4.3 in detail. With increasing K_I value, the fracture surface has different appearances. Accordingly, at the initiation stage, intergranular crack propagation is observed in a zone close to the fatigue area (Fig. 4.9). When the value of K_I is approximately K_{ISCC}, partially transgranular pseudo-

TABLE 4.3. LOW MAGNIFICATION FEATURES OF THE FRACTOGRAPH

Sample	Material	Test condition	Fractograph feature
E267	Zr-4,SRA	350°C iodine 10000Pa	In the zone of stress corrosion crack propagation, there are many flutes parallel to the direction of crack growth, these flutes are evident and continuously penetrate the whole zone of SCC. At the late stage of crack propagation, the flutes are deeper and some flutes branch.
E263	Zr-4,SRA	400°C iodine 100Pa	Features are similar to E267, but the flutes are more marked.
E226	Zr-4,RXA	350°C iodine 100Pa	Fractograph is characterized by many flutes vertical to the direction of crack propagation.
E272	Zr-2,RXA	350°C iodine 10000Pa	Fractograph appears more even than other samples described above. The chevron pattern can be identified on the fracture surface.

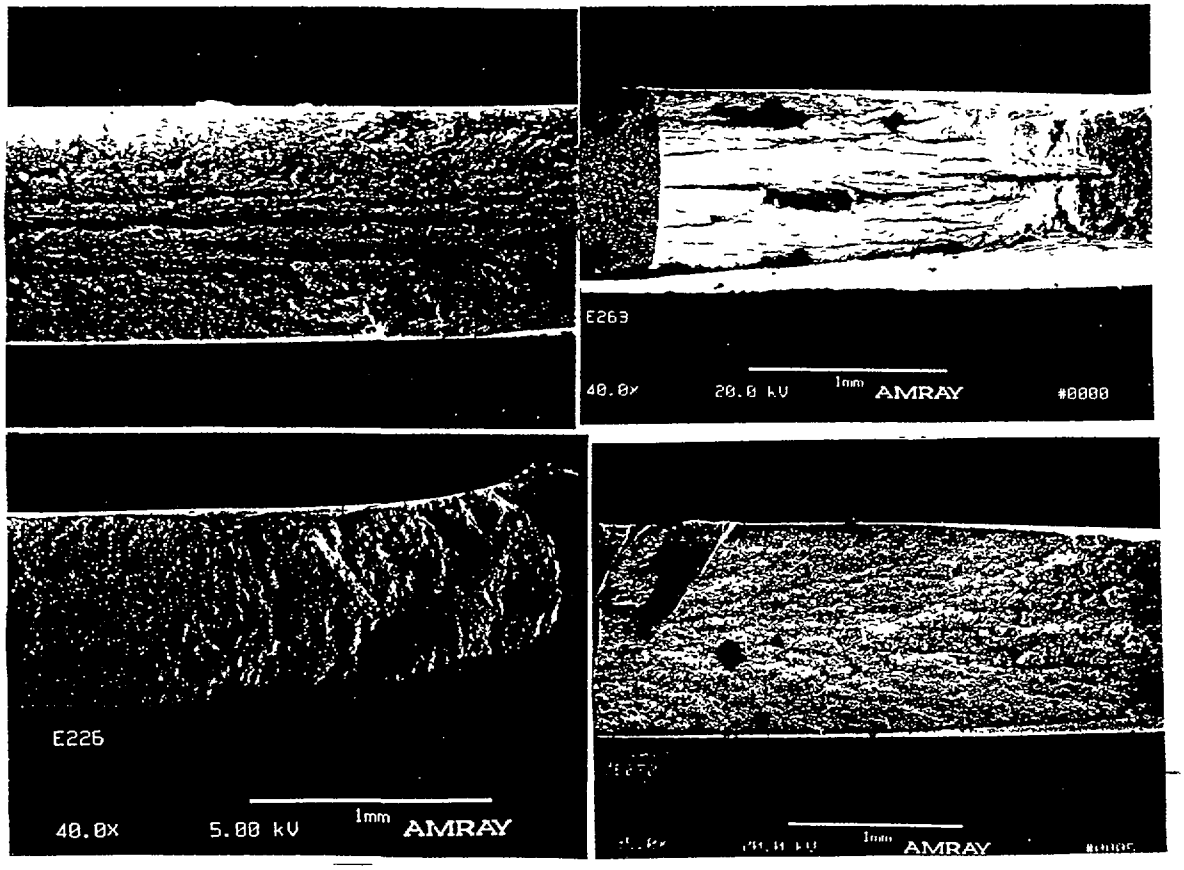

Fig. 4.8. Low magnification SEM micrograph of the fractures.

cleavage and secondary grain-boundary cracking are observed on the fracture surface (Fig. 4.10). At a crack propagation stage, the fracture is a typically brittle crack; the pseudo-cleavage penetrates both a single grain or several grains (Fig. 4.11).

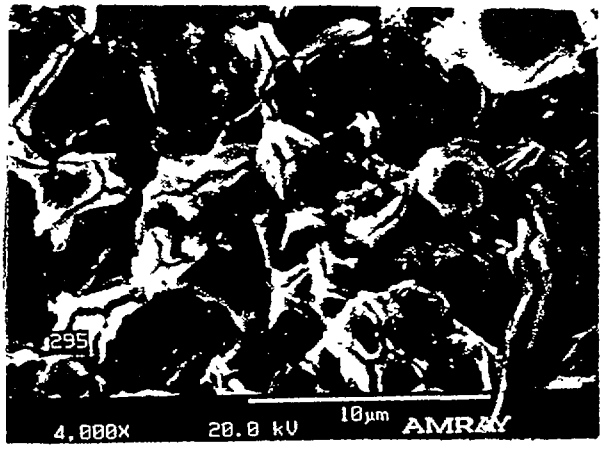

Fig. 4.9. intergranular crack.

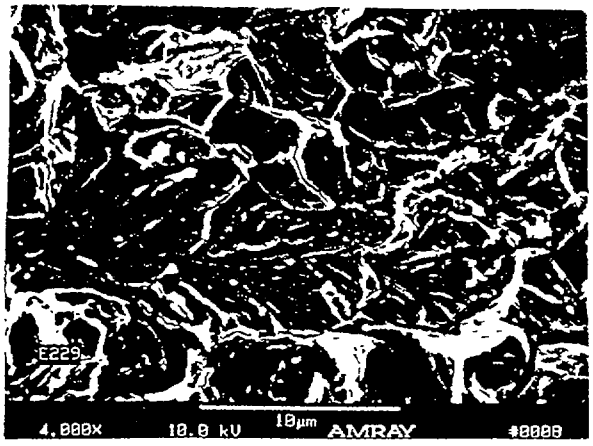

Fig. 4.10. intergranular and transgranular crack.

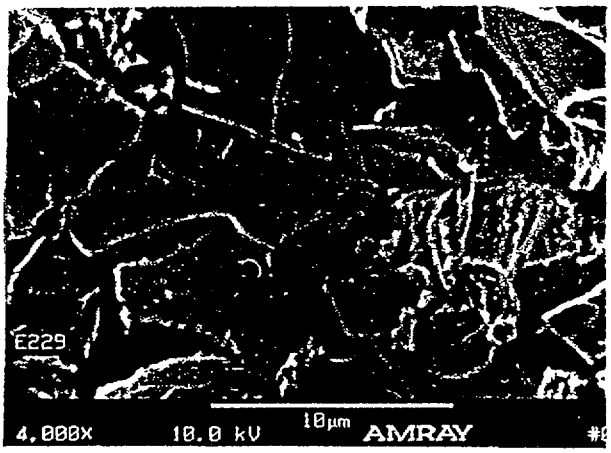

Fig. 4.11. transgranular pseudo-cleavage.

4.4. DISCUSSION

4.4.1. Behaviour during localized deformation

When the applied stress is less than the critical shear stress, metal deformation would include elastic deformation. Under prolonged loading, the plastic deformation of the metal would occur slowly and continuously, that is "creep". However, creep behaviour of the metal depends on the loaded time and test temperature. As soon as pellet-clad mechanical interaction (PCMI) is produced during water reactor operation, creep occurs in the fuel cladding. Creep is a plastic deformation which leads to the dislocation density rapidly increasing, when work hardening will be produced [4.3]. It is known that the microstructure and physical properties of the fuel cladding change pronouncedly during creep [4.4,4.5]. At higher temperatures and higher stresses, voids or micro-cracks will create in the grain boundaries. The creep mechanism at lower temperatures and high stresses is generally referred

to as dislocation climb plus glide (CPG) [4.6]. Many studies have shown the creep behaviour of the Zircaloys to depend on the operating temperature, alloy content, material condition and operating stress [4.4,4.7].

In the 1970s, Williams et al. found that, during straining, a sudden drop of the load occurred for the irradiated Zircaloy-2, which corresponded to the formation of the macroscopic shear bands [4.4]. In the 1990s, Fregonese et al. have examined the three prismatic slip systems {1010}<1210> activated on the basal plane within the grain by TEM. According to this analytical result, they proposed a mechanism for the formation of dislocation-loop free channels. In other words, the activated basal slip results in the formation of loop free channels, then the further deformation takes place in the channels instead of spreading in the hardened matrix, and leads to a strain softening behaviour. That is at steady state, the thermal recovery offsets strain hardening. This mechanism can explain why a sudden drop of the load occurred for irradiated Zircaloy-2 during straining [4.8].

Dislocation pile up in the channels or dislocation channels intersect with obstacles, e.g. grain boundaries, slip-band boundaries and second-phase particles, where the dislocation density is increased, which induced stress concentration [4.3].

In this work, the selected loads in the strain testing is corresponded to typical loads in our SCC testing. Strain-time curves consist of a transient creep and a steady–state creep. Transient creep is mobile dislocation first moving while loading and then creep rate decreases with time as resistance to continued strain builds up through strain hardening. Creep behaviour is dominated by dislocation climb and glide. When the selected stress is large enough then a crack grows in the material [4.9]. The relationship between localized deformation regions on a microscopic scale and stress corrosion cracking (SCC) should be noticed.

4.4.2. Behaviour of iodine-induced stress corrosion cracking

Stress corrosion cracking is a process of material failure produced by the combined action of strain induced by residual or applied stress and a corrosive environment. Under the co-action of the two main factors, a crack would occur in the material after a given time. Some investigators have observed that iodine-induced initial cracks on the surface of the cladding occur preferentially in the highly-deformed regions [4.6,4.10]. In an iodine environment, intergranular cracks initiate at the site about tens micrometers from the surface.

4.4.2.1. Feature on fracture surface

According to the observed morphology on the fracture surface, the features of the fracture can be divided into three types: split along grain boundary, pseudo-cleavage connecting with plastic tearing and smooth pseudo-cleavage. An initial stage is the predominantly intergranular cracking close to the fatigue area [4.11]. It is caused by electrochemical corrosion at lower stress levels and depends on material microstructure and the corrosive environment. With increasing stress, the K_I value in the localized deformation area becomes greater than K_{Iscc}, and a transgranular crack along the basal plane in a preferred direction will occur. Once the crack propagates beyond the strain field generated by the obstacles, K_I could drop back below K_{ISCC}, the transgranular crack would then stop and an intergranular crack would grow. The above-mentioned process repeating would lead to intergranular cracking replacing transgranular cracking during SCC [4.12,4.13].

Slip systems will activate on prism planes when the resolved shear stress is much lower than the critical resolved shear stress (CRSS) for any <c+a> slip system. Dislocation glide takes place almost exclusively on the prism planes where the flutes develop along the intersections of the prism planes. Intergranular cracks would grow along the grain boundaries. Fluting is preferred at low strain rates. Steps observed on pseudo-cleavage planes are due to dislocation jogs. The smooth pseudo-cleavage planes are induced by rapid deformation of the low plasticity cracks.

4.4.2.2. Effect of iodine concentration

The most frequent tests were either constant load tests, where the time to failure is expressed versus the applied stress in the iodine environment, or constant strain rate tests, where the reduction in ductility due to iodine were analyzed [4.14]. With iodine concentration increasing, the rate of crack propagation is evidently faster. The time to failure at lower iodine concentrations ($3x10^{-5}$ $g.I_2.cm^{-2}$) was in the range of 200-1000h, and the time to failure at higher concentration ($3x10^{-3}$ $g.I_2.cm^{-2}$) was less than 3h [4.15]. When iodine is adsorbed on a plane, a decrease in the surface free energy of this plane and the crack propagation is favoured [4.16]. The higher the iodine content, the more the material caustic embrittlement is, according to a liquid metal embrittlement mechanism.

4.4.2.3. Effect of the test temperature

For the recrystallization annealed material, with test temperature increasing, the rate of crack propagation is obviously faster. For the stress-relieved annealed material, the time to the onset of unstable crack growth for the SCC lifetime is unaffected. It is indicated by Limback that creep the rate increases with increasing temperature. When temperature increases, stress relaxation will be rapid. However, when temperature the lies between 230 °C and 510°C, the high reaction rates will lead to cracking [4.15].

4.4.2.4. Effect of material state

The material state includes chemical composition, heat-treatment, grain size, second phase particles and texture. For the different states in Zircaloy-4, susceptibility to iodine SCC is evidently different. Recrystallized specimens were more resistant to iodine SCC than the stress-relieved specimens during iodine-induced SCC. $K_{I\text{-}SCC}$ is greater in recrystallized material compared to stress-relieved material [4.17]. The nucleation step is the longest part of the SCC lifetime [4.14]. An initiation stage is controlled by the intergranular corrosion rate, the corrosive behaviour depends on the grain size, distribution of second-phase particles and impurities [4.18]. At the initiation stage during iodine-induced stress corrosion cracking (SCC), regions of intergranular propagation in recrystallized material are observed [4.17]. At crack initiation, the crack is growing by intergranular corrosion regardless of the type of loading, in the early stages, the stress level has little effect on the corrosion rate [4.19].

When K_I is higher than K_{ISCC} the crack propagation rate is fast, and the morphology of the SCC fracture surface appears as a brittle fracture. It has a markedly crystallographic fracture such as transgranular and transgranular pseudo-cleavage. Many river-pattern steps on the pseudo-cleavage face were observed. In the case of Zircaloy, pseudo-cleavage occurs on the basal plane [4.15,4.20,4.21]. The crack propagation on the basal plane is enhanced by a strong decrease in the surface free energy of this plane when iodine is adsorbed [4.16]. The behavior of recrystallized material is better than the same stress-relieved material, due to the texture that influences iodine SCC behavior strongly [4.18]. Workers have studied the effect

of precipitate distribution on the crack path [4.22]. They find that, for clean grain boundaries, a largely intergranular crack path results. While the presence of second-phase particles in the grain boundaries produces transgranular crack branching at the sites of the particles. Other workers have examined the effect of grain size on the growth rate of stress corrosion cracking (SCC) in Zircaloy. The material was recrystallized at different temperatures to give grain sizes between 4μm and 10μm. No statistically significant difference was observed [4.23].

The behaviour of SCC and creep in the specimens of the different orientation reveals the marked difference due to the texture. Texture can be divided into two kinds: deformed texture and recrystallized texture. After recrystallizing, new grains' orientation in the metal will keep in regular relation with the matrix orientation. Annealing temperature and the initial deformed texture will influence recrystallization texture, it can be strengthening effects on material properties.

4.5. CONCLUSIONS

1. The behaviour of the creep resistance is better for the L-T specimen than for T-L specimen due to the texture difference.

2. With an increase in the iodine concentration, the rate of crack propagation in the SCC test was raised at the same test temperature.

3. The rate of crack propagation increases with test temperature.

4. The fracture by iodine induced SCC can be divided into three types: intergranular cracks, transgranular pseudo-cleavage mixing with intergranular cracks and smooth pseudo-cleavage.

5. The behaviour of the recrystallization annealed materials is better than for the same type of material when of stress-relief annealed, due to texture influence.

REFERENCES TO CHAPTER 4

[4.1] COX, B., J. Nucl. Mater., 172 (1990), 249-292

[4.2] BRAMWELL, I. and TICE, D. R., Co-ordinated Research Programme (CRP) on Stress Corrosion Cracking (SCC) in Zirconium Alloys-Information for participating Laboratories, (1994)

[4.3] ONCHI, T., RAYANO, H. and HIGASHIGUCHI, Y., J. Nucl. Mater., 88(1980), 226-235

[4.4] WILLIAMS, C. D., ADAMSON, R. B. and OLSHAUSEN, K. D., Report NEDM -- 12458 (1974) General Electric Company, San Jose, CA.

[4.5] CAUSEY, A. R., ELDER, J. E., HOLT, R. A., and FLECK, R. E., "On the anisotropy of in-reactor creep of Zr-2.5%Nb tubes", Proc. Int. Symp. on Zirconium in the Nuclear Industry: Tenth international symposium, ASTM STP 1245, GARDE, A. M. and BRADLEY, E. R. Eds., American Society for Testing and Materials, Philadelphia, PA 1994, pp202-220

[4.6] FRANKLIN, D. G., LUCAS, G. E., and BEMENT, A. L., "Creep of Zirconium Alloys in Nuclear Reactors", ", Proc. Int. Symp. on Zirconium in the Nuclear Industry ASTM 815, American Society for Testing and Materials, West Conshohocken, PA, 1983

[4.7] KNORR, D. B. and NOTIS, M. R., J. Nucl. Mater., 56 (1975), 18-24

[4.8] FREGONESE, M., REGNARD, C., ROUILLON, L., LEFEBVRE, F. AND C. LEMAIGNAN, C., "Failure Mechanisms of Irradiated Zr alloys Related to PCI: Activated Slip Systems, Localized Strains and Iodine Induced Stress Corrosion Cracking", Proc. Int. Symp. on Zirconium in the Nuclear Industry: Twelfth Symposium, ASTM STP 1354, American Society for Testing and Materials, West Conshohocken, PA, 1999.

[4.9] LIMBACK, M. and ANDERSSON, T., "A Model for Analysis of the Effect of Final Annealing on the in-and out–of–Reactor Creep Behaviour of Zircaloy Cladding", Proc. Int. Symp. on Zirconium in the Nuclear Industry: Eleventh symposium, ASTM STP 1295, BRADLEY, E. R. and SABOL, G. P. Eds., American Society for Testing and materials, West Conshohocken, PA, 1996, pp 448-468

[4.10] HOFMANN, P., J. Nucl. Mater., 125(1984), 85-95

[4.11] COX, B. AND WOOD, J. C., Proc. Electrochemical Society Symp. On Corrosion Problems in Energy Conversion and Generation, Ed. Tedmon Jr., C. S. (ECS, New York, 1974) p.275

[4.12] MILLER, A. K., CHALLENGER, K. D., SMITH, E. RANJAN, G. V. and CIPOLLA, R. C. Electric Power Research Institute, Report NP-856 (August 1978)

[4.13] KUBO, T., WAKASHIMA, Y., IMAHASHI, H. and NAGAI, M. J. Nucl. Mater., 132(1985)

[4.14] BRUNISHOLZ, L. and LEMAIGNAN, C. Proc. 7th. Int. Symp. on Zirconium In the Nuclear Industry, ASTM-STP 939 (American Society for Testing and Materials, Phiadelphia, PA, 1987) p 700

[4.15] WOOD, J. C., J. Nucl. Mater., 45(1972/73)105

[4.16] HWANG, S. K. and HAN, H. T., J. Nucl. Mater., 161(1989)175-181

[4.17] KNORR, D. B. and PELLOUX, R. M., Met.Trans, 13A(1982)73-83

[4.18] SCHUSTER, I. and LEMAIGNAM, C., J. Nucl. Mater., 189(1992)157-166

[4.19] SCHUSTER, I. and LEMAIGNAM, C., Zirconium in the nuclear industry: Eighth International Symposium, ASTM STP1023, VAN SWAM, L.,F.,P. and EUCKEN, C. M. Eds., American Society for Testing and Materials, Philadelphia, PA, 1989.pp.535-547

[4.20] JONES, R. L., CUBICCIOTTI, D. and SYRETT, B. C. J. Nucl. Mater., 91(1980)277

[4.21] ADAMSON, R. B.,J. Nucl. Mater., 82(1980), 363

[4.22] KUBO, T., WAKASHIMA, Y., IMAHASHI, H. and NAGAI, M., Proc. 2nd Int. Symp. on Environmental Degradation of Materials in Nuclear Power Systems-Water Reactors. Monter ey, CA, September 1985, TMS/ANS/NACE, p 34; and ResMech., 20(1987)217

[4.23] NORRING, K., HAAG, Y. and WIKSTROM, C., J. Nucl. Mater., 105(1982)231-23

Chapter 5

STRESS CORROSION CRACKING OF ZIRCONIUM ALLOY FUEL CLADDING IN INDIA

5.1. INTRODUCTION

IAEA sponsored Co-ordinated Research Project (CRP) on "stress corrosion cracking of zirconium alloy fuel cladding" was initiated in the year 1994 for a better understanding of the pellet clad interaction (PCI) failures involving zirconium alloys in the presence of iodine. As part of this programme, precracked Zircaloy specimens were exposed to flowing iodine vapour at temperatures of 300 and 350°C and the crack growth behaviour was investigated. This report consists of the results obtained and the experience gained from these tests conducted under this programme.

5.2. EXPERIMENTAL

5.2.1. Materials

Zircaloy -2 in the recrystallised (RX) condition and Zircaloy - 4 in the recrystallised as well as in the stress relief annealed (SRA) conditions were used for these experiments. Zircaloy - 2 specimens having specific orientations in the L-T and T-L directions were also tested. A few Zircaloy - 2 specimens having L-T and T-L orientations were tested to find creep growth in an Argon atmosphere, without iodine, at 350°C. All of the specimens were supplied by the Agency.

5.2.2. Loading system and glass chamber

Dead weight via a lever mechanism was applied on the specimens kept in a Pyrex glass chamber. Iodine kept in a separate container bulb outside this glass chamber was vapourised by heating the container at 40, 65 and 100°C and was then carried to the glass chamber containing the specimen by a carrier gas, Argon. The concentration of iodine in the glass chamber was thus maintained by controlling the temperature of the iodine container and the flow. rate of Argon gas.

5.2.3. Crack growth measurement — DCPD calibration

Crack growth in the specimens was monitored following the direct current potential difference (DCPD) method. A stabilized DC constant current source having 0. 1 % accuracy was used to pass ± 1 Amp current through the lead wires, made of Zircaloy - 2, fixed on the shoulders of the specimens, the direction of current flow being changed automatically after each 100 s. The output potential drop across the crack was recorded by a microvolt precision strip chart recorder continuously during each experiment.

A DCPD calibration curve was developed by loading blank specimens of known and different pre-crack lengths and recording the DCPD output. A best fit analysis of the DCPD output data gave a fourth order equation of the form:

$$a = -2.841+6.099\ (V/V_0)-1.594\ (V/V_0)^2+0\ .271\ (V/V_0)^3-0.019\ (V/V_0)^4$$

where V_0 is the potential output in the absence of any crack and V is the potential drop at various crack lengths, a. The resultant calibration curve representing the normalized voltage (V/V_0) versus crack length was used for the measurement of crack growth in actual experiments.

5.3.1. Crack growth in recrystallised and stress relieve annealed specimens

Fig. 5.1 shows the crack growth behaviour in recrystallised and stress relieve annealed Zircaloy - 4 specimens at 300'C and at iodine bulb temperature of 65'C, whereas Fig. 5.2 shows the crack growth behaviour in recrystallised Zircaloy - 2 at the same iodine bulb and test temperatures as above. For all these alloys, both Zircaloy - 4 and Zircaloy - 2 , $K_{I\text{-}SCC}$ was within 5 to 10 MPa$\sqrt{m}$. However, $K_{I\text{-}SCC}$ of SRA alloys was noticed to be in the higher side of the above limit. A common trend was that all the recrystallised alloys showed first and second stages of crack growth involving a long plateau region, whereas in the stress relieved alloys the third stage of cracking was reached mostly within 10 to 15 MPa$\sqrt{m}$ involving a rapid unstable crack growth.

Fig. 5.2 also shows the effect of test temperature on the crack growth rate in Zircaloy - 2. Increase in test temperature from 300 to 350°C resulted in higher crack growth rate. A similar effect was observed in case of Zircaloy - 4 as shown in Fig. 5.3. However, an increase in temperature did not have any appreciable effect on $K_{I\text{-}SCC}$,

An increase in iodine bulb temperature from 40 to 65°C at a test temperature of 300°C resulted in unstable crack growth at lower applied stress intensities, 10 to 12 MPa$\sqrt{m}$, in Zircaloy - 4 as shown in Fig. 5.4. Higher crack growth rates were recorded in Zircaloy - 2 due to the increase in iodine bulb temperature from 40°C to 65 or 110°C. It can be seen in Fig. 5.5 that the plateau crack growth rate for Zircaloy - 2 at 40°C iodine bulb temperature and at 350°C test temperature was of the order of 10^{-8} m/sec, whereas at 65 and 110°C iodine bulb temperatures and at the same test temperature, the plateau crack growth rate was of the order of 10^{-6} m/sec as represented in Fig. 5.6.

5.3.2. Crack growth in L-T and T-L oriented specimens

None of the specimens having L-T orientations and which were exposed to a test temperature of 350°C had failed at the iodine bulb temperature of 65°C.

Two out of three specimens oriented in the T-L direction failed when tested at 350°C and at 65°C iodine bulb temperature. Figs. 5.7 and 5.8 represent the crack growth behaviour of these specimens. Both first and second stages of crack growth were recorded before final fracture. $K_{I\text{-}SCC}$ was noticed to be within 12 to 16 MPa$\sqrt{m}$.

5.3.3. Creep growth

Crack extension due to creep at 350'C in both the L-T and T-L oriented specimens was found to be insignificant up to an applied load of 250 kg. Hence no correction was made in the crack velocities recorded in the SCC tests.

5.3.4. Fracture surface examination

Fracture surfaces of the failed specimens were examined under scanning electron microscope. Overall, three distinct zones were identified on the fracture surfaces, - i) a bright ductile pre-cracked area, ii) a brittle iodine-SCC cleavage/fluted area and iii) a ductile/dimple overload failure zone. The first and third zones in all the specimens appeared identical due to the obvious reasons. The second zones which were representative of

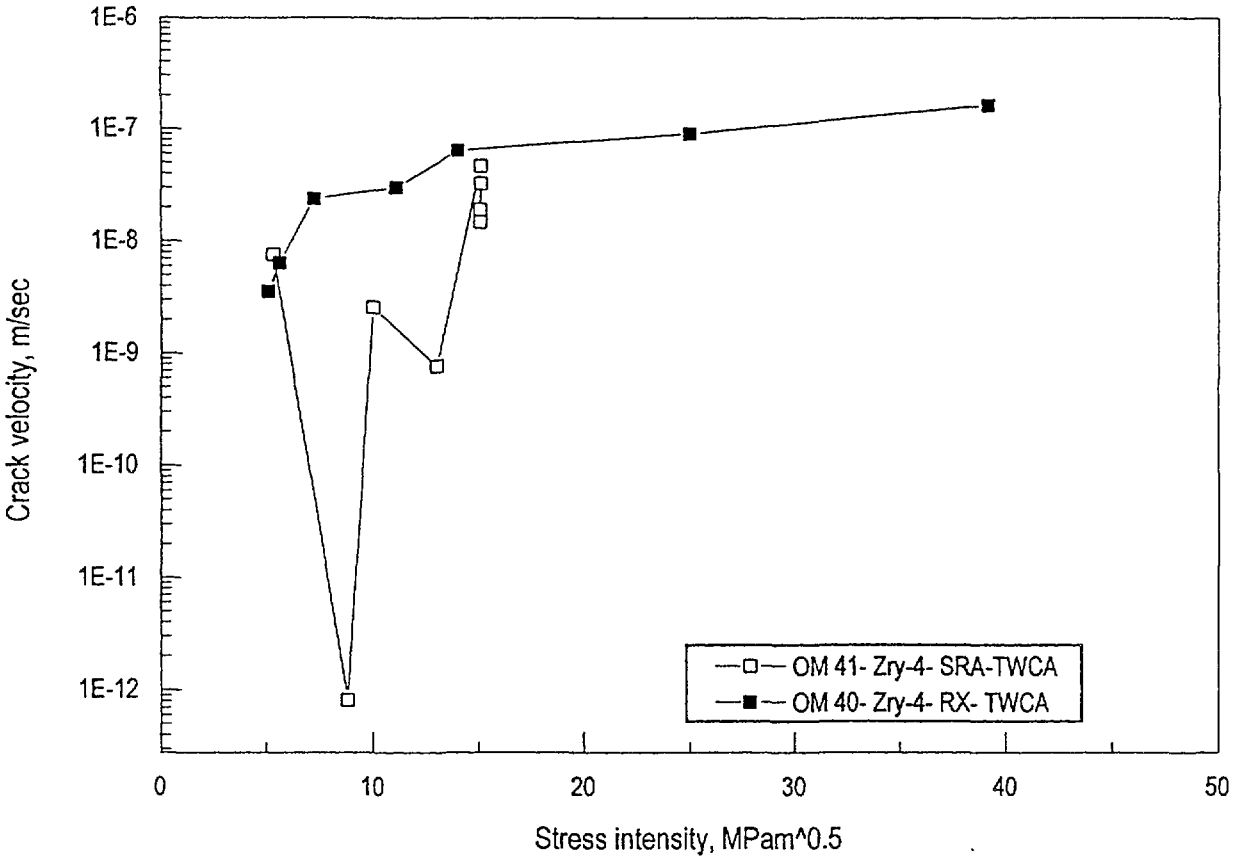

Fig. 5.1. Crack growth behaviour in Zircaloy-4, test temperature –300 ℃, iodine bulb temperature -65 ℃.

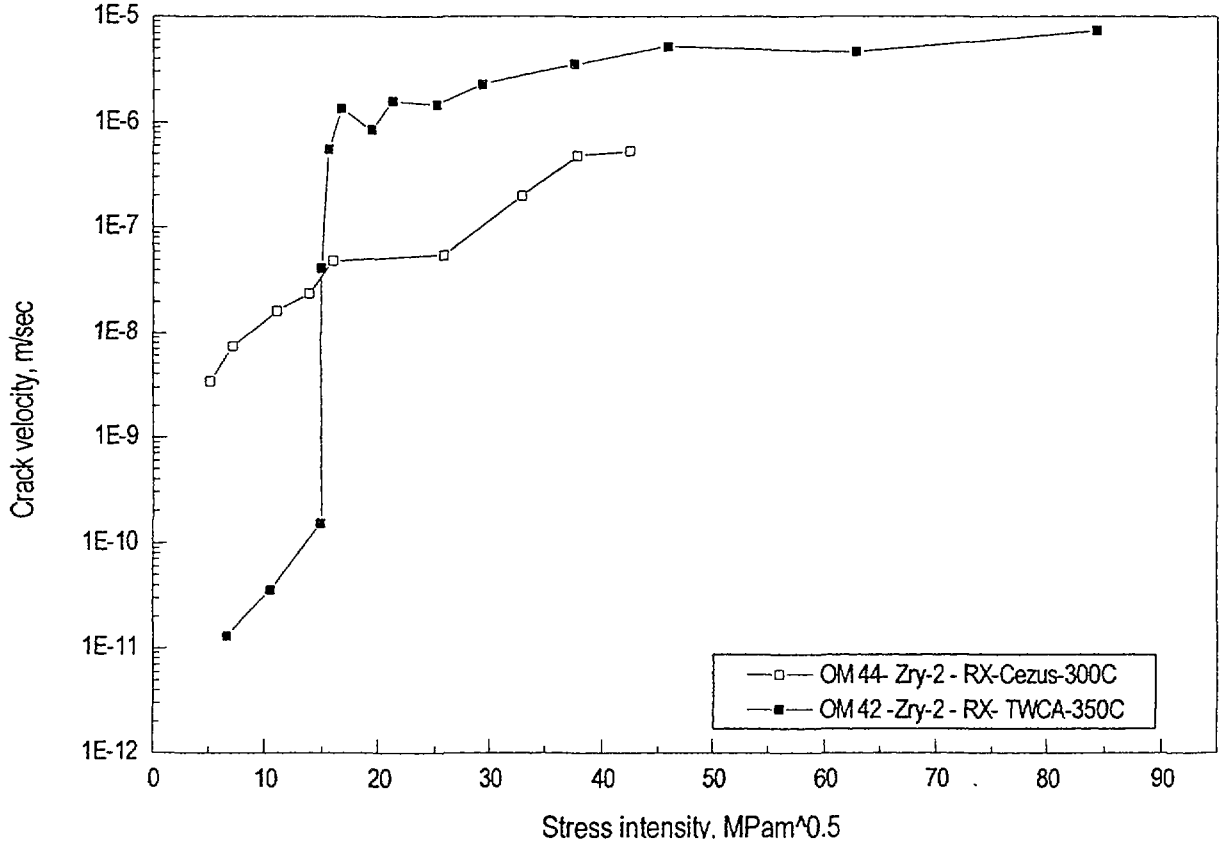

Fig. 5.2. Crack growth behaviour in Zircaloy-2, test temperatures –300 ℃ and 350 ℃, iodine bulb temperature –65 ℃.

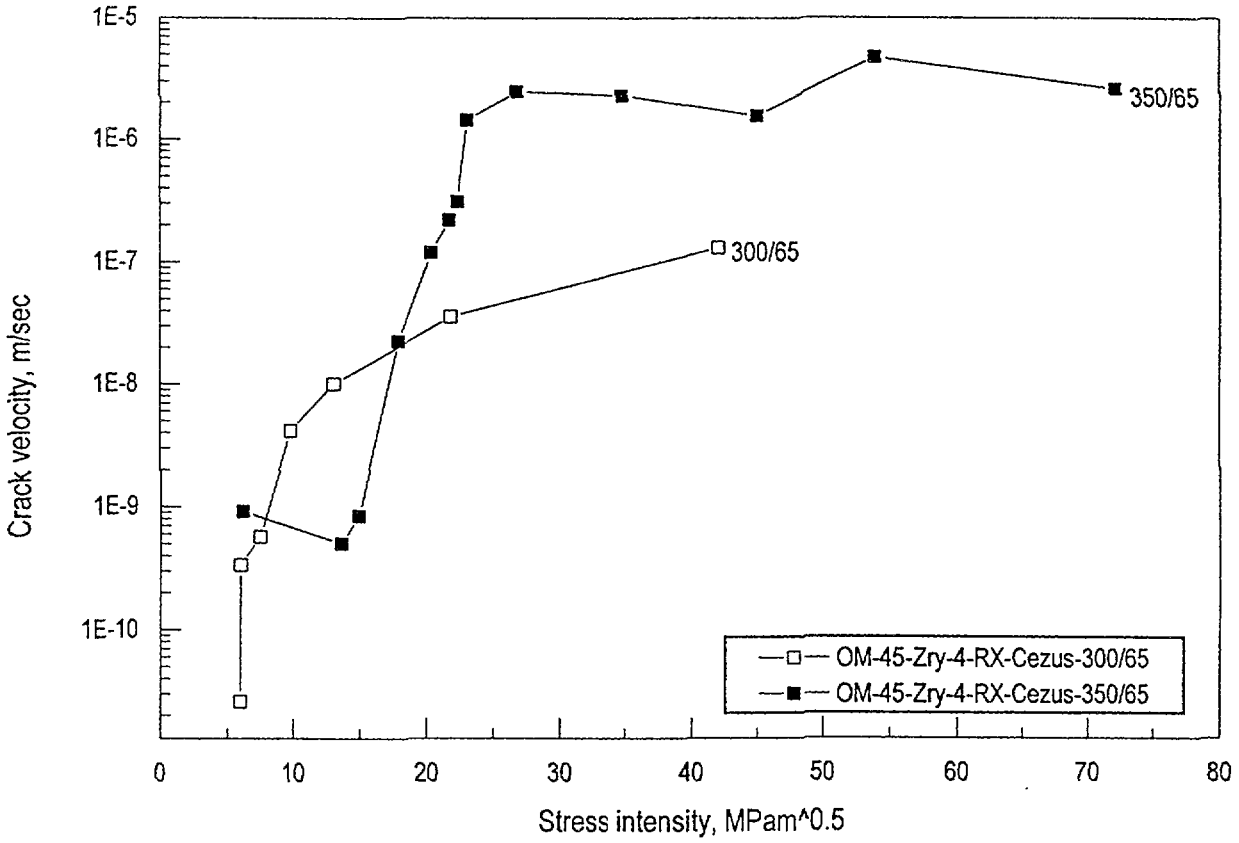

Fig. 5.3. Variation in crack velocities in Zircaloy-4 at test temperatures of 300 ℃ and 350 ℃, iodine bulb temperature –65 ℃.

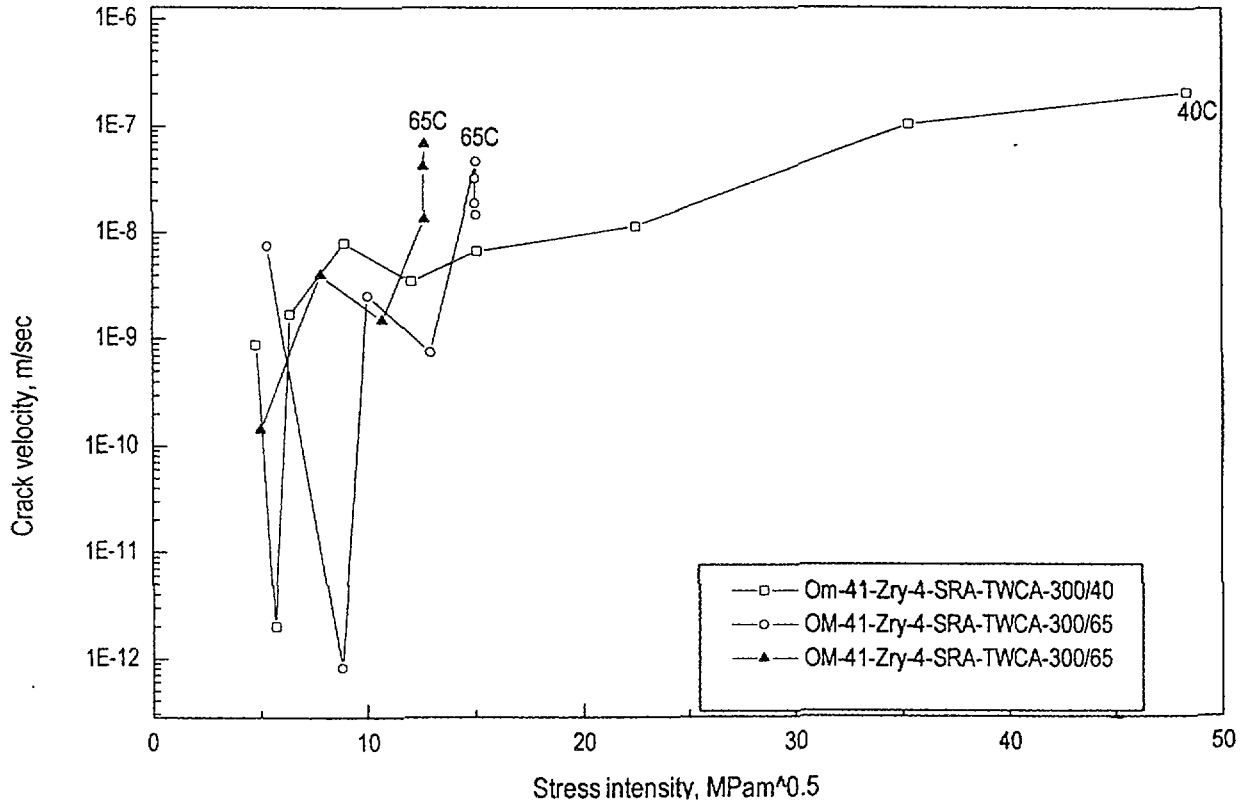

Fig. 5.4. Variation in crack velocities in Zircaloy-4 at a test temperature of 300 ℃, iodine bulb temperatures 40 and –65 ℃.

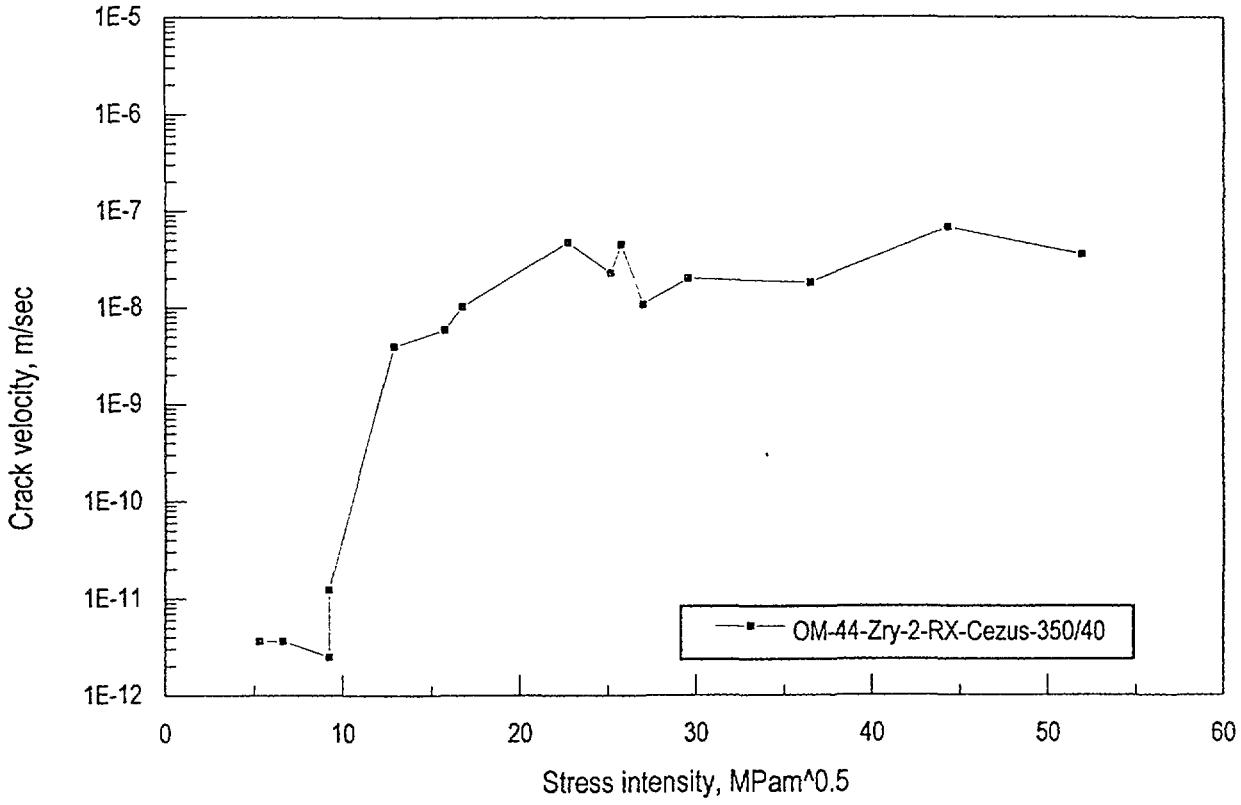

Fig. 5.5. Variation in crack velocity in Zircaloy-2 at a test temperatures of 350 ℃, iodine bulb temperature –40 ℃.

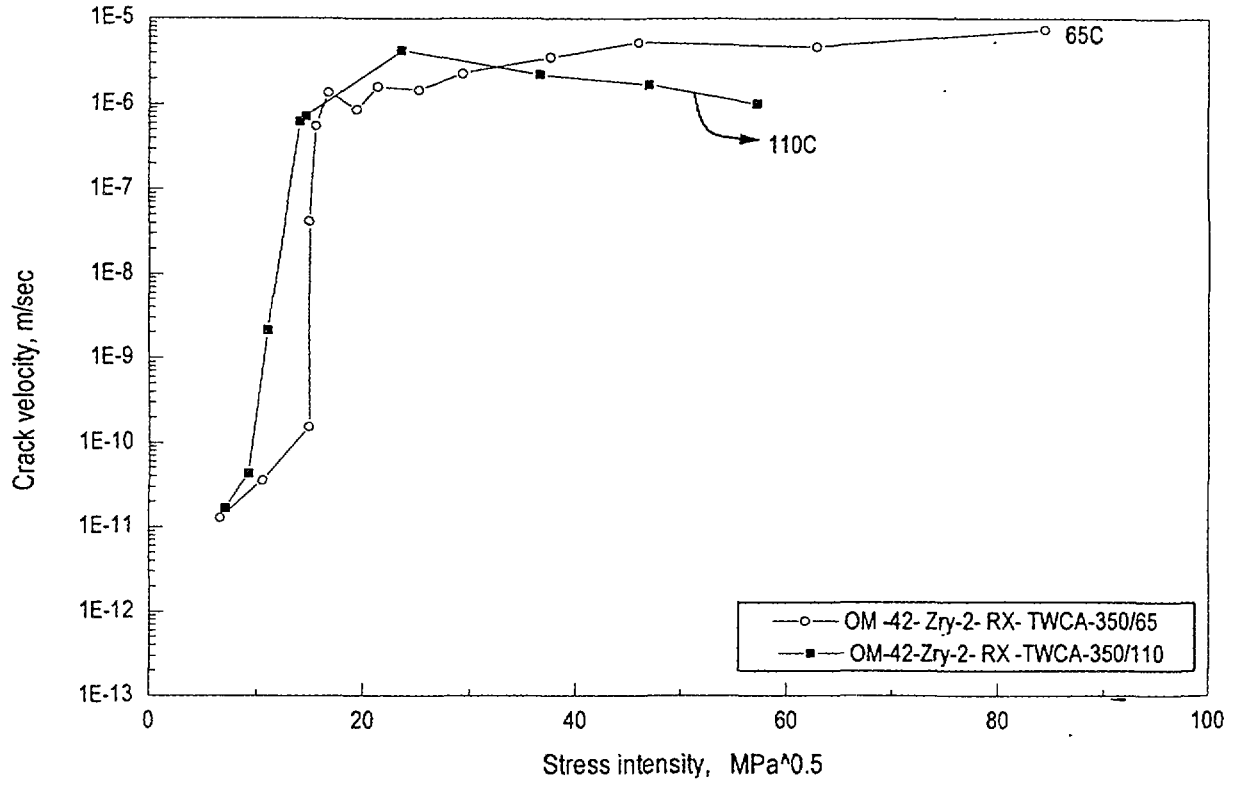

Fig. 5.6. Variation in crack velocity in Zircaloy-2 at test temperatures of 350 ℃, iodine bulb temperature –65 and 110 ℃.

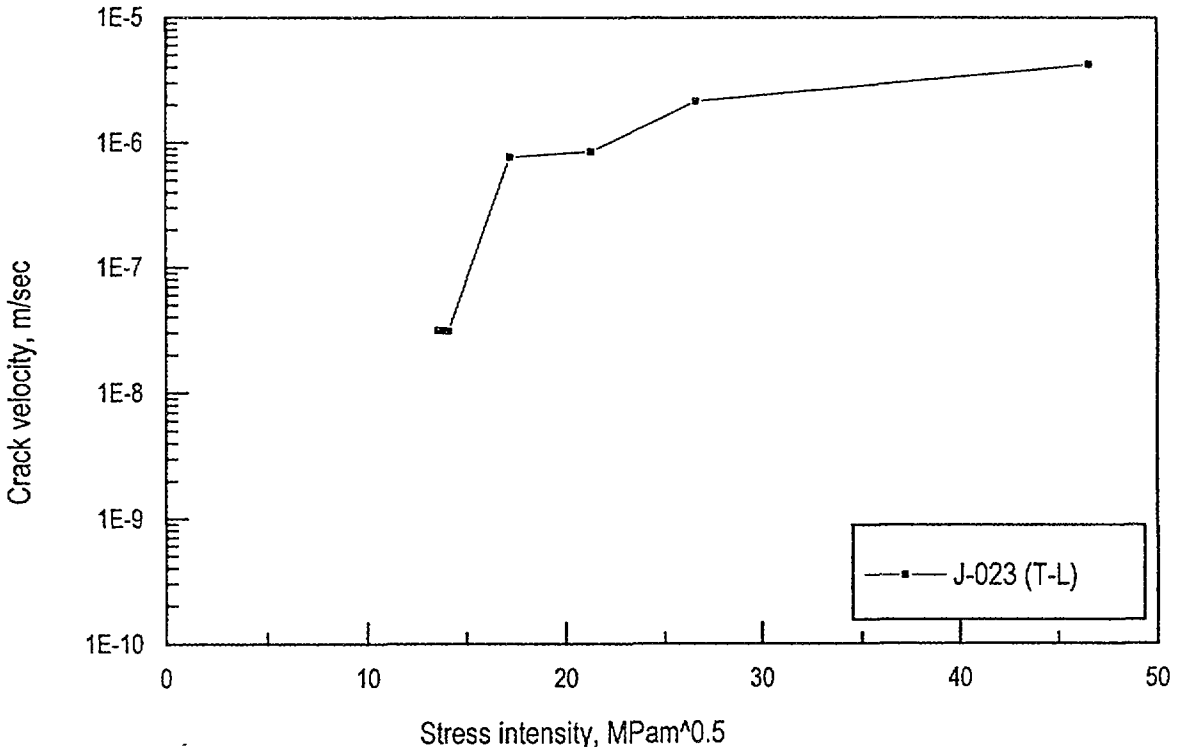

Fig. 5.7. Variation in crack velocity in Zircaloy-2 at test temperatures of 350 ℃, iodine bulb temperature –65 ℃.

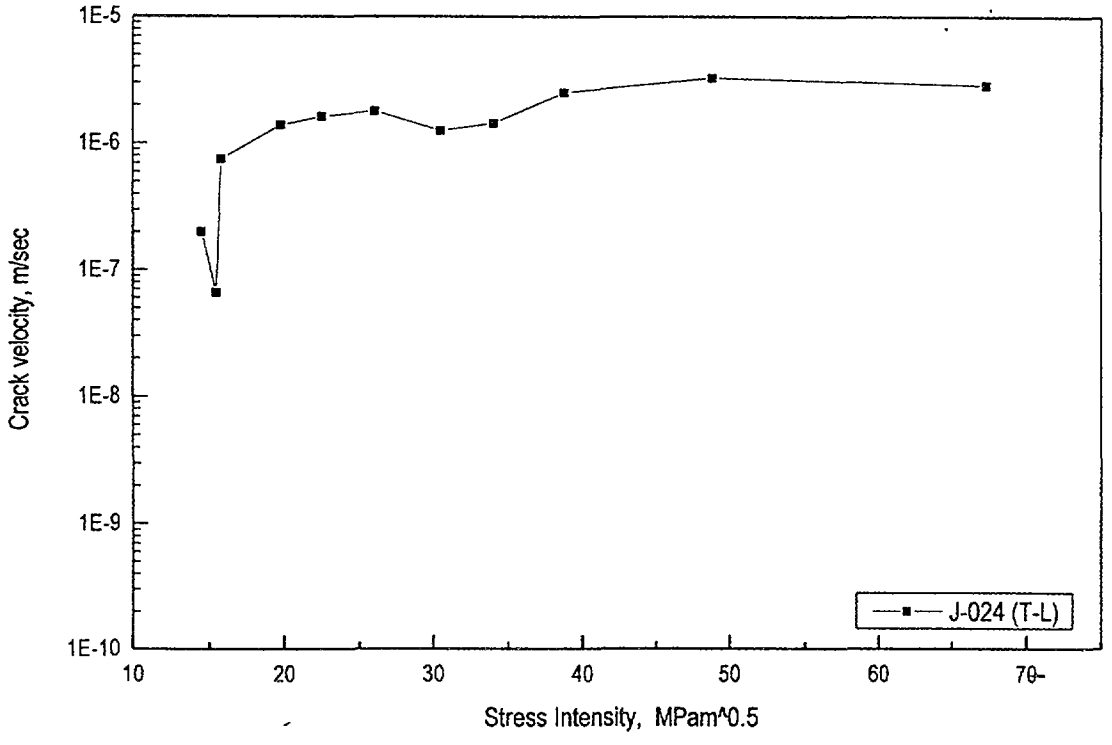

Fig. 5.8. Variation in crack velocity in Zircaloy-2 at test temperatures of 350 ℃, iodine bulb temperature –65 ℃.

iodine-SCC, appeared to be strongly influenced by the iodine partial pressure and the metallurgical history of the individual specimens. In some cases, secondary cracks were observed on the specimen surfaces running parallel to the main crack. A cleavage type morphology was clearly evident in most of the specimens as shown in Fig. 5.9. In addition, the characteristic 'flute' morphology was identified in a few cases. Typical cleavage fracture was also observed on the fracture surfaces of the T-L oriented specimens.

Fig. 5.9. Typical fracture surface appearance of Zircaloy samples failed in SCC tests at 300-350 °C in flowing iodine vapour at a partial pressure of 100 Pa (iodine bulb temperature 40 °C)

5.4. DISCUSSION

Considering the metallurgical conditions, no significant difference was observed in the $K_{I\text{-}SCC}$ values of the recrystallised and the stress relieved alloys. For both the heat treatment conditions, $K_{I\text{-}SCC}$ values were in the range of 5 to 10 MPa$\sqrt{m}$. Similarly, for the differences in the compositions between Zircaloy-4 and Zircaloy-2, no pronounced effect was observed on $K_{I\text{-}SCC}$. However, the stress relieved alloys (Zircaloy-4 and Zircaloy-2) were prone to unstable cracking at much lower stress intensity levels as compared to the recrystallised alloys. Thus, the recrystallised alloys, because of their extended second stage or plateau crack growth region over a long range of stress intensity values, appeared to be more resistant to iodine vapour before complete fracture at higher applied stresses.

Specimens having L-T orientations were highly resistant to iodine SCC as no crack growth was observed in any of these specimens. Maximum load applied in these tests was 230 kg. However, specimens oriented in the T-L directions were susceptible to iodine - SCC. $K_{I\text{-}SCC}$ values for these specimens seem to be higher than those for the recrystallised and stress relief annealed specimens of Zircaloy - 2 and Zircaloy - 4.

Increases in temperature and iodine concentrations were observed to increase crack velocity in general as well as to decrease stress intensity at which unstable cracking was initiated in stress relieved alloys. The present investigation was carried out with 1 min thick specimens. Thus, the results obtained with these specimens seem to reflect more about the cracking behaviour of actual cladding tubes.

5.5. CONCLUSIONS

The following conclusions could be drawn on the basis of the results obtained in the study of crack propagation behaviour of thin and pre-cracked zirconium alloys in flowing iodine vapour at 300 and 350°C:

1) The threshold stress intensity for crack initiation, $K_{I\text{-}SCC}$, was seen to fall within a limited range of 5 to 10 MPa$\sqrt{m}$, irrespective of alloy composition and heat treatment.

2) A pronounced difference was noticed in the crack growth behaviour of the recrystallised and stress relieved Zircaloy-4 and Zircaloy-2 alloys, a long plateau or 2nd stage crack growth being observed in case of the recrystallised alloys.

3) Specimen orientations, vis-à-vis texture, have a pronounced effect on susceptibility to iodine scc.

4) Increase in temperature and iodine concentration, in general, accelerated the crack velocity.

5) Examination of fracture surfaces of failed specimens revealed cleavage and fluted regions typical of iodine-SCC of zirconium alloys.

Chapter 6

IODINE STRESS CORROSION CRACKING RESULTS IN ZIRCONIUM ALLOYS IN THE REPUBLIC OF KOREA

6.1. EXPERIMENTAL RESULTS FROM DYNAMIC IODINE SUPPLY SYSTEM

Fig. 6.1 shows the dynamic flowing system for SCC tests, which was composed of a stainless steel chamber, iodine supply bath, PTFE tubes for connecting the components, vacuum equipment, and heating furnace. The constant loading was applied through Inconel 600 stems using a cantilever beam with dead weights. Conax fittings with a PTFE sealant were inserted in the testing chamber for penetrating the loading stem, DCPD power lines and iodine supplying tubes. A constant iodine pressure was supplied by sweeping high purity Ar gas through an iodine container in a water bath.

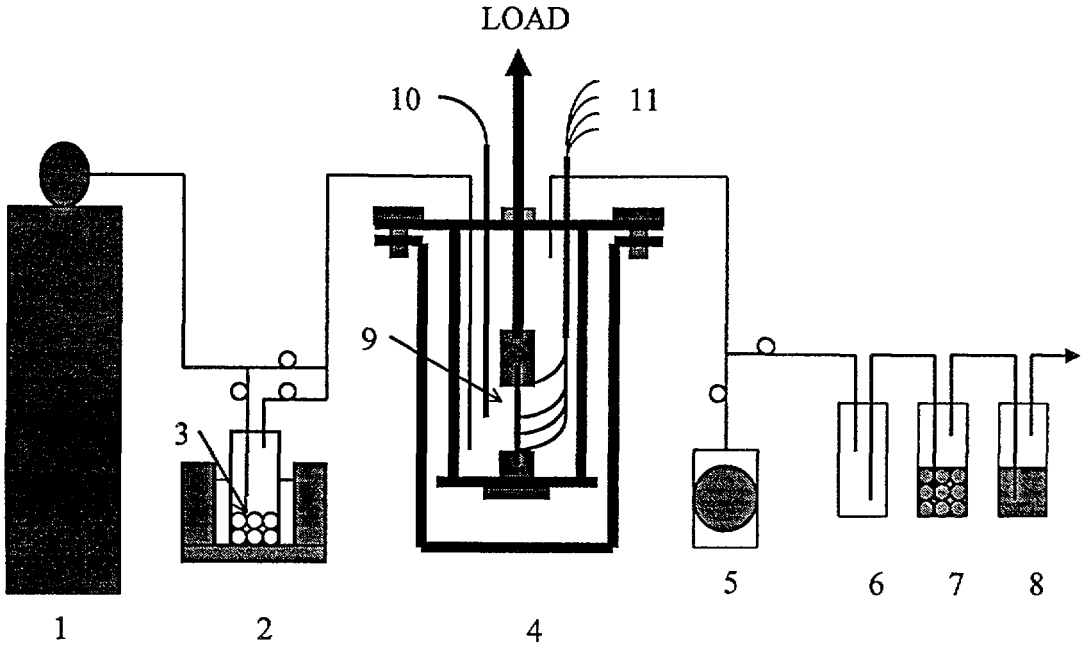

1. Ar gas
2. Heating mantle
3. Iodine container
4. Test chamber
5. Vacuum pump
6. Molecule sieve
7 & 8. Ethanol bath
9. Specimen
10. Thermocouple
11. Power lines

Fig. 6 1. Schematic diagram of dynamic flowing system.

A DCPD technique was used to monitor the SCC crack length with time. Four DCPD power lines of Zr wire were attached to the edge of a specimen. Oxidized Zircaloy-4 bushings and sleeves gave the electrical insulation between specimen and loading stems. A calibration curve for crack length was determined from a curve of crack length vs. DCPD output voltage which was supplied by the host laboratory. The crack length which was calculated from the DCPD output voltage was corrected using a measured crack length.

6.1.1. Test matrix and specimens

A. SCC tests using dynamic flowing system

- OM40 : recrystallized Zircaloy-4 (Wah Chang)

test temperature : 350 °C

iodine pressure : 1,000 Pa

test specimen : E214, E215, E216, E217 (T-L orientation)

- OM41 : stress relief annealed Zircaloy-4 (Wah Chang)

test temperature : 350 °C

iodine pressure : 1,000 Pa

test specimen : E240, E246, E268 (T-L orientation)

- OM44 : recrystallized Zircaloy-2 (Cezus)

test temperature : 350 °C

iodine pressure : 1,000 Pa

test specimen : E283, E402, E408 (T-L orientation)

B. Texture effect tests using dynamic flowing system

J series

test temperature : 300, 350 °C

iodine pressure : 0 Pa, 1000 Pa

test specimen : J008, J009, J010, J011 (L-T orientation)

J025, J026, J027, J037 (T-L orientation)

C. SCC tests using static system

- OM41 : stress relief annealed Zircaloy-4 (Wah Chang)

test temperature : 300 - 400 °C

iodine pressure : 10,000 Pa

test specimen : E241, E242, E243, E244, E245, E247 (T-L orientation)

- OM44 : recrystallized Zircaloy-2 (Cezus)

test temperature : 300, 350 °C

iodine pressure : 10,000 Pa

test specimen : E278, E279, E280, E281, E282 (T-L orientation)

6.1.2. Calculating the crack lengths

A DCPD calibration curve was determined from the voltage-crack length data which were supplied by the host laboratory. To normalize the DCPD voltage, the reference voltage at

zero crack length, V_o, was calculated from the mathematical equation of DCPD curve as follows.

$$V_o = V_{ini}/(1.0 + 1.713(a_i/b) + 2.6936(a_i/b)^2 - 2.9123(a_i/b)^3 + 5.282(a_i/b)^4)$$

where V_{ini} = measured voltage at initial at test temperature after loading, a_i = initial pre-cracked crack length, b = specimen width

The DCPD calibration curve of the normalized voltage was determined by a fitting program to obtain a mathematical description.

$$a/b = -0.8234 + 1.1467(V/Vo) - 0.3963(V/Vo)^2 + 0.0732(V/Vo)^3 - 0.0054(V/Vo)^4$$

6.1.3. Calculating the stress intensity factor, K

The stress intensity factor was calculated using the following equation.

$$K_I = K_o\,(1.12 - 0.23(a/b) + 10.6(a/b)^2 - 21.7(a/b)^3 + 30.4(a/b)^4)$$

$$K_o = \sigma\,\sqrt{(\pi\, a)}$$

6.1.4. Measurement of texture

Texture of OM40 (recrystallized Zircaloy-4, Wah Chang) and OM44 (recrystallized Zircaloy-2, Cezus) was measured using X-ray technique. Figs. 6.2 and 6.3 are the pole figures of the basal plane for OM40 and OM44. The textures showed the typical texture of rolled plate of Zircaloy. The normal direction of basal plane (0002) orients at 35° to the transverse direction, and the peak level of basal plane at 35 ° is 7.3 for OM44, and 4.8 for OM40.

6.2. RESULTS AND DISCUSSION OF SCC OF ZIRCALOY

6.2.1 Creep tests

At test temperatures of 300 to 350°C, creep appeared to affect the crack length during SCC testing. In particular, in the SCC threshold region below 10^{-6} mm/sec of crack velocity, the DCPD output voltage change significantly affects the SCC crack length calculation. In order to correct the crack lengths, creep behaviour was measured in the SCC test conditions. The creep tests were carried out using the same technique as for SCC testing, but without the iodine supply. Crack length was calculated from the DCPD data using the same equation as for SCC. The velocity and stress intensity so obtained were used for comparison with the SCC results, but do not represent real creep behaviour because the DCPD change comes also from crack blunting and tearing.

1) E402 (OM44, 300 °C)

Fig. 6.4 shows the crack length as a function of time at 300 °C. The load applied was from 15 kg to 34 kg for more than 1 day at each weight. The change in crack length was very small during loading at each weight below 32 kg, but the crack length jumped a certain amount just after applying an additional weight. At 34 kg, the crack length showed a creep curve with primary, secondary and tertiary stages. The final crack length was about 5 mm with crack opening displacement of 5 mm.

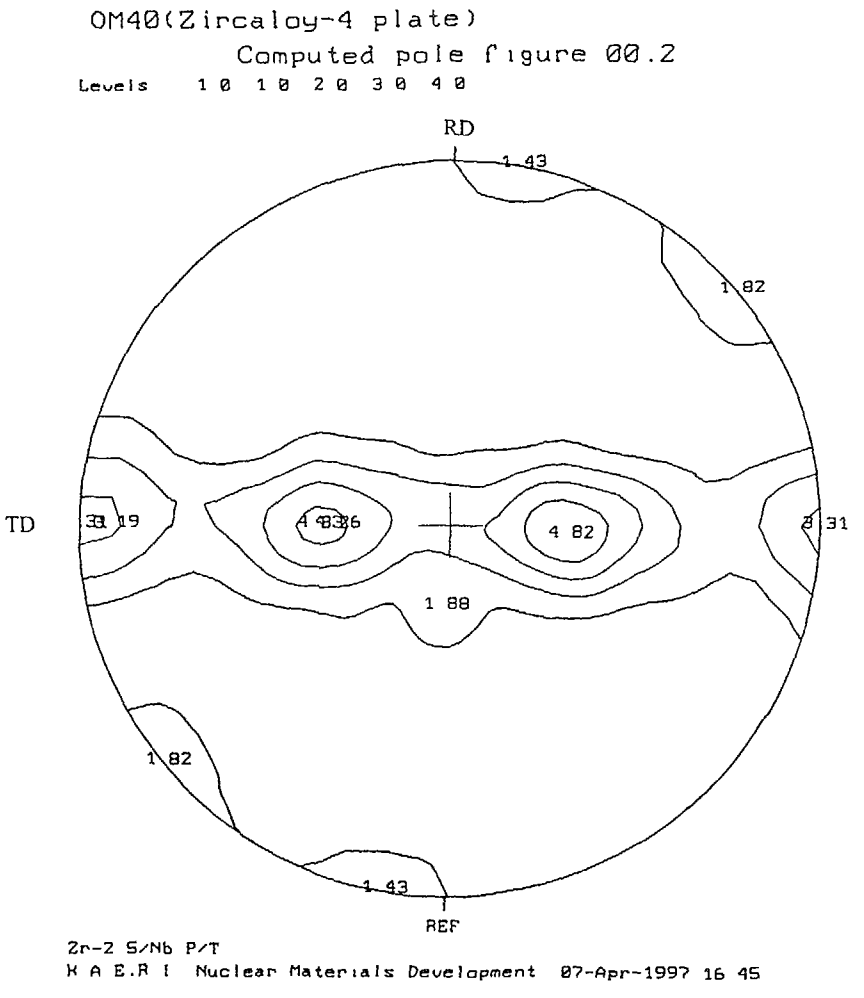

Fig. 6.2. Pole figure of basal plane (0002) in OM40.

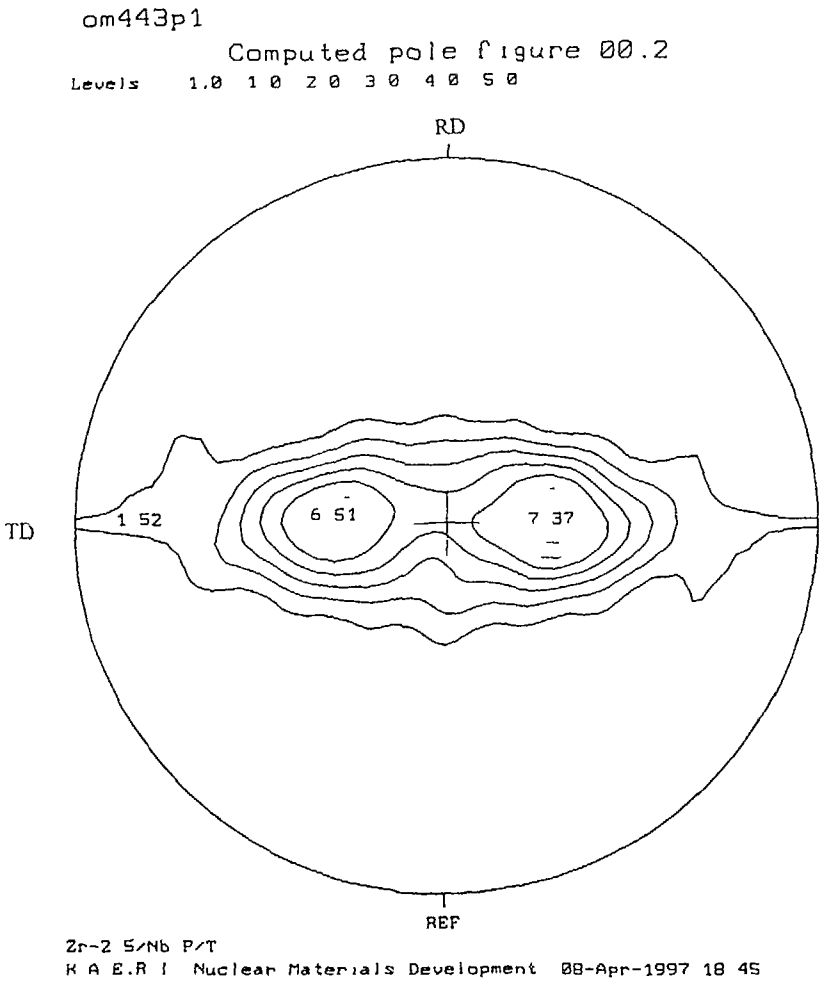

Fig. 6.3. Pole figure of basal plane (0002) in OM44.

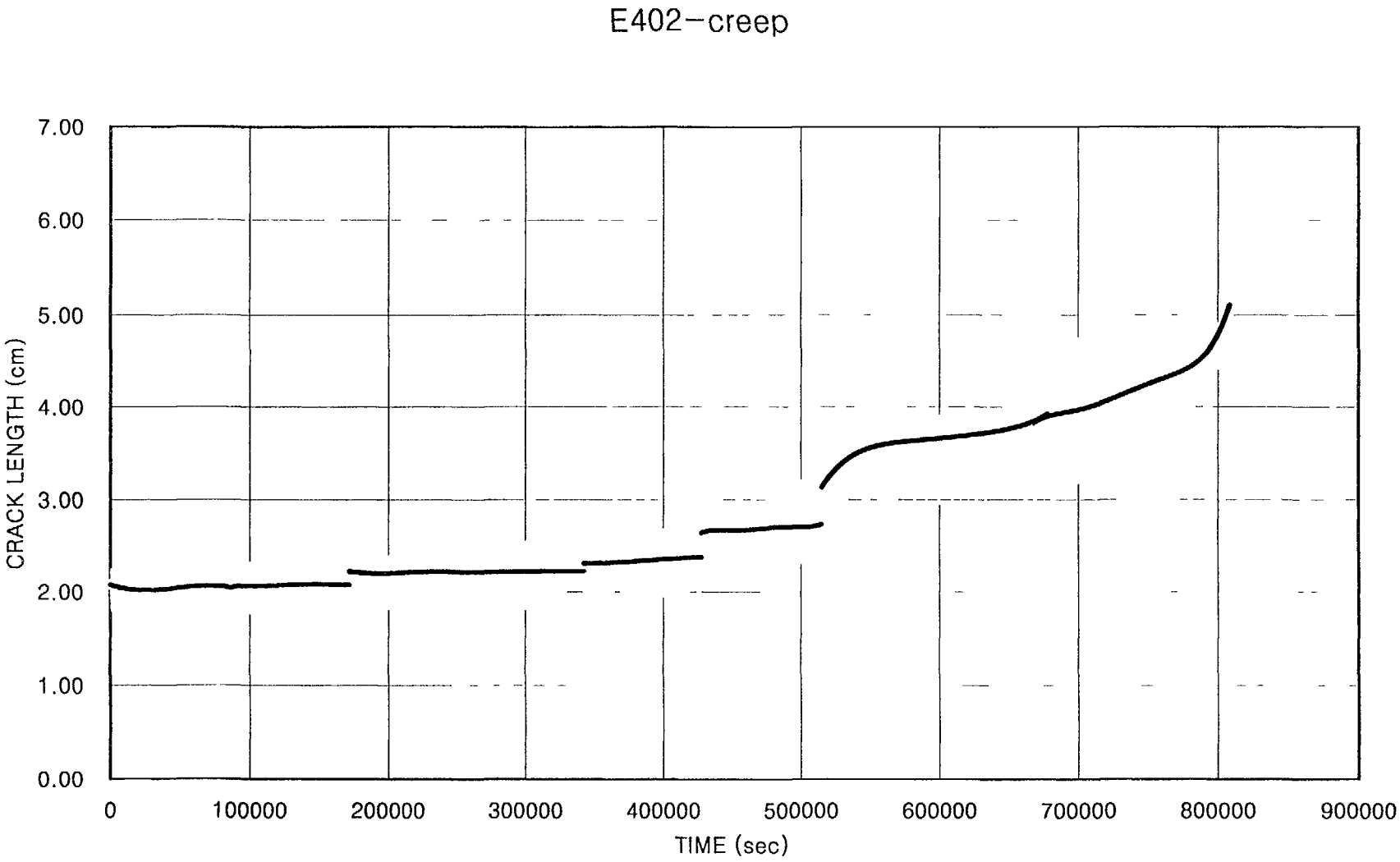

Fig. 6.4. A creep curve of E402 at 300℃.

Fig. 6.5 shows the velocity vs. stress intensity plot which is calculated from the crack length in Fig. 6.4. Below 32 kg load (25 MPa$\sqrt{m}$ of stress intensity), the velocities did not change with load in the order of 10^{-7} mm/sec, though the crack length did jump at each step to a higher load. At 34 kg load (above 30 MPa$\sqrt{m}$), the velocity in the primary creep stage was 1 x 10^{-5} mm/sec, but the velocity in the secondary stage dropped to the order of 10^{-6} mm/sec and increased with the stress intensity.

2) J009 (350 °C))

The creep behaviour at 350 °C is summarized in Fig. 6.6. The velocities were very low, of the order of 10^{-7} mm/sec, below about 20 MPa$\sqrt{m}$ of stress intensity (15 kg load). Above 24

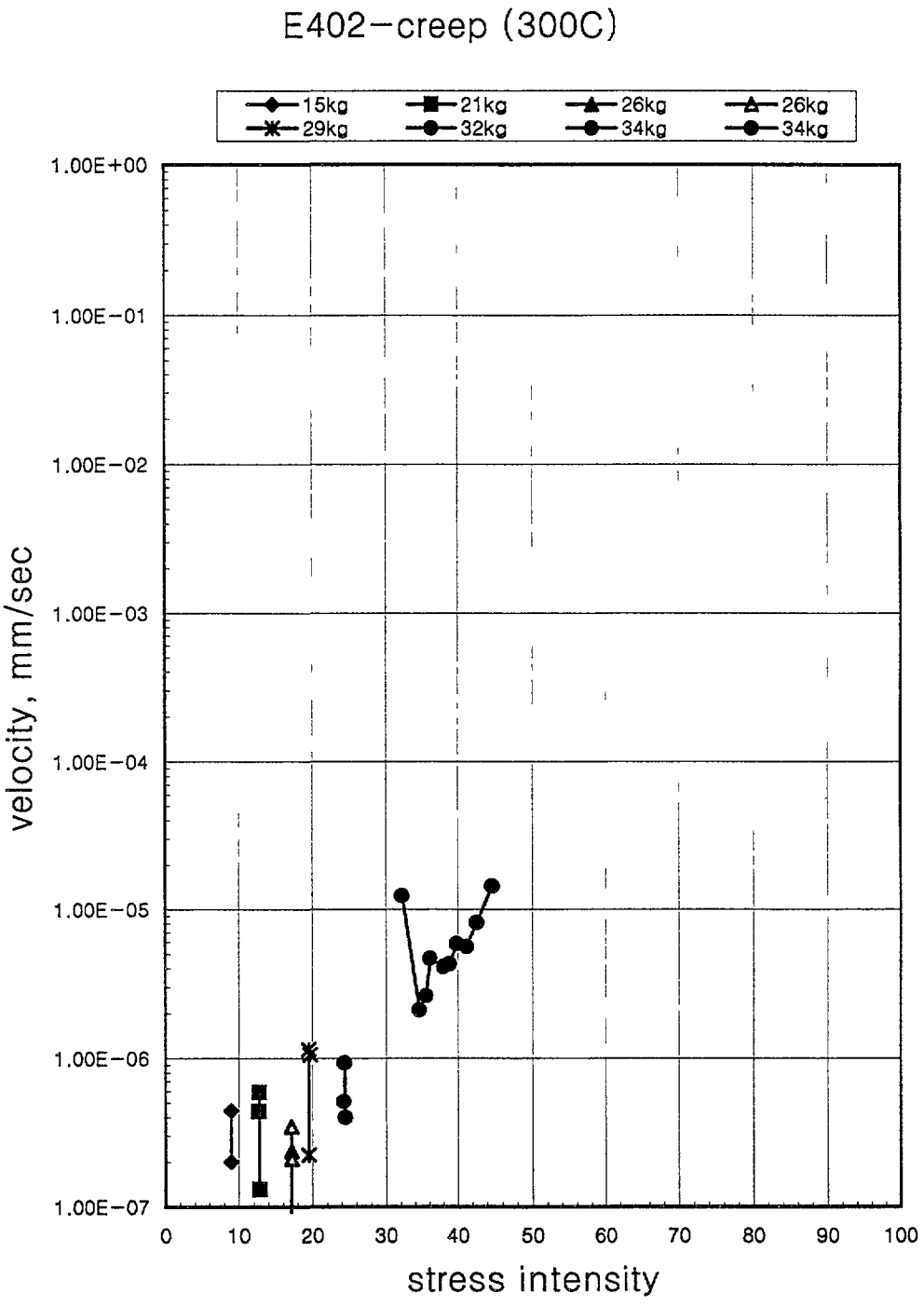

Fig. 6.5. The creep velocity of E402 as a function of stress intensity factor (300 ℃).

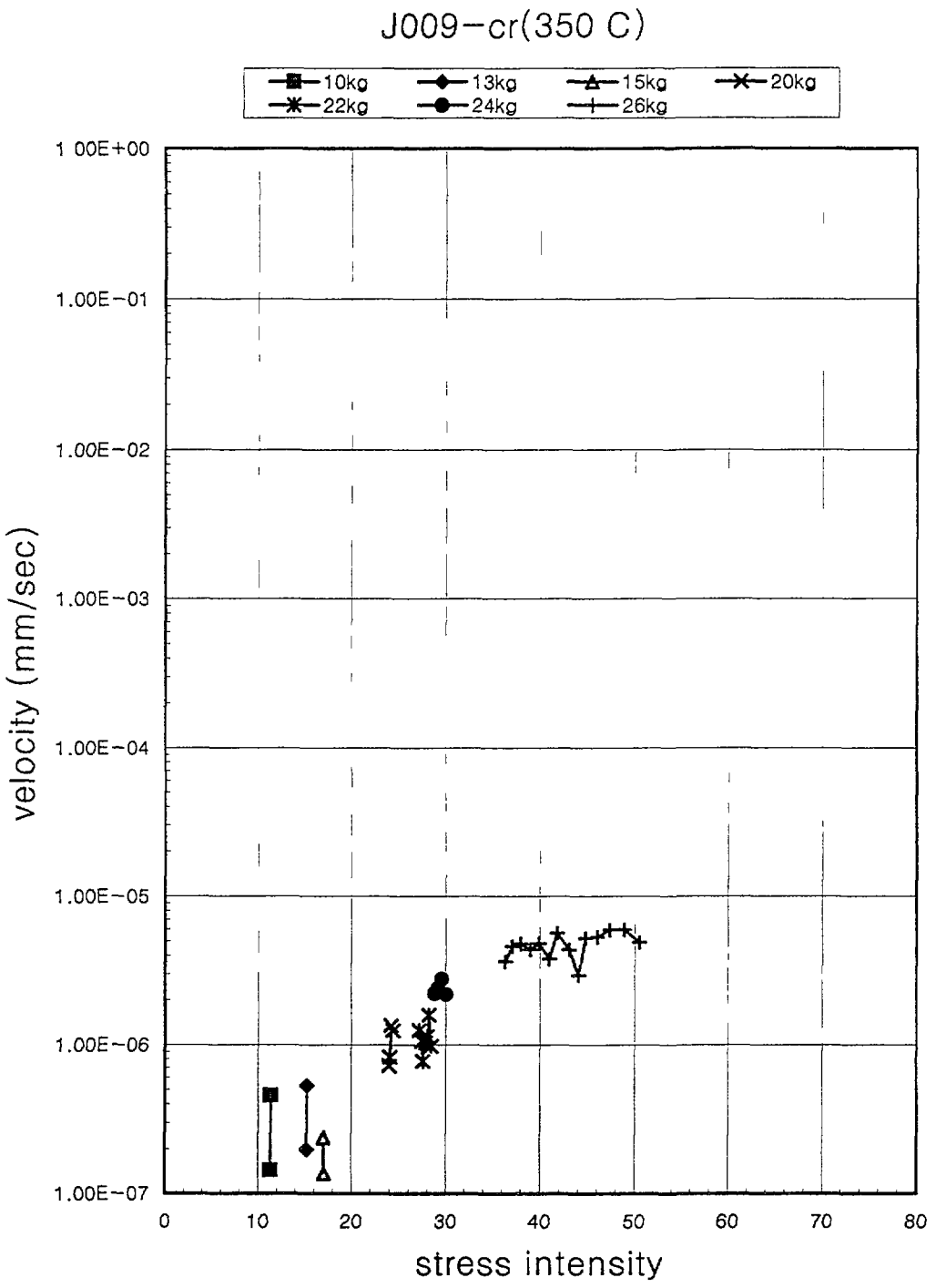

Fig. 6.6. The creep velocity of J009 as a function of stress intensity factor (350 ℃).

MPa√m (20 kg load), the velocity was distinguishable in the order of 10^{-6} mm/sec. However, the velocity did not go above 1 x 10^{-5} mm/sec even up to 50 MPa√m. The crack was not developed, but rather was blunted.

6.2.2. SCC propagation rate of OM40 (recrystallized Zircaloy-4, Wah Chang)

1) E216 (350 °C, 1000 Pa)

- Test temperature : 353 °C
- Iodine Concentration : 1000 Pa (63 °C)

Table 6.1 summarizes the test conditions and results such as test date, DCPD voltage, load, calibrated crack length, stress intensity factor, crack propagation rate, and etc. Fig. 6.7 shows the crack propagation rate as a function of the stress intensity factor. The curve of SCC crack velocity vs. stress intensity is a typical SCC curve, which is divided into SCC stage I (stress-dependent region), II (stress-independent plateau region), and III (mechanical rupture region). The SCC stage I appeared from $1x10^{-6}$ mm/sec at 10.6 MPa$\sqrt{m}$ of stress intensity, and the stage II is after 18 MPa$\sqrt{m}$ with plateau velocity of $4x10^{-4}$ mm/sec. Stage III has not appeared at a up to 34 MPa$\sqrt{m}$.

Fig. 6.8 Photo (a) shows the surface of a specimen with an SCC crack, and Fig. 6.9 shows the crack path at a high magnification. The surface of the specimen was coloured dark gray due to the slight oxidation, and the crack was opened by deformation. The microstructure was a recrystallized one, and the SCC crack mode was mostly transgranular with some intergranular. A yellow substance like an iodine compound was shown in Fig.6.10 at the crack tip.

2) E214 (350 °C, 1000 Pa)

- Test temperature : 350 °C

- Iodine Concentration : 1000 Pa (65 °C)

Table 6.2 summarizes the test results for E214, and the SCC crack velocity is shown in Fig. 6.7. The SCC crack had not propagated at below 9 MPa$\sqrt{m}$ of stress intensity. SCC stage I in which the crack velocity increased rapidly with stress intensity, appeared at a velocity of $4x10^{-7}$ mm/sec at 9 MPa$\sqrt{m}$. After about 20 MPa$\sqrt{m}$, the velocity approached the $4.5x10^{-4}$ mm/sec velocity of the plateau region in SCC stage II.

Fig. 6.8 Photo (b) shows the specimen with a crack length of 5.3 mm after 140 hours testing. In Fig. 6.11, the fracture surface was divided into notch, precrack, SCC region, and mechanical fracture region. The SCC region shown was relatively flat. The SCC fracture morphology, in Fig. 6.12 Photo (a), was transgranular with river patterns, and crevices caused by secondary cracks between the grains. The SCC transgranular crack plane was inclined from the normal direction of the fracture surface, indicating that the SCC crack of Zircaloy should propagate along the basal plane (0001) of hcp structure. The specimen is T-L orientation, and the pole peak of the basal plane in OM40 was measured at 35° to the longitudinal direction of the specimen. The SCC morphology at the end of the crack (about 5 mm) showed also transgranular mode without ductile mode, in Fig. 6.12 Photo (b).

3) E217 (350 °C, 1000 Pa)

- Test temperature : 350 °C

- Iodine Concentration : 1000 Pa (63 °C)

Table 6.3 summarizes the test results of E217. The DCPD output voltage was unstable at the beginning stage due to temperature variations. The SCC crack had a very slow velocity of $5x10^{-7}$ mm/sec at 10 MPa$\sqrt{m}$ (initial loading 13.7 kg), and increased with loading (SCC stage I). SCC stage II appeared after 25 MPa$\sqrt{m}$, approaching $7x10^{-4}$ mm/sec crack velocity in the plateau region.

TABLE 6.1. SUMMARY OF TEST CONDITIONS AND RESULTS FOR E216 (OM40, 350°C)

OM40 (E216)
thickness = 0.101 cm
precrack = 0.215 cm
width = 1.3 cm
iodine = 63 C
temperature = 353 C
current = 2.50 A
Vo = 1.4639
1.4681

date of current data	elapsed time	temp (C)	volt	load(kg)	v/vo	a/b	crack,cm (DCPD)	crack(cal) cm	a/b(cal)	Ki	Ki,mean	velocity (mm/sec)	
97-02-01 15:51	0	350	1.973	13.7	1.348	0.164	0.213	0.215	0.165	10.6	10.6	1.14E-06	
97-02-02 1:50	599	353	1.984	13.7	1.355	0.167	0.217	0.219	0.169	10.7	10.8	1.72E-06	
97-02-02 7:50	959	353	1.994	13.7	1.362	0.170	0.221	0.223	0.171	10.9	10.9	3.52E-06	
97-02-02 10:45	1134	353	2.004	13.7	1.369	0.173	0.224	0.227	0.174	11.0	11.1	2.72E-06	
97-02-02 13:45	1314	353	2.012	13.7	1.374	0.175	0.227	0.229	0.177	11.1	11.1	9.95E-07	
97-02-02 18:52	1621	353	2.017	13.7	1.378	0.176	0.229	0.231	0.178	11.2	11.2	1.78E-06	
97-02-02 23:59	1928	353	2.026	13.7	1.384	0.179	0.232	0.235	0.180	11.3	11.5	2.84E-06	
97-02-03 9:11	2480		2.052	13.7	1.402	0.186	0.242	0.244	0.188	11.7	11.8	2.93E-06	
97-02-03 15:17	2846		2.070	13.7	1.414	0.191	0.248	0.250	0.193	11.9	12.0	3.12E-06	
97-02-03 20:17	3146		2.082	13.7	1.422	0.194	0.253	0.255	0.196	12.1	12.2	4.20E-06	
97-02-03 23:47	3356		2.097	13.7	1.432	0.198	0.258	0.260	0.200	12.3	12.4	3.89E-06	
97-02-04 3:47	3596		2.113	13.7	1.443	0.203	0.264	0.266	0.204	12.5	12.6	4.09E-06	
97-02-04 7:05	3794		2.127	13.7	1.453	0.207	0.269	0.270	0.208	12.7	12.8	6.10E-06	
97-02-04 9:45	3954		2.144	13.7	1.465	0.211	0.274	0.276	0.213	13.0	14.0		
97-02-04 9:45	3954		2.156	15.7	1.469	0.213	0.276	0.278	0.214	15.0	15.1	3.77E-05	
97-02-04 10:15	3984		2.176	15.7	1.482	0.218	0.283	0.285	0.219	15.3	15.6	7.31E-05	
97-02-04 10:47	4016		2.218	15.7	1.511	0.229	0.297	0.299	0.230	16.0	16.2	1.37E-04	
97-02-04 10:59	4028		2.248	15.7	1.531	0.236	0.307	0.309	0.238	16.5	16.9	2.15E-04	
97-02-04 11:11	4040		2.296	15.7	1.564	0.248	0.323	0.324	0.250	17.2	17.6	2.15E-04	
97-02-04 11:23	4052		2.338	15.7	1.593	0.259	0.336	0.338	0.260	17.9	18.4	2.47E-04	
97-02-04 11:35	4064		2.396	15.7	1.632	0.272	0.354	0.355	0.273	18.9	19.5	2.97E-04	
97-02-04 11:47	4076		2.468	15.7	1.681	0.289	0.376	0.377	0.290	20.2	21.0	3.88E-04	
97-02-04 11:59	4088		2.566	15.7	1.748	0.311	0.404	0.405	0.311	21.9	22.9	3.29E-04	
97-02-04 12:14	4103		2.675	15.7	1.822	0.334	0.434	0.434	0.334	23.8	25.0	4.29E-04	
97-02-04 12:26	4115		2.795	15.7	1.904	0.357	0.465	0.465	0.358	26.1	27.4	4.55E-04	
97-02-04 12:38	4127		2.93	15.7	1.996	0.383	0.498	0.498	0.383	28.8	30.3	4.60E-04	

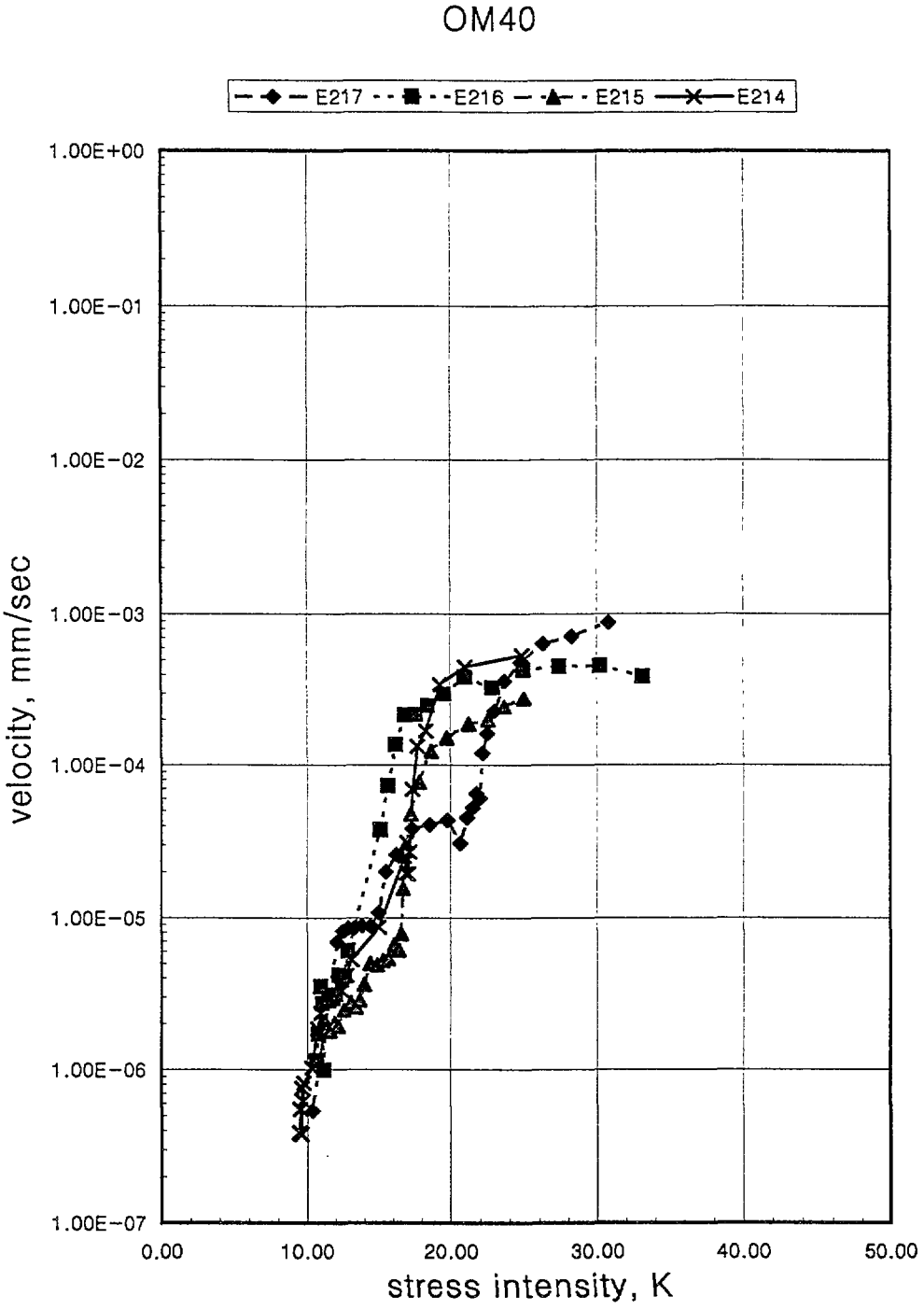

Fig. 6.7. The SCC propagation rate of OM40 as a function of stress intensity factor (350 ℃).

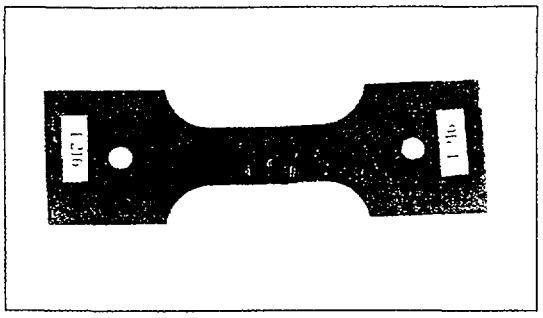

(a) E216

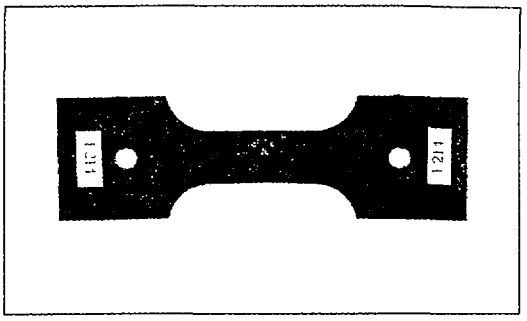

(b) E214

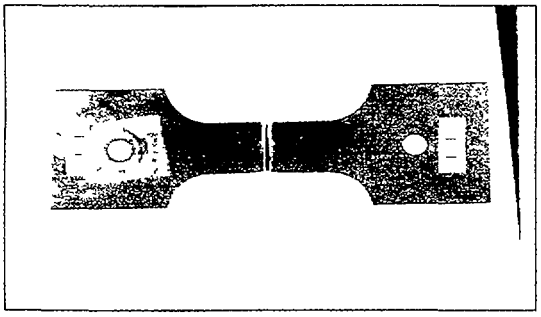

(c) E217

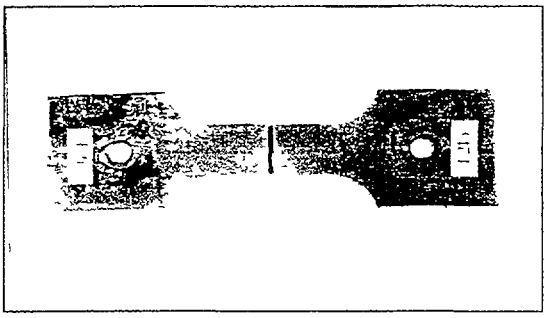

(d) E215

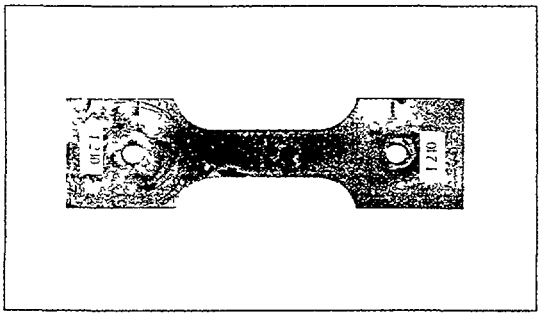

(e) E240

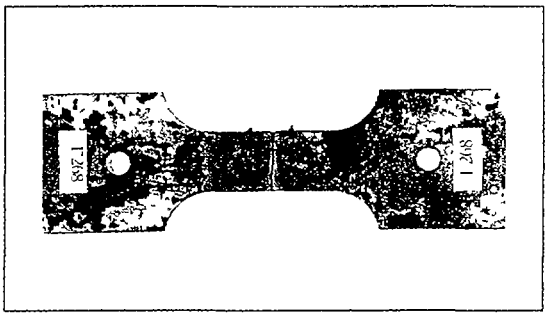

(f) E268

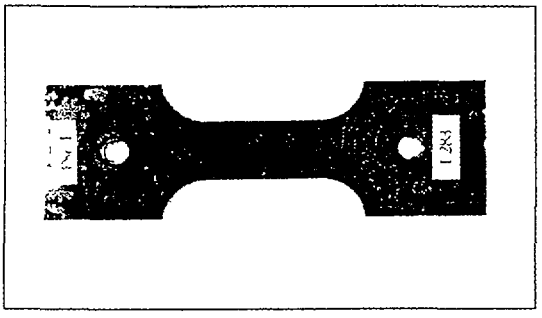

(g) E283

Fig. 6.8. Shape of tested specimens.

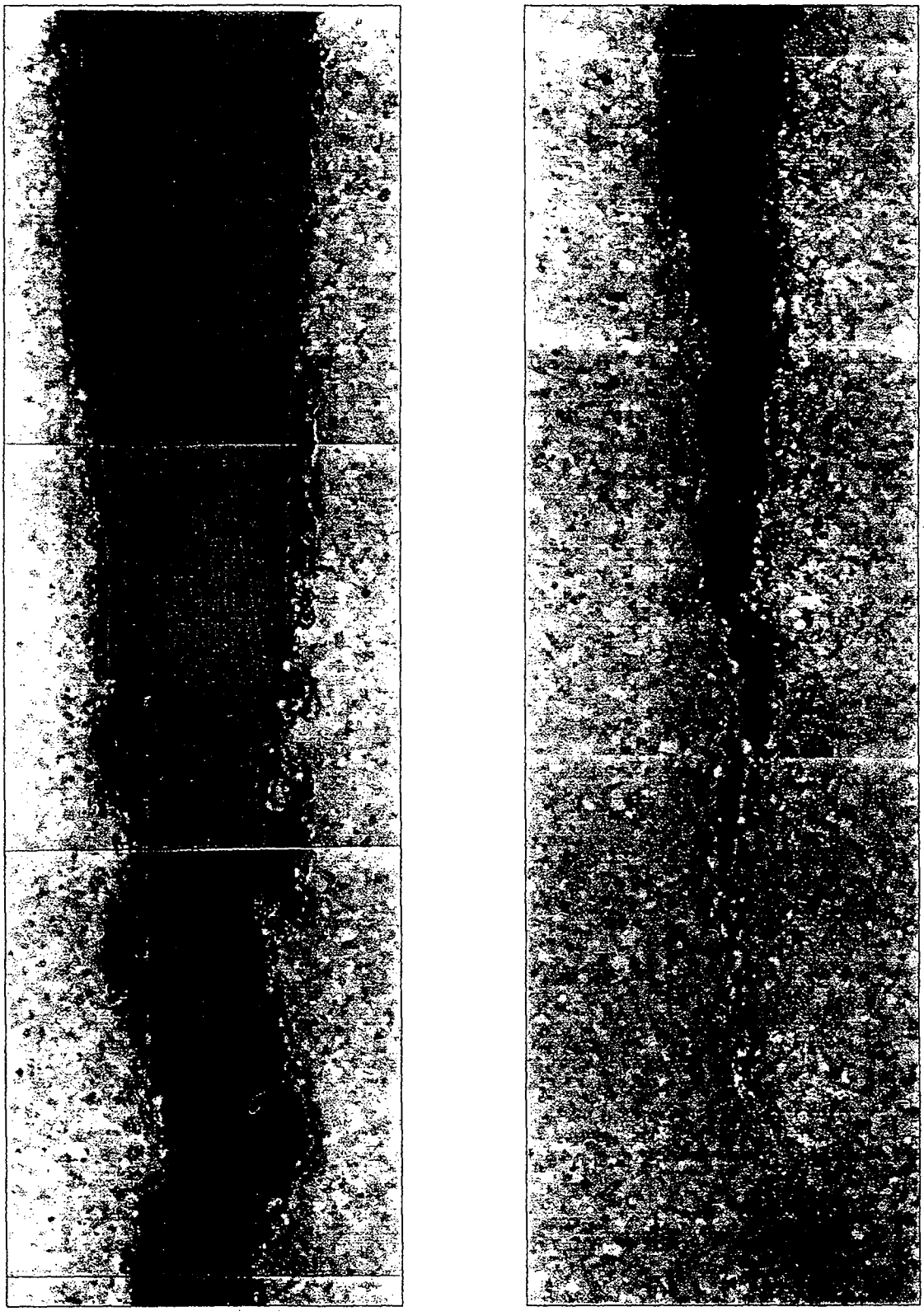

Fig. 6.9. SCC crack shape of E216.

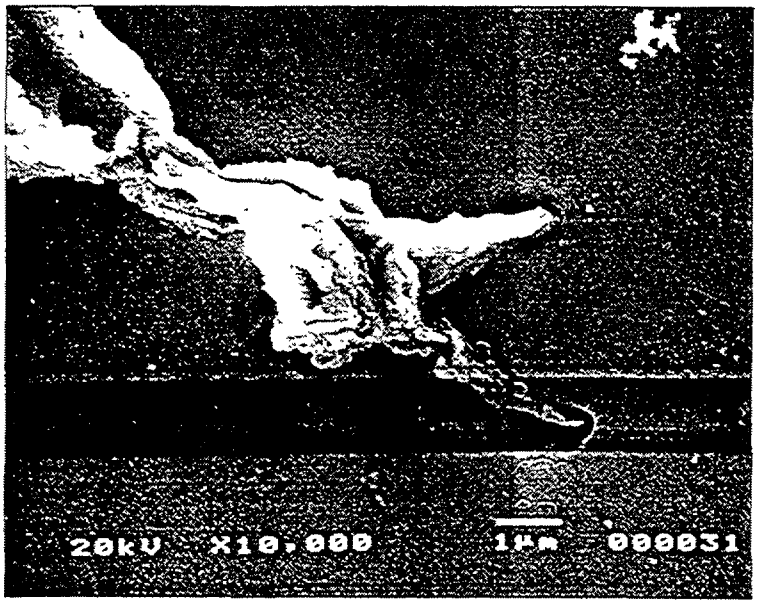

Fig. 6.10. SEM surface morphology at crack tip of E216.

Fig. 6.8 Photo (c) is the surface of the split specimen with a grey colour due to surface oxidation. Figs. 6.13 and 6.14 show the fracture surface and its transgranular mode. The fractography was similar to that of E214.

4) E215 (350 °C, 1000 Pa)

- Test temperature : 352 °C

- Iodine Concentration : 1000 Pa (65 °C)

Table 6. 4 and Fig. 6.7 summarize the test results for E215. A constant load of 14.25kg was applied for the whole test duration. The SCC curve showed stage I from a velocity of $2x10^{-6}$ mm/sec at 11 MPa$\sqrt{m}$, and after 19 MPa$\sqrt{m}$ the velocity increased slowly to $2x10^{-4}$ mm/sec to enter stage II region.

Fig.6.8 Photo (d) shows the split specimen of E215 coloured gray due to oxidation and reaction with iodine. Figs. 6.15 and 6.16 show the fractography. The fracture surface was relatively flat, and showed a ductile mode mechanical rupture after 7 mm. Fig. 6.16 Photo (a) shows the initial SCC crack region at the fatigue-precrack tip. The SCC crack propagated along the basal planes inclined to the precrack surface, and the inclined SCC cracks made periodical steps between cracks. The fracture mode was transgranular with river patterns, and fluting-like morphology was very seldom observed as shown in Fig 6.16 Photo (b).

5) Summary of SCC crack propagation rate for OM40 (summary of 350 °C, 1000 PaI_2)

The SCC crack propagation rate of OM40 (recrystallized Zircaloy-4, Wah Chang) is summarized in Fig. 6.7 as a function of the stress intensity factor at a test temperature of 350 °C and an iodine pressure of 1000 Pa. The velocity vs. stress intensity curves showed the typical SCC curves which are composed of stage I (crack velocity increased rapidly with stress intensity due to occurrence of SCC), stage II (crack velocity is constant due to SCC) and stage

TABLE 6.2. SUMMARY OF TEST CONDITIONS AND RESULTS FOR E214 (OM40, 350)

OM40-4 (E214)
thickness = 0.101 cm
precrack = 0.22 cm
width = 1.3 cm

iodine = 65 C
temperature = 350 C
current = 2.50 A
Vo = 1.6578
1.6600

date of current data	elapsed time	temp (C)	volt	load(kg)	v/vo	a/b	crack,cm (DCPD)	crack(cal) cm	a/b(cal)	Ki	Ki,mean	velocity (mm/sec)
97-02-18 15:46	0	350	2.25	10	1.357	0.168	0.218	0.220	0.169	7.8	7.8	
97-02-19 12:55	1269		2.25	10	1.357	0.168	0.218	0.220	0.169	7.8	8.6	
97-02-19 12:55	1269		2.253	12	1.357	0.168	0.218	0.220	0.169	9.4	9.4	
97-02-19 13:08	1282		2.255	12	1.358	0.168	0.219	0.221	0.170	9.4	9.5	3.90E-07
97-02-19 22:55	1869		2.259	12	1.361	0.169	0.220	0.222	0.171	9.5	9.5	5.56E-07
97-02-20 9:12	2486		2.265	12	1.364	0.171	0.222	0.224	0.172	9.6	9.6	3.80E-07
97-02-20 19:12	3086		2.269	12	1.367	0.172	0.223	0.225	0.173	9.6	9.6	7.58E-07
97-02-21 5:12	3686		2.277	12	1.372	0.174	0.226	0.228	0.176	9.7	9.7	6.27E-07
97-02-21 11:14	4048		2.281	12	1.374	0.175	0.227	0.230	0.177	9.7	9.8	8.18E-07
97-02-21 17:00	4394		2.286	12	1.377	0.176	0.229	0.231	0.178	9.8	10.3	1.03E-06
97-02-21 17:55	4449		2.287	13	1.378	0.176	0.229	0.232	0.178	10.6	10.7	1.86E-06
97-02-22 1:30	4904		2.302	13	1.387	0.180	0.234	0.237	0.182	10.8	10.9	2.35E-06
97-02-22 9:25	5379		2.322	13	1.399	0.185	0.240	0.243	0.187	11.1	11.4	
97-02-22 9:25	5379		2.327	13.75	1.402	0.186	0.242	0.245	0.189	11.8	12.0	5.22E-06
97-02-22 16:16	5790		2.366	13.75	1.425	0.196	0.254	0.258	0.198	12.3	12.4	3.32E-06
97-02-22 22:16	6150		2.388	13.75	1.439	0.201	0.261	0.265	0.204	12.6	12.7	4.18E-06
97-02-23 4:16	6510		2.416	13.75	1.455	0.208	0.270	0.274	0.211	12.9	13.1	5.31E-06
97-02-23 8:16	6750		2.440	13.75	1.470	0.213	0.277	0.282	0.217	13.2	15.0	8.70E-06
97-02-24 9:05	8239		2.7	13.75	1.627	0.270	0.352	0.360	0.277	16.8	16.8	2.53E-05
97-02-24 9:18	8252		2.707	13.75	1.631	0.272	0.354	0.362	0.278	16.9	16.9	1.95E-05
97-02-24 9:30	8264		2.712	13.75	1.634	0.273	0.355	0.363	0.279	16.9	17.0	3.12E-05
97-02-24 9:42	8276		2.72	13.75	1.639	0.275	0.357	0.365	0.281	17.1	17.1	1.94E-05
97-02-24 9:54	8288		2.725	13.75	1.642	0.276	0.358	0.367	0.282	17.1	17.2	2.71E-05
97-02-24 10:06	8300		2.732	13.75	1.646	0.277	0.360	0.369	0.283	17.2	17.4	6.93E-05
97-02-24 10:18	8312		2.750	13.75	1.657	0.281	0.365	0.374	0.287	17.5	17.7	1.33E-04

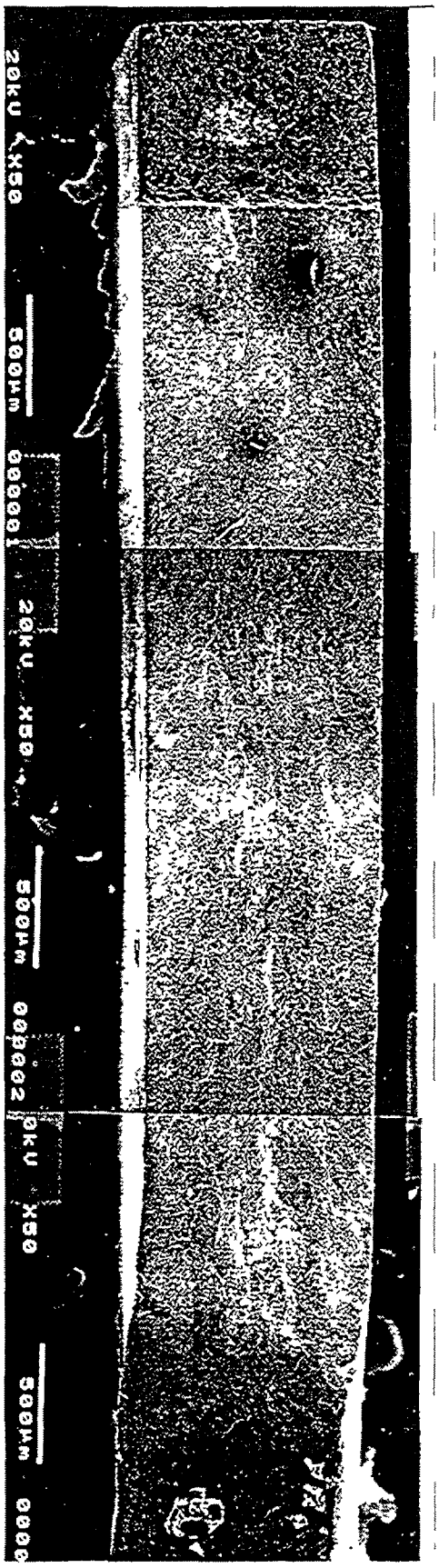

Fig. 6.11. Fracture surface of E214.

(a)

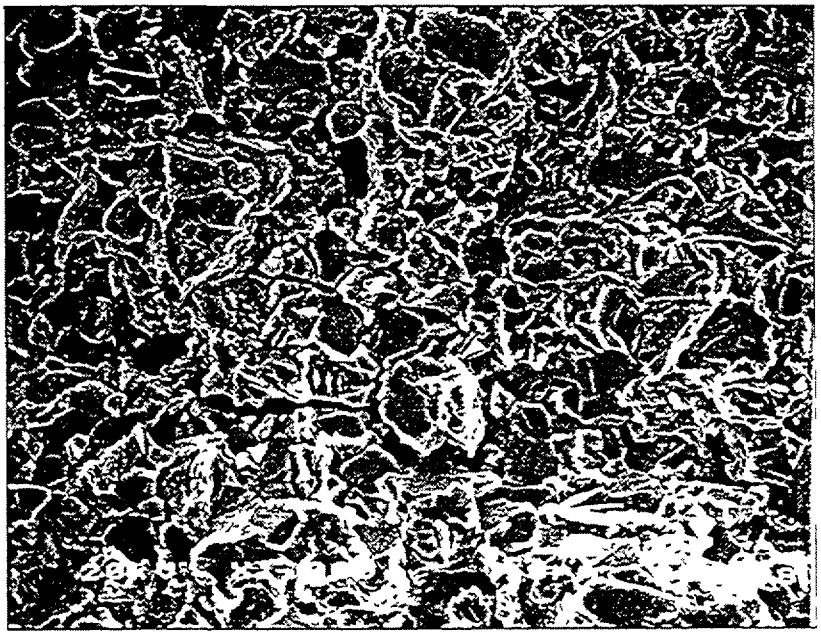

(b)

Fig 6.12. Fractographs of E214.

III (crack velocity increased rapidly again due to mechanical rupture). In these results, the SCC stage III was not measured due to the limitation of the DCPD voltage recording equipment range.

The SCC stage I in this recrystallized Zircaloy-4 (OM40) was measured from 9 MPa$\sqrt{m}$ to 19 MPa$\sqrt{m}$. The SCC crack propagation rate during the SCC stage II between 20 and 30 MPa$\sqrt{m}$ was between 4 and 7 x10^{-4} mm/sec under the test conditions of 350°C and 1000 PaI_2.

TABLE 6.3. SUMMARY OF TEST CONDITIONS AND RESULTS FOR E217 (OM40, 350°C)

OM40 (E217)

thickness = 0.101 cm
precrack = 0.205 cm
width = 1.3 cm

iodine = 63 C
temperature = 350 C
current = 2.50 A

Vo = 1.3823
1.3956

date of current data	elapsed time	temp (C)	volt	load(kg)	v/vo	a/b	crack,cm (DCPD)	crack(cal) cm	a/b(cal)	Ki	Ki,mean	velocity (mm/sec)	
97-01-28 14:55	0	346	1.837	13.7	1.329	0.156	0.202	0.205	0.158	10.2	10.3		
97-01-28 18:28	213	350	1.845	13.7	1.335	0.158	0.205	0.208	0.160	10.3	10.3		
97-01-28 22:29	454	350	1.845	13.7	1.335	0.158	0.205	0.208	0.160	10.3	10.4	5.40E-07	
97-01-29 9:14	1099		1.850	13.7	1.338	0.160	0.207	0.210	0.162	10.4	11.2		
97-01-29 9:15	1100		1.869	15.7	1.339	0.160	0.208	0.211	0.162	11.9	12.1	6.94E-06	
97-01-29 12:03	1268		1.886	15.7	1.351	0.165	0.215	0.218	0.168	12.2	12.5	8.15E-06	
97-01-29 16:29	1534		1.918	15.7	1.374	0.175	0.227	0.231	0.178	12.8	13.2	8.55E-06	
97-01-29 21:55	1860		1.96	15.7	1.404	0.187	0.243	0.248	0.190	13.5	14.1	8.87E-06	
97-01-30 5:55	2340		2.026	15.7	1.452	0.206	0.268	0.273	0.210	14.7	15.2	1.34E-05	
97-01-30 10:15	2600		2.082	15.7	1.492	0.222	0.288	0.294	0.226	15.7	16.2	2.59E-05	
97-01-30 12:26	2731		2.138	15.7	1.532	0.237	0.308	0.315	0.242	16.7	17.4	3.84E-05	
97-01-30 14:10	2835		2.206	15.7	1.581	0.254	0.331	0.338	0.260	18.0	18.6	4.07E-05	
97-01-30 15:37	2922		2.269	15.7	1.625	0.270	0.351	0.360	0.277	19.2	20.0	3.95E-05	
97-01-30 17:42	3047		2.359	15.7	1.690	0.292	0.380	0.389	0.299	20.9	21.1	4.54E-05	
97-01-30 18:10	3075		2.383	15.7	1.707	0.298	0.387	0.397	0.305	21.4	21.6	5.88E-05	
97-01-30 18:34	3099		2.41	15.7	1.727	0.304	0.395	0.405	0.312	21.9	22.1	9.03E-05	
97-01-30 18:46	3111		2.431	15.7	1.742	0.309	0.401	0.412	0.317	22.3	22.5	1.62E-04	
97-01-30 18:52	3117		2.45	15.7	1.755	0.313	0.407	0.418	0.321	22.7	23.0	2.27E-04	
97-01-30 18:58	3123		2.477	15.7	1.775	0.319	0.415	0.426	0.328	23.3	23.7	3.64E-04	
97-01-30 19:04	3129		2.521	15.7	1.806	0.329	0.427	0.439	0.338	24.2	24.8	4.84E-04	
97-01-30 19:10	3135		2.581	15.7	1.849	0.342	0.444	0.456	0.351	25.4	26.3	6.38E-04	
97-01-30 19:16	3141		2.663	15.7	1.908	0.359	0.466	0.479	0.369	27.2	28.3	7.16E-04	
97-01-30 19:22	3147		2.759	15.7	1.977	0.378	0.491	0.505	0.389	29.4	30.8	8.78E-04	
97-01-30 19:28	3153		2.883	15.7	2.066	0.401	0.522	0.537	0.413	32.3			

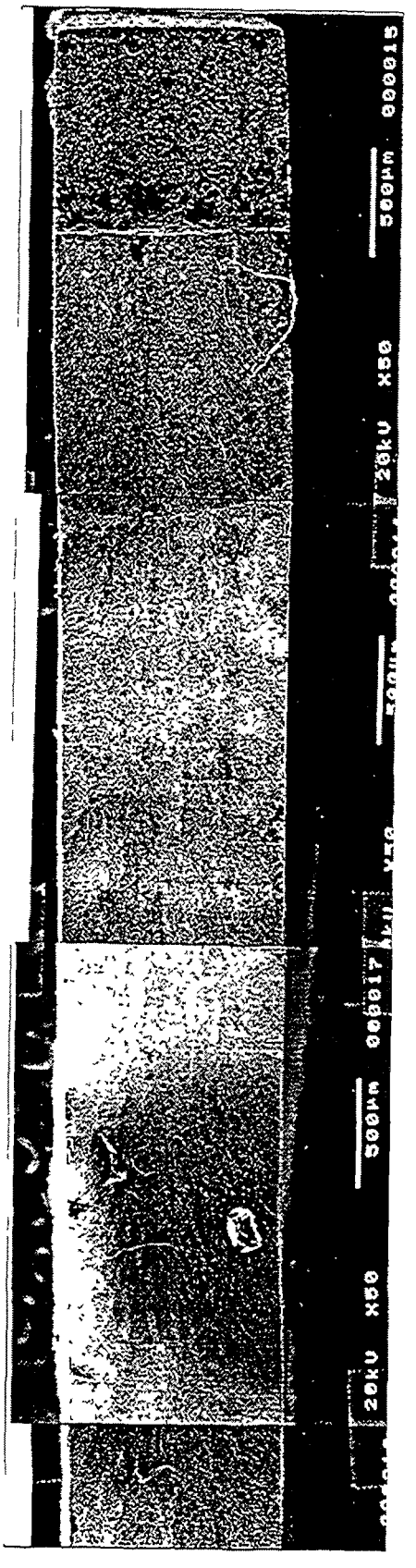

Fig. 6.13. Fracture surface of E217.

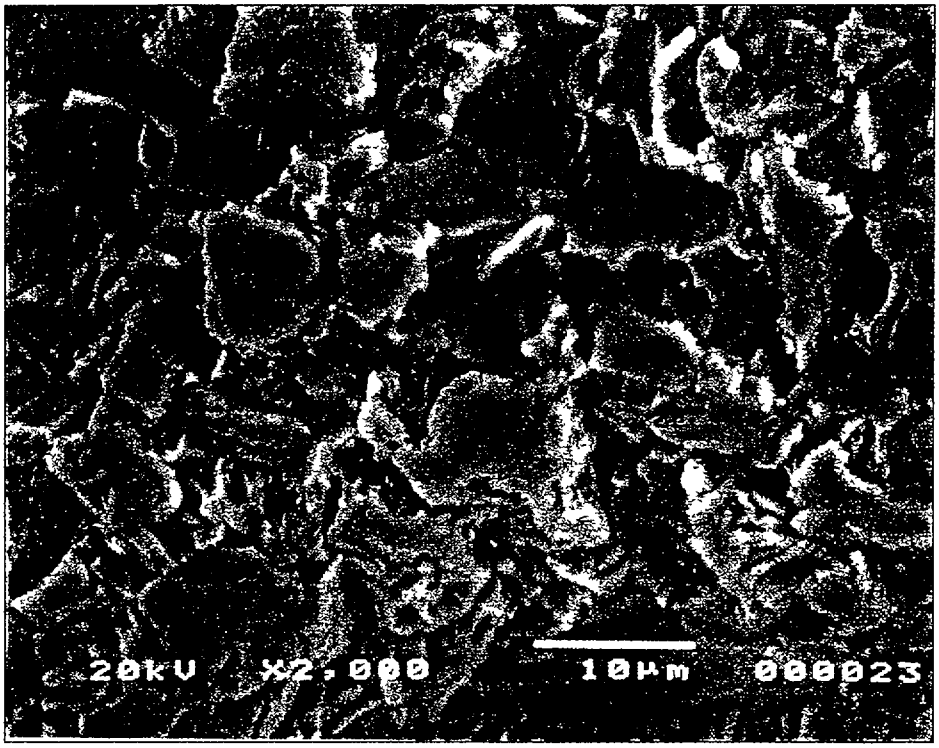

Fig. 6.14. Fractograph of E217.

The creep behaviour has an influence on the SCC velocity as shown in Fig. 6.6. The threshold value of SCC, K_{ISCC}, can be determined by a criterion of 10^{-6} mm/sec. The K_{ISCC} of the recrystallized Zircaloy-4, OM40, was about 9.5 MPa$\sqrt{m}$ at 350°C. This value was higher than the 5.4 MPa$\sqrt{m}$ value reported by Brunisholtz and Lemaignan [6.1]. who measured a recrystallized Zircaloy-4 tube by an internal pressurization method at 350°C, but was close to 9.8 MPa$\sqrt{m}$ by Knorr et al. who made measurements in the T-L direction of Zircaloy-4 plate (f=0.33) by a double cantilever beam technique at 320°C. The reason for the difference in the K_{ISCC} value is not clear, but a difference in the stress condition due to the different test methods could be one reason. In general SCC resistance is higher during uniaxial stress SCC testing than in biaxial stress testing. The SCC velocity of 4 to $7x10^{-4}$ mm/sec in the plateau region in this test is close to the result of Knorr et al. ($1x10^{-4}$ mm/sec) under uniaxial stress conditions, but much lower than the result of Brunisholtz and Lemaignan [6.1] (>$1x10^{-1}$ mm/sec) under biaxial stress conditions.

The fracture mode was mostly transgranular fracture with river patterns. The SCC crack should propagate along the basal planes, so that the transgranular surface was inclined to the fracture surface because of the 35° inclined basal planes due to the rolling process.

6.2.3. SCC propagation rate of OM41 (stress relieved Zircaloy-4, Wah Chang)

1) E240 (350 °C, 1000 Pa)

- Test temperature : 350 °C

- Iodine Concentration : 1000 Pa (67 °C)

TABLE 6.4. SUMMARY OF TEST CONDITIONS AND RESULTS FOR E215 (OM40, 350°C)

OM40-3 (E215)
thickness = 0.101 cm
precrack = 0.22 cm
width = 1.3 cm

iodine = 65 C
temperature = 353 C
current = 2.50 A
Vo = 1.5310

date of current data	elapsed time	temp (C)	volt	load(kg)	v/vo	a/b	crack,cm (DCPD)	crack(cal) cm	a/b(cal)	Ki	Ki,mean	velocity (mm/sec)
97-02-11 17:00	0	352	2.078	14.25	1.357	0.168	0.218	0.220	0.169	11.2	11.2	2.07E-06
97-02-11 19:00	120		2.082	14.25	1.360	0.169	0.219	0.221	0.170	11.2	11.3	1.86E-06
97-02-12 0:00	420		2.091	14.25	1.366	0.171	0.223	0.225	0.173	11.4	11.6	1.81E-06
97-02-12 17:00	1440		2.121	14.25	1.385	0.179	0.233	0.236	0.181	11.8	11.9	2.03E-06
97-02-12 23:00	1800		2.133	14.25	1.393	0.183	0.237	0.240	0.185	12.0	12.2	1.93E-06
97-02-13 12:00	2580		2.158	14.25	1.410	0.189	0.246	0.249	0.192	12.4	12.6	2.48E-06
97-02-14 0:00	3300		2.188	14.25	1.429	0.197	0.256	0.260	0.200	12.8	13.1	2.76E-06
97-02-14 12:00	4020		2.222	14.25	1.451	0.206	0.268	0.272	0.209	13.3	13.4	2.57E-06
97-02-14 18:00	4380		2.238	14.25	1.462	0.210	0.273	0.277	0.213	13.5	13.7	2.87E-06
97-02-15 0:00	4740		2.256	14.25	1.474	0.215	0.279	0.284	0.218	13.8	14.0	3.63E-06
97-02-15 6:00	5100		2.279	14.25	1.489	0.220	0.286	0.291	0.224	14.1	14.4	4.98E-06
97-02-15 12:00	5460		2.311	14.25	1.509	0.228	0.297	0.302	0.232	14.6	14.9	4.90E-06
97-02-15 18:00	5820		2.343	14.25	1.530	0.236	0.307	0.313	0.241	15.1	15.3	5.22E-06
97-02-15 22:00	6060		2.366	14.25	1.545	0.242	0.314	0.320	0.246	15.5	15.6	5.38E-06
97-02-16 2:00	6300		2.39	14.25	1.561	0.247	0.322	0.328	0.252	15.8	16.1	6.64E-06
97-02-16 6:00	6540		2.420	14.25	1.581	0.254	0.331	0.338	0.260	16.3	16.4	6.13E-06
97-02-16 8:00	6660		2.434	14.25	1.590	0.258	0.335	0.342	0.263	16.5	16.6	7.84E-06
97-02-16 9:00	6720		2.443	14.25	1.596	0.260	0.338	0.345	0.265	16.6	16.7	1.56E-05
97-02-16 9:30	6750		2.452	14.25	1.602	0.262	0.340	0.348	0.267	16.8	16.9	2.76E-05
97-02-16 10:00	6780		2.468	14.25	1.612	0.265	0.345	0.353	0.271	17.0	17.3	4.78E-05
97-02-16 10:30	6810		2.496	14.25	1.630	0.272	0.353	0.361	0.278	17.5	17.8	7.72E-05
97-02-16 11:00	6840		2.542	14.25	1.660	0.282	0.367	0.375	0.289	18.2	18.7	1.23E-04
97-02-16 11:24	6864		2.602	14.25	1.700	0.295	0.384	0.393	0.302	19.2	19.8	1.51E-04
97-02-16 11:48	6888		2.678	14.25	1.749	0.311	0.404	0.415	0.319	20.4	21.3	1.87E-04
97-02-16 12:12	6912		2.776	14.25	1.813	0.331	0.430	0.441	0.340	22.1	22.6	1.99E-04
97-02-16 12:24	6924		2.83	14.25	1.848	0.341	0.444	0.456	0.351	23.0	23.6	2.44E-04

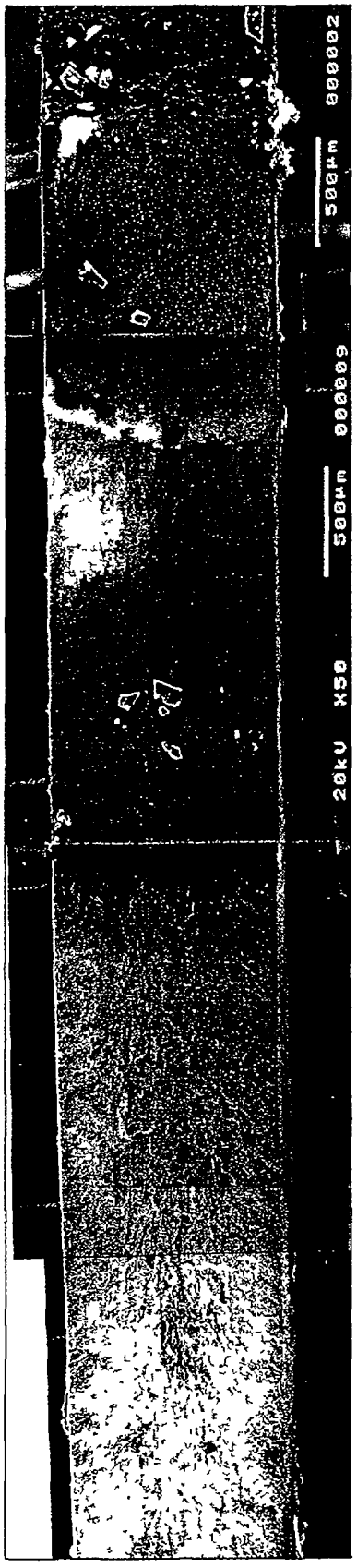

Fig 6.15. Fracture surface of E215.

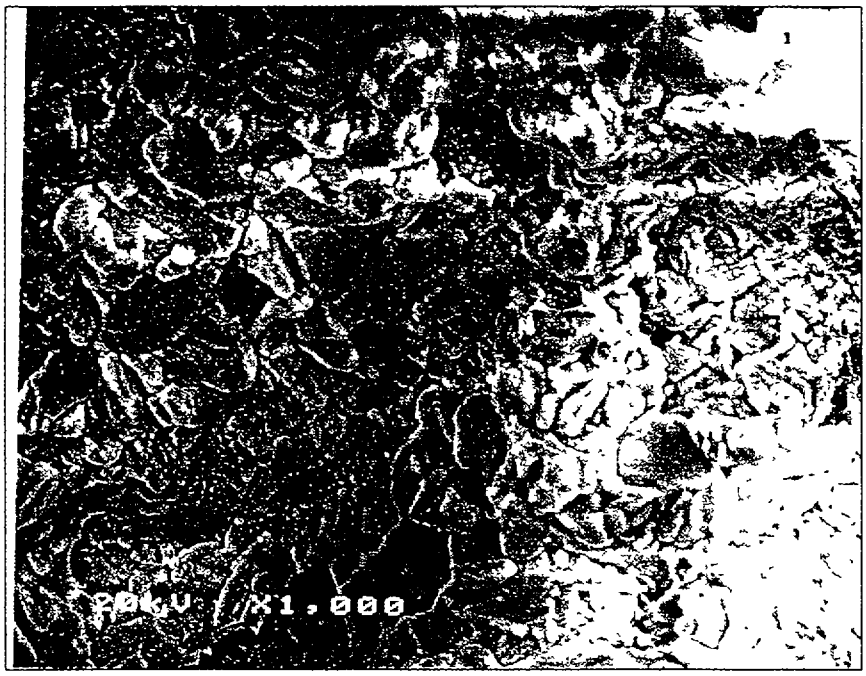

(a)

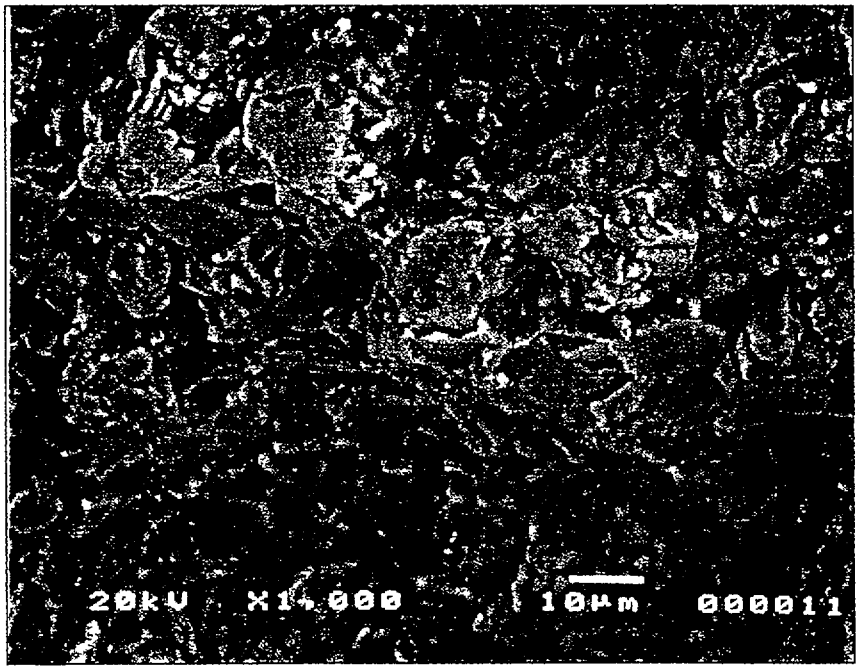

(b)

Fig. 6.16. Fractographs of E215.

Table 6.5 summarizes the results for E240. The initial load was 12 kg, and the SCC crack grew 2.9 mm after 57 hours under 13 kg loading. Fig. 6.8 Photo (e) is the specimen surface, which shows a grey colour from surface oxidation and reaction with iodine. Fig. 6.17 is an SEM photograph at the crack tip, showing surface pitting due to etching. Fig. 6.18 shows the SCC crack. The microstructure of OM41 is a stress-relieved with elongated grains due to

TABLE 6.5. SUMMARY OF TEST CONDITIONS AND RESULTS FOR E240 (OM41, 350°C)

OM41-3 (E240)
thickness = 0.102 cm
precrack = 0.205 cm
width = 1.298 cm

iodine = 67 C
temperature = 349.5 C
current = 2.50 A

Vo = 1.4828

date of current data	elapsed time	temp (C)	volt	load(kg)	v/vo	a/b	crack,cm (DCPD)	rack(cal cm	a/b(cal	Ki	Ki,mean	velocity (mm/sec)
97-03-24 23:51	0	349.5	1.9714	12	1.330	0.156	0.203	0.205	0.158	8.9	8.9	4.80E-07
97-03-25 8:55	544		1.975	12	1.332	0.157	0.204	0.207	0.159	8.9	9.0	2.14E-06
97-03-25 13:26	815		1.983	12	1.337	0.159	0.207	0.210	0.162	9.0	9.4	
97-03-25 13:27	816		1.987	13	1.340	0.160	0.208	0.212	0.163	9.8	9.9	
97-03-25 14:38	887		1.994	13	1.344	0.162	0.211	0.215	0.165	9.9	10.0	4.56E-06
97-03-25 16:25	994		2.000	13	1.349	0.164	0.213	0.218	0.168	10.0	10.1	3.00E-06
97-03-25 20:56	1265		2.012	13	1.357	0.167	0.218	0.222	0.171	10.2	10.4	6.72E-06
97-03-26 0:56	1505		2.035	13	1.372	0.174	0.226	0.232	0.179	10.6	10.8	1.00E-05
97-03-26 3:56	1685		2.0603	13	1.390	0.181	0.235	0.243	0.187	10.9	11.3	1.05E-05
97-03-26 9:09	1998		2.108	13	1.422	0.194	0.252	0.263	0.202	11.7	12.0	1.17E-05
97-03-26 13:13	2242		2.151	13	1.450	0.206	0.267	0.280	0.215	12.3	12.5	1.43E-05
97-03-26 14:41	2330		2.170	13	1.463	0.211	0.274	0.287	0.221	12.6	12.9	1.79E-05
97-03-26 16:36	2445		2.201	13	1.485	0.219	0.284	0.300	0.231	13.1	13.2	1.40E-05
97-03-26 17:36	2505		2.214	13	1.493	0.222	0.289	0.305	0.235	13.3	13.9	1.81E-05
97-03-26 21:36	2745		2.283	13	1.540	0.240	0.311	0.331	0.255	14.4	14.8	1.91E-05
97-03-26 23:36	2865		2.3204	13	1.565	0.249	0.323	0.345	0.265	15.1	15.2	1.92E-05
97-03-27 0:36	2925		2.339	13	1.578	0.253	0.329	0.351	0.271	15.4	15.6	2.28E-05
97-03-27 1:36	2985		2.362	13	1.593	0.259	0.336	0.360	0.277	15.7	16.0	2.63E-05
97-03-27 2:36	3045		2.389	13	1.611	0.265	0.345	0.369	0.284	16.2	16.5	2.97E-05
97-03-27 3:36	3105		2.419	13	1.632	0.272	0.354	0.380	0.293	16.7	17.1	4.01E-05
97-03-27 4:36	3165		2.461	13	1.660	0.282	0.366	0.394	0.304	17.4	17.9	4.74E-05

TABLE 6.5 (CONT.)

97-03-27 5:36	3225		2.512	13	1.694	0.293	0.381	0.411	0.317	18.3	18.8	4.87E-05
97-03-27 6:36	3285		2.565	13	1.730	0.305	0.396	0.429	0.330	19.3	20.0	6.41E-05
97-03-27 7:36	3345		2.637	13	1.778	0.320	0.416	0.452	0.348	20.6	21.9	8.76E-05
97-03-27 8:52	3421		2.768	13	1.867	0.347	0.451	0.492	0.379	23.2		
	off						0.451	0.492				

* 0.492: measured crack length

* 0.451/0.492: this value is used for correcting the crack length in following sheet in which specimen is fully splitted after test not to measure the real crack length

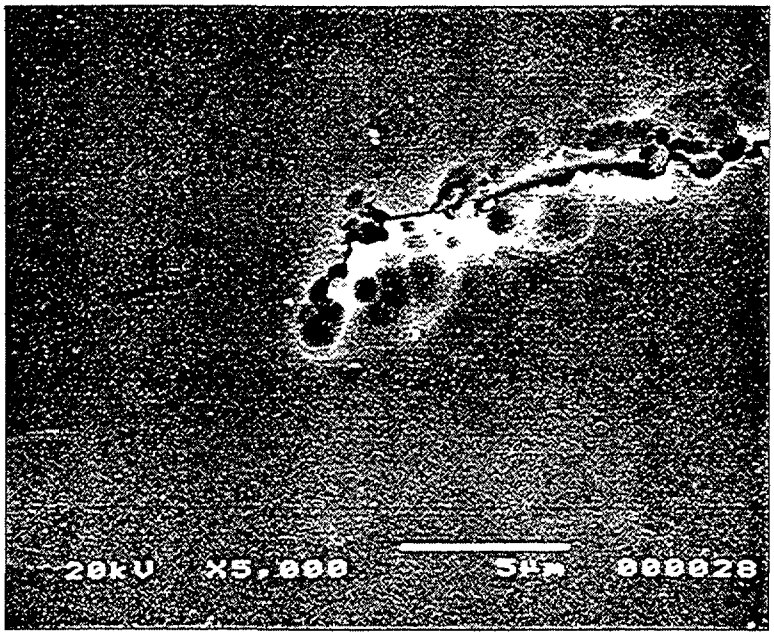

Fig. 6.17. SEM morphology at crack tip of E240.

the rolling process. The SCC crack propagated with changes in direction rather than being straight. The COD of the SCC crack in the stress relieved OM41 was small in comparison with that for recrystallized OM40.

Fig. 6.19 shows the SCC crack velocity as a function of stress intensity factor, indicating the typical SCC curve. The SCC velocity was $5x10^{-7}$ mm/sec at the initial stress intensity of 8.9 MPa$\sqrt{m}$, and increased rapidly with increasing stress intensity (SCC stage I). The SCC stage II (plateau region) appeared after 17 MPa$\sqrt{m}$.

2) E246 (350 °C, 1000 Pa)

- Test temperature : 349 °C

- Iodine Concentration : 1000 Pa (65 °C)

Table 6.6 summarizes the results for E246. The specimen was completely split after 74 hours under 13.5 kg loading. The SCC velocity in Fig. 6.19 was $1.4x10^{-6}$ mm/sec at the initial stress intensity of 9.2 MPa$\sqrt{m}$, and increased rapidly up to 16 MPa$\sqrt{m}$. The SCC velocity in the SCC stage II region after 18 MPa$\sqrt{m}$ was $7x10^{-4}$ mm/sec.

Fig. 6.20 is the fracture surface. The stress relieved OM41 showed secondary crack-like valleys along the crack direction, rather than the flat surface as in the recrystallized OM40. Fig. 6.21 Photo (a) is a fractograph at the boundary between the precrack and the SCC crack showing the secondary cracks. The secondary cracks were formed between the inclined transgranular SCC fracture regions which were caused by inclined basal planes in the textured structure. The ductile tearing mode as shown in OM40 was not observed between the precrack tip and the SCC region in OM41. Fig. 6.21 Photos (b) and (c) are typical fractographs in SCC stage I and II, respectively. The fracture mode was similar in both stages I and II. On the rolled

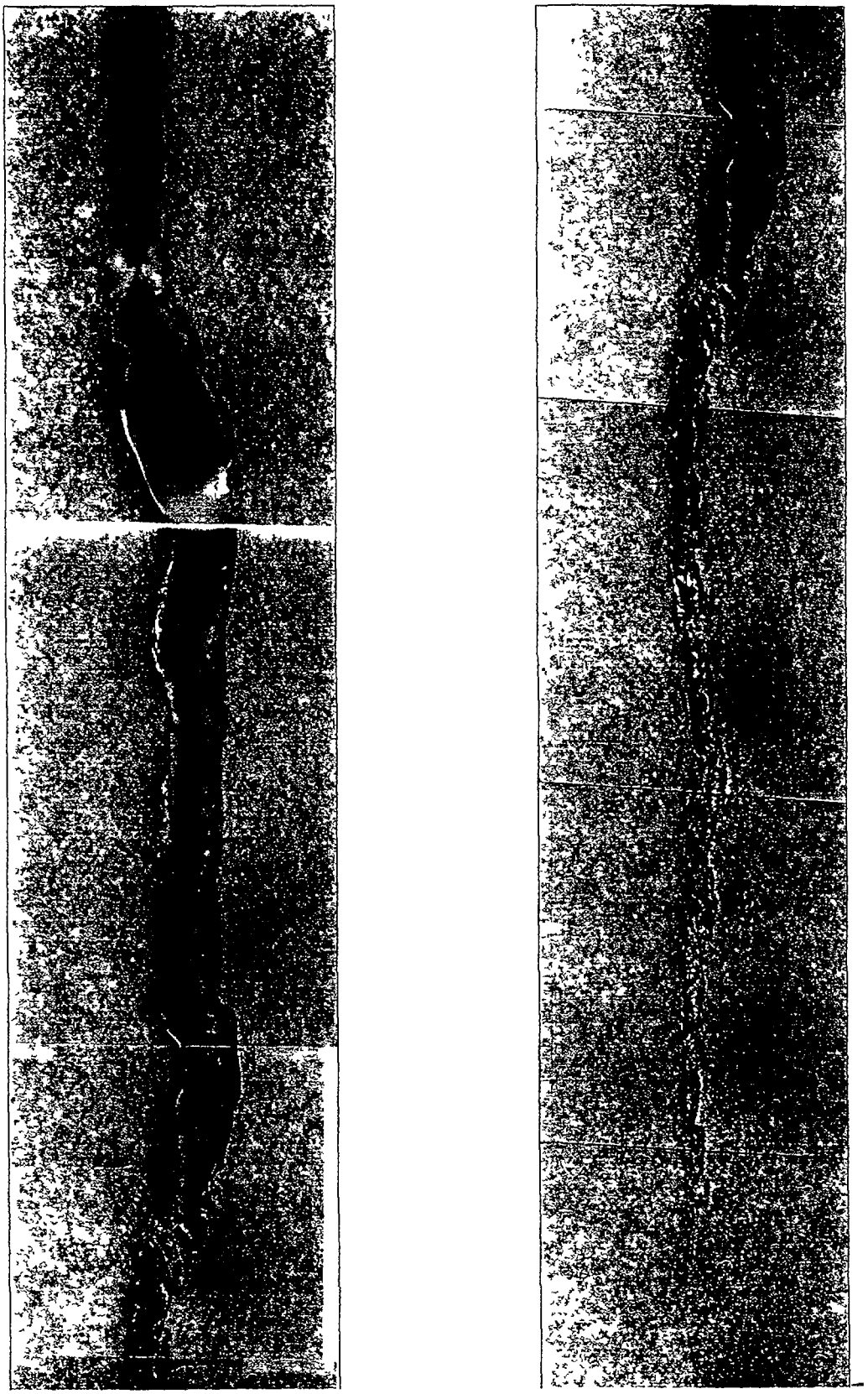

Fig. 6.18 SCC crack morphology of E240.

structure it wasn't possible to distinguish if the fracture mode was transgranular or intergranular. The fracture surfaces were elongated along the SCC crack direction, and inclined from the overall crack surface due to the inclined basal plane in the textured structure.

3) E268 (350 °C, 1000 Pa)

- Test temperature : 350 °C

- Iodine Concentration : 1000 Pa (65 °C)

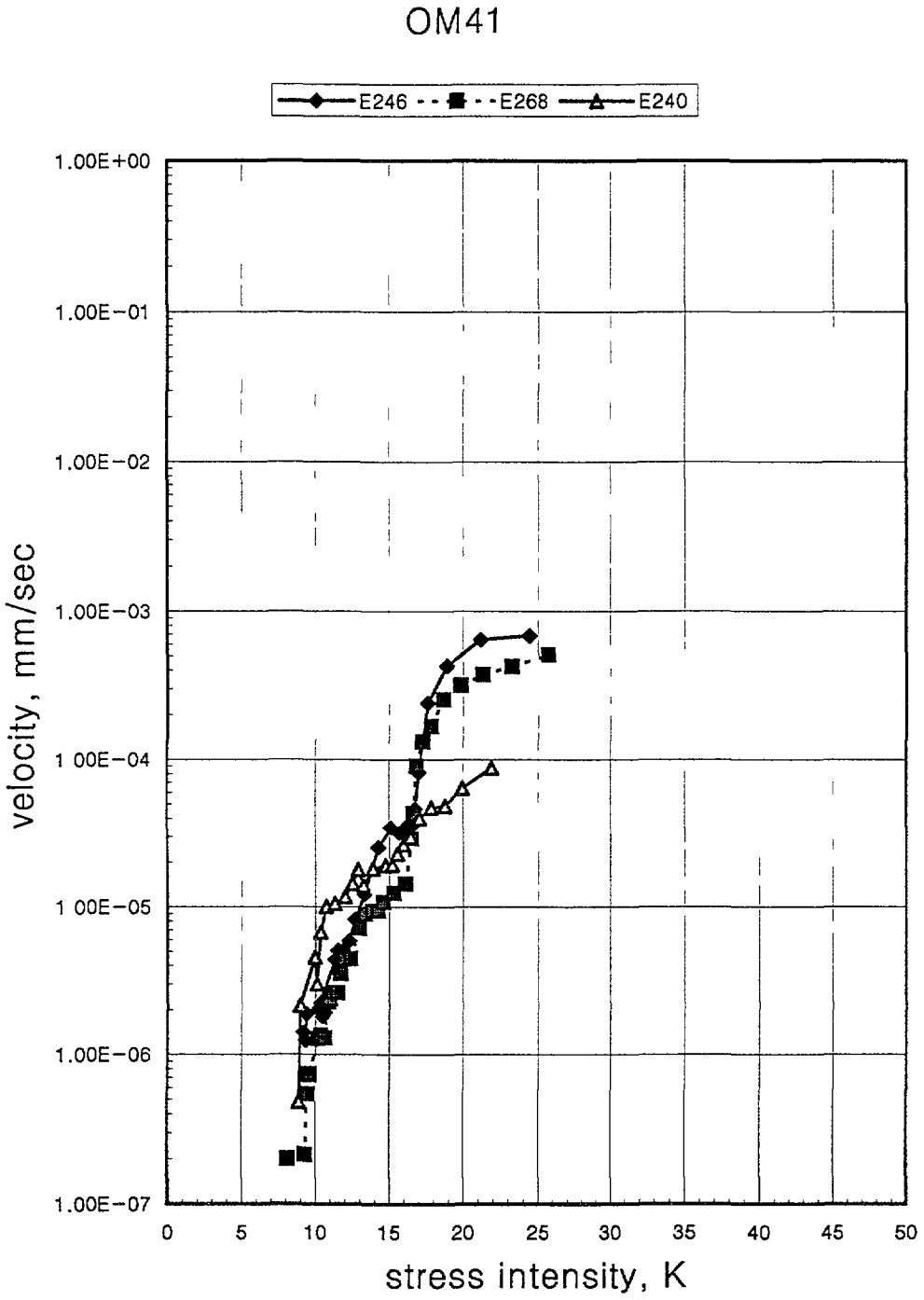

Fig. 6.19. The SCC propagation rate of OM41 as a function of stress intensity factor (350 ℃).

TABLE 6.6. SUMMARY OF TEST CONDITIONS AND RESULTS FOR E246 (OM41, 350°C)

OM41-1 (E246)
thickness = 0.102 cm
precrack = 0.214 cm
width = 1.297 cm

iodine = 65 C
temperature = 349 C
current = 2.50 A

Vo = 1.4241

date of current data	elapsed time	temp (C)	volt	load(kg)	v/vo	a/b	crack,cm (DCPD)	crack(cal) cm	a/b(cal)	Ki	Ki,mean	velocity (mm/sec)
97-03-05 18:04	0	349	1.918	12	1.347	0.163	0.212	0.214	0.165	9.2	9.2	1.42E-06
97-03-06 1:08	424	349	1.926	12	1.352	0.166	0.215	0.218	0.168	9.3	9.3	1.25E-06
97-03-06 9:08	904	349	1.934	12	1.358	0.168	0.218	0.221	0.171	9.4	9.4	1.88E-06
97-03-06 13:06	1142	349	1.94	13	1.362	0.170	0.221	0.224	0.173	10.3	10.4	2.22E-06
97-03-06 18:40	1476	349	1.950	13	1.369	0.173	0.224	0.228	0.176	10.4	10.5	1.80E-06
97-03-07 0:08	1804	349	1.958	13	1.375	0.175	0.228	0.232	0.179	10.6	10.7	1.93E-06
97-03-07 9:01	2337	349	1.972	13	1.385	0.179	0.233	0.238	0.184	10.8	10.2	2.04E-06
97-03-07 13:11	2587	349	1.979	13.5	1.390	0.181	0.235	0.241	0.186	11.3	11.4	4.39E-06
97-03-07 15:07	2703		1.986	13.5	1.395	0.183	0.238	0.244	0.188	11.4	11.5	5.06E-06
97-03-07 18:27	2903		2.000	13.5	1.404	0.187	0.243	0.250	0.193	11.7	11.9	5.10E-06
97-03-08 1:00	3296		2.028	13.5	1.424	0.195	0.254	0.262	0.202	12.1	12.3	5.89E-06
97-03-08 5:00	3536		2.048	13.5	1.438	0.201	0.261	0.271	0.209	12.5	12.7	8.24E-06
97-03-08 8:57	3773		2.076	13.5	1.458	0.208	0.271	0.282	0.218	12.9	13.3	1.21E-05
97-03-08 13:06	4022		2.120	13.5	1.489	0.220	0.286	0.301	0.232	13.7	14.3	2.52E-05
97-03-08 16:00	4196		2.186	13.5	1.535	0.238	0.309	0.327	0.252	14.8	15.1	3.46E-05
97-03-08 17:00	4256		2.218	13.5	1.557	0.246	0.320	0.339	0.262	15.4	15.7	3.19E-05
97-03-08 18:00	4316		2.248	13.5	1.579	0.254	0.330	0.351	0.270	15.9	16.3	3.56E-05
97-03-08 19:00	4376		2.282	13.5	1.602	0.262	0.341	0.364	0.280	16.6	16.6	3.63E-05
97-03-08 19:12	4388		2.289	13.5	1.607	0.264	0.343	0.366	0.282	16.7	16.8	4.64E-05
97-03-08 19:24	4400		2.298	13.5	1.614	0.266	0.346	0.370	0.285	16.9	17.0	8.20E-05
97-03-08 19:36	4412		2.314	13.5	1.625	0.270	0.351	0.375	0.289	17.2	17.6	2.42E-04
97-03-08 19:48	4424		2.362	13.5	1.659	0.281	0.366	0.393	0.303	18.1	18.9	4.29E-04
97-03-08 20:00	4436		2.450	13.5	1.720	0.302	0.392	0.424	0.327	19.8	21.2	6.45E-04
97-03-08 20:12	4448		2.590	13.5	1.819	0.333	0.432	0.470	0.363	22.6	24.4	6.86E-04
97-03-08 20:24	4460		2.750	13.5	1.931	0.365	0.475	0.520	0.401	26.2	13.1	

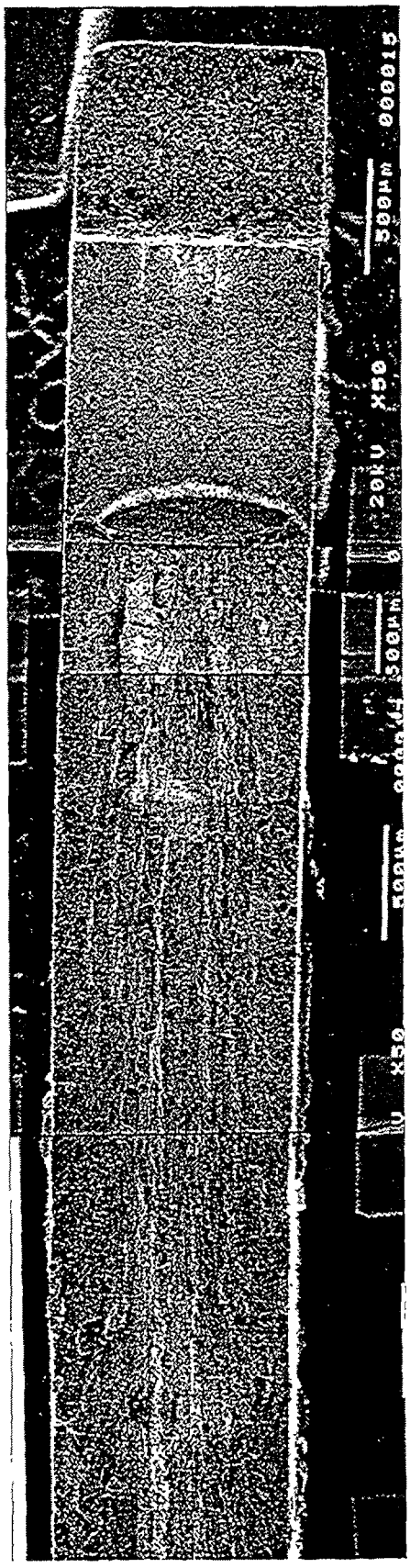

Fig. 6.20. Fracture surface of E246.

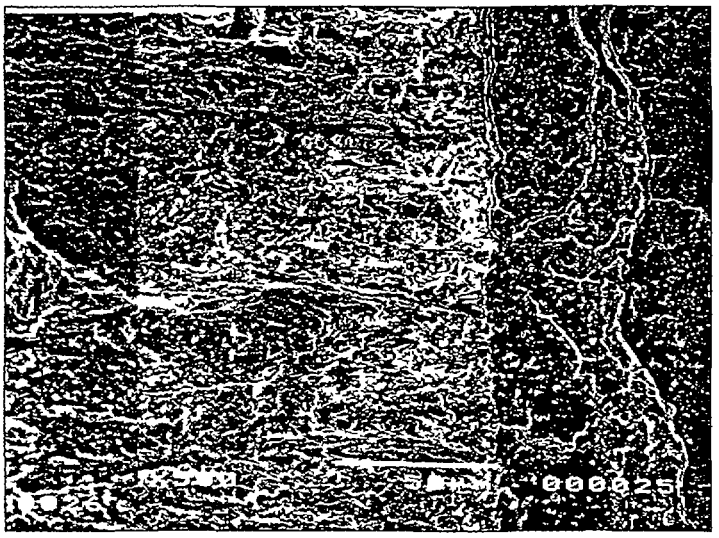

(a)

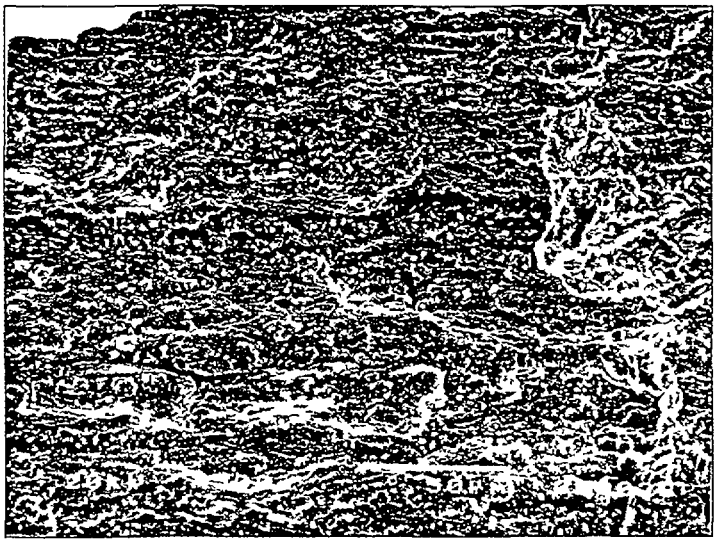

(b)

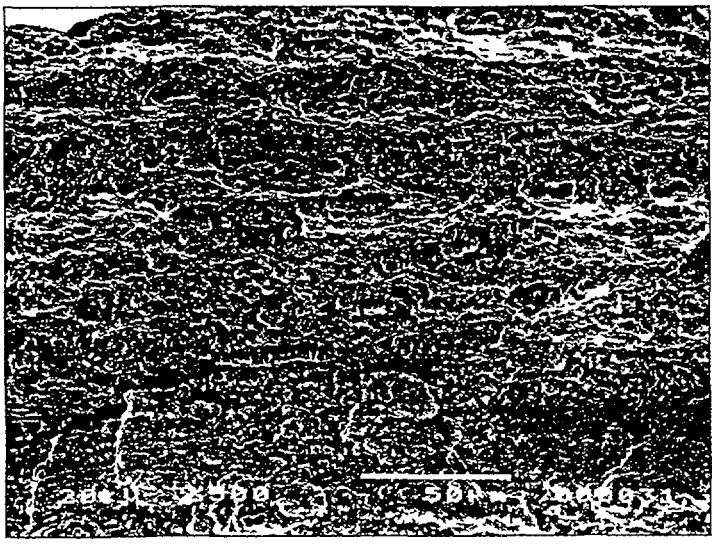

(c)

Fig 6 21. Fractographs of E246

Table 6.7 summarizes the results for E268. The specimen was completely split after 200 hours under 13 kg loading. The SCC crack velocity started from $2x10^{-7}$ mm/sec at 8.1 MPa$\sqrt{m}$, and after 18 MPa$\sqrt{m}$ the stage II appeared with a plateau velocity of $5x10^{-4}$ mm/sec, as shown in Fig. 6.19.

Fig. 6.8 Photo (f) shows the split specimen, and Fig. 6.22, the fracture surface. The morphologies were typical of SCC fractographs.

4) Summary of SCC crack propagation rate for OM41 (summary of 350 °C, 1000 PaI_2)

The results on stress relieved Zircaloy-4 (OM41) are summarized in Fig. 6.19. The SCC crack propagation rate of SRA Zircaloy-4 showed the typical SCC curve such as a stress intensity-dependent region (stage I) and a stress intensity independent region (plateau stage II).

The threshold stress intensity of SCC (K_{ISCC}) in SRA Zircaloy-4 (OM41) was about 9 MPa$\sqrt{m}$ at 350 °C. The crack propagation rate in the SCC stage II region was increased to between 5 and 7 $x10^{-4}$ mm/sec above 18 MPa$\sqrt{m}$.

The 9 MPa$\sqrt{m}$ of K_{ISCC} was higher than the 3.4 MPa$\sqrt{m}$, and the SCC velocity was lower than the 1E-3 mm/sec which were obtained by Brunisholtz and Lemaignan [6.1] using an internal pressurization method with SRA Zircaloy-4 tubes. The difference in test methods could account for the different values, for the same reasons as discussed for OM40.

In comparison with RX Zircaloy-4 (OM40), SRA Zircaloy-4 (OM41) was more sensitive to SCC, resulting in a lower threshold SCC stress intensity factor and a little higher SCC velocity. Brunisholtz and Lemaignan [6.1] reported the same result, that the threshold SCC value was lower in SRA than in RX Zircaloy-4. It is, however, known that the threshold stress intensity for SCC is low in RX Zircaloy-4, but the failure strain is higher than for SRA Zircaloy-4 because the RX Zircaloy-4 has lower tensile strength. These results suggest that the evaluation of SCC should be considered in respect of both threshold stress and propagation rate.

6.2.4. SCC propagation rate of OM44 (recrystallized Zircaloy-2, Cezus)

1) E283 (350 °C, 1000 Pa)

- Test temperature : 350 °C

- Iodine Concentration : 1000 Pa (65 °C)

The test started from an initial loading of 13 kg, but stopped at 19.25 kg loading after 135 hours because the DCPD power lines became detached (details in Table 6.8).

The SCC crack velocity is shown in Fig. 6.23 as a function of stress intensity. The SCC velocity was of the order of 10^{-7} mm/sec at between 8 and 11 MPa$\sqrt{m}$. Above 11 MPa$\sqrt{m}$ the velocity increased rapidly with stress intensity to show stage I.

Fig. 6.8 Photo (g) is the surface of the specimen, and Fig. 6.24 is a fractograph after splitting at liquid nitrogen temperatures. The SCC crack length was 0.2 mm. The fracture surface of OM44 in Fig. 6.25 was similar to OM40, and showed equiaxed interganular and transgranular grains with some residual ductile webs.

TABLE 6.7. SUMMARY OF TEST CONDITIONS AND RESULTS FOR E268 (350°C)

OM41-2 (E268)
thickness = 0.102 cm
precrack = 0.205 cm
width = 1.298 cm

iodine = 65 C
temperature = 350 C
current = 2.50 A

Vo = 1.4802
1.4908

date of current data	elapsed time	temp (C)	volt	oad(kg	v/vo	a/b	rack,c (DCPD	rack(cal cm	/b(cal	Ki	Ki,mean	velocity (mm/sec)
97-03-11 18:11	0	350	1.968	10	1.330	0.156	0.203	0.205	0.158	7.4	7.8	
97-03-12 16:30	1339		1.968	11	1.330	0.156	0.203	0.205	0.158	8.1	8.1	2.01E-07
97-03-13 16:38	2787		1.972	11	1.332	0.157	0.204	0.207	0.159	8.2	8.7	
97-03-13 16:39	2788		1.987	12.5	1.333	0.157	0.204	0.207	0.160	9.3	9.3	2.14E-07
97-03-14 9:29	3798		1.99	12.5	1.335	0.158	0.206	0.208	0.161	9.3	9.4	
97-03-14 12:38	3987		1.997	12.5	1.339	0.160	0.208	0.211	0.163	9.4	9.5	5.43E-07
97-03-14 18:21	4330		1.999	12.5	1.341	0.161	0.209	0.212	0.164	9.5	9.5	7.31E-07
97-03-15 9:20	5229		2.009	12.5	1.347	0.163	0.212	0.216	0.167	9.6	9.6	7.39E-07
97-03-15 12:04	5393		2.010	13	1.348	0.164	0.213	0.217	0.167	10.0	10.0	
97-03-15 13:29	5478		2.014	13	1.351	0.165	0.214	0.219	0.168	10.1	10.3	1.28E-06
97-03-16 13:31	6920		2.040	13	1.368	0.172	0.224	0.230	0.177	10.5	10.6	1.29E-06
97-03-17 9:13	8102		2.062	13	1.383	0.178	0.232	0.239	0.184	10.8	10.9	2.32E-06
97-03-17 17:10	8579		2.078	13	1.394	0.183	0.238	0.246	0.189	11.0	11.2	2.62E-06
97-03-18 3:10	9179		2.101	13	1.409	0.189	0.246	0.255	0.196	11.4	11.6	3.01E-06
97-03-18 13:32	9801		2.129	13	1.428	0.197	0.256	0.266	0.205	11.8	11.9	4.42E-06
97-03-18 17:31	10040		2.145	13	1.438	0.201	0.261	0.273	0.210	12.1	12.4	4.45E-06
97-03-19 3:31	10640		2.185	13	1.466	0.211	0.275	0.289	0.222	12.7	13.0	7.16E-06
97-03-19 9:05	10974		2.222	13	1.490	0.221	0.287	0.303	0.233	13.3	13.7	9.27E-06
97-03-19 15:37	11366		2.280	13	1.529	0.236	0.306	0.325	0.250	14.2	14.6	1.05E-05
97-03-19 20:00	11629		2.325	13	1.559	0.247	0.321	0.341	0.263	14.9	15.3	1.24E-05
97-03-20 0:00	11869		2.374	13	1.592	0.259	0.336	0.359	0.277	15.7	16.1	1.44E-05
97-03-20 3:00	12049		2.418	13	1.622	0.269	0.350	0.375	0.289	16.5	16.8	5.45E-05

TABLE 6.7. (CONT.)

97-03-20 3:36	12085		2.452	13	1.645	0.277	0.360	0.387	0.298	17.0	17.3	1.33E-04
97-03-20 3:48	12097		2.480	13	1.664	0.283	0.368	0.396	0.305	17.5	17.8	1.68E-04
97-03-20 4:00	12109		2.516	13	1.688	0.291	0.378	0.408	0.315	18.2	18.7	2.56E-04
97-03-20 4:12	12121		2.572	13	1.725	0.303	0.394	0.427	0.329	19.2	19.8	3.19E-04
97-03-20 4:24	12133		2.644	13	1.774	0.319	0.414	0.450	0.346	20.5	21.3	3.75E-04
97-03-20 4:36	12145		2.732	13	1.833	0.337	0.438	0.477	0.367	22.2	23.2	4.25E-04
97-03-20 4:48	12157		2.836	13	1.902	0.357	0.464	0.507	0.391	24.3	25.7	5.11E-04
97-03-20 5:00	12169		2.968	13	1.991	0.382	0.496	0.544	0.419	27.2		
97-03-20 9:00	12409			13								
	off		split				0.451	0.492				

* 0.451/0.492: this value is used for correcting the crack length
the value is come from the correcting factor for E240

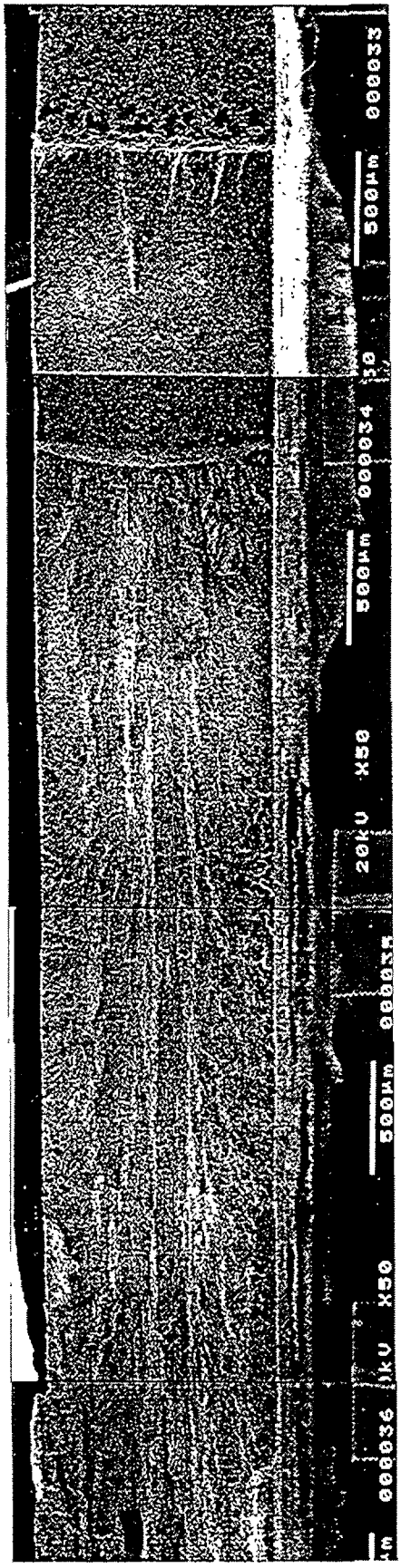

Fig. 6.22. Fracture surface of E268.

TABLE 6.8. SUMMARY OF TEST CONDITIONS AND RESULTS FOR E283 (350°C)

OM44-T2-1 (E283)

thickness = 0.12 cm
precrack = 0.205 cm
width = 1.298 cm

iodine = 65 C
temperature = 350 C
current = 2.50 A

Vo = 1.27
1.27

date of current data	elapsed time	temp (C)	volt	oad(kg	v/vo	a/b	rack,c (DCPD	ack(ca cm	/b(cal	Ki	Ki,mean	velocity (mm/sec)
97-04-02 18:33	0	350	1.694	13	1.33	0.16	0.20	0.21	0.2	8.2	8.2	6.07E-07
97-04-03 13:05	1112		1.702	13	1.34	0.16	0.21	0.21	0.2	8.3	8.9	5.01E-07
97-04-03 18:41	1448		1.704	15	1.34	0.16	0.21	0.21	0.2	9.6	9.6	
97-04-03 18:53	1460		1.707	15	1.34	0.16	0.21	0.21	0.2	9.6	9.7	4.92E-07
97-04-04 9:04	2311		1.712	15	1.34	0.16	0.21	0.21	0.2	9.7	10.0	3.87E-07
97-04-04 13:45	2592		1.713	16	1.34	0.16	0.21	0.21	0.2	10.4	10.4	
97-04-04 13:53	2600		1.715	16	1.34	0.16	0.21	0.21	0.2	10.4	10.4	6.31E-07
97-04-04 17:51	2838		1.716	16	1.35	0.16	0.21	0.22	0.2	10.4	10.5	3.45E-07
97-04-05 10:20	3827		1.720	16	1.35	0.16	0.21	0.22	0.2	10.5	10.6	4.02E-07
97-04-05 17:13	4240		1.7261	16	1.35	0.17	0.22	0.22	0.2	10.6	10.6	1.04E-07
97-04-06 10:28	5275		1.727	16	1.36	0.17	0.22	0.22	0.2	10.6	10.7	5.10E-07
97-04-06 17:30	5697		1.730	16	1.36	0.17	0.22	0.22	0.2	10.7	10.9	1.61E-07
97-04-07 8:56	6623		1.732	16.5	1.36	0.17	0.22	0.22	0.2	11.1	11.2	1.64E-06
97-04-07 10:37	6724		1.734	17	1.36	0.17	0.22	0.22	0.2	11.4	11.5	1.40E-06
97-04-07 17:59	7166		1.741	17	1.37	0.17	0.22	0.23	0.2	11.6	11.5	
97-04-08 9:03	8070		1.746	19.25	1.37	0.17	0.22	0.23	0.2	13.2	13.3	2.42E-05
97-04-08 9:30	8097		1.754	19.25	1.38	0.18	0.23	0.23	0.2	13.4	13.5	2.72E-05
97-04-08 9:48	8115		1.760	19.25	1.38	0.18	0.23	0.24	0.2	13.5		
PL failure												
	off						0.45	0.49				

* 0.451/0.492: this value is used for correcting the crack length
the value is come from the correcting factor for E240

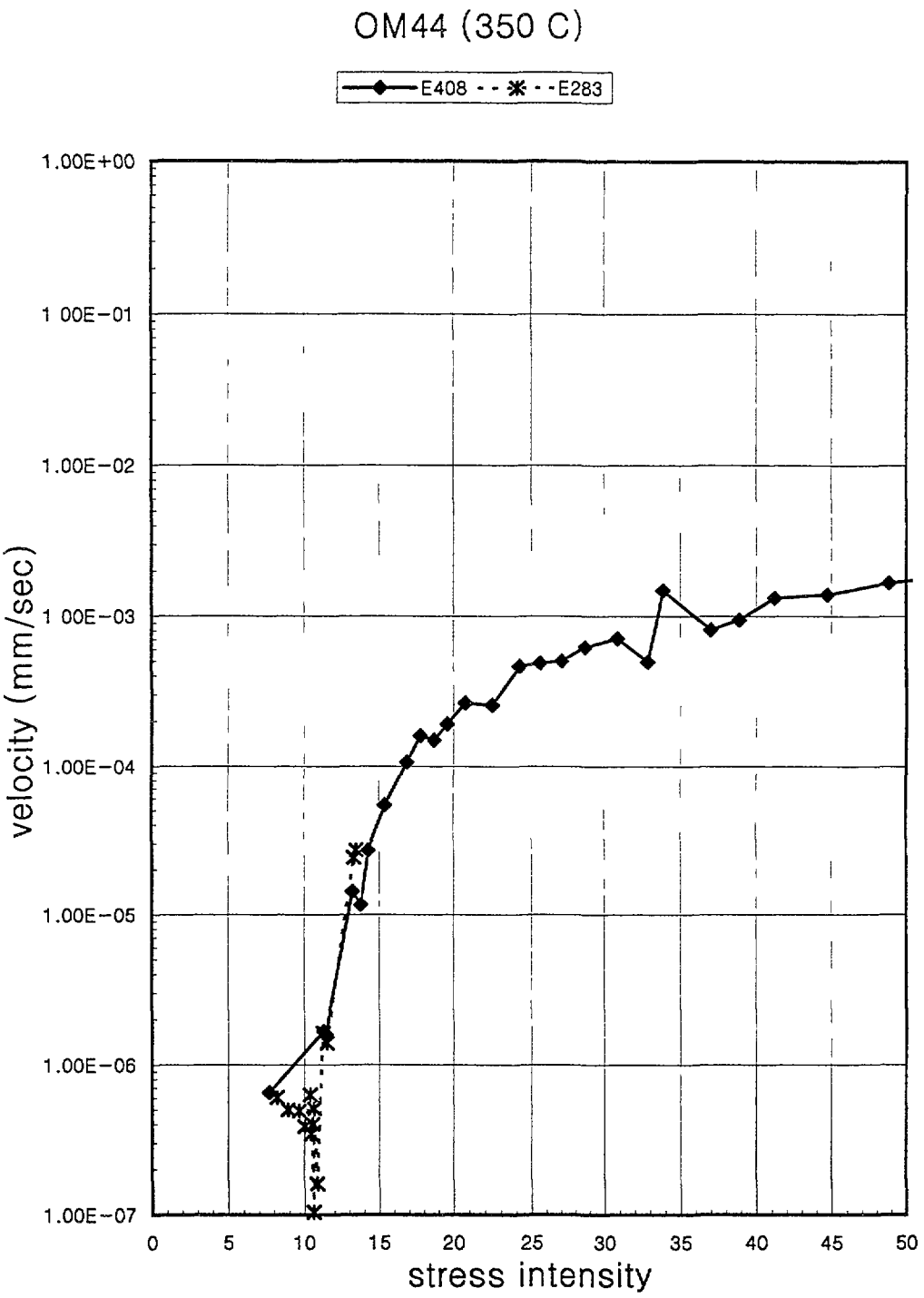

Fig 6.23. The SCC propagation rate of OM44 as a function of stress intensity factor (350 ℃)

2) E408 (350 °C, 1000 Pa)

- Test temperature : 349 °C

- Iodine Concentration : 1000 Pa (60 °C)

The SCC velocity as a function of stress intensity is shown in Fig. 6.23. The initial load was 14.5 kg, and the final load was 23 kg Below 10 MPa$\sqrt{m}$, the velocity was in the creep

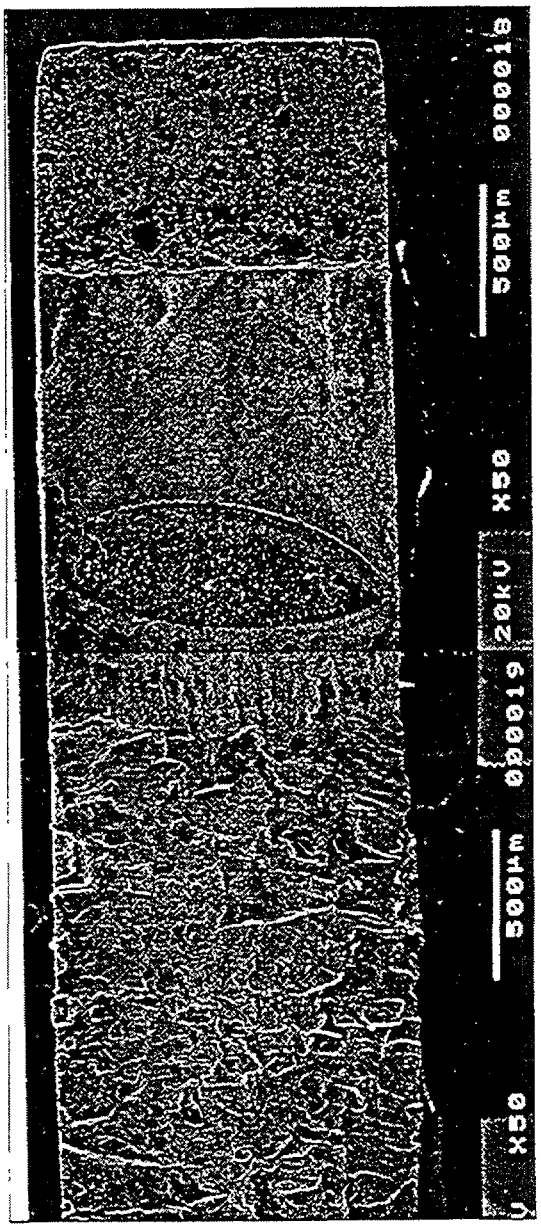

Fig. 6.24. Fracture surface of E283.

range. From 11 MPa√m, the velocity increased rapidly, and after 20 MPa√m the velocity became flat at $1x10^{-3}$ mm/sec. Allowing for creep, the K_{ISCC} was 11 MPa√m. The velocity was between 2 and $7x10^{-4}$ mm/sec between 20 and 30 MPa√m. These results indicated that the SCC resistivity of the RX Zircaloy-2 (OM44) was similar to or a little higher than the RX Zircaloy-4 (OM40).

6.2.5. Effect of texture on SCC propagation rate

6.2.5.1 T-L orientation

1) J037 (350 °C, 1000 Pa)

- Test temperature: 350 °C

- Iodine concentration: 1000 Pa

Fig. 6.25. Fractograph of E283.

In the T-L orientation the SCC crack propagates relatively easily along the basal planes inclined about 35° to the crack, because the basal plane is parallel to the crack direction in spite of 35° incline. The velocity vs. stress intensity curve at 350 °C is similar to the previous results of OM40 or OM41, as shown in Fig. 6.26. The initial load was 10 kg, and finished at 12 kg. The crack velocity increased rapidly with stress intensity above 10 MPa$\sqrt{m}$, and then showed the plateau region above about 20 MPa$\sqrt{m}$. The plateau region seemed to be divided into two stages: 8 to 9 x 10^{-4} mm/sec in the range of 20 to 35 MPa$\sqrt{m}$ and 3 x 10^{-3} mm/sec above 40 MPa$\sqrt{m}$. The fracture surface was similar to that for the SRA Zircaloy-4 (OM41). The subcracks between the inclined fracture facets were parallel to the crack direction as shown in Fig. 6.27, consistent with the basal plane array.

2) J026 (300 °C, 1000 Pa)

- Test temperature: 300 °C

- Iodine concentration: 1000 Pa

The SCC behaviour for the T-L orientation at 300 °C is shown in Fig. 6.26. The starting load was 10 kg, but the ending load was 17 kg, higher than that at 350 °C. The velocity vs. stress intensity curve at 300 °C was similar to the one at 350 °C, but went to higher stress intensities. Below 15 MPa$\sqrt{m}$, the velocity was very low, consistent with creep only, and then increased rapidly to a plateau region. The plateau velocity was about 1 x 10^{-3} mm/sec in the stress intensity range 30 to 60 MPa$\sqrt{m}$.

6 2 5 2 L-T orientation

1) J010 (350 °C, 1000 Pa)

- Test temperature· 350 °C

- Iodine concentration: 1000 Pa

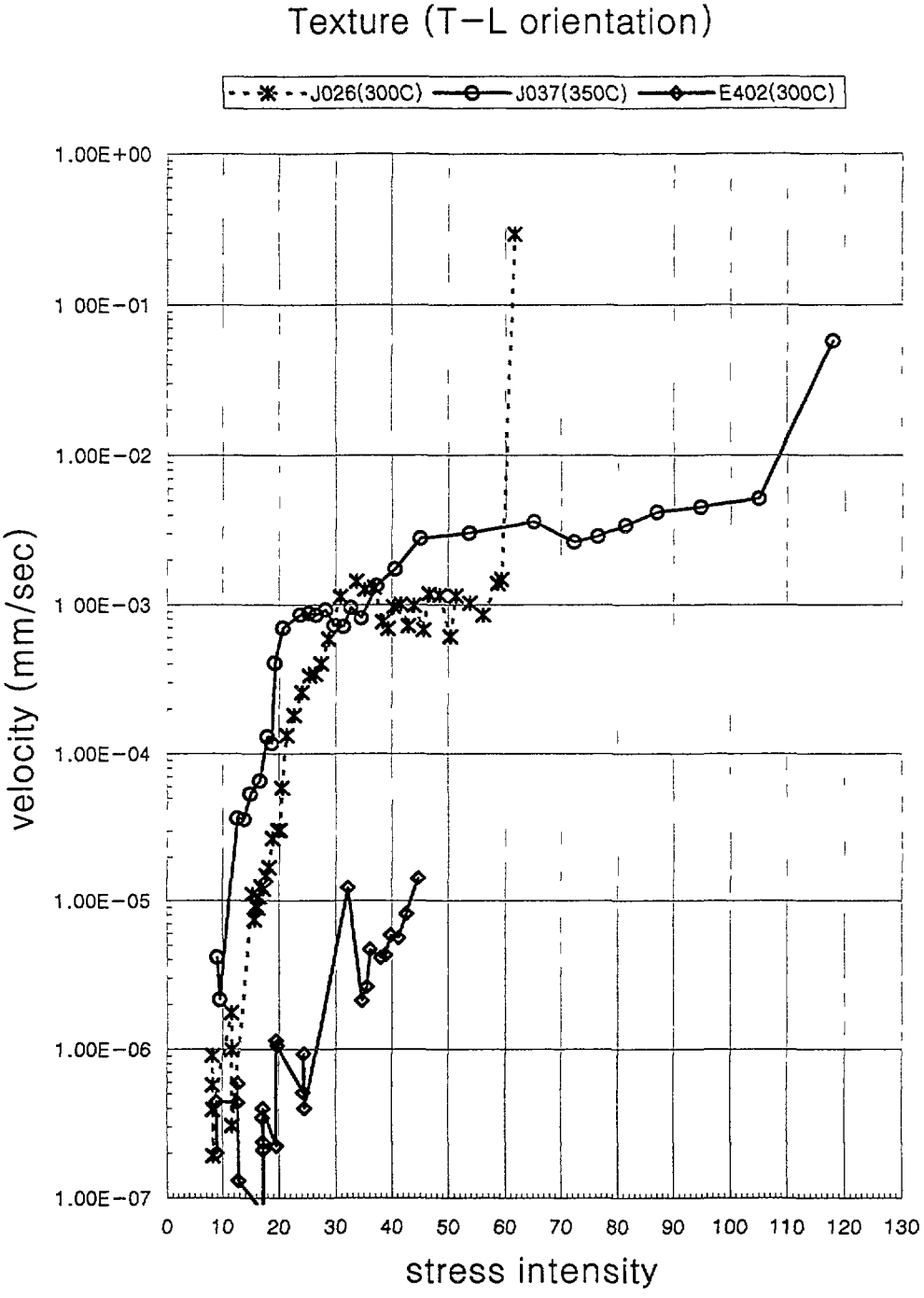

Fig. 6.26 The SCC propagation rate of T-L specimens as a function of stress intensity factor.

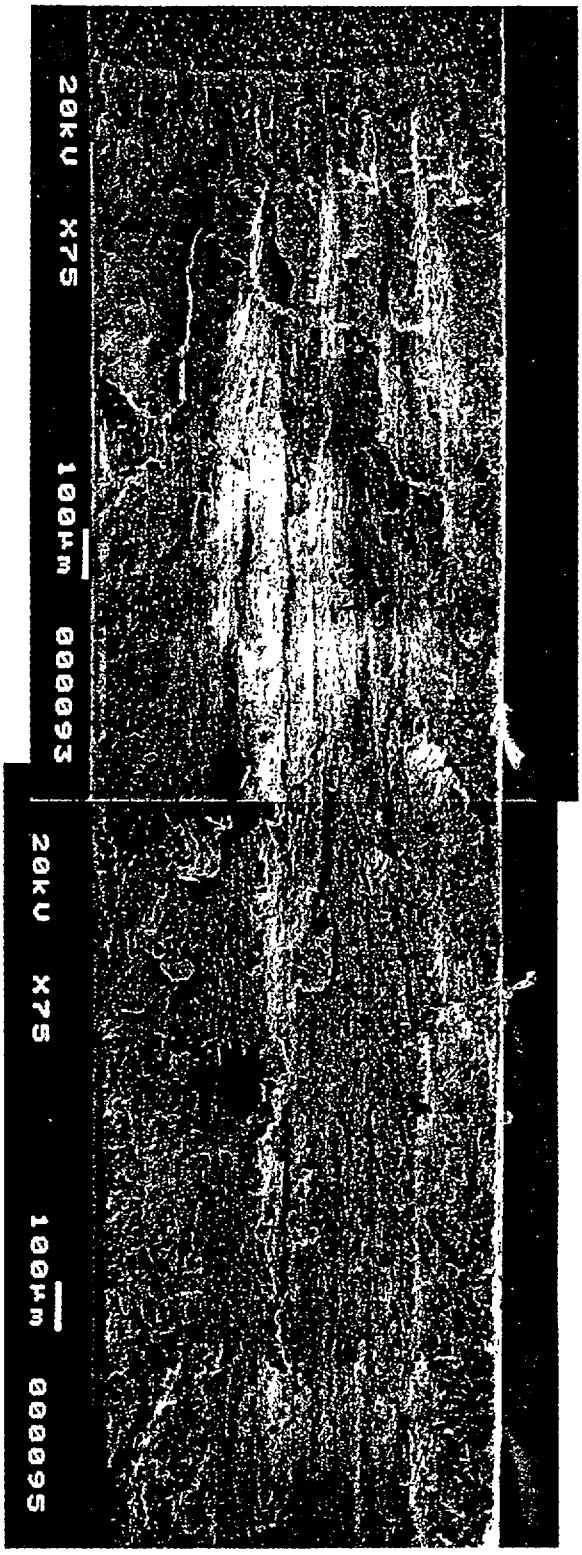

Fig. 6.27. Fractograph of J037.

In the L-T orientation the SCC crack propagates with greater difficulty because the basal planes are located vertically and inclined 35° to the crack direction. The load started from 10 kg, and ended at 20 kg, higher than that for the T-L orientation. The velocity vs. stress intensity curve was quite different from the curve for T-L orientation, as shown in Fig. 6.28.

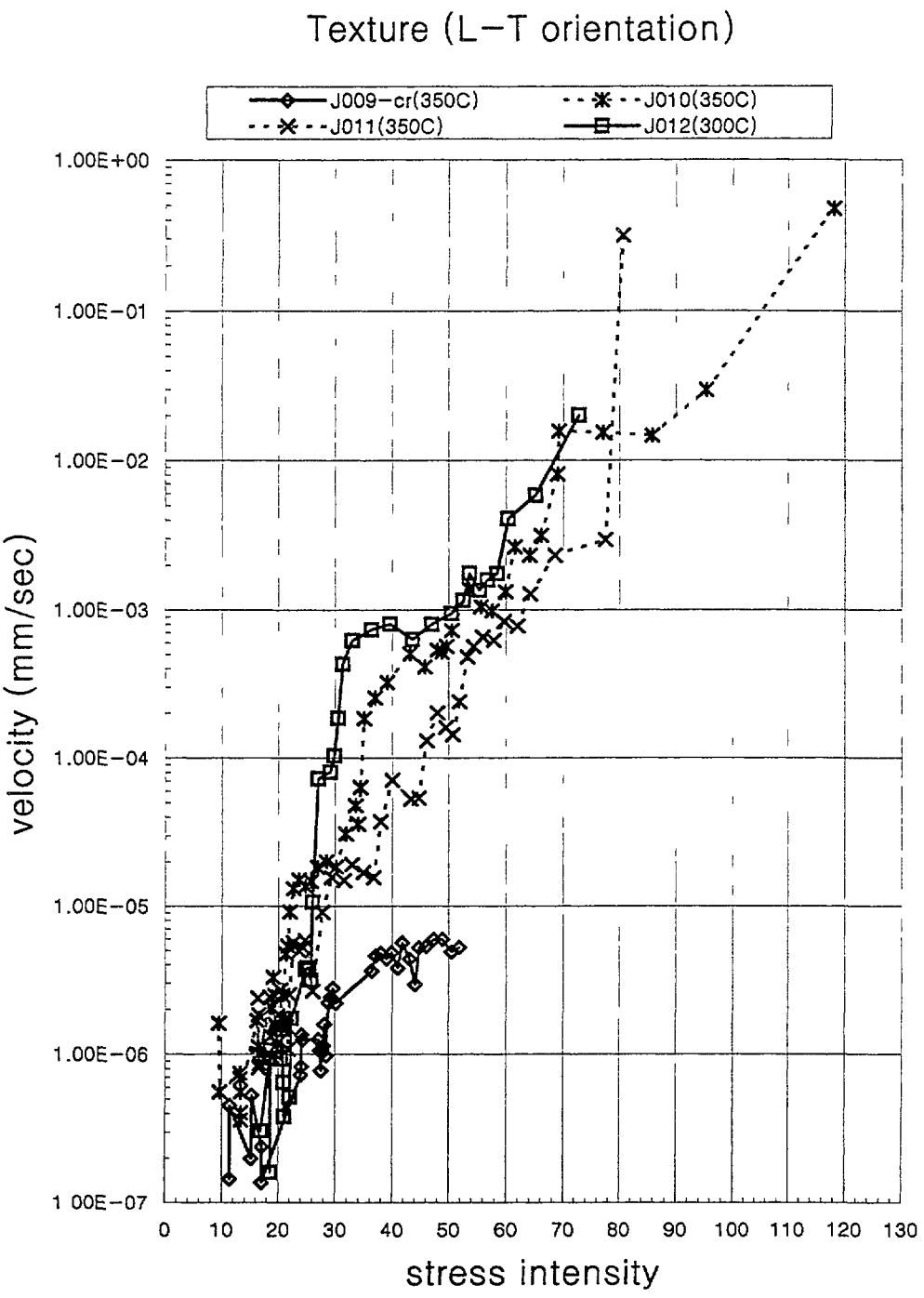

Fig 6.28 The SCC propagation rate of L-T specimens as a function of stress intensity factor.

The velocity was relatively low, and did not show the plateau region. The velocity remained at levels consistent with creep only below 20 MPa$\sqrt{m}$, then increased gradually with stress intensity, followed by mechanical rupture. The fracture surface was very rough up to about 3 mm crack propagation, and then changed to a flat ductile tearing mode as shown in Fig. 6.29. The deep subcracks were not parallel, but inclined about 35°.

2) J011 (350 °C, 1000 Pa)

- Test temperature 350 °C

- Iodine concentration: 1000 Pa

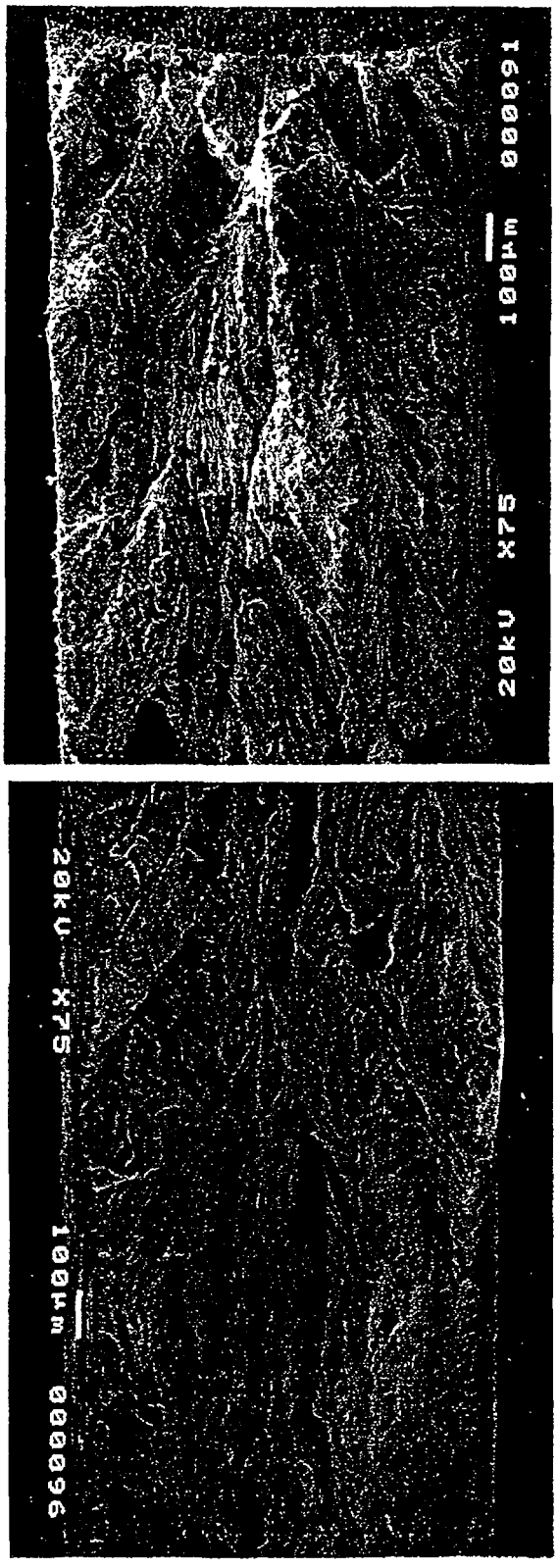

Fig. 6.29. Fractograph of J010.

Fig. 6.28 shows the velocity vs. stress intensity curve at 350 °C. The SCC behaviour of J011 was the same as for J010, in which a plateau velocity was not achieved. The threshold value of K_{ISCC} was about 20 MPa$\sqrt{m}$.

3) J012 (300 °C, 1000 Pa)

- Test temperature: 300 °C

- Iodine concentration: 1000 Pa

Fig. 6.28 shows the velocity vs. stress intensity curve at 300 °C. The load started at 20.5 kg, and increased to 27.2 kg. The SCC behaviour at 300 °C was similar to that at 350 °C, although higher stress intensity levels were achieved. Below 25 MPa$\sqrt{m}$, the velocity indicated creep only. Above 25 MPa$\sqrt{m}$, the velocity increased rapidly with stress intensity followed by rupture.

6.2.5.3 Effect of texture on SCC (summary)

Zircaloy SCC cracks propagate along the basal planes of the hcp structure, so that SCC behaviour is dependent on specimen texture. Because the basal poles incline to the tangential direction of the rolled plate, the basal planes in the T-L oriented specimens are parallel to the SCC crack, although 35° incline to the crack surface. In contrast, the L-T oriented specimens have the basal planes perpendicular to the SCC crack tip, so that the crack is hard to propagate.

The effects of texture on SCC at 300 and 350°C are summarized in Figs. 6.30 and 6.31. The figures show the difference in the SCC velocity as a function of the crack orientation. The behviour in the T-L oriented specimens was the typical of SCC, which is composed of three stages. The plateau region of the SCC velocity was of the order of 10^{-3} mm/sec. In the L-T oriented specimens, however, the velocity increased gradually until rupture occurred, without achieving the plateau region. The velocity was the same order as for creep at low stress intensity, but increased much faster at higher stress intensity levels. The fractographs showed the expected effects of texture, namely that the arrangement of basal planes determines the SCC crack path. The L-T oriented specimens showed a very rough fracture surface with deep subcracks, the directions of which were consistent with the basal planes.

6.2.6. SCC test results using a static system

A static system was recommended at the initiation stage of the CRP, but it was not effective due to iodine depletion at long test times. So after the first meeting, the static system (constant iodine amount) was changed to a dynamic flowing system (constant iodine pressure). Some specimens of OM41 and OM44 were cracked using the static system. The iodine was supplied at constant amount before testing, so the iodine reacted with and adsorbed on the stainless steel test chamber of the static system. This resulted in a drastically decreasing iodine pressure not sufficient to develop SCC. Thus, the tests that were planned to get the threshold SCC value couldn't be performed successfully because iodine depletion and surface oxidation precluded long testing times. In addition, DCPD power lines were attached to the surface rather than to the edge of the specimen, so the DCPD output voltage was measured in a step-like curve rather than in a continuous curve with test time. The SCC crack velocity, therefore, was calculated as an average velocity from the step-like DCPD voltage vs time curve.

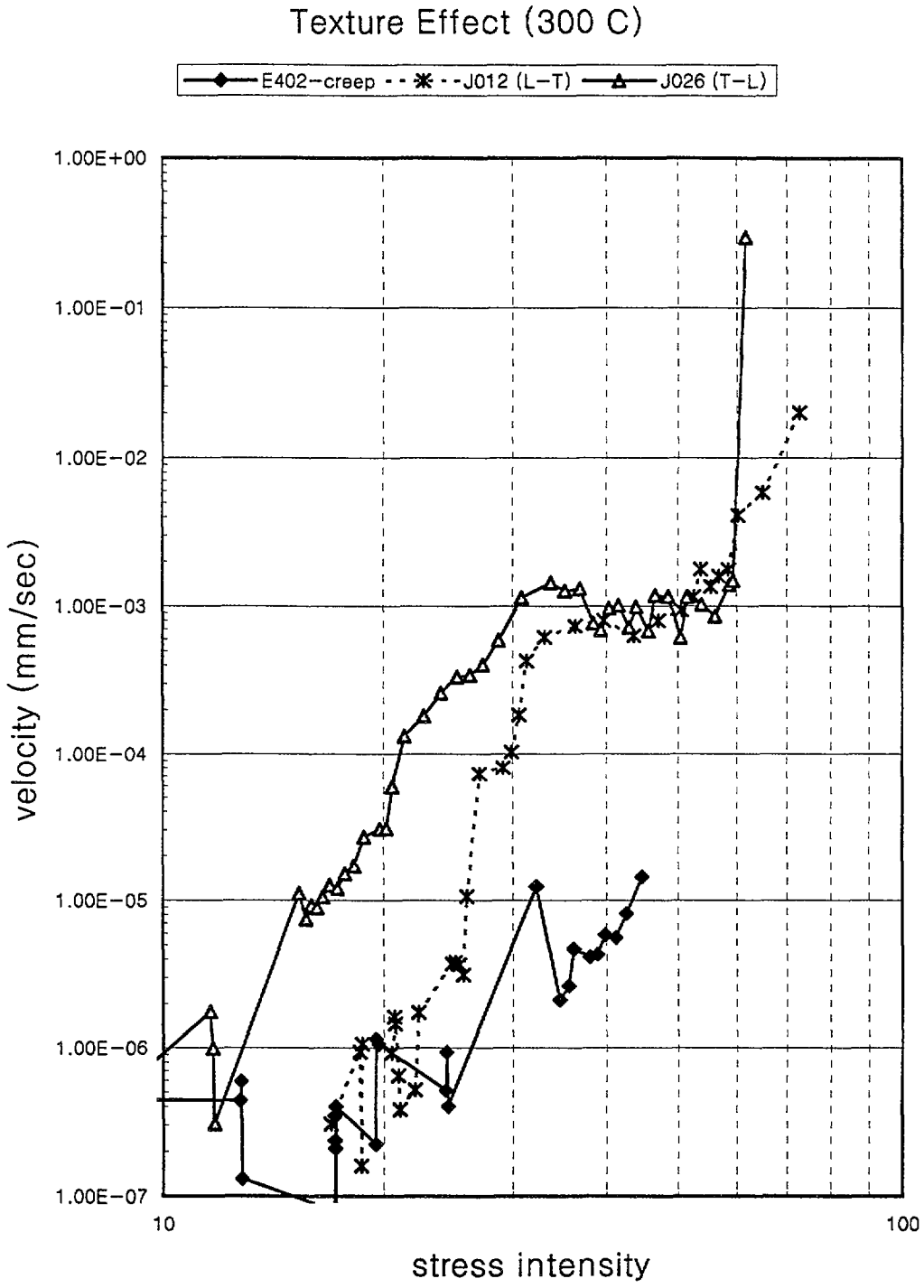

Fig. 6.30. The effect of texture on the SCC propagation rate at 300 ℃.

A. OM44 (recrystallized Zircaloy-2, Cezus)

1) E282 (350°C, 10,000 Pa I_2)

The test started under initial loading of 14 kg (K=8.5 MPa$\sqrt{m}$), but the SCC crack was not developed after 110 hours under 28 kg loading. The fatigue-precrack was blunted after 110 hours.

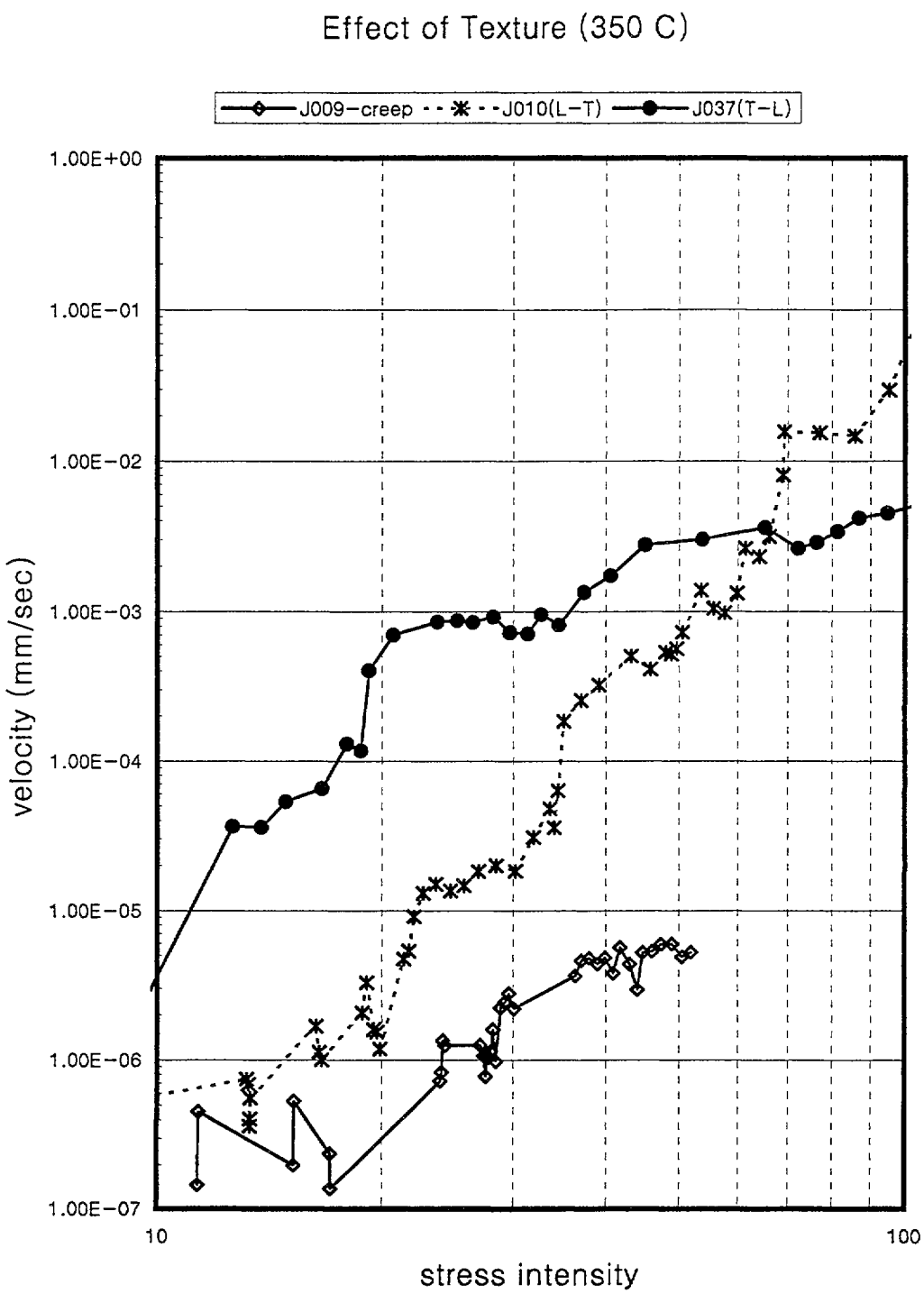

Fig. 6.31. The effect of texture on the SCC propagation rate at 350 ℃.

2) E281 (350°C, 11,000 Pa I_2)

The test started under an initial loading of 19.5 kg (K= 12 MPa$\sqrt{m}$), but the DCPD power lines became detached after 20 hours. The SCC crack length was measured at 0.25 mm after testing. The average SCC velocity was 3.4×10^{-6} mm/sec, calculated from the crack length divided by the total testing time.

3) E278 (350°C, 11,000 Pa I_2)

- Test temperature : 350°C

- Iodine concentration : 11,000 Pa

The test started under an initial loading of 22 kg, and after 25 hours the specimen split completely. Table 6.9 summarizes the results for E278. The limitation of the DCPD voltage measurement didn't allow monitoring of the initial crack. Fig. 6.32 shows the SCC crack velocity as a function of stress intensity. The SCC stages II and III appeared, but stage I was not detected. The plateau SCC crack velocity was about $1x10^{-4}$ mm/sec with a large scatter band in the stress intensity range 15 to 32 MPa$\sqrt{m}$. Above 32 MPa$\sqrt{m}$, the SCC crack velocity increased rapidly to show stage III.

Fig. 6.33 is the fracture surface, showing secondary cracks along the SCC crack. A similar mixed intergranular and transgranular fracture mode to OM40 was observed in the fractographs. In the SCC stage III region, the ductile mode appeared after 3 mm crack propagation due to mechanical rupture as shown in Fig.6.34 Photo (c).

4) E279 (300°C, 10,000 Pa I_2)

- Test temperature : 300°C

- Iodine concentration : 10,000 Pa

Table 6.10 summarizes the results for E279. The test started under 25.3 kg loading, and stopped at 3.5 mm crack length after 17 hours. The DCPD voltage output was recorded in a step-like curve with time, so the average crack velocity was calculated from the output voltage change divided by the duration of each step. As shown in Fig. 6.35, the SCC crack velocity was $2x10^{-5}$ mm/sec at initial stress intensity of 15.4 MPa$\sqrt{m}$, and increased rapidly, and approached to 2 to $3x10^{-3}$ mm/sec in the plateau SCC stage II region above 25 MPa$\sqrt{m}$.

5) E280 (300°C, 10,000 Pa I_2)

- Test temperature : 300°C

- Iodine concentration : 10,000 Pa

Table 6.11 summarizes the results for E280. Fig. 6.35 shows the average crack velocity which increased rapidly in the stress intensity range of 15 to 23 MPa$\sqrt{m}$ in the SCC stage I region.

6) Summary of OM44 using a static system

In a static system, SCC tests should be performed with a short time duration under sufficiently high loading, because iodine the concentration decreases with test time due to reaction with or adsorption on the testing chamber. These tests experienced the same phenomenon and did not develop SCC cracks under initially low loadings. In addition, the difficulty in attaching the DCPD power lines limited the continuous measurement of the crack length.

TABLE 6.9. SUMMARY OF TEST CONDITIONS AND RESULTS FOR E278 (OM44, 300°C)

TEST #2-3 (OM44-3 E278)

iodine = 670 mg 11,000 Pa thickness = 1.21 mm
temperature = 350 C precrack = 2.1 mm

time	temp(C)	volt	load(kg)	Ki	v/vo	a/b	rack lengt	velocity (mm/sec)
0	350		22.5	14.01	1	0.15	2.1	
3	350		21.5	13.38	1	0.15	2.1	
170	348		21.5	13.38	1	0.15	2.1	
230	347	2.53	23.5	14.63	1	0.15	2.1	
770	350	2.58	23.5	15.66	1.032	0.17	2.3	3.19E-05
860	350	2.64	23.5	16.58	1.056	0.18	2.5	4.71E-05
920		2.7	23.5	17.50	1.08	0.19	2.6	6.15E-05
980		2.78	23.5	18.75	1.112	0.21	2.8	6.01E-05
1040		2.86	23.5	20.01	1.144	0.22	3.1	5.86E-05
1100		2.94	23.5	21.29	1.176	0.24	3.3	8.54E-05
1160		3.06	23.5	23.26	1.224	0.26	3.6	3.62E-04
1176		3.2	23.5	25.64	1.28	0.29	3.9	3.66E-04
1190		3.33	23.5	27.94	1.332	0.31	4.2	1.78E-04
1226		3.5	23.5	31.08	1.4	0.34	4.6	9.08E-05
1250		3.56	23.5	32.24	1.424	0.35	4.7	4.77E-05
1280		3.6	23.5	33.02	1.44	0.35	4.8	7.04E-05
1310		3.66	23.5	34.21	1.464	0.36	5.0	6.87E-04
1315		3.76	23.5	36.26	1.504	0.38	5.2	8.36E-02
1316		8	23.5	185.16	3.2	0.75	10.2	
1490		9.2	23.5	273.46	3.68	0.83	11.3	

The results for the average SCC velocity for the recrystallized Zircaloy-2 (OM44) are shown in Figs. 6.32 and 6.35. The SCC crack velocity at the SCC stage II region of OM44 was about $1x10^{-4}$ mm/sec in the stress intensity range of 15 to 32 MPa$\sqrt{m}$ and 2 to $3x10^{-3}$ mm/sec after 25 MPa$\sqrt{m}$ at 350°C and 300°C, respectively. The threshold stress intensity factor was inferred to decrease with increasing test temperature. These results suggested that a static system needed a high load to produce the SCC in a short time, so that the system was inadequate for measuring crack propagation rates.

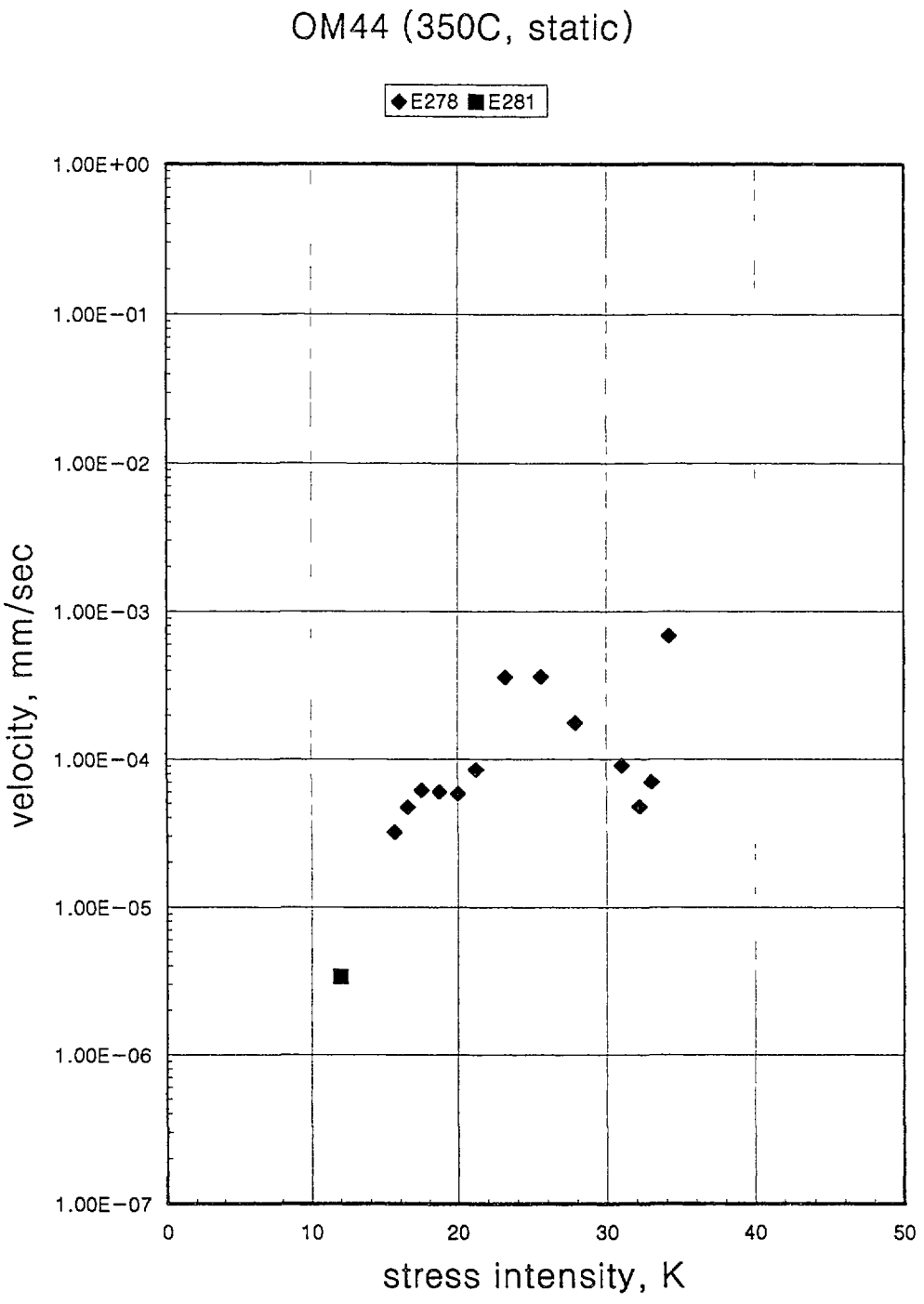

Fig. 6.32. The SCC propagation rate of OM44 in the static system (350℃).

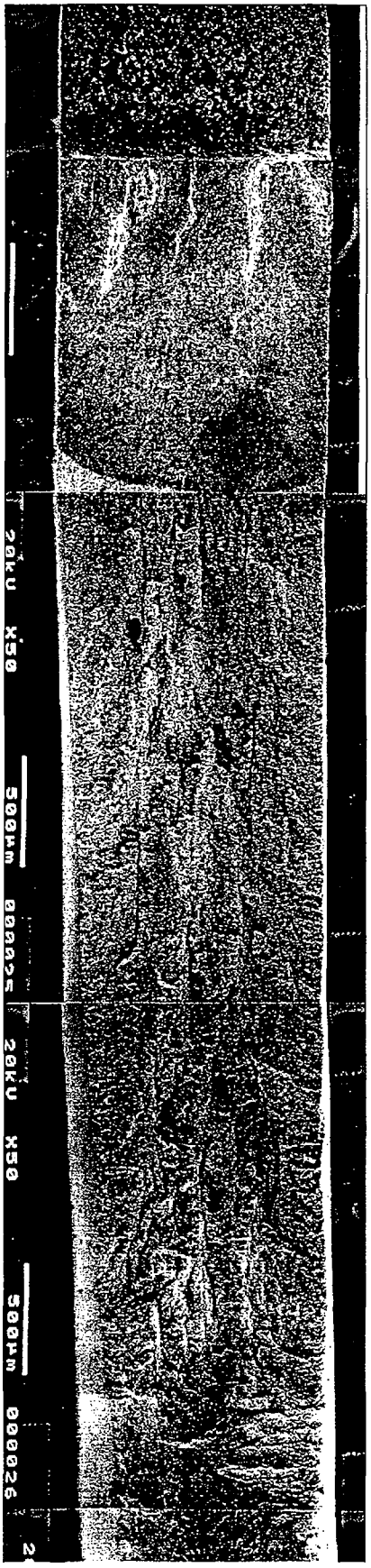

Fig. 6.33. Fracture surface of E278.

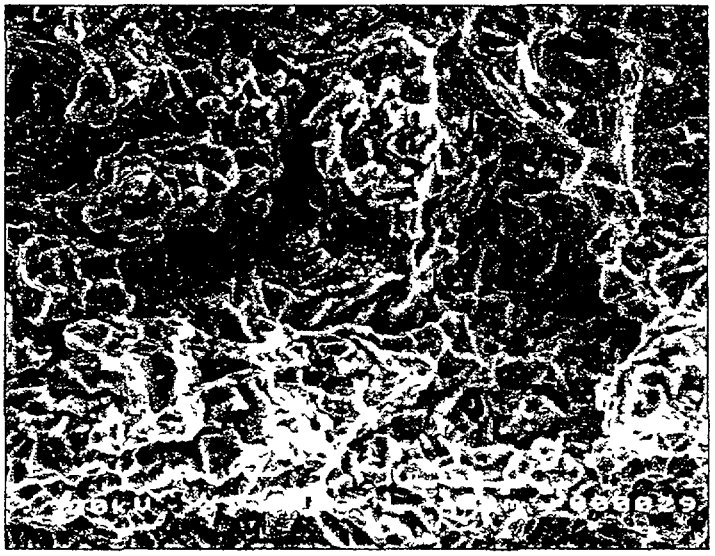

(a)

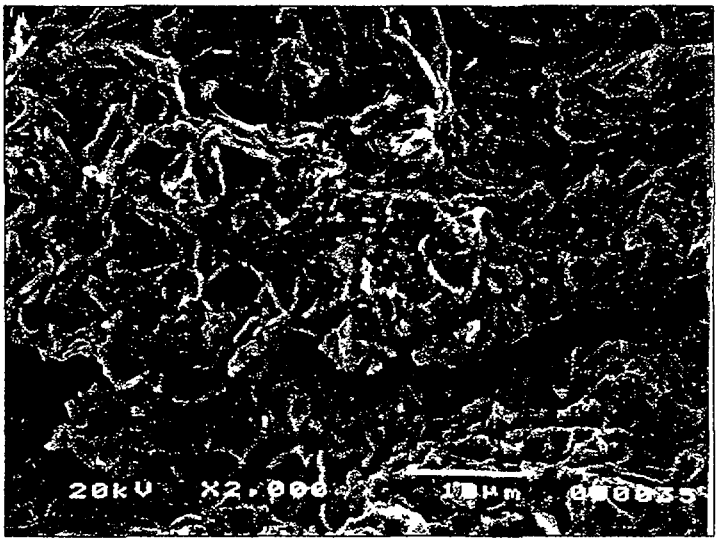

(b)

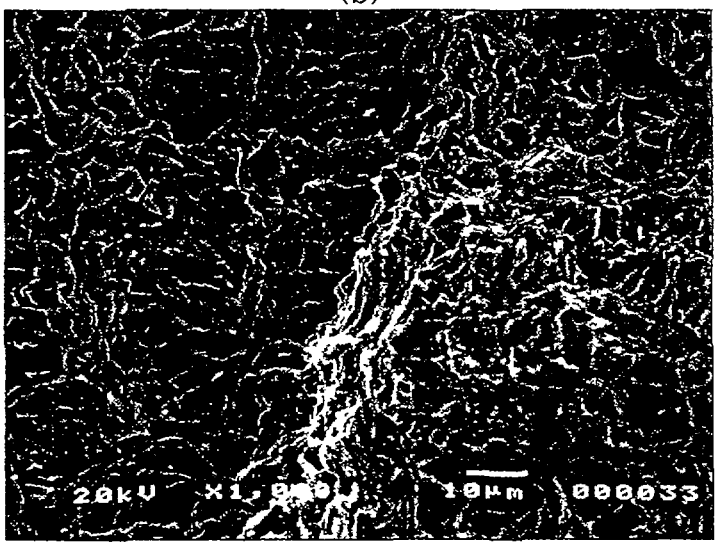

(c)

Fig. 6.34. Fractographs of E278.

TABLE 6.10. SUMMARY OF TEST CONDITIONS AND RESULTS FOR E279 (300°C)

TEST #2-4 (OM44-4 E279)

iodine = 650 mg (10,000 Pa)
temperature = 300 C
current = 2.99 A

thickness = 1.21 mm
precrack = 2.05 mm
width = 13 mm

time	temp(C)	volt	load(kg)	Ki	v/vo	a/b	crack length	velocity, mm/sec
					-			avrg
0	297	2.1	25.3	15.66	1.01	0.16	2.05	
30	298	2.1	25.3	15.66	1.01	0.16	2.05	
65	298	2.08	25.3	15.54	1.00	0.15	2.05	
120	298	2.08	25.3	15.54	1.00	0.15	2.05	5.95E-06
180	298	2.1	25.3	15.74	1.01	0.16	2.07	8.68E-06
300	298	2.1	25.3	15.74	1.01	0.16	2.07	
480	299	2.1	25.3	15.74	1.01	0.16	2.07	
600	300	2.08	25.3	15.35	1.00	0.15	2.00	
833	301	2.2	25.3	17.69	1.06	0.18	2.41	1.26E-04
847	300	2.2	25.3	17.69	1.06	0.18	2.41	
855	299	2.25	25.3	18.67	1.08	0.19	2.58	2.11E-05
900	296	2.25	25.3	18.67	1.08	0.19	2.58	
945	296	2.25	25.3	18.67	1.08	0.19	2.58	
958	296	2.29	25.3	19.47	1.10	0.20	2.71	1.63E-04
1005	296	2.29	25.3	19.47	1.10	0.20	2.71	
1013	296	2.29	25.3	19.47	1.10	0.20	2.71	
1019	296	2.48	27.3	25.18	1.19	0.25	3.30	2.93E-03
1022	296	2.66	27.3	29.35	1.28	0.29	3.83	3.78E-03
1026	296	3	22	30.62	1.44	0.36	4.74	2.47E-03
1027	296	3.06	22	31.95	1.47	0.37	4.89	
		3.33						

crack=2.9/4.3/4.9 mm

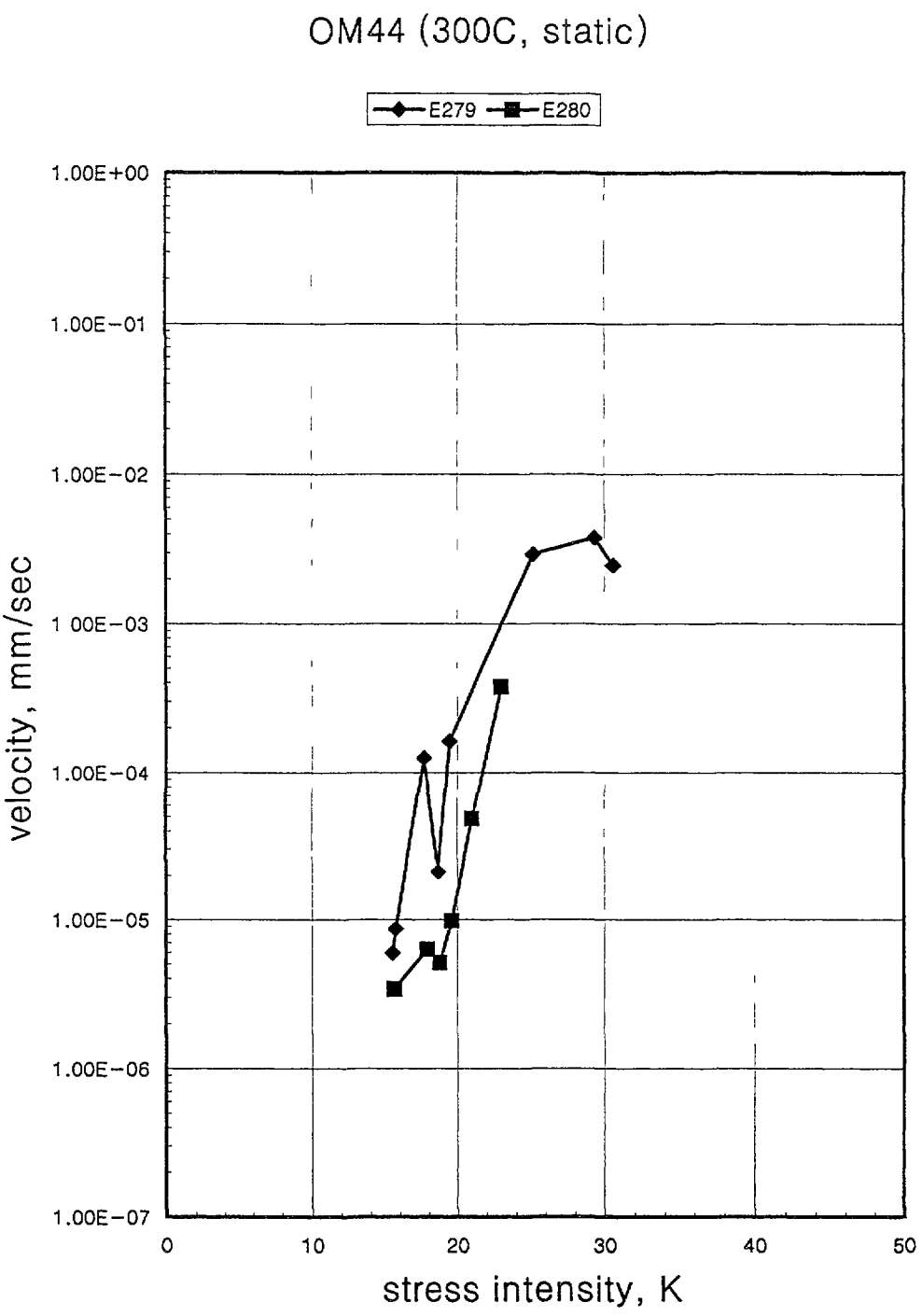

Fig. 6.35. The SCC propagation rate of OM44 in the static system (300 ℃).

B. OM41 (stress relieved Zircaloy-4, Wah Chang)

These tests were carried out during the first stage of the program, and thus a number of difficulties, especially the detachment of the DCPD power lines, caused tests to fail.

1) E247 (350°C, 17,000 Pa) - failed

2) E244 (400°C, 18,000 Pa) - failed

TABLE 6.11. SUMMARY OF TEST CONDITIONS AND RESULTS FOR E280 (300°C)

TEST #2-5(OM44-5 E280)

thickness = 1.21 mm
precrack = 2.05 mm
width = 13 mm

iodine = 650 mg
temperature = 300 C
current = 2.99 A

10,000 Pa

date	time	temp(C)	volt	load(kg)	Ki	v/vo	a/b	rack lengt	velocity (average)
15:20	0	298	1.95	24.5	15.05	1	0.15	2.05	
18:00	160	298	1.95	25.5	15.66	1	0.15	2.05	3.41E-06
8:20	1020		1.95	25.5	15.66	1	0.15	2.05	
10:00	1120		2	25.5	16.52	1.03	0.16	2.19	
11:00	1180		2.02	25.5	16.94	1.04	0.17	2.26	
12:20	1260	296	2.03	26	17.48	1.04	0.17	2.30	
15:00	1420		2.04	26	17.70	1.05	0.17	2.33	
17:22	1540		2.04	26.3	17.90	1.05	0.17	2.33	6.30E-06
19:35	1635		2.05	26.3	18.12	1.05	0.18	2.37	
15:30	2890	296	2.05	27.3	18.81	1.05	0.18	2.37	5.12E-06
19:28	3128		2.05	27.3	19.09	1.05	0.18	2.44	
20:00	3160		2.07	27.8	19.61	1.06	0.18	2.44	9.82E-06
23:00	3340		2.1	27.8	20.30	1.08	0.19	2.54	
9:40	3984	296	2.1	28.8	21.03	1.08	0.19	2.54	4.84E-05
10:43	4044		2.15	29.8	23.01	1.10	0.20	2.72	3.76E-04
10:59	4059	296	2.25	29.8	25.54	1.15	0.23	3.06	
12:00	4120	296	2.24	29.8	25.28	1.15	0.23	3.02	
13:00	4180	296	2.28	30	0.00	1.17	0.24		
12:00	5560		2.3	30	0.00	1.18	0.24		
off									

blunting

3) E243 (300°C, 18,000 Pa) - failed

4) E242 (300°C, 18,000 Pa) - failed

5) E241 (350°C, 17,000 Pa) - failed

6) E245 (350°C, 17,000 Pa)

The test started under 22.5 kg loading, and the specimen split completely after about five minutes. The average crack velocity was about $6x10^{-3}$ mm/sec at 17 MPa$\sqrt{m}$. Fig. 6.36 is the fracture surface of E245. The fracture surface showed a brittle mode at the initial stage (Fig. 6.37 Photo (a)), but deformation marks after 3 mm of crack progression. The fractographs indicated a ductile tearing mode at 3 mm crack length as shown in Fig. 3.37 Photo (b).

6.3. SUMMARY

1) Creep tests: Below 25 MPa$\sqrt{m}$ of stress intensity, the velocities did not change with load in the order of 10^{-7} mm/sec, though the crack length did jump at each step to a higher load. Above 30 MPa$\sqrt{m}$, the velocity was $1x10^{-5}$ mm/sec in the primary creep stage, but the velocity dropped to the order of 10^{-6} mm/sec and increased with the stress intensity in the secondary stage. Creep has an influence on the SCC propagation rate in the low stress intensity range, especially in the threshold region of stress intensity for SCC. In order to determine the threshold stress intensity, the creep velocity in the order of 10^{-7} mm/sec should therefore be removed from the SCC results.

2) Threshold stress intensity: The SCC curves of velocity vs. stress intensity showed the typical SCC characteristics that are composed of stages I, II and III. The SCC stage I in the RX Zircaloy-4 (OM40) was measured from 9 MPa$\sqrt{m}$ to 19 MPa$\sqrt{m}$. The threshold stress intensity for SCC at 350°C, K_{ISCC}, was about 9, 9.5, and 11 MPa$\sqrt{m}$ for the SRA Zircaloy-4 (OM41), the RX Zircaloy-4 (OM40), and the RX Zircaloy-2 (OM44), respectively.

3) SCC propagation rate: The SCC crack propagation rate at the SCC stage II appeared above 20 MPa$\sqrt{m}$. The plateau velocity in stage II at 350°C and 1000 PaI_2 seemed to be divided into two groups: 4 to $8x10^{-4}$ mm/sec in the range 20 to 40 MPa$\sqrt{m}$ and 1 to $3x10^{-3}$ mm/sec above 40 MPa$\sqrt{m}$. The SCC resistivity of the RX Zircaloy-2 (OM44) was similar to or a little higher than the RX Zircaloy-4 (OM40). In comparison with RX Zircaloy-4 (OM40), SRA Zircaloy-4 (OM41) had a lower threshold SCC stress intensity factor and a slightly higher SCC velocity, indicating that SRA Zircaloy-4 was more sensitive to SCC. It is, however, known that the threshold stress of SRA Zircaloy-4 in an internal pressurization SCC test is higher, and that the failure strain is lower than RX Zircaloy-4 because the SRA Zircaloy-4 has a higher tensile strength. These results suggest that the evaluation of SCC should be considered in respect of both threshold stress and propagation rate.

4) Effect of texture: The behaviour of the T-L oriented specimens was typical of SCC, which is composed of three stages. The plateau region of the SCC velocity was of the order of 10^{-3} mm/sec. The L-T oriented specimens, however, showed a gradually increasing velocity until rupture occurred, without the plateau SCC region, similar to a creep-like behaviour. The velocity of the L-T oriented specimens was the same order as for creep at low stress intensity, but increased with stress intensity much faster than for creep. The L-T

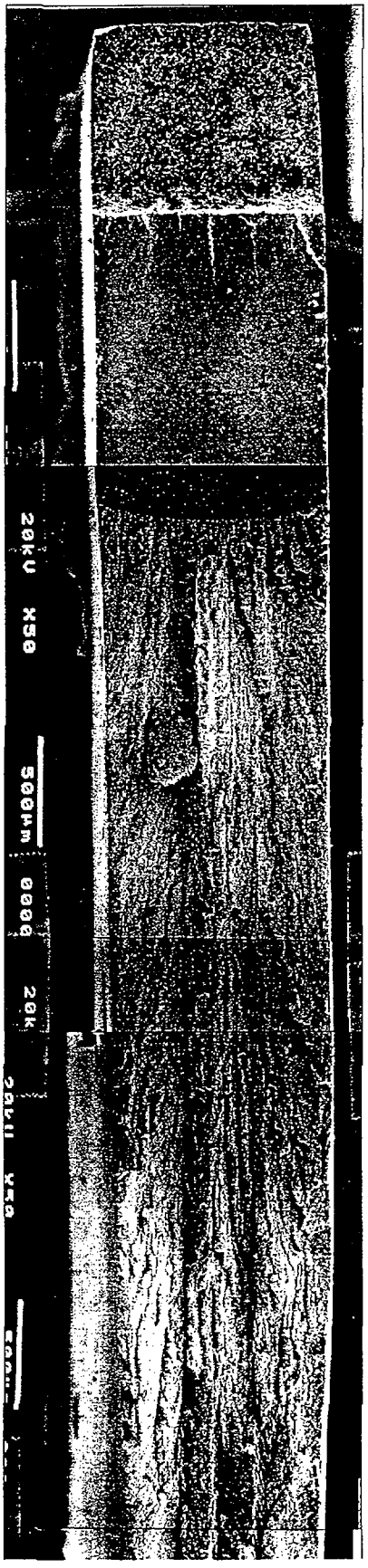

Fig. 6.36. Fracture surface of E245.

oriented specimens showed a very rough fracture surface with deep subcracks which had directions which were consistent with the basal planes.

5) The fracture mode in the RX Zircaloy was mostly transgranular fracture with river patterns. The transgranular surface was inclined to the fracture surface because of the 35° inclination of the basal planes due from the material texture. An intergranular mode

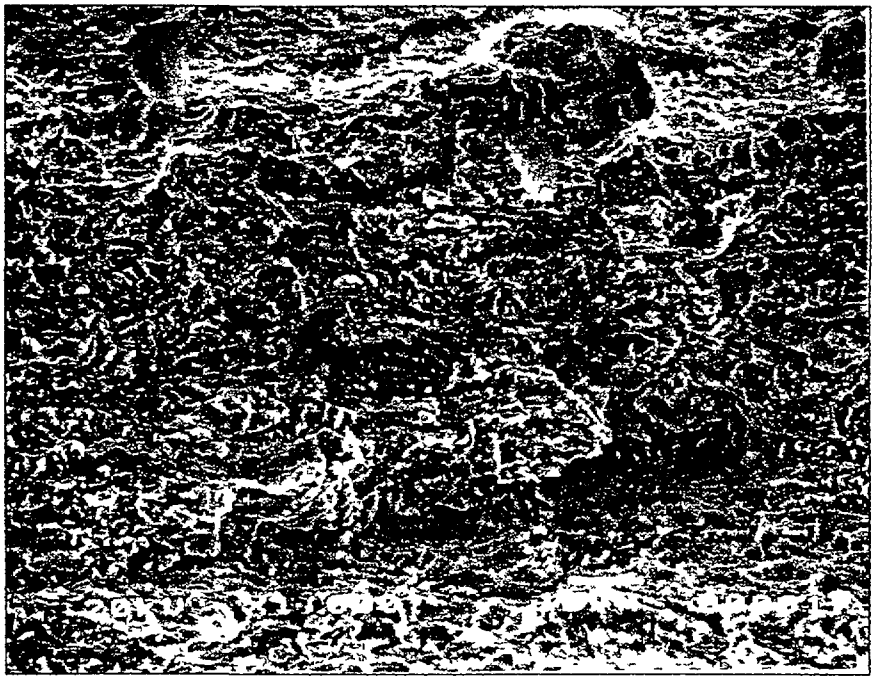

(a)

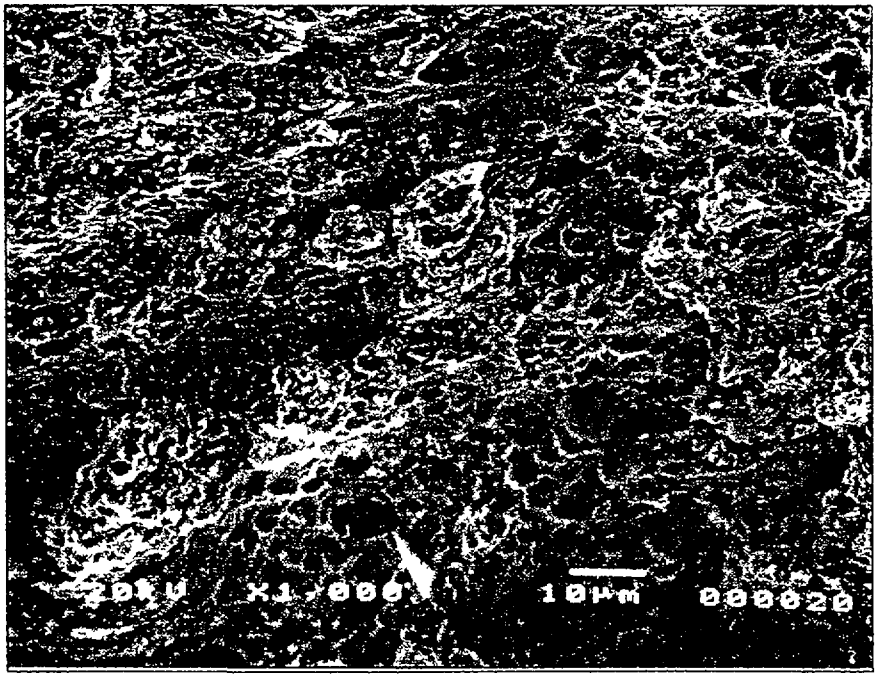

(b)

Fig. 6.37. Fractographs of E245.

and flutting were sometimes observed. The rolled structure in the SRA Zircaloy made it difficult to distinguish the fracture between transgranular and intergranular modes. The fracture surfaces were elongated along the SCC crack direction, and inclined from the crack surface due to the inclined basal planes by the rolling process.

6) In a static system, SCC tests have to be performed in a short time duration under sufficiently high loading, because iodine concentration decreases drastically due to reaction with or adsorption on the testing chamber. A static system was inadequate to measure the crack propagation rate which requires long testing times.

REFERENCE TO CHAPTER 6

[6.1] BRUNISHOLZ L., LEMAIGNAN C., "Iodine induced stress corrosion cracking of Zircaloy fuel cladding: Initiation, growth", Zr in Nuclear Industry 7th Internl. Symp. Strasbourg, France. ASTM STP 939, (1987) 700 - 716.

Appendix 1

CHARACTERISATION OF MATERIALS

A1.1. TENSILE PROPERTIES

The mechanical properties of the test materials were determined by cutting tensile specimens from the sheet material in the TL orientation, the same orientation as used for the majority of specimens in the CRP. These were then heated to 350°C in air and tested in a Zwick 1464 tensile machine to determine the 0.2% proof strength and ultimate tensile strength (UTS). The cross-head displacement rate was chosen to give 0.3% strain per minute. The results were as follows:

Material	Specimen I/D	0.2% Proof strength (MPa)	UTS (MPa)	% elongation
Wah Chang RXA Zr-4 (OM40)	G071	147	222	47
	G072	144	220	49
Wah Chang SRA Zr-4 (OM41)	G073	320	363	31
Cezus RXA Zr-2 (OM44)	G075	161	230	53

The following room temperature data were supplied by Teledyne Wah Chang on recrystallised Zr-2 (considered to be mechanically identical to recrystallised Zr-4) as follows:

Orientation	Yield strength (MPa)	UTS (MPa)	% elongation
Longitudinal	469	520	26
Transverse	376	540	27

Information was also supplied by Cezus on their materials as follows:

Temperature	Orientation	Yield strength (MPa)	UTS (MPa)	% elongation
Room temperature	Longitudinal	395	521	30
Room temperature	Transverse	443	495	27
300°C	Longitudinal	138	263	42
300°C	Transverse	159	233	39

The plastic zone size can be determined using the equation:

$r_y = 1/2\pi\ (K_I/\sigma_{ys})^2$

Using the 350°C yield stress data, the maximum allowable value of K_I can be calculated for which the plastic zone size is less than the width of the particular material. This gives maximum valid stress intensity factors for each material of:

Recrystallised Zr-4 (Teledyne Wah Chang, OM40)	12 MPa√m
Stress-relief annealed Zr-4 (Teledyne Wah Chang, OM41)	25 MPa√m
Recrystallised Zr-2 (Cezus)	14 MPa√m

A1.2. TEXTURE

A1.2.1. Method

Composite specimens of the recrystallised and stress relief annealed Zr-4 from Teledyne Wah Chang and recrystallised Zr-2 from Cezus (materials OM40, OM41 and OM44 respectively) were made by stacking sections taken from the sheet materials and mounting to create specimens with a larger surface area (Fig. A1.1). Such specimens were made for measurements of the texture in the L and T directions; a small piece of the sheet was also used to take measurements normal to the surface (N direction).

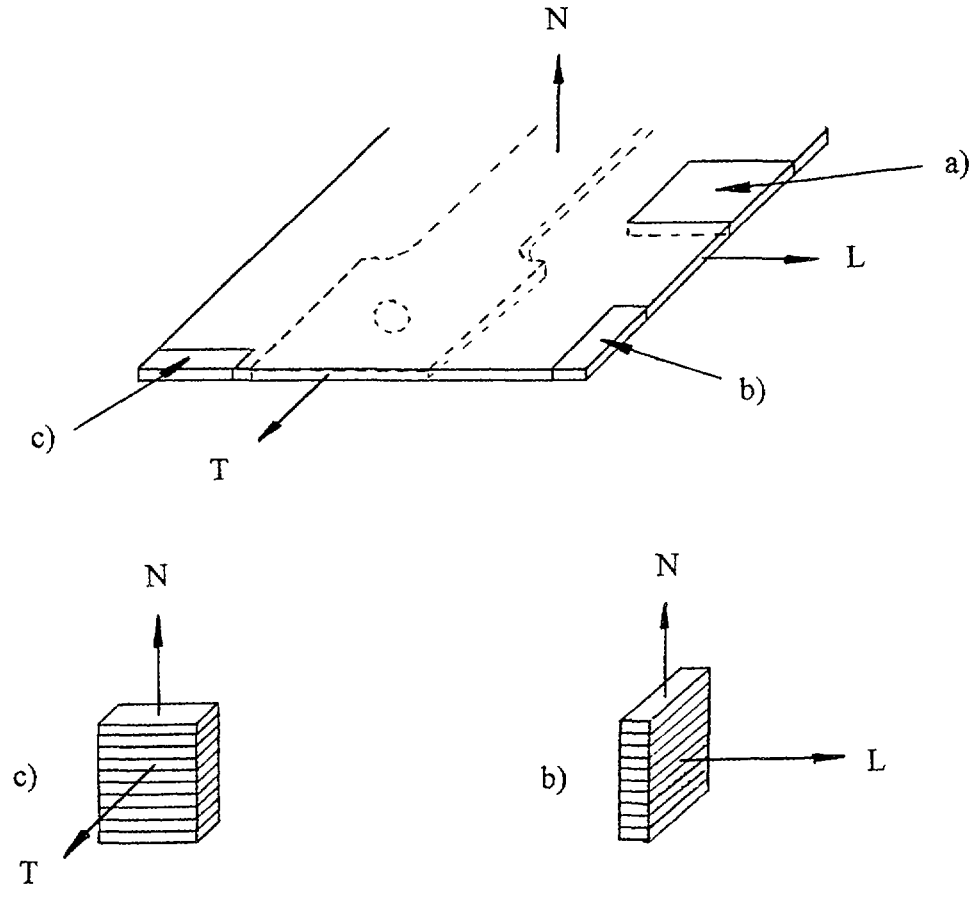

FIG. A1-1. Schematic diagram showing the method of sample preparation to increase the surface area for X-ray diffraction texture measurements.

All measurements were carried out on a purpose built automated texture goniometer, based on the Siemens D500 diffractometer. Cu Kα radiation was used at 40KV, 30mA with a graphite monochromator in the diffracted beam. The goniometer was controlled by a microVAX 3300, on which the data are also processed. All measured data sets were stored on the microVAX, and backed up onto magnetic tape. Before and after the measurements, the alignment of the goniometer was checked using an established procedure. In this procedure a (111) cut silicon single crystal was used to ensure that the Bragg angle at tilt of $\phi = 0$ and 70.5° deviated from the absolute angle by less than 0.03° 2ϕ and the intensity decrease due to defocusing was minimised and essentially constant around a ϕ=70.5° circle. A HIPed Zircaloy powder was used to determine the loss in intensity that occurs as the tilt angle on a texture goniometer is increased from 0 to 90°. The data so generated were then used to correct the intensities in all pole figures for this defocus effect. In all 4 pole figures i.e. (10.0), (00.2), (10.2) and (11.0) were measured, for each sample without its removal from the holder. Background measurements were made at 30° and 80° 2ϕ. Data were collected in the reflected mode by continuous scanning at 5° step sizes of tilt and rotate up to a maximum tilt angle of 85°. The collected data points were corrected by subtracting the background, adjusting for defocusing (using the random HIPed sample of Zircaloy) and then normalising.

To calculate the f-factors, the pole figures were processed in the following way. To ensure that the integration of the intensities within the pole figure totals 100% (which can only be ensured for a complete pole figure), the incomplete experimental pole figures and the defocus curves were adjusted for the missing intensity by copying the 85° data to 90°. This has been found to give the best approximation to a complete pole figure without resorting to the very lengthy procedure of collecting data from a transmission specimen and then matching the reflection and transmission data. Although all the pole figures showed 4 fold symmetry, the very small variations in intensity at equivalent positions in each quadrant of the pole figure need to be allowed for. This was carried out by averaging the intensities at equivalent positions in each quadrant. This has the effect of making each figure symmetrical.

A1.2.2. Results for Zr-4

(00.2) pole figures from the Teledyne Wah Chang Zr-4 samples (OM40 and OM41) with the N, L and T orientations are given in Fig. A1.2 and Fig. A1.3, respectively. Both samples were found to have the same texture type and have their basal pole rotated around 30° about the rolling direction (compare Fig..A1.2 a) and b)).

Sample orientation produced corresponding rotations of poles, Fig. A1.2 b) and c) and Fig. A1.3 b) and c), with respect to the normally directed (00.2) pole figures. This is illustrated graphically in the schematic (00.2) pole figures (Fig. A1.4). Corresponding schematic diagrams depicting the various orientations N, L and T with the respective rolling (RD), transverse (T) and longitudinal (L) directions of the samples are also shown in Fig. A1.4.

While the texture types were the same in the samples, one has been given a recrystallization treatment (OM40) and the other a stress relief anneal (OM41). The recrystallization treatment has brought about a weakening in the pole figure intensity and also a degree of relaxation of the contours.

The f-factors calculated from the pole figures for the recrystallised material are given in Fig. A1.2, while those for the stress-relief annealed sample are given in Fig. A1.3. For each

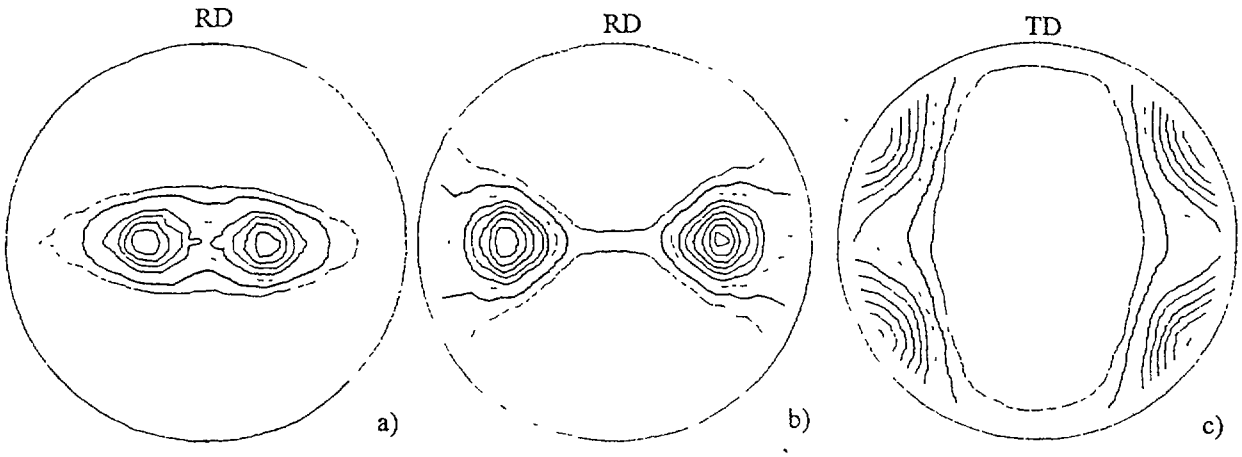

a)

	f_{002}	f_{100}	f_{110}
N	0 561	0.234	0.260
L	0 121	0.445	0.412
T	0 318	0.321	0.328

b)

	f_{002}	f_{100}	f_{110}
N	0.537	0.289	0.277
L	0.134	0.396	0 403
T	0.329	0.316	0.320

c)

	f_{002}	f_{100}	f_{110}
N	0.548	0.337	0 299
L	0.145	0.327	0 364
T	0.307	0.336	0.338

FIG. A1-2. (00.2) pole figures and tables of f-factors for Teledyne Wah Chang recrystallised Zr-4 (material OM40) from the a) normally (N) oriented sample, b) from the longitudinally (L) oriented sample and c) from the transversely (T) oriented sample.

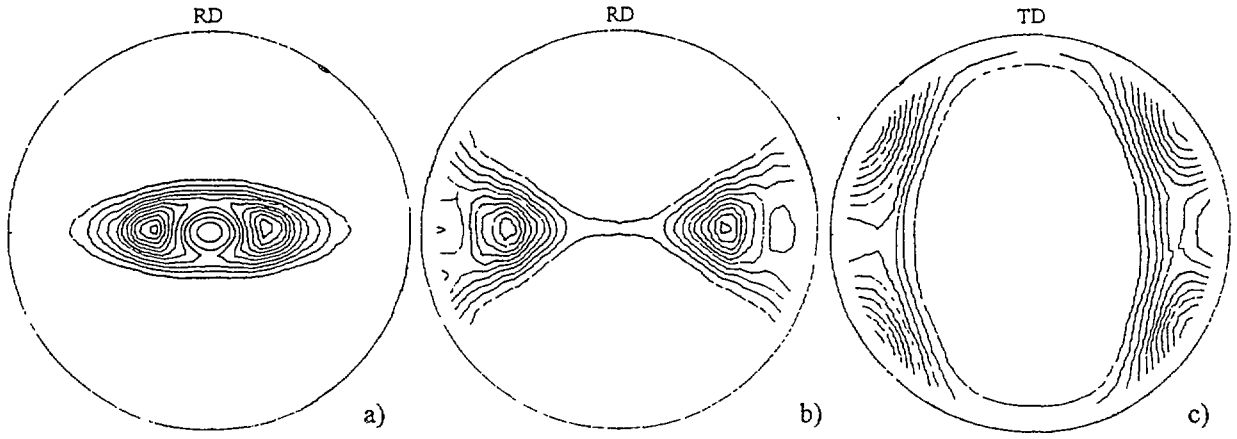

a)

	f_{002}	f_{100}	f_{110}
N	0.602	0.210	0.243
L	0.104	0.437	0.424
T	0.294	0.353	0.334

b)

	f_{002}	f_{100}	f_{110}
N	0.564	0.289	0.252
L	0.124	0.335	0.376
T	0.312	0.376	0.373

c)

	f_{002}	f_{100}	f_{110}
N	0.590	0.330	0.284
L	0.113	0.366	0.395
T	0.296	0.304	0.321

FIG. A1-3. (00.2) pole figures and tables of f-factors for Teledyne Wah Chang stress-relief annealed Zr-4 (material OM41) from the a) normally (N) oriented sample, b) from the longitudinally (L) oriented sample and c) from the transversely (T) oriented sample.

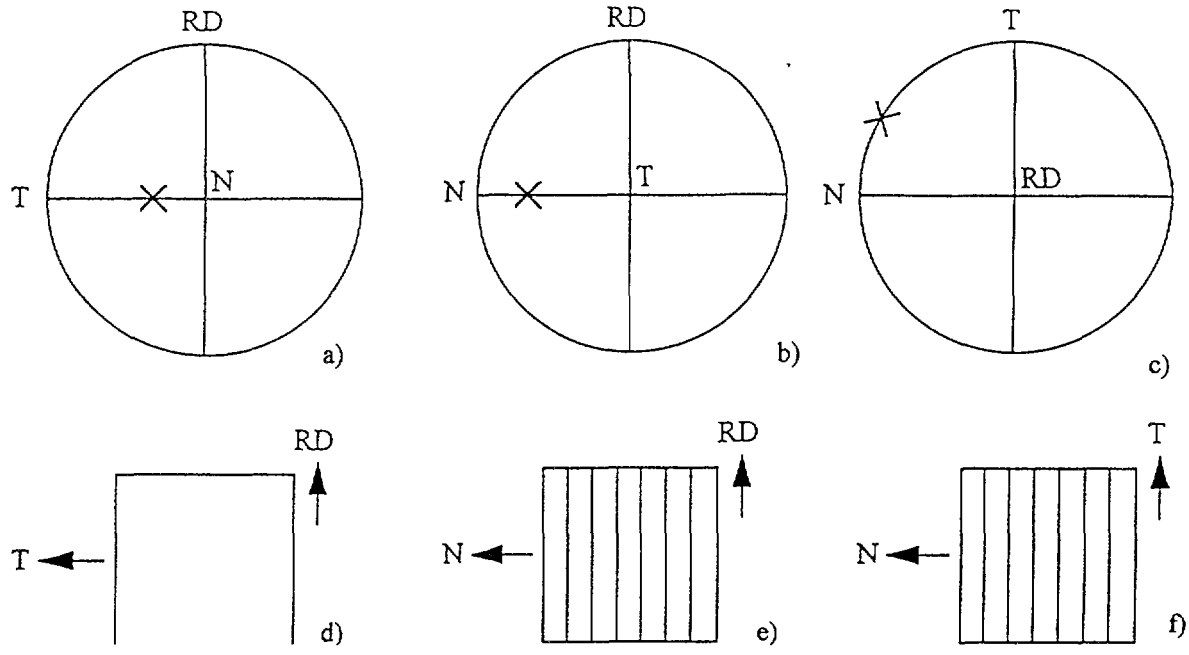

FIG. A1-4. Schematic pole figures showing a) the position of the (00.2) pole rotated about 30° about the rolling direction (RD), b) the same pole but with the normal rotated through 90° about the rolling direction, and c) as in b) but with a further rotation of 90° about the normal direction. Fig. d), e) and f) depict the sections of the samples corresponding to the orientations in pole figures a) to c).

material, the pole figures were taken normal to the sheet surface (labelled a) in each figure) and were generated from the surface of the sheet material, so that any variation in texture through the sheet thickness would not be observed. For the pole figures in the transverse direction (labelled c)), the peaks in intensity were at the edge of the pole figure so that some information for calculating f-factors was missing. The pole figures labelled b) taken in the longitudinal direction were the most complete and so the most confidence can be placed in the f-factors from this sample. It is clear from these tables that there was little change in the f-factors owing to differences in either heat treatment or orientation.

A1.2.3. Results for Zr-2

The (00.2) pole figures from the Cezus recrystallised Zr-2 sample (OM44) with the N, L and T orientations are given in Fig. A1.5. These were again similar to those found in the Zr-4 samples and have their basal pole rotated around 30° about the rolling direction. The f-factors calculated from the pole figures are also given in Fig. A1.5. The f_{002}-factors were slightly higher than those calculated for the Zr-4 materials, indicating a slightly stronger texture. Fig. A1.6 is a (0002) pole figure provided by Cezus regarded as typical for this material. The pole figure and f-factors were in good agreement with those determined during this investigation.

A1.3. GRAIN SIZE

Cezus reported that their material had an ASTM grain size of 12, which was equivalent to 5.6 μm. This was in reasonable agreement with the value of 4.8μm reported by the Chinese investigation (Appendix 2). It was assumed that these values were averages in the three orthogonal directions and do not reflect the fact that the grains will be elongated in the rolling direction.

A1.4. CHEMICAL COMPOSITION

The chemical compositions provided by the manufacturers for the Wah Chang Zr-4 (OM40 and OM41) and the Cezus materials are tabulated below:

Elements	Teledyne Wah Chang Zr-4 (OM40 & OM41) (%)	Cezus Zr-2 (OM44) (%)	Cezus Zr-4 (OM45) (%)
Cr	0.12	0.115	0.11
Fe	0.22	0.18	0.21
Fe+Cr	0.34	0.295	0.32
O	0.111	0.12	0.11
Si	0.0092	-	-
C	0.0152	-	-
Sn	1.31	1.35	1.35

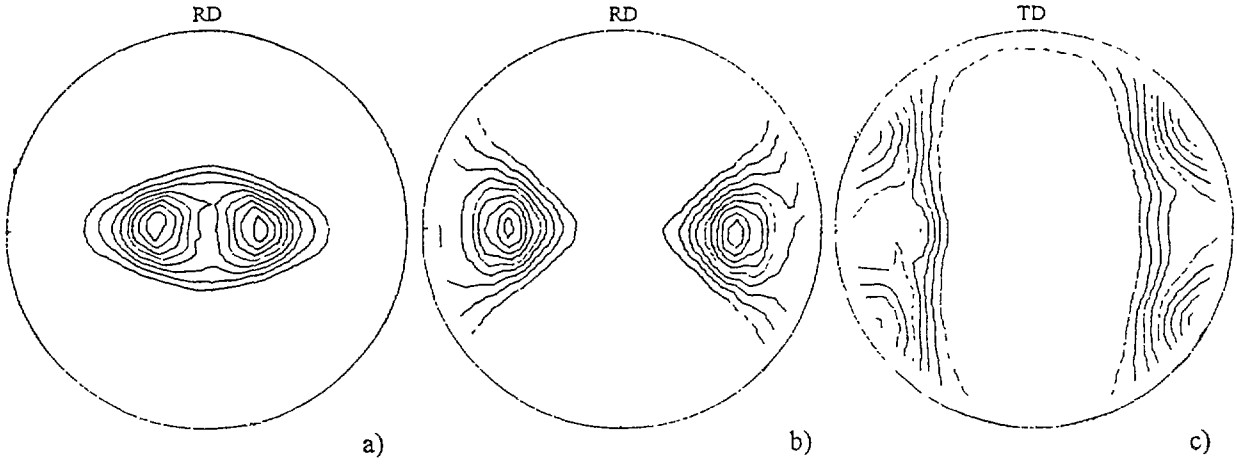

a)

	f_{002}	f_{100}	f_{110}
N	0.621	0.200	0.248
L	0.119	0.427	0.404
T	0.260	0.373	0.348

b)

	f_{002}	f_{100}	f_{110}
N	0.591	0.278	0.256
L	0.143	0.343	0.367
T	0.267	0.378	0.377

c)

	f_{002}	f_{100}	f_{110}
N	0.585	0.253	0.233
L	0.136	0.454	0.448
T	0.279	0.294	0.319

FIG. A1-5. (00.2) pole figures and tables of f-factors for Cezus recrystallised Zr-2 (material OM44) from the a) normally (N) oriented sample, b) from the longitudinally (L) oriented sample and c) from the transversely (T) oriented sample.

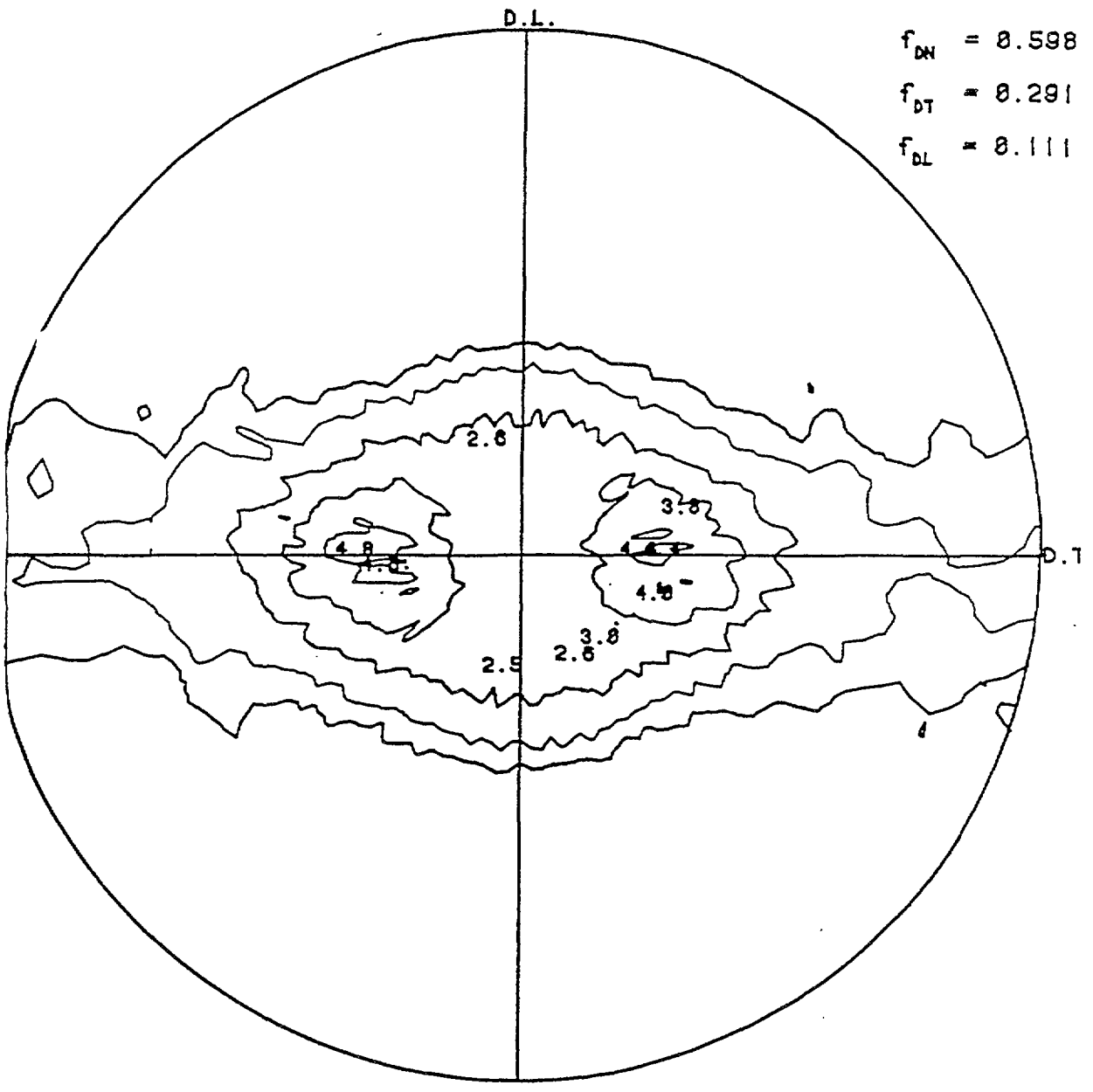

FIG. A1-6. (0002) pole figure and f-factors provided by Cezus, regarded as typical for their sheet material.

Appendix 2

CHARACTERISATION OF MATERIALS BY CHINESE PARTICIPANT

A2.1. SAMPLING AND ANALYSIS PROCEDURE

In order to analyse the influence of various microstructural factors on SCC behaviour, specimens cut from the tested tensile samples were used to examine the grain size, texture, second phase particles and fractographes. The method is described in detail below:

A2.1.1. Grain size analysis

A slice about 10mm×10mm was cut from each sample to prepare for metallographic analysis, as shown in Fig. A2.1. After grinding and polishing mechanically, the slice was eroded by first electropolishing and then anodizing to show up the grain boundaries clearly. A MeF-3A metallographic microscope was used to observe and record the grains.

A2.1.2. Second phase precipitates

Small slips about 3×7mm were cut from the tensile specimen as shown in Fig. A2.2 to be used to prepare the thin foils for TEM. Thin foils were obtained by first mechanically grinding, then chemically thinning with a solution of mixed nitric acid and hydrofluoric acid (HNO_3:HF:H_2O=45:10:45, vol.) until a thin disc was produced, 3mm in diameter. Finally, the foils were polished with a jet electropolishing unit. The electrolytic bath consisted of 85% CH_3COOH and 15%$HClO_4$ and the polishing voltage was 35-40V, DC. A TEM-200CX was used to analyse the morphology, distribution and size of the second phase precipitation.

A2.1.3. Fractographic analysis

The stress corrosion cracking (SCC) growth tests had been stopped when the length of crack reached 5-6mm. The samples which had been tested were broken open along the crack after cooling with liquid nitrogen. An AMRAY 1845FE SEM was adopted to examine the fractograph.

A2.1.4. Texture determination

Texture samples were cut from tensile specimens in accordance with Fig. A2.3, and then chemically polishing using a mixed solution of nitric acid, hydrofluoric acid and water. Specific orientations of specimens were used to produce direct pole figures and f-factors f_n, f_r f_t, as shown in Fig. A2.3.

A2.2. EXPERIMENTAL RESULTS

A2.2.1. Grain size and morphology

The grain size of four materials are given in Table A2.1. It was found that, for Zircaloy in the recrystallized and stress-relieved states, the grain size was obviously different. The grains in the recrystallization annealed material tended to have equiaxed grains, whereas the grains in the stress-relieved material were mostly elongated in the rolling direction. The extent of recrystallization in the OM40 and OM42 materials was reater than the OM44 material (Fig. A2.4).

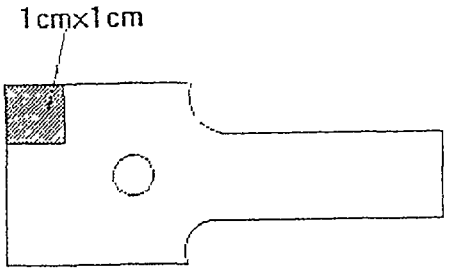

FIG. A2-1. Metallographic specimens.

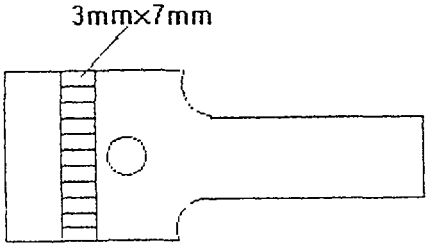

FIG. A2-2. Specimen cut for TEM foils.

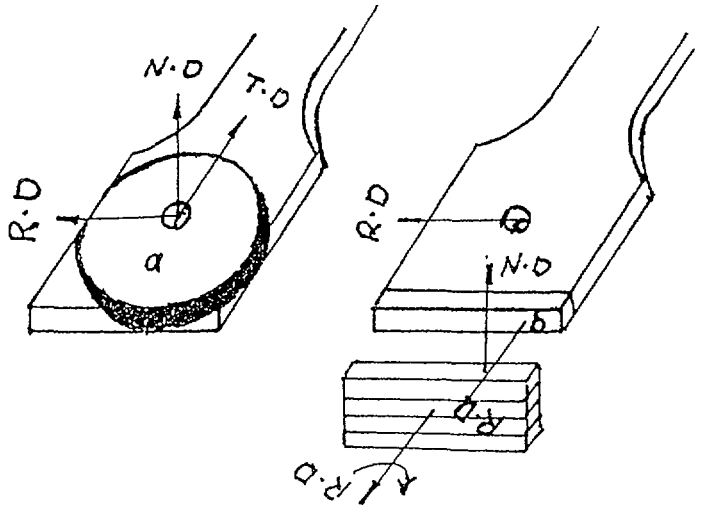

FIG. A2-3. Sample preparation method for texture determination.

TABLE A2-1. THE AVERAGE SIZE OF GRAINS

No.	Material	Average grain size (μm)
OM40	Zr-4, RXA	5.6
OM41	Zr-4, SRA	3.3
OM42	Zr-2, RXA	6.3
OM44	Zr-2, RXA	4.8

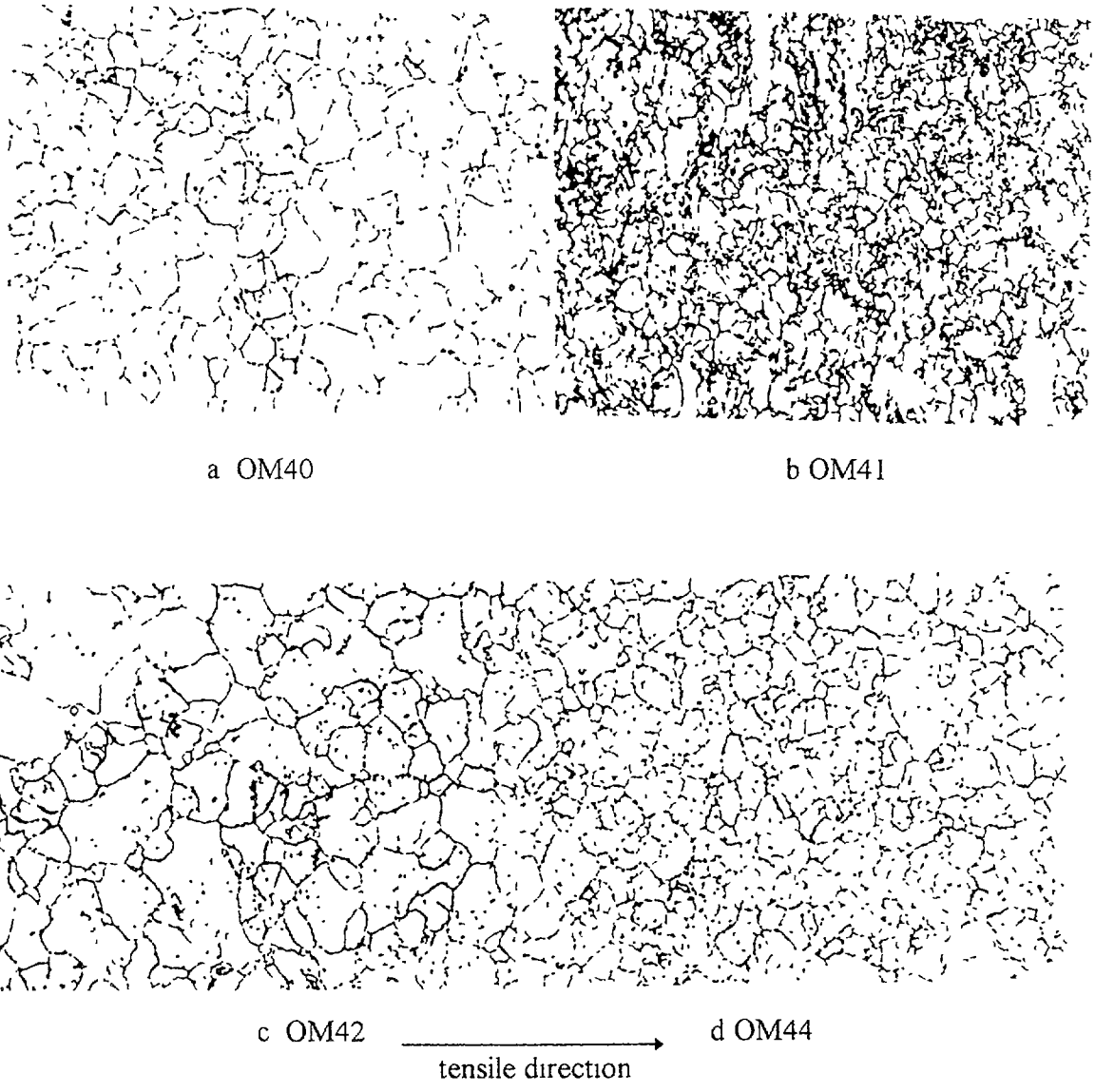

FIG. A2-4. Microstructure of the different Zirconium alloys.

A2.2.2. Second phase precipitates

The average value of the precipitate size in the four materials was calculated and is given in Table A2.2 The precipitates in annealed Zircaloys can be observed by transmission microscopy. It was observed that the precipitates in OM40 (Zr-4, RXA) were very fine and were dispersed randomly in the matrix, most of them within the grains Precipitates could be observed both within grains and at grain boundaries in OM41 (Zr-4, SRA). The size and distribution of the precipitates OM42 (Zr-2, RXA) and OM44 (Zr-2, RXA) were very similar (Fig. A2 5)

TABLE A2-2. AVERAGE VALUE OF SECOND PHASE SIZE

No.	Material	Second phase size (μm)
OM40	Zr-4, RXA	0 095
OM41	Zr-4, SRA	0 108
OM42	Zr-2, RXA	0.094
OM44	Zr-2, RXA	0.096

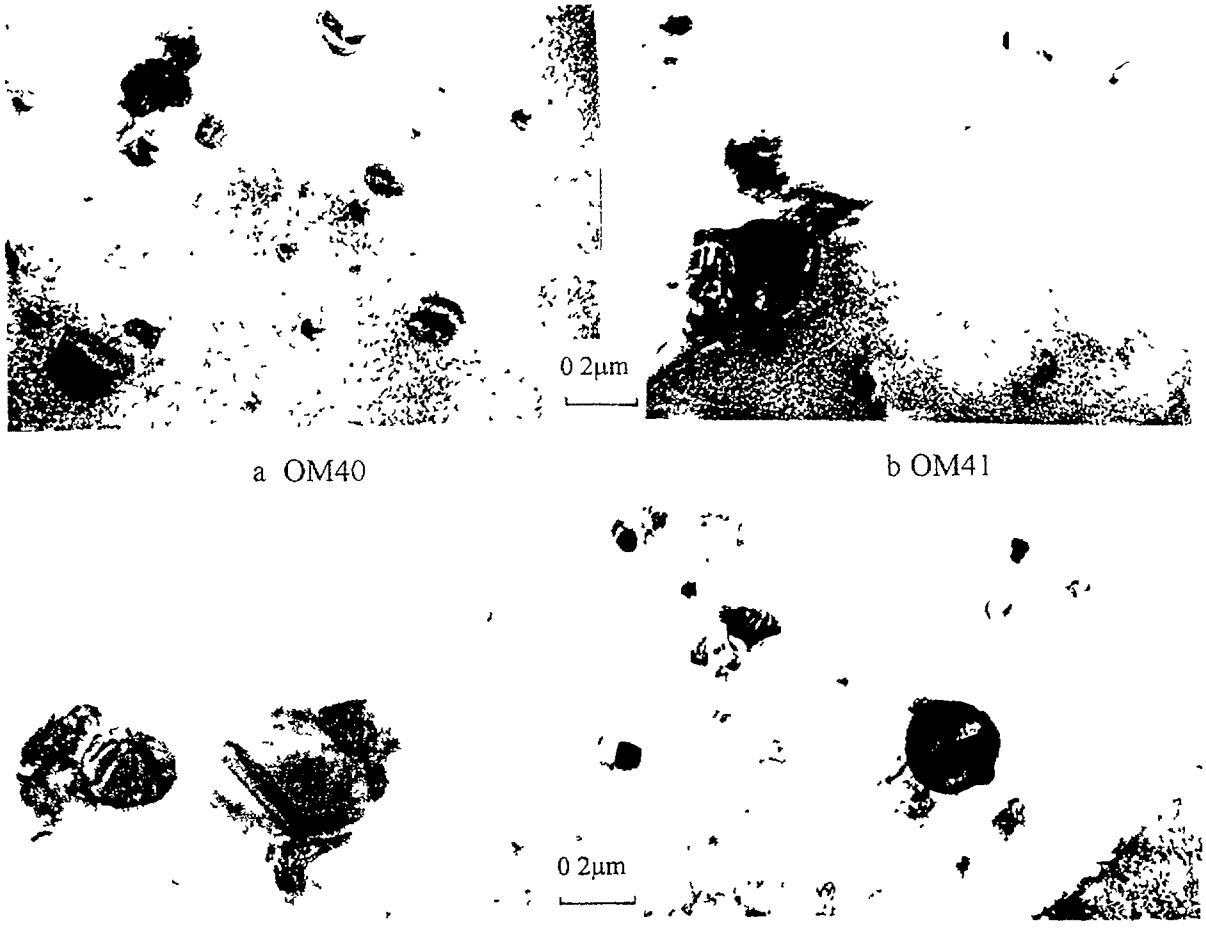

a OM40 b OM41

c OM42 d OM44

FIG A2-5 TEM image of the second phase particles in Zirconium alloys

A2.2.3. Texture

The (0002) pole figures were determined on OM40, OM41, OM42 and OM44 samples, as shown in Fig. A2.6. Texture parameters are given in Table A2.3. The texture of the material was defined by the deviation angle ϕ^* of the c-axis orientation maxima, i.e. from the plate's normal direction to the tensile direction.

TABLE A2-3. TEXTURE PARAMETERS

Sample	Material condition	Texture			
		ϕ^* (deg.)	f_t	f_n	f_r
OM40(Zr-4)	RXA	40	0.330	0.549	0.123
OM41(ZR-4)	SRA	35	0.300	0.607	0.098
OM42(ZR-2)	RXA	35	0.308	0.580	0.114
OM44(ZR-2)	RXA	30	0.261	0.620	0.124

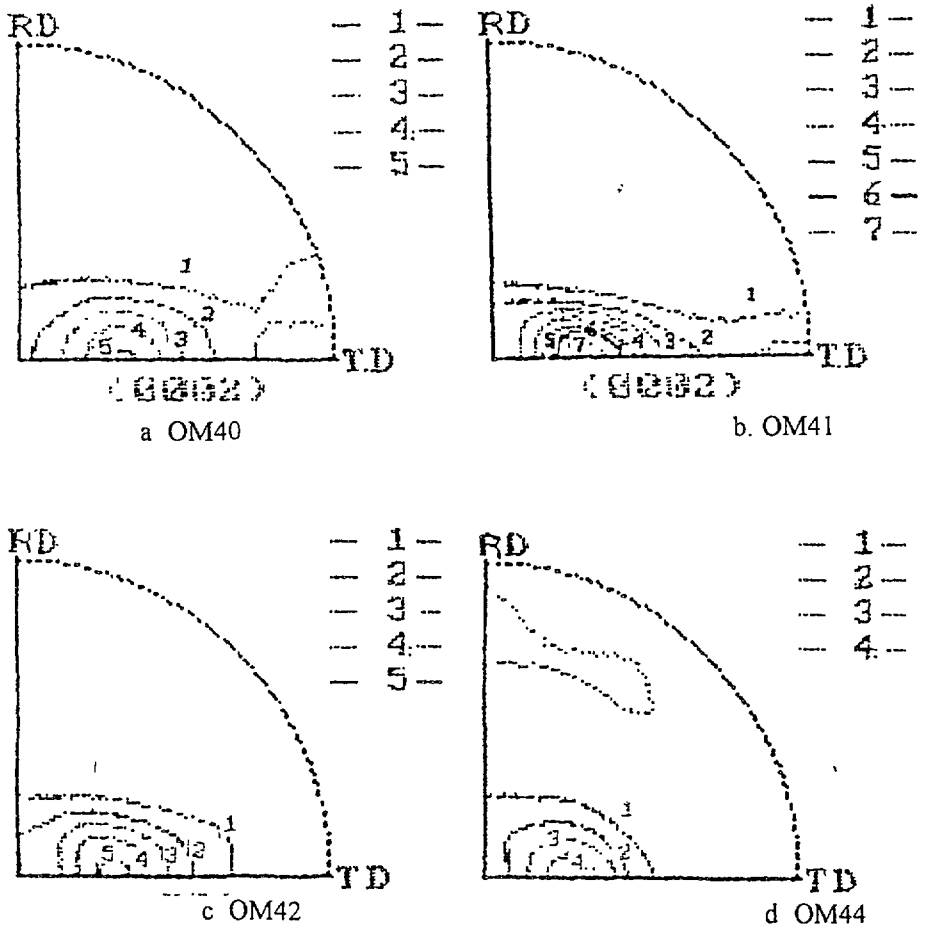

FIG. A2-6. (0002) pole figures of OM40, OM41, OM42, OM44 samples.

Appendix 3
TEST MATRIX

The purpose of the test programme was to investigate the effect of temperature, iodine concentration and stress on SCC crack propagation on the range of available materials. Three temperatures and three iodine concentrations were chosen for study. The temperatures chosen were 300, 350 and 400°C; the iodine concentrations were chosen to be approximately an order of magnitude apart at 100, 1000 and 10000 Pa partial pressures. These were achieved by heating the iodine in the supply chamber to 40, 65 or 110°C respectively. It was intended that most tests would be done in duplicate, in order to enable experimental scatter in the data to be assessed. The number of tests required to produce results, in duplicate, on all materials at three temperatures and iodine concentrations was beyond the scope of this CRP. The decision was therefore taken to concentrate the test matrix on the recrystallised and stress-relief annealed Zr-4 from Teledyne Wah Chang and the recrystallised Zr-2 from Cezus, with a few exploratory tests on the other available materials. The tests that were completed are summarised below. All these were on specimens in the TL orientation.

A3.1. ZIRCALOY-4 MATERIALS

A3.1.1. Recrystallised Zr-4 from Teledyne Wah Chang (OM40)

	100 Pa I_2	1000 Pa I_2	10000 Pa I_2
300°C	X	x	
350°C	X	x	
400°C	X		

A3.1.2. Stress relief annealed Zr-4 from Teledyne Wah Chang(OM41)

	100 Pa I_2	1000 Pa I_2	10000 Pa I_2
300°C	x	x	
350°C	x	x	x
400°C	x	x	

A3.1.3. Recrystallised Zr-4 from Cezus (OM45)

	100 Pa I_2	1000 Pa I_2	10000 Pa I_2
300°C		x	
350°C		x	
400°C			

A3.2. ZIRCALOY-2 MATERIALS

A3.2.1. Recrystallised Zr-2 from Cezus (OM44)

	100 Pa I_2	1000 Pa I_2	10000 Pa I_2
300°C	x	x	x
350°C	x	x	x
400°C	x		

A3.2.2. Recrystallised Zr-2 from Wah Chang (OM42)

	100 Pa I_2	1000 Pa I_2	10000 Pa I_2
300°C			
350°C		x	x
400°C			

Towards the end of the CRP, each participating laboratory also performed an investigation of the effect of texture on stress corrosion crack propagation rate. Tests were performed in duplicate on specimens of stress relief annealed Zr-4 (material OM41) in the TL and LT orientations under the same test conditions of 350°C and 1000 Pa I_2. The subsidiary aim of these tests was to monitor the success of the technology transfer element of the CRP by establishing the magnitude of the scatter between the test results from each laboratory after each had become more proficient in their experimental technique through experience of building and operating their facilities.

Each participating laboratory also performed tests to establish the magnitude of primary and secondary creep and its contribution to apparent crack propagation as monitored on the potential drop crack monitoring equipment. A specimen of each orientation (TL and LT) of the stress-relief annealed Zr-4 was exposed in an inert atmosphere at 350°C to a load typical of the initial load in the SCC tests. Primary and secondary creep were monitored via a change in potential across the crack opening (and apparent change in crack length). The load was then increased in steps typical of those used in the SCC tests and primary and secondary creep was again measured. Any voltage change after loading in the SCC tests which did not significantly exceed that in the creep test could then be eliminated from the crack propagation results.

CONTRIBUTORS TO DRAFTING AND REVIEW

Bramwell, I.	AEA Technology, United Kingdom
Cox, B.	University of Toronto, Canada
De, P.K.	Bhabha Atomic Research Centre, India
Di, Zhongxin	Nuclear Power Institute of China, China
Ghosal, S.K.	Bhabha Atomic Research Centre, India
Haddad, R.	Comisión Nacional de Energía Atómica, Argentina
John, J.T.	Bhabha Atomic Research Centre, India
Lemaignan, C.	CEA, France
Li, Cong	Nuclear Power Institute of China, Chengdu, China
Li, Qiang	Nuclear Power Institute of China, China
Loberse, A.N.	Comisión Nacional de Energía Atómica, Argentina
Maruffo, S.	Comisión Nacional de Energía Atómica, Argentina
Novikov, V.	Research Institute of Inorganic Materials, Russian Federation
Palmer, I.	BNFL, Salwick, United Kingdom
Pan, Ying	Nuclear Power Institute of China, China
Peng, Qian	Nuclear Power Institute of China, China
Peng, Xiaoming	Nuclear Power Institute of China, China
Ritchie, I.	International Atomic Energy Agency
Ryu, Woo-Seong	Korea Atomic Energy Research Institute, Republic of Korea
Tice, D.	AEA Technology, United Kingdom